WAVE TRANSFORMATION OVER OBSTACLES AND ITS INFLUENCE ON A TIDAL TURBINE.

Jose Manuel Rivera Camacho

Thesis submitted for the
Degree of Doctor of Philosophy

Energy Systems Research Unit

Department of Mechanical & Aerospace Engineering
University of Strathclyde
December 20 2022

University of Strathclyde Engineering

- 己六才より物の形状を写の癖ありて半百の此より数々画図を顕すといえども七十年前画く所は実に取るに足ものなし
七十三才にして稍　禽獣虫魚の骨格草木の出生を悟し得たり
故に八十六才にしては益々進み九十才にして猶其　奥意を極め一百歳にして正に神妙ならん与欠　百有十歳にしては一点一格にして生るがごとくならん願くば長寿の君子予言の妄ならざるを見たまふべし - Hokusai

  “I have drawn things since I was 6. All that I made before the age of 65 is not worth counting. At 73 I began to understand the true construction of animals, plants, trees, birds, fishes, and insects. At 90 I will enter into the secret of things. At 110, everything - every dot, every dash - will come to **life**”

- τὸν ἥλιον τοῖς ὁρωμένοις οὐ μόνον οἶμαι τὴν τοῦ ὁρᾶσθαι δύναμιν παρέχειν φήσεις, ἀλλὰ καὶ τὴν γένεσιν καὶ αὔξην καὶ τροφήν, οὐ γένεσιν αὐτὸν ὄντα...
καὶ τοῖς γιγνωσκομένοις τοίνυν μὴ μόνον τὸ γιγνώσκεσθαι φάναι ὑπὸ τοῦ ἀγαθοῦ παρεῖναι, ἀλλὰ καὶ τὸ εἶναί τε καὶ τὴν οὐσίαν ὑπ᾽ ἐκείνου αὐτοῖς προσεῖναι, οὐκ οὐσίας ὄντος τοῦ ἀγαθοῦ, ἀλλ᾽ ἔτι ἐπέκεινα τῆς οὐσίας πρεσβείᾳ καὶ δυνάμει ὑπερέχοντος - Plato

  “The sun **light** provides not only the power of being seen for things seen but, as I think you will agree, also their generation and growth and nurture, although it is not itself generation...
  Similarly, with things known, you will agree that the good is not only the cause of their becoming known but the cause that they are, the cause of their state of being, although the good is not itself a state of being but something transcending far beyond it in dignity and power”

- La obscuridad del sepulcro no es mas que el refuerzo para el glorioso sol y la oscuridad de la noche, sirve para revelar el esplendor de las estrellas - Nezahualcoyotl

  “The **darkness** of the sepulchre is but the strengthening couch for the glorious sun, and the obscurity of the night but serves to reveal the brilliancy of the stars.

Declaration of authenticity and author's rights

This thesis is the result of the author's original research. It has been composed by the author and has not been previously submitted for examination which has led to the award of a degree.

Signature: _____

Date:_____11/12/2022_____

DEDICATION:

To the three small brothers that I love, you will be always my pride. To a Geographer and a Pedagogue, which filled me with books my whole life and supported me during all these years. I still remember many of those books.

To my uncle who always found a way to keep me engaged with science and politics.

To my secondary school professor of Maths, Msr Rosario who never gave up on teaching algebra to the worst pupil she had.

To the ones that dedicated time that I think will never be able to re-pay properly as Tjiana, Seli, Valentina, Alessandra, Mariana, Atenea, Mona, Ioanna, and to all their circle of friends and family that shared time with me; a list so large that included times where we shared Christmas, birthdays, dinners or even a simple talk. You all have a piece of this small heart.

To the ones that made me come here following their trail, Mariel, David, and Jonathan which are family and friends even in the distance.

To Enrique, Alex, Gerardo, Steph, Julie, Geddes, Liviu, Sofia, Erin and many others for their attention given in many situations when need it.

To Professors Gerardo, Blanca, Alethia, Maribel, Aurelio, Casas, Alejandro and Norma who supported me, taught me and pushed me to keep moving forward. Thanks to all people in the automation department. To the people in the marine energy group at Strathclyde university.

To Dr Rodolfo Silva, Col. E. Jensen, and people from diverse institutions that I bothered with questions through all these years, the list is large that I could never finish with this. Beware all of you, because now I have 10x times more questions than before!.

To the large list of Oceanographers, Linguists, Biologists, Programmers, Physicists, people in public/private service, Botanists, Military, Economists, Engineers, Astronomers, Teachers, Archers, Musicians, Writers, and people in Arts and Social sciences that I admire and consider people that are deeply valuable to me. To all of you thanks for enlarging my world and giving meaning to my search.

To Patrick who passed too soon and many others that very sadly left us this past two years, also thanks to all his family, especially Eileen and Mahiri.

To Kristen, Katje, Yazin, Amira, Maryam and their families for adopting me as soon as I arrived at the office, and of course the many amazing people I knew since then as Andrew, Laura, Martin, Rida, Almahdi, Noor, Khaula, Seabo, Behrang, Paulo, Sarah, Donnagh, Ivy, Carmina, Hayam, Michelle, etc.

To Javy, Yose, Rafa, Elsa, Rolando, Israel, Diego, Abelardo, Vero, Ricardo and many other friends in Mexico.

To all my friends around the Pacific, Atlantic basins, and people with whom I've made friends in the everyday life.

To the ones that I have left behind.

And finally to **my ignorance** cause without it, I would not be here trying to satisfy my need to know just a bit more.

List of figures

Page

Chapter 1

Chapter 2

Chapter 3

Chapter 4

Chapter 5

Chapter 6

Chapter 7

Appendix

List of tables

Chapter 1

Chapter 2

Chapter 3

Chapter 4

Chapter 5

Chapter 6

Chapter 7

Appendix

Acknowledgements:

I would like to thank SENER and CONACyT, as without their support this degree would not be possible. Thanks also to the government that held the belief that renewables, energy and sustainability should be a priority to invest. Thanks to the team behind all the work that makes it possible for us to conduct research abroad, not only the institutions but the broad group that directly or indirectly made this possible. To all institutions whose data and tools helped me as the National Oceanic and Atmospheric Administration, the Scripps Institute of Oceanography, the United States Geology Survey and the International Hydrographic Administration.

Thanks also to all the team behind the tidal and marine energy research at the University of Strathclyde. Specially thanks to my supervisor Mr Cameron Johnstone and also Dr Stephanie E. Ordonez Sanchez, as without their guidance and freedom they gave me this work would not be possible. Would like to thank also to the people behind the department of Naval Architecture, and Ocean Marine Engineering, as they provided us with the experimental facilities.

To Ms Diane McArtur and all her team behind the administrative process during my PhD. To Dr Sandy Day and Dr Shaisuai Dai for their help during the experimental phase of my thesis, as also thanks to the people on the Engineering department workshops.

Abstract

Tidal and marine energy has been explored extensively in recent years. Part of the studies made in the area includes the resource available, the design challenges, the environmental impact and other important areas for research and development. One of these research areas focuses on the mechanical response of tidal turbines to different operational environments. The operational environment can depend on factors such as wave weather, turbulence and flow velocity. The changes in these factors will affect the mechanical performance of the device.

This thesis explores the changes in the mechanical performance markers, which are the turbine torque and thrust, to swell wave systems with moderate to low amplitude. The work also explores how a non-even seabed, characterised here as a regular bathymetry rise, can affect the wave parameters such as wave height and wavelength, changing the unsteady flow before and after the geographical obstacle and resulting in a different mechanical turbine response.

The thesis first explores the wave propagation over an uneven bottom using classic theory and expanding into the subject with experiments and validation of the theories using physical scenarios resembling normal turbine deployment in the ocean. As the classical theory of wave propagation is frequency non-variant, theories are explored to expand comprehension of the phenomena by addressing frequency variant solutions under larger depths relative to the wave wavelength, which in our case cover periods from 6s to 14s at depths between 28m and 42m.

The formulations explored are validated against experiments in a wave tank. Wave conditions are designed to scale wave heights, depths, and periods to the mentioned depth to ensure a good representation of the dynamic behaviour of the waves propagating in the tank. The experiments show how frequency variant theories can predict more closely the changes

in the wave amplitude and wavelength when a wave propagates over obstacles of limited length. Amplitude changes, and also changes in the wavelength and velocity, are measured and detected. However, the latter two prove to be harder to measure. The changes in both the amplitudes and lengths correlate in many cases to each other in the experiments. When the wave path has been obstructed, the length for larger waves is reduced and their amplitude increases consistently for larger waves. Validation shows a close relationship between frequency variant theories and the results obtained in the test campaign.

The formulations validated are then used to modify a Blade Element Moment Theory (BEMT) model which calculates the mechanical torque and thrust of a tidal turbine. A sensitivity analysis is carried out using the BEMT model to understand how different parameters such as the wave height, current, wave period, and depth ratio between the original depth and the obstacle affect the mechanical turbine response. The results show how wave height is the most important parameter and current velocity is the second. The formulations are then used to model a specific location for tidal turbine deployment in a real case study with data gathered from real buoy systems.

Simulation for the case study occurs in three types of wave weather using long swells with low amplitude, smaller period swells with steeper heights, and a mixed case using some wind-wave components with larger heights. The model output shows the large influence of swells on the mechanical performance of the turbine, being the largest contributor to the torque and thrust variation with the thrust and the torque being 60% and 40% larger, than conditions with shorter periods but steeper waves. The study also shows how the inclusion of a simple irregular seabed interacting with large wave components can affect the expected mechanical response in our model. The results show how these small changes, paired with the wave propagation under larger wave heights, change the simulated mechanical response by 50% of their original value when we compare the different responses to each type of wave weather.

Work made here seeks to highlight the importance of other environmental factors different than extreme wave loads, current velocity or turbulence that can affect the mechanical behaviours of a tidal turbine device. Particularly it aims to expand our understanding of how the sudden changes in a field of waves produced by local bathymetry irregularities, could modify the forces on a tidal turbine device by integrating with the waves which later propagate into a tidal turbine. These factors could prove to be important to the turbine fatigue or loads depending on their relative impact compared to other already explored factors such as extra waves.

Nomenclature

Symbol	Quantity	Symbol	Quantity
ρ	Density	Δ	Increase
g	Gravity	L_o	Initial wavelength
ω	Angular frequency	$\therefore$	Therefore
a	Amplitude	$\cdot$	Dot product
k,λ	Wave number, wavelength	i	Imaginary
t	Time	&,^	Logical and
T,f	Period, frequency	$x^+ \rightarrow a$	Goes to a from right
x,y,z	Coordinates or directions	$x^- \rightarrow a$	Goes to a from left
$\oint$	Closed area integral	~	Approximately
∇	Gradient	$\neq$	Not equal
$\frac{\partial}{\partial x}, \frac{\partial}{\partial y}, \frac{\partial}{\partial z}$	Partial derivate	$E[\varphi]$	Energy on φ
$\|\|$	Logical or	η	Wave surface profile
$\Longleftrightarrow$	Logical, if and only if	τ	Period
$\rightarrow$	Tends to	Σ	Sum of terms
>>	Larger than, used here to denote quantities 2 orders of magnitude larger.	*	Product
<<	Smaller, used here to denote quantities 2 orders of magnitude smaller.	P	Polynomial
$\perp \perp$	Logical not related	O	Order of
$\nexists$	Non-existence	Xm,Xs	Non-defined lenght, non-defined time
φ	Potential function	σ	Standar deviation
h_d,h_i	Upstream depth	σ’	Viscosity
h_t,H	Downstream depth	U∞	stream velocity
Kt	Coefficient of transmission	30º	º Denotes grades in a circle in clockwise direction
Kr	Coefficient of reflection	-123.5,33.5	Latitude, longitude pair

Symbol	Quantity	Symbol	Quantity
Tr	*Thrust*	*Tq*	*Torque*

Note: This thesis expresses all quantities as MKS units.

1 Introduction

1.1 Tidal turbines and marine energy

Due to the high demand for energy in the last four decades, there has been a race in energy production; industries like gas, fracking, offshore wind and solar have broadened their market footprint. Promising projects like hydrogen-based technologies have been rushing to occupy the market, with possible solutions in the feasible future to feed our energy needs. During the last two decades, the world also saw a set of looming environmental problems. Part of those challenges is climate change, pollution, and the extinction of hundreds of species. The world governments, realising the coming challenges to the environment, energy, and economy, have shifted their research and focus to carbon-neutral technologies and renewables. In the solar-wind sector alone, growth has been considerable from 2010 to 2020, increasing their participation from less than 2% to more than 10% by 2021 [1].

Technological developments during the last 30 years gave rise to another promising new renewable technology housed in our planet's seas: marine energy. Marine energy comprises technologies able to harvest energy from the sea, and the energy that can be harvested through mechanical or chemical means is one of the largest available forms of energy on the planet. Two of the main technologies in the field are tidal stream and current devices. Tidal streams and currents use the ocean flows to set a turbine in motion, and the flows interact with the blades of a rotor producing movement. The movement is transmitted to a generator through a shaft. The theoretical energy to be harvested is calculated to be around 45,000 TW for all ocean-based technologies, with a potential that could be larger than 130,000 TWh per year according to IRENA [1]. The potential for the more mature technologies is theoretically divided into approximately 2,985 GW net and 3,702 GW of gross energy wave energy as mentioned by Mørkt et al [2] and theoretical potentials between 1 TW for tidal stream [3] to 3 TW per

year [4] if tidal range is added. The numbers for potential energy can have a wide variation for both. Specifically in the case of tidal energy, which is addressed in this work, they vary depending on the method used to quantify the resource.

The resource can be quantified as a theoretical resource or potential power to be extracted. Most of these methods evaluate a general simplified model of the tidal components, flow, and arrays of tidal devices with simple fluid interactions. An important case is the Pentland Firth, where the study made by Drapper et al [5] provides a theoretical potential of 4.2 GW, placing turbines across the strait and calculating the maximum available power**.** The studies are however based on the method proposed by Garret and Cummins [6], calculating the average power produced by the turbine and taking into account the turbine drag. A more realistic approach to the amount of theoretical power available is given when the model includes the interaction between the turbine blades and the fluid, the reduction of the flow velocity as it passes through it, non-steady flow, and other parameters, reducing the power available and giving a more practical power extraction [7]. Adcock et al found the available power to be around 1.9 GW in the Pentland Firth [8]. However, exploiting all tidal resources is still far from possible due to economical limitations such as project cost, energy price, maintenance cost, interconnection, and other factors such as the variability of flow velocity. These factors reduce the economical viability, giving an even lower quantity or “economically feasible resource”.

Another challenge for these new technologies is the predictability of the resources. The resource characterisation and its availability play another important role in the amount of available energy. Even if tides are predictable with the main constituents identified in the literature [9], the prediction of the flows produced by them is not as accurate as the tides. Studies carried out by Polagye et al [10] have found variations in the flow that can be predicted with harmonic analysis, first in the current flow with variations in times scales around one hour, second by turbulence, with variations of half a meter in peak currents of 2.0 m/s, and third, spatially along the sea floor.

Despite all constraints, some companies already offer commercial-ready devices, and many others are still in development, with many areas still in the early stages of research. Areas such as the mechanical response to large-time deployment and failure detection are still being researched. As most devices are expensive, solutions have been developed to model their mechanical responses, using computational-mathematical models. As modelling can be time consuming and might require powerful hardware, special attention has been given to fast deployment tools. Improvement in the tools and models to describe the device's response to the flow would help to reduce costs and improve deployment. These improvements have been an important area of development in the industry and research, to understand not only the device behaviour but also the ocean fluid dynamics. A basic diagram of a tidal turbine can be seen in Figure 1.1.

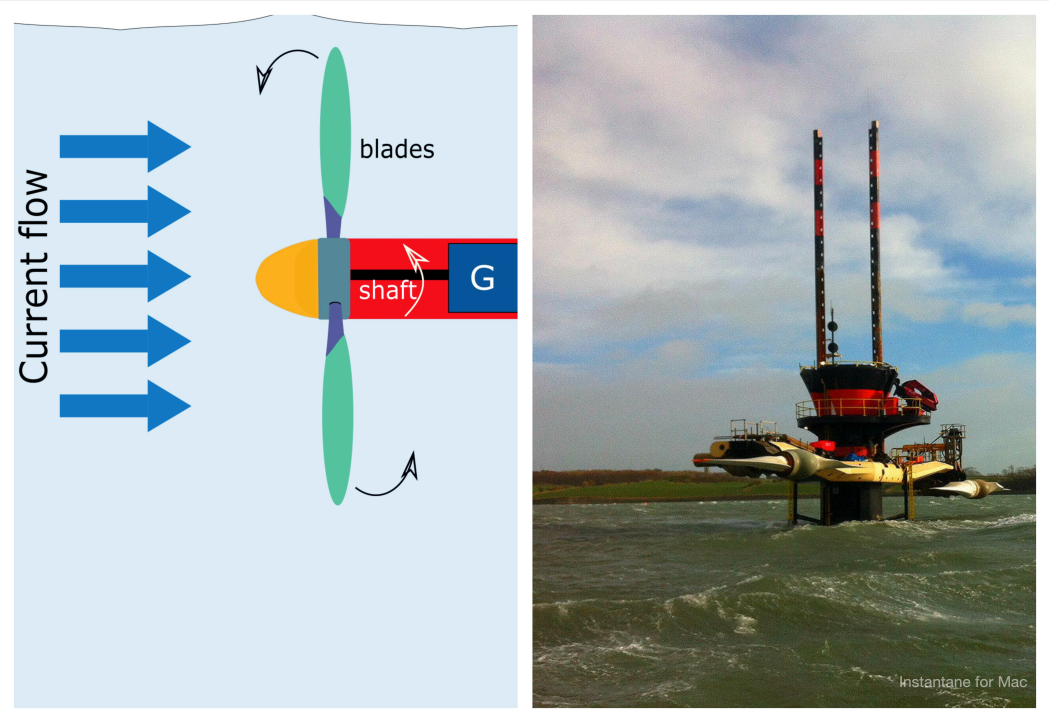

Figure 1.1: Left: basic general diagram of a stream tidal turbine. Current flows will exert a force over the turbine blades, causing them to rotate. The movement is then transferred to a generator G through a shaft. Right: image of the SeaGen tidal turbine, its blades shown in a resting position above the water.

The inner mechanics of the machines are complex, as the device is subjected to the forces exerted by the sea. The device's mechanical

performance will vary depending on the ocean hydrodynamics of the basin where it is placed. As we mentioned, the principal forces analysed here are the ones produced by waves.

The waves produce unsteady velocities in the water column, and these changes will have an impact on the underwater flow, composed of the waves and the current. The results of the research related to flow modelling have proved useful for the modelling and design of tidal devices. The positive results have helped to install tidal stream devices in recent years which are more compact and easier to deploy than the first large tidal stream devices. The results of these last developments led to the blooming of studies related to areas as diverse as social, biological, and natural sciences, legislation, and engineering. In engineering, the areas of mechanical performance, ocean weather monitoring, geographical survey, and device modelling saw a big leap forward. The device's modelling uses computational tools such as BEMT, RANS, CFD, and lift theory, and most of these tools have already matured into robust methods that help to study the turbine's hydrodynamics.

BEMT is known to give satisfactory results at faster speeds, compared to other available methods such as BEM-CFD, reporting divergences in the power coefficient of the turbine of 5.4% [11]. However, BEMT is not capable of analysing as complete and detailed a structural interaction as CFD. Despite this, BEMT is still regarded as a method that can help to make key decisions in the early stages of turbine modelling.

However, there are still many challenges, and some of them can be linked to local constraints in the area of deployment, such as turbulence or geographical constraints that can modify the flow or waves around the turbine.

1.2 State of the problem

Tidal stream turbines will be affected by the oscillation of the velocity field and a significant component of this oscillation will be produced by the waves. Medium depths can shelter devices against local wind waves, as the wave influence will decay fast into the water column; however, this will not be true for larger systems. Many studies have been conducted on extreme weather conditions with large amplitude waves; however, little attention has been given to the continuous forces and loads produced by swell fields.

Swells possessing larger wavelengths could reach devices installed at large depths. The possible interaction between the larger wave systems and the underwater obstacles links our problem to the device's placement, as the wave's physical characteristics will change after crossing seafloor irregularities. The seafloor profile or bathymetry is known to affect the wave amplitude, but this could also have important effects on the wavelength and wave period and subsequently on the turbine mechanical responses which are sensitive to the unsteady flow produced by the waves.

The work conducted here is focused on the study of the far swell field as shown in Figure 1.2, as its large wavelengths could reach the seafloor.

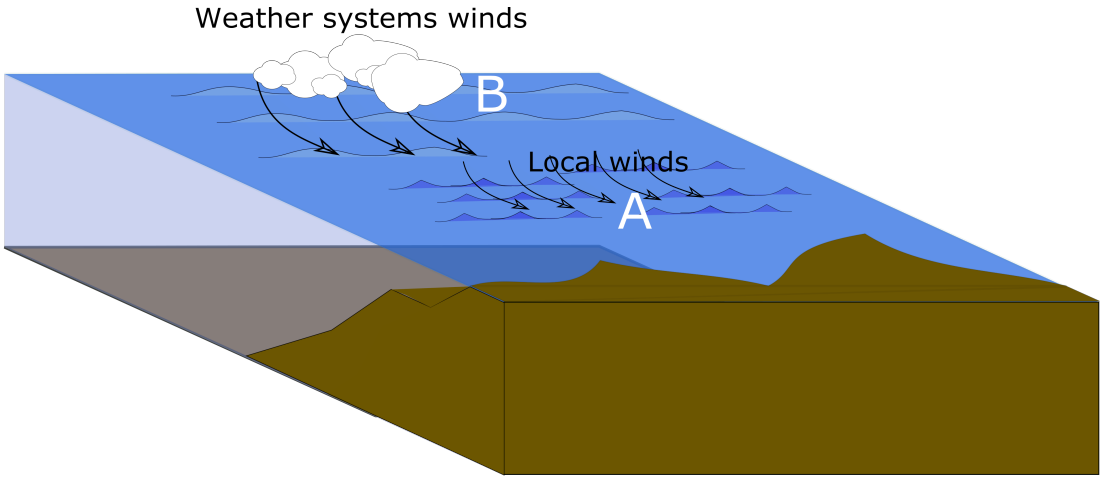

Figure 1.2: The distant wave field in zone B is produced by weather systems far away from the coast, meanwhile the local wind or local weather systems in zone A will produce steeper waves called wind waves.

Swell waves are important due to their overall dominant nature in the sea. The swell dominance is mentioned in Chapter 2. Swell systems are always present at most of the world's coastlines. Even on calm days, waves produced thousands of kilometres away in the open ocean will travel to the coast where a tidal device could be deployed. Larger swells will be consequently forced upon obstacles at the bottom of the ocean and this interaction will modify the waves after they propagate over the obstacle, thus modifying the loads subsequently felt by a turbine. This is a case which has not been studied by other authors and could modify the predicted mechanical response of a turbine. It is known that load variation in mechanical components can produce fatigue, and these loads will be transmitted along with the turbine components.

In our case, we can identify two important scenarios:

1. A turbine is exposed to wave weather that is composed mostly of swell systems and how this component affects the turbine's mechanical response.
2. How a turbine's mechanical response changes when a turbine is placed after or over a sudden change in depth can modify the shape and behaviour of very large wave systems that are able to interact with the sudden shelf rise.

The mathematical modelling of this is presented in Chapter 3, and Chapter 2 introduces the phenomena and provides a literature review of past models and experiments made by other authors.

The hypothesis behind the work can be resumed in two parts, first:

“The mechanical response of a tidal stream turbine to unsteady components caused by long systems with low amplitude will have a different impact on the response of the system from the ones caused by wind waves or steeper systems.” In order to test this, wave systems representing swell systems are

used in a BEMT model along with a sensitivity analysis to compare how a tidal turbine model behaves in two different wave conditions.

And the second:

“A long wave propagating from point A to point B crossing an obstacle will modify its amplitude and period, then any turbine placed in these two different points will experiment with two different mechanical responses to the loads caused by the changes in the wave parameters.” This is tested by experiments made in a wave tank measuring wave propagation over an obstacle, where the obstacle and depth are scaled to conditions that could resemble a tidal turbine deployment. These conditions are then used in a tidal turbine model to observe the changes in the mechanical response at two different positions, before and after the obstacle.

1.3 Thesis objectives and research questions

As the technology matures and devices are deployed into open ocean areas, different types of wave weather, and possible changes induced over the waves by external factors such as bathymetry changes, could modify the device loads. This will then have an impact on other turbine parts. The unsteady flow and its changes are a vital part of not only the mechanical response but also the energy harvested. The study of these responses and changes under different conditions can help us to expand the understanding of the device response under different physical constraints, which in turn can open other study cases for more complex scenarios.

The main research questions in this thesis are as follows:

A) Is there a given relationship between the changes produced in a wave after it propagates over an obstacle and its incident period?

B) Which variables are important for wave propagation over an obstacle and how do they influence it?

C) Given a tidal turbine placed above a bathymetry change, could the wave trains propagated over the obstacle modify substantially the mechanical performance of the device after the wave trains change some of their parameters such as the wave height?

D) What are the effects of swell systems on the mechanical output of the tidal turbine rotor and its blades, compared to other types of wave weather?

2 Literature review

2.1 Energy, Renewables and Marine Energy

The modern era as we know started with the invention of the steam machine, a pivotal moment that marks the beginning of mankind's production of goods, development of tools, and increasing comfort in ways never seen before. This mechanical revolution needed power and the main resource for this was cheap and abundant energy. Energy by itself is one of the main pillars not only of economic development, but also food production, healthcare, transportation of goods, and technological development. The need for energy to power the different aspects of human development is reflected in its consumption, and the world has increased this consumption drastically by 83 times from the early 19th century to the 21st century [12].

2.1.1 Energy and renewable energy

Our main source of energy has changed during the last two centuries due to the development of new extractive technologies and the amount of power needed by society. At end of the 19th century, the world saw a steady rise in the use of hard coal and lignite. Both sources of energy occupied 95% of the world's commercial value; meanwhile, hydrocarbons were only approximately 2.37%. The beginning of the 20th century saw an inverse proportional change and hydrocarbons and gas won a huge market share [13]. However at the end of the century, other sources of energy such as renewables and nuclear started to shift the energy balance. Nowadays, according to the most recent SDG7 report [14], renewables had a share of 17.5% in the energy market by 2016. The growth experienced by renewable energy was mainly focused on solar, wind, and hydro. The growth of renewable energy markets during this last phase was focused on the American continent, Europe, and East/South Asia, as can be seen in Figure 2.1.

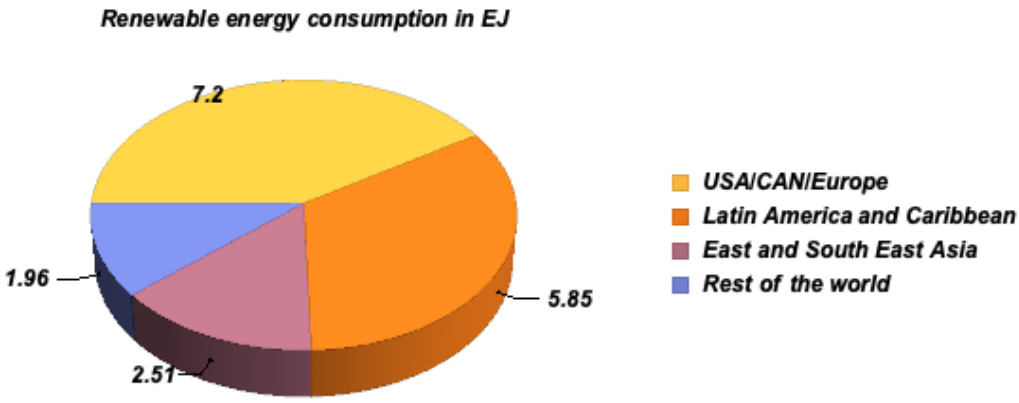

Figure 2.1: Renewable energy market share by world region in ExaJoules, EJoule = 10^{18} Joules

2.1.2 Energy and renewable energy in the last 50 years

Energy and renewable sources of energy became a focus of legislation and development during the past fifty years, and a renewed effort of development came under the banner of multinational organisations. This effort has grown around a set of ideas to secure the world's sustainable growth. The ideas cover a broad range of areas including political, social, economical, energy, and environmental development. Some of these ideas promote openness in the energy market, the increase of renewable energy sources, the need to tackle climate change, and the development of new ways to promote and use low to zero-carbon energy. The main drivers behind this change are climate change, pollution, and a dynamic energy market that seeks to diversify its production while securing cheap prices.

The continuous push to work on these new paradigms of growth increased the renewable energy share and its development. Both processes then began to drop prices to a competitive range against fossil fuels. During these 3 decades, solar and wind saw continuous growth and development. The effort made in this area was bolstered by energy and climate multinational agreements in Kyoto, Paris, and Montreal, despite its shortcomings and the complexity behind its success [15]. It is now at the beginning of the 21st century that a more mature energy market, political willingness, and environmental compromises have made it possible to

increase investment and research in clean energies. As mentioned before, the main winners behind this success were wind and solar energy, but both suffer intermittency depending on climatic factors. Solutions for intermittency have been proposed such as smart grids [16] and support storage [17], [18]. The problems of intermittent renewable energy could be solved if we could rely on a more predictable source of renewable power, the answer to which lies in a stable and periodic energy exchange that occurs in the different areas of the ocean basin.

2.1.3 Marine renewable energy

Marine renewable energy is the area that studies the use of the different forms of energy flux in the ocean to produce electrical energy or mechanical work. The physical principles to use the ocean as a power source are as ancient as mankind, and these methods use the difference of pressure or velocity flows to produce mechanical power. This use of the sea or river flows to produce work has been known by several ancient civilisations. The main mechanics of these ancient devices used water wheel effects, wheels connected using simple transmission mechanisms, to convert the flows into mechanical work. The relationship between tidal flows of water and civilisation goes back to settlements in the Middle East, an area known to sustain tides of considerable magnitude. The use of these tidal devices was linked to harvesting and crops, as the water was used to sustain the fields and the flow to process the crops in ancient communities. Examples of the ancient use of tides are spread around the zone comprising Iran to Greece. Greeks used this principle to power mechanical mills and produce flour [19]. Other important historical places lie in ancient cities such as بَـصرة (al-Baṣrah) in Iraq [20], Εύριπο (Euripus), and Κεφαλλονιά (Cephalonia) where they used tidal devices to mill seeds or crops [21]. Some of these historical places are shown in Figure 2.2, and they still nowadays hold archeological research on the ancient use of tides today [22].

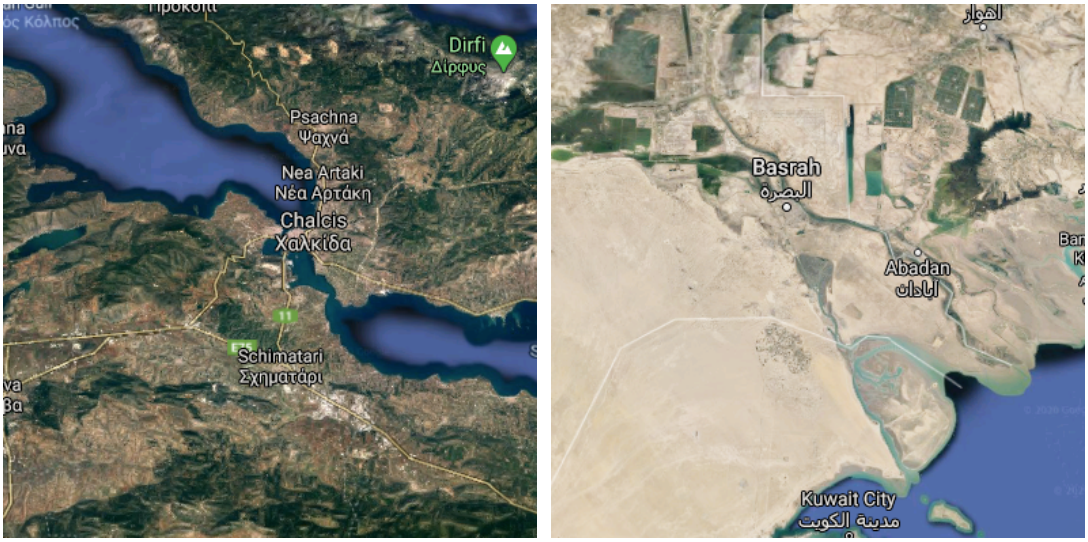

Figure 2.2: Ancient places of tidal energy usage as a means of mechanical work. Left: Euripus, Greece. Right: al-Baṣrah, modern Iraq.

Following advances in the next centuries, the available technology gave rise to tide mills in medieval Europe but it was not until the late 19th century, with the arrival of the first hydroelectric devices, that the modern era of hydrokinetic energy exploitation began. The new devices consisted of an electrical generator connected to a turbine using a shaft, and a flow of water was used to move the turbine. To obtain the water flow to power the turbine, this system uses an artificial basin filled with the convergence of river flows. The artificial structure to contain the water is widely known in engineering as a dam. After the dam is filled to a certain height, the water is released through a set of apertures in the structure. It was not until 1924 that the U.S. government seriously considered harvesting the energy produced by the sea movement using these same mechanics [23]. The proposal used a dam system to contain tides around the northeast coast, but it was never built and in 1966 France became the first country to implement a similar project at La Rance. The French project currently operated by Électricité de France was the last serious development in tidal and marine engineering before the beginning of the 21st century. Over the past 20 years, marine energy development has increased sharply. The renewed effort was sustained not only due to economics, but also due to the maturity reached in diverse areas. Development in natural sciences, engineering, coastal studies, environmental science, biology, and geography and methods in maths,

fluids, statistics, and computing powered this revolution. The idea behind this renewed push is that, given the enormous energy stored at the ocean basin, this could be a reliable source of energy to exploit. The advantages of using the sea to harvest energy are numerous and include its stable source and low carbon footprint.

2.1.4 The source of marine renewable energy

The energy transfer in the sea and the planetary convection are the biggest fluxes of planetary energy annually. The large energy flux in the ocean is due to its vastness, occupying 71% of the planet's surface. The two main phenomena driving this flow are the thermal radiation of the sun and the gravitational Earth-Sun-Moon system. The first will intervene directly in the weather and is the driving force behind the wave systems. The gravitational pull is responsible for the sea-level oscillation better known as a tide. The sun's radiation accounts for at least $1353 W/m^2$ of energy in the upper atmosphere [24], the rest of the energy being absorbed on its trajectory through the ocean surface, covering $361.1 \times 10^6 km^2$. This radiation transmits approximately 36.1 trillion watts, just after reaching the ocean surface. The ocean absorbs this heat via its upper layer, and the heat absorbed through this process is converted into wind, thermal energy, currents, chemical gradients, and mass gradients. This is a very broad range of complex life and chemical processes, shown in Figure 2.3.

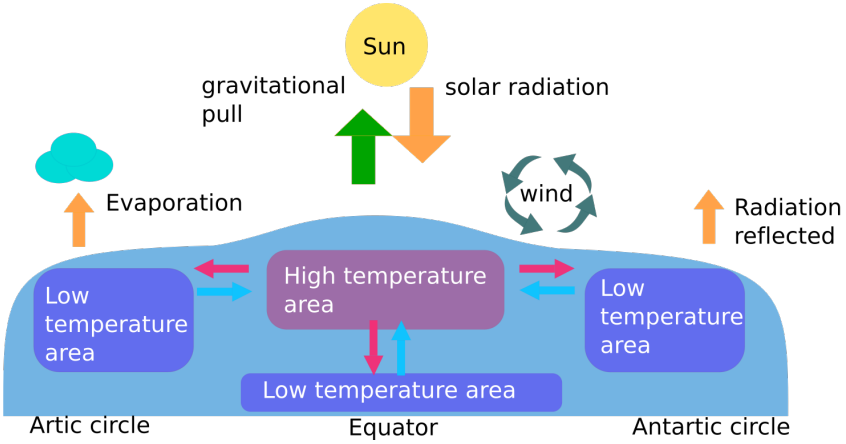

Figure 2.3: Simplified model of the sea-Sun energy exchange.

Tides drive big flows of the water stream, a movement caused by a dilatation on the sea surface which is itself caused by the Sun-Moon gravitational force. The streamflow moves around the planet, and the flow floods vast coastal areas around the world periodically. In some geographical localities, this flow is amplified by the physical on-site characteristics. Energy stored in tides is so large that in the open ocean they can lift the sea surface by $0.5m$. This effect might not sound impressive but if we put it in perspective we can see its real strength. If we model a cylinder of water with an average depth of $3km$, raising this cylinder $1m$ over the surface will be equivalent to lifting it 95 times the height of the Statue of Liberty.

These examples and numbers tell us about the vast amount of energy in the sea. As we mentioned before, this energy can be harvested using several technologies that use different forms of energy exchange.

2.1.5 Tidal and wave energy

If we disregard the already established wind offshore energy, several candidates for extracting energy from the sea arise. Some of them are ocean temperature gradient converters, salinity basins, and other more traditional approaches that use existing technology to harvest kinetic energy in the form of flows (stream) or the oscillations produced by waves. From this family of technologies, salinity basins and temperature gradients are the least developed. Salinity basins use the difference in salinity between two fluids. The readiness of this technology is low and, currently, there are two main concepts being explored: Pressure Retarded Osmosis Power Plants and Reversed Electro Dialysis power plants [25]. However, challenges in scalability remain and there is uncertainty surrounding costs. Thermal energy converters, better known as OTEC technologies, currently have a few small demonstrators such as the Makai plant, which has a capacity of $100kW$ [26]. These devices have been demonstrated to be able to work in parallel with other services such as desalinisation processes, such as the one owned by the Saga University in Japan which uses an Uehara cycle. This is a closed

cycle [27], adding improvements to the Kalina cycle. However, there are obstacles such as deployment and thermal pollution, and impacts of fluid exhausts and operational costs [28].

Meanwhile, stream and wave energy converters are currently the more mature in readiness and technical experience, with devices tested at full scale [29]. Stream and wave are also the more direct approaches to harvesting energy, so industry and research have focused on these areas. Wave energy converters use the oscillation produced by the waves due to their amplitude variation in time. The oscillations are converted into a mechanical movement and subsequently into electrical energy. Waves are the predominant phenomenon on the sea surface and the energy estimates for this resource range from 10,000TWh to 2000TWh per year available for extraction [30]. Waves are widely regarded as a global solution to marine energy harvesting, despite their apparent seasonality [31]. One of the main challenges to the wave energy converter devices is their complex designs which can have an impact on the supply chain.

The other main type of marine energy device is based on stream flows which are generated by the movement of a body of water. The flow is the product of a mass of water moving at some velocity. This is defined as $\dot{Q}$ and given by equation 2.1 where ρ is the fluid density and v is the fluid velocity [32].

$$\dot{Q} = \int \rho v dV \qquad 2.1$$

Devices like these use a continuous or periodic flow of water to move a turbine. This technology relies heavily on wind turbine technology, hydrokinetic dams, and the flow velocity. As equation 1.2 states, the flow depends on its velocity and density. It is known that water currents are slower than wind velocities, but water has a higher density of 1025kg/m^3 [33]. Variables that can alter the flow-delivered power are the flow cross-sectional area and also its velocity. Both variables are important because a larger or stronger flow will produce more energy, increasing the flow, since the flow is constrained and/or increases its velocity as in Figure 2.4.

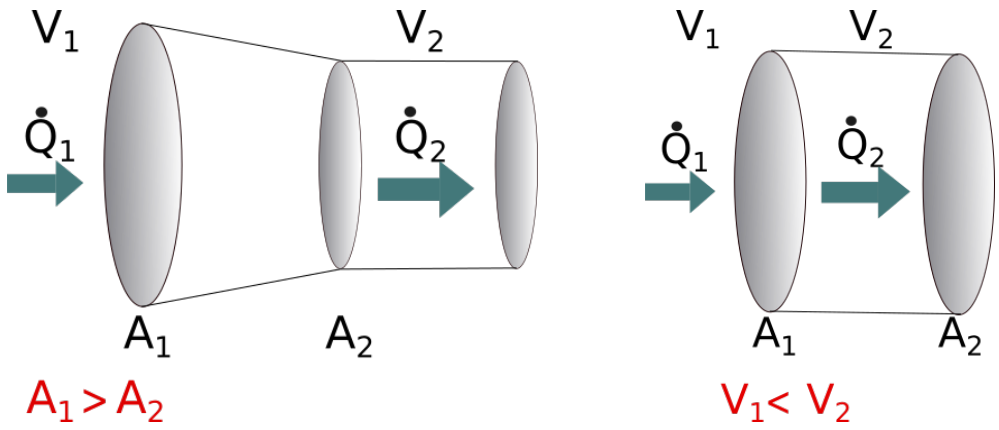

Figure 2.4: Left image showing the increase in flow after volume constriction and right showing an increase in flow after an increase in velocity.

2.2 Phenomena driving the ocean flow: currents, tides, and waves

The current flows in the ocean come from a variety of sources but all are linked to the energy flux exchange between the sun-moon-atmosphere-ocean system. Some of the sources are listed below:

- Flows due to a difference in the sea chemistry composition like salinity, sediments, or biological suspended particles
- Flows due to a difference in density like thermal gradients (Gulf Stream).
- Tides due to gravitational forces (Bay of Fundy/Pentland Firth/San Francisco Bay)
- Flows due to the interaction between the upper ocean layer and the wind
- Wind wave transport and Swell wave transport.
- A combination of the last four and their interaction with the Coriolis effect

The actual technologies available for tidal stream energy are focused on the tidal and thermal gradient flow. These technologies rely on high speed to moderate velocities on the sea or straits to exploit the resource. The flows, as seen in Figure 2.4, will vary depending on the on-site physical

constraints. Geographical features like straits, isles, chains, different basin depths and wave occurrence will increase or decrease the flow strength. In this work, we will focus on the interaction between current flows produced by the tides and long-wave systems under some underwater topographical constraints, better known as bathymetry.

2.2.1 Tide and current flows

Tides are the movement of massive wave components in the ocean masses, which are produced by the gravitational pull of the moon-sun system. The gravity of the two bodies exerts an attractive pull over the sea, and the interconnected basins of the ocean will react by trying to climb to the source of these forces, as we see in Figure 2.5.

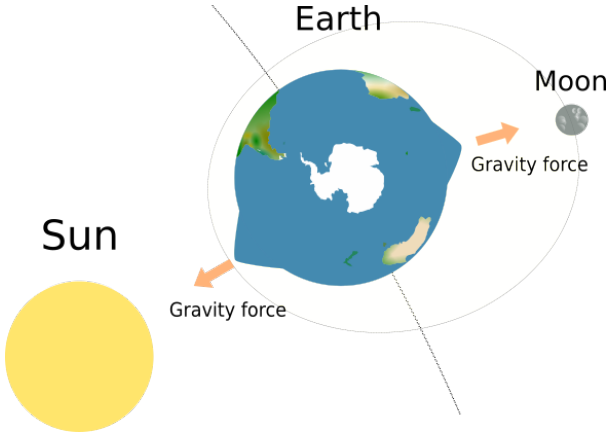

Figure 2.5: Earth subjected to the gravity of the sun-moon system, producing tides depending on the position of these celestial bodies.

As the Earth rotates, the surge flow of water moves around the globe following the Moon-Sun gravity, shown in Figure 2.6.

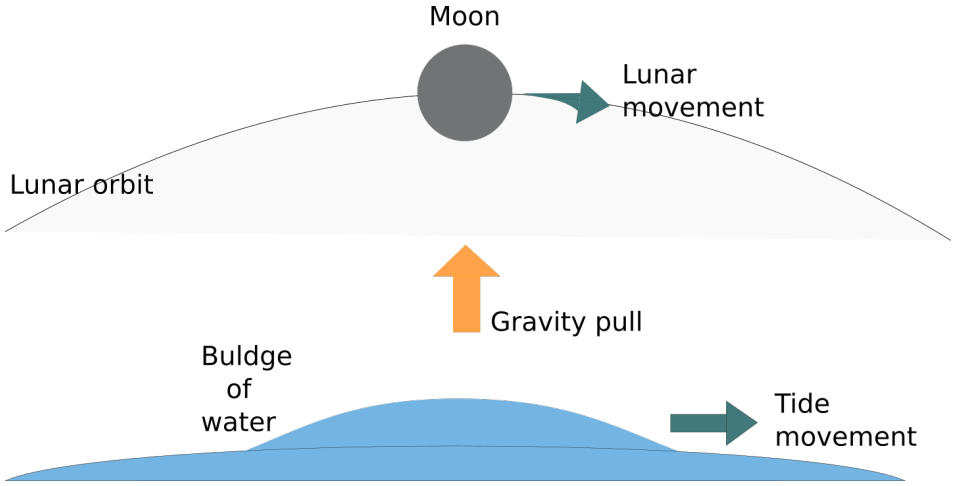

Figure 2.6: Tide moving due to the Moon's position around Earth.

The resulting flow will produce the flood and ebb cyclical pattern. The interaction between the basins and the gravitational systems produces very complex patterns of harmonics. The patterns arise from the three-body interaction, the delays in the tidal reaction due to the orbiting speed of the Moon-Earth, and the resonance periods of each basin. In the coastal areas, this tidal flow will produce a tidal current stream. Tidal current streams amplify their strength not only depending on the physiographical constraints such as the contours of the land but also due to the depth of the basin where this tide is moving. Shallower areas like continental shelf will amplify the tide elevation, and also constrained channels producing stream flows. Tidal stream flows can be easily harvested by tidal stream energy converters, and also currents produced by thermal gradients. Some examples of these thermal gradients are the Gulf of Mexico stream and the Kuroshio current, both of which are ocean span phenomenons with relatively high velocities. An example of streamflow can be found in the Arcaibh-Orkneyjar (Orkney) archipelago [34]. The increase in speed is due to the change in a cross-sectional area where the flow moves, as we saw in equation 1.2 and Figure 2.4. This phenomenon is easily explained by the Venturi effect and the Bernoulli principle: as the flow enters a constrained geographical area the flow must gain speed, which can be seen in the vertical cuts of the seabed profile in Figure 2.7 and Figure 2.8 in the Orkney case.

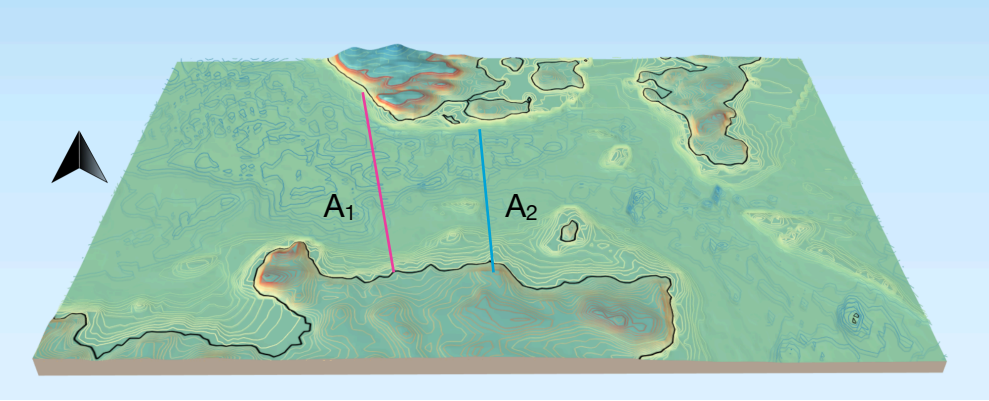

Figure 2.7: Map showing the distance between Rora Head (Orkney) and Dunnet Head (Scotland), and a mid sector between the Orkney archipelago and mainland Scotland.

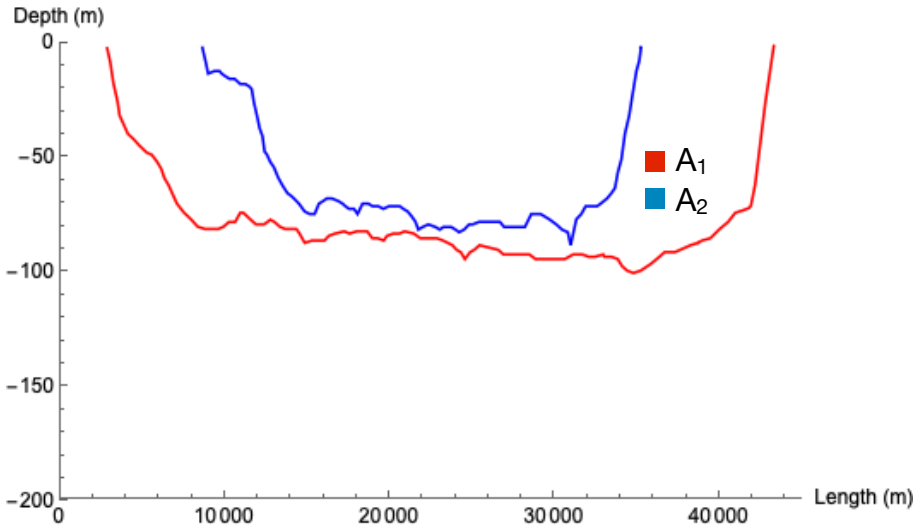

Figure 2.8: Bathymetry cut showing the area reduction, cuts from an area open to the sea in the Pentland Firth (Red), and a mid section in (Blue).

$$\dot{Q}_1 = \dot{Q}_2 \tag{2.2}$$

$$\int \rho v_1 dV = \int \rho v_2 dV \tag{2.3}$$

$$\int \rho v_1 dA_1 = \int \rho v_2 dA_2 \tag{2.4}$$

From equation 2.2 the flux must be the same as in equation 2.3, which implies the next relationship in equation 4.2: $A_1 > A_2 \Rightarrow v_1 < v_2$. The area reduction and equation 2.4, imply that the flow in the middle part of a strait is pushed at a higher speed v_2. This reduction can be seen if we calculate the overall cross-sectional area in Figure 2.8. The cross-sectional planes between Rora Head and Dunne Head have an overall 60% reduction in area. The high velocity constrained the first phases of tidal research and testing, so projects were focused in scattered geographical locations due to the high velocities needed. Some places where research has been focused or proposed are shown next page in Figure 2.9.

Higher velocity currents pose a complex scenario because they can produce more energy but higher energy fluxes also produce extreme forces that turbines must withstand. Research has suggested that high velocities appear to be linked to a peak in the bending moments on the turbine blades [35], and that they have a sensible impact and influence on the turbine's trust [36]. The higher velocity sites are mostly found between straits, a

geographical feature which shelters them from most of the open sea wave weather.

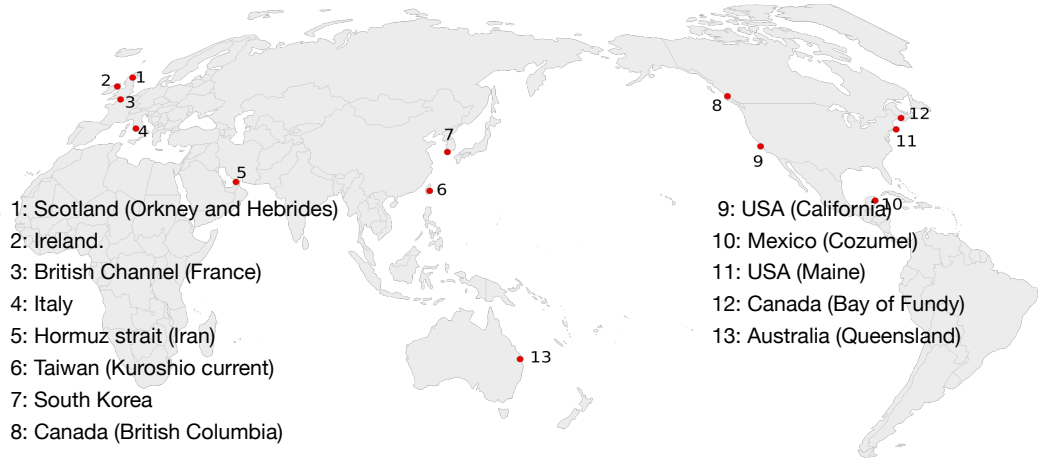

Figure 2.9: Map showing some proposed and used sites addressed by today's energy research.

The protection provided by narrow straits is evident in the Orkney area, as the Pentland Firth is only exposed to a narrow angle of wave incidence. The angles of wave incidence are related to the zones of wave formation and in the Orkney case these are the North Atlantic and the North Sea. Even with a narrow angle of wave incidence, geographical areas such as the Pentland Firth can have a wide exposure to swells depending on the season. According to research, the Pentland strait has a lower wave energy exposure in its mid-sectional area most of the year [37], except for the winter season [38]. The swell seasonality could be explained by storm systems located in the North Atlantic basin, at which site swell incidence can be seen next page in Figure 2.10.

These channels and narrow passages that provide higher energetic flows most of the time have been widely studied; however, improvement in low-speed technologies has moved developers/researchers to new areas. The new areas can have a combination of medium speed and open sea space. Open sea environments with technologies that allow lower current speeds are not exempt from problems as devices will be probably exposed to a wider range of wave weather conditions.

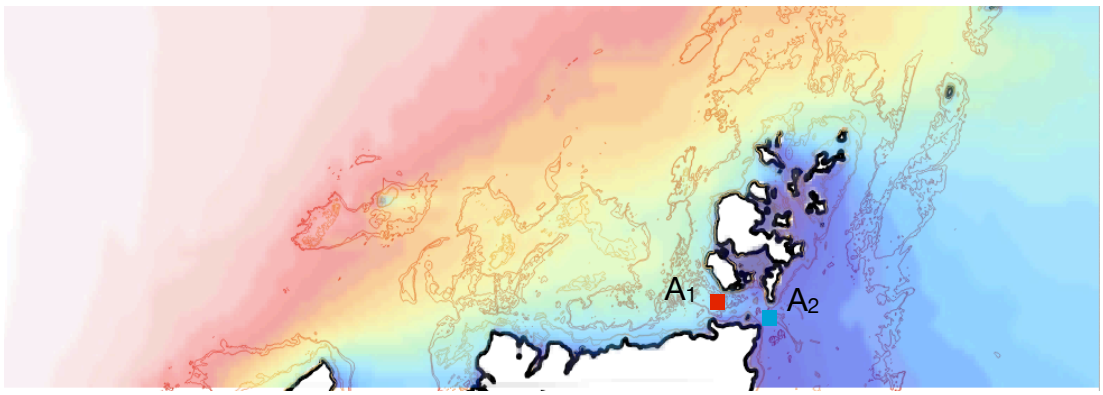

Figure 2.10: Map showing the average wave energy on Orkney per year, adapted from [38]. Bathymetry contours for 100 and 50 metres are shown as the correctional positions for cuts on Figures 2.7 and 2.8.

2.2.2 Waves

Waves are produced when the wind blows over the sea surface. The weather systems that power wave production are fuelled by the sun's radiation and the temperature differences in different sections of the atmosphere. As the wind is an active part of the sea energy system exchange, it interacts strongly with the ocean surface. The energy exchange of the wind will transmit part of its kinetic energy to the ocean's upper layer. Winds continuously pushing the sea surface in the same direction will slowly move the surface in the same direction. The viscosity between the sea layers will start the push the water below, thus forming waves. Light winds will produce small ripples, which will increase in strength and size, and waves will increase in size depending on three factors, the time duration of the wind blowing, wind velocity and the distance that the wind can blow in the same direction (fetch). Any velocity field produced in the ocean will be disturbed by the waves moving across, an example of which is a swell moving over a tidal flood. As currents and tidal current streams can be presented in relatively unsheltered locations, they will be a main component of the flow velocity field. Waves are divided into categories depending on their period T or frequency f. The principal characteristics that define wave behaviour in the ocean basins are its period T, wavelength λ, amplitude ($H/2$ or A),

velocity c, and the depth they move in h_d. We can see its physical definition in Figure 2.11.

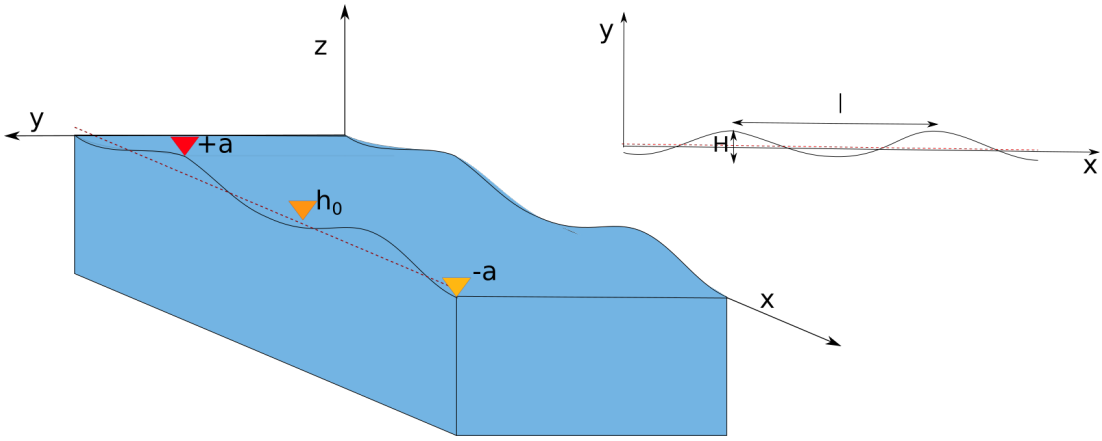

Figure 2.11: The wave's principal characteristics are: amplitude ($+a/-a$), its wavelength (λ or l), the undisturbed level (h_o), the wave height 2a (H), and its frequency f.

As the wind blows over a large fetch or increases in strength, waves will grow in size from centimetres to several metres, and as the waves increase in size, they will differentiate from each other. Waves increasing in size will also increase the distance between each crest, a distance that is also called wavelength λ. The time that it takes for a crest of the wave to reach the position of the crest after it is called the wave period T. The total field of wave energy in the sea is called the wave spectrum. The sea wave spectrum is composed of the energy and periods of the waves presented in any sea condition. The range of the wave periods of the sea spectrum can be seen in Figure 2.12, and the different periods depend on the forces causing the waves.

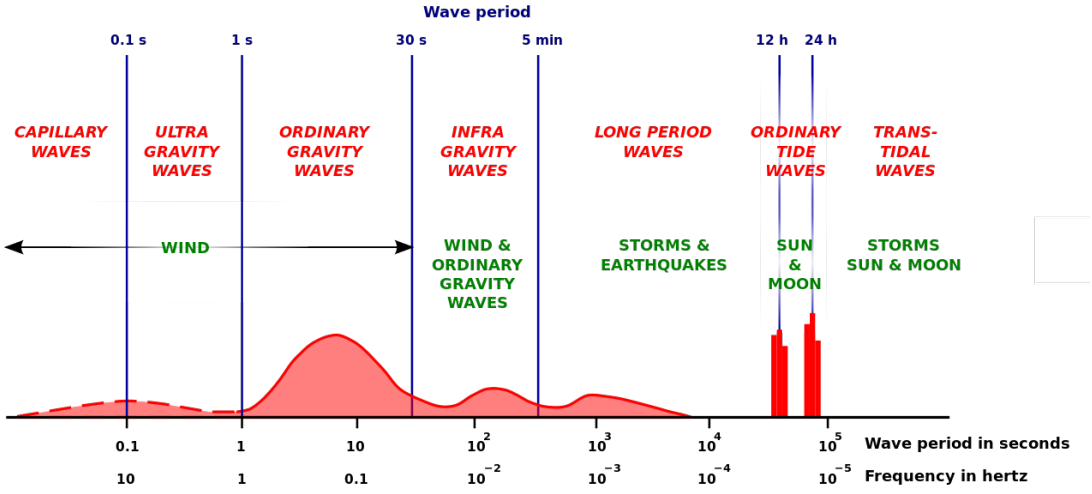

Figure 2.12: Wave spectrum covering from tenths of a second to $10^5 s$ waves [39].

Waves with short periods will be dominated by the effects of the viscosity and these are called capillarity waves. As the waves grow due to the wind, the ratio of the inertial forces disrupts the viscous-gravity balance. When the balance is broken due to high-speed winds, gravity becomes the dominant force.

As gravity takes the lead this produces gravity waves. Gravity waves can range from tenths of a second and lengths smaller than a metre to massive storm systems generating waves of 300m in length and heights over 10m. Waves with larger wavelengths will leave the weather systems that produce them at a greater speed compared to shorter waves due to the dispersion relationship [40]. As the waves leave the weather systems, the wind stops delivering energy to the surface. In the absence of wind, crests will start to fall as the equilibrium of energy exchange has been broken.

The waves that are no longer in equilibrium with the wind and have left their storm systems are called swells. Their periods are usually larger than 9-10s as a rule of thumb. As current tidal sites are usually sheltered against incident waves due to reduced geographical exposition, this will lower the probability of large wave exposure; however, this effect is reduced as we move outside the geographically constrained areas. In more exposed places, waves will play a more important role in the tidal phenomena and velocities.

Research has found that waves can not only have an impact on the wave stream resource, thus reducing its availability by almost 10$\%$ with waves of moderate height at H=1-2m and T=11s [41], but that waves can increase in size by 150% to 200%, depending on the current/wave direction. This plays a direct role in dissipating or increasing wave energy by 60% [42].

Waves could also lead to extreme loads on a tidal stream device, and this load appears to be related to their amplitude/wavelength ratio or steepness λ/H [43]. Forces produced by the water's oscillation will also play a major role in the loading forces on a tidal turbine rotor and its fatigue. Studies show that the significant wave height at large periods of 15s will

cause the fatigue margin to reduce from 30% to 8% [44]. Other researchers have also shown how waves will produce force variation on the rotor, which will affect the power peak output [45]. The unsteady forces that will be caused by waves are expected to be transmitted to the internal components of the turbine, and unsteady sea environment conditions will have implications for the device's lifecycle and durability [46]. Waves will have several implications for dynamic stability of moored devices deployed at sea. Waves with regular periods appear to show stability points that might depend on the wave condition, meanwhile, irregular conditions appear to show chaotic behaviour [47].

2.3 Wind waves, swell waves, and their seasonal and geographical distribution across the sea

Wind waves and swells are not evenly distributed on the sea independently of being a predominant phenomenon which is due to the seasonality of the storm systems. Storm systems move across the globe due to the change in seasons and so do the direction and distribution of the swell wave systems.

2.3.1 Wind waves and swell seasonal predominance

Wind waves and swells behave differently. A windy sea inside or close to a storm system has a very large amount of random wavelengths, heights, and directions. Calm seas will have a set of long-spaced swell waves with soft heights and well-defined directions. Systems will mix along their path with another more random spectrum that is less dominant, containing soft wind waves or other swells. Regardless of the geographical zone, studies have shown that swell can carry more than 60% of the wave energy on the overall wave spectrum [48]. Swells also have a probability of over 80%, thus dominating the wave sea weather. This probability has been measured using satellite oceanographic surveys [49], as seen in Table 2.1.

Swell probability					
Months	MAM	JJA	SON	DJF	Total
Norther Ocean	84.2	89.6	84.4	78	**82.8**
Souther Ocean	89.5	85.1	89.5	93	**88.9**
Global	**87.6**	**86.8**	**87.5**	**87.4**	**86.6**

Table 2.1: Probability distribution of swell dominance on the wave spectrum for the months March-April-May (MAM), June-July-August (JJA), September-October-November (SON), and December-January-February (DJF) on both ocean hemispheres.

The explanation behind swell dominance is partially related to the weather spatial variation in the ocean. As winters produce storm systems in the polar areas, the swells radiate from the most extreme northern and southern areas across the central parts of the ocean basins. Warm months, on the other hand, will offer other swell sources. In the summer months, the seas near the tropics will gather thermal energy and fuel giant storm systems. The storm systems can grow to become hurricanes or supercells and systems will produce radiating swells from the tropical zones to the other basin areas. As the weather pattern oscillates on a planetary scale, swells' point of radiation will vary. Regardless of the geographical source variation, swells will be always present on the spectrum due to the constantly varying weather conditions.

2.3.2 Wind waves and swell geographical distribution

The importance of the swell in tidal energy consists of its periodic nature, spectrum predominance, and consistency across any weather conditions. Swells will form a characteristic component of the load and force variation that affects a tidal stream turbine device. The long-distance propagation of swells that fuels its predominance can be explained by the different interconnected ocean basins, as can be seen next page in Figure 2.13.

As the spatial and geographical distribution is dominated by the seasonal distribution, swells and wind waves will depend directly on the sea weather of their shared origin. As we mentioned, the main difference is that swells with larger periods T>10s will need a large sustained weather system. Winds blowing in the same direction for several hours or days are necessary to produce large waves that will later convert into swells after leaving their weather systems. As mentioned before, this depends on the fetch which is the distance that the waves cover in the weather system that injects energy into them. The larger and more sustained the systems, the larger the swells and the bigger the waves produced. On the coast of California, it is known that swells can arrive from distant locations such as the West of Russia or the Southern zone of the Pacific [50].

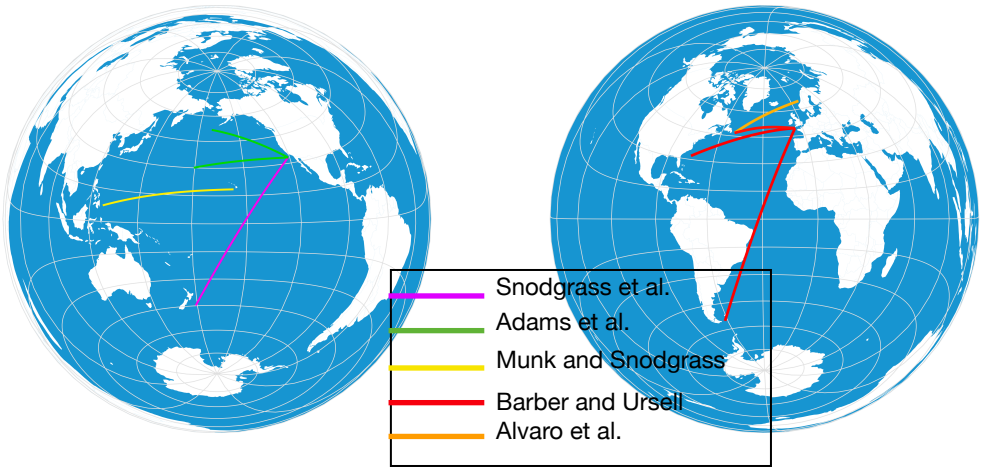

Figure 2.13: Swells arriving from a great circle path. Direction of propagation is west to east in all cases.

Snodgrass show a swell propagation over 7000km [51], [52]; studies confirm these events also occur in the Atlantic basin, where wave trains are constrained due to geographic features [53] or seasonal storms [54]. These long-wave swell systems show a complex relationship with global water oscillations, which cause waves to increase statistically in length and size depending on the global weather pattern, which is predictable [55].

2.4 Waves, their properties, and interaction with currents

2.4.1 Waves and current velocity field across the water column

The current flows produced in the sea can be simplified as a horizontal motion along the seabed, with a shear profile near the seabed. The ideal flow motion at a velocity v will have just a principal velocity component on the horizontal direction x. The current will have a decaying profile as it moves vertically to the bottom, and the current value will be zero at the bottom h_d. The current depth dependence, which is a function of z, can be seen in Figure 2.14. Another factor that will affect the current profile is the possibility of turbulence induced by obstacles [56], but this physiographical feature is not explored here. Waves on the other side will induce oscillatory motions on the water column as seen in Figure 2.15, and their velocity components are horizontal $V_{\varphi x}$ and vertical $V_{\varphi y}$.

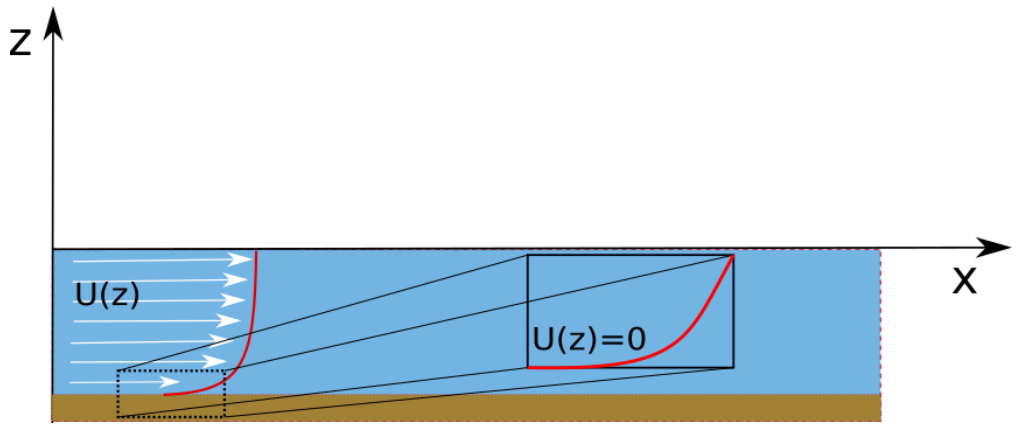

Figure 2.14: Wave current profile in ideal conditions will have a shear stress across the water column depth (*z*). At the bottom the velocity will be zero.

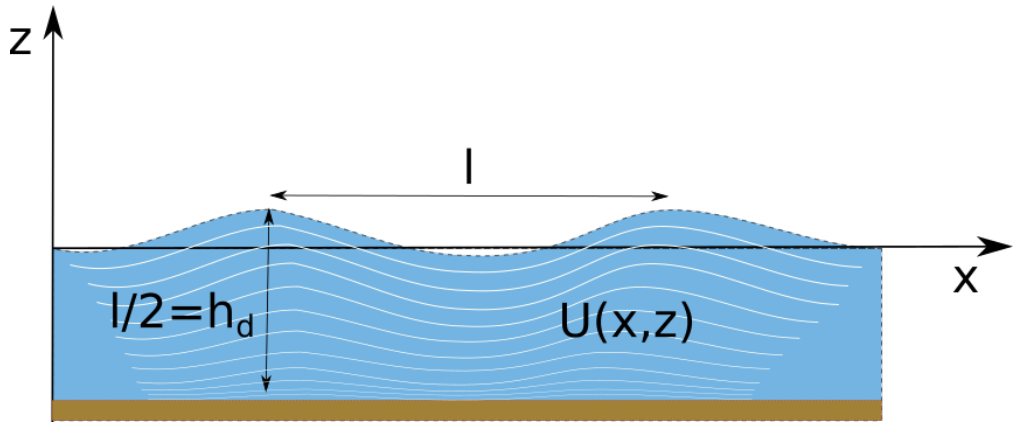

Figure 2.15: Waves will induce a horizontal and vertical velocity field, both time and spatial dependent.

Waves are known to induce a vertical decreasing velocity field. Short wind waves will produce a rapid decaying distortion across the water column. Swells in the other part might reach the bottom where most of the tidal stream devices can be installed. In general waves and currents will interact, and the interaction result will be a mixed velocity field.

The field components resulting from this interaction can be seen in equations 2.5 to 2.7. Linear deep water theory velocities are used in equations 2.8 and 2.9.

$$U(z) = V_c \left(1 - \frac{h_0}{z}\right)^{1/n} \quad 2.5$$

$$U_x = U(z) + V\varphi_x(x,t); \quad 2.6$$

$$U_z = V\varphi_z(x,t); \quad 2.7$$

$$V_{\varphi x}(x,t) = \omega\alpha f\,(z)\,Sin[(t,x)] \quad 2.8$$

$$V_{\varphi y}(x,t) = \omega\alpha f\,(z)\,Cos[(t,x)] \quad 2.9$$

In these equations h_o is the sea depth, V_c is the current flow, z is the vertical distance from these floor to the surface, w is the angular frequency and α is the wave amplitude.

As tidal stream turbines harness energy from the current flow, the underwater velocity field will define its performance and the available energy. As swells can reach the deepest parts of the sea, they will imprint an important quantity of energy underwater depending on their length and size. A wave will exert its kinetic energy at depths proportional to half its wavelength. Figure 2.16 depicts the wave velocity at different depths. The figures describe a linear swell with period T=12s and a moderate amplitude a=1.5m on waters with depths above 200m. Figure 2.16 uses Airy (linear) wave theory for its calculation [57].

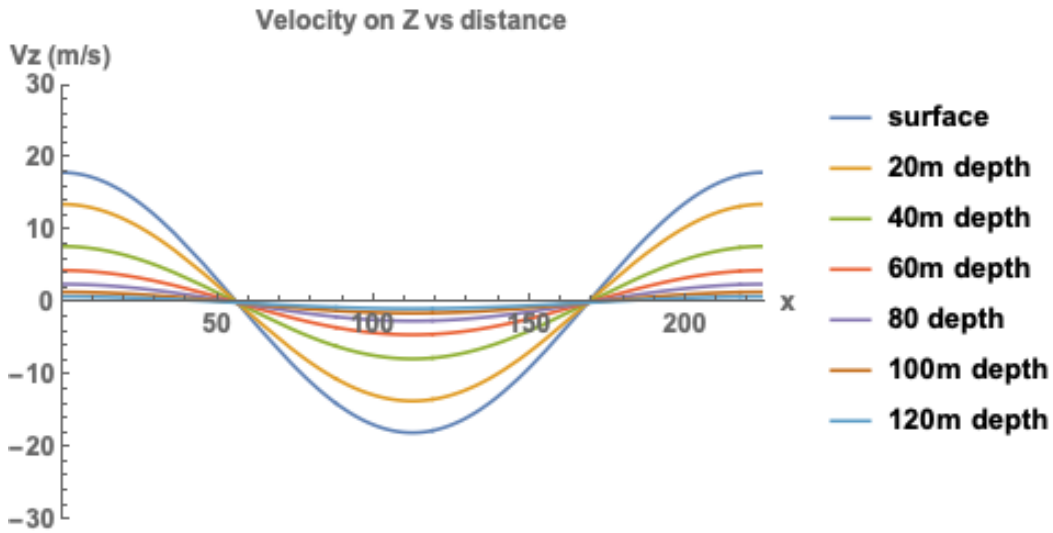

Figure 2.16: Velocity field in the vertical direction. Here the positive axis is measured from the sea bottom.

2.4.2 Waves with large wavelength and low amplitude conditions and their characteristics

Waves in the sea are usually steeper. Certain mathematical and physical conditions need to be met for Airy's theory to be used [58]. The conditions for this theory to be used are defined by H/λ<<1 and $H\lambda^2/h_d^3$<<1, however requirements can be reduced in deep waters. In deep water conditions, we only need the wave steepness H/λ to suffice [59], but only if the relationship $25H=\lambda$ is true. Long wave trains crossing the ocean have low amplitudes, and these amplitudes are the results of energy losses. Energy losses related to air turbulence [60] or ocean [61] can reduce wave heights from H=4.5m to H=1m [62]. Swells, however, can easily satisfy these weakly linear conditions in transitional waters. Swells with moderate heights H=4.0m and lengths over 100m can be a normal occurrence. Wave motion will also depend on the depth they move. Waves moving at large depths will develop a circular velocity profile which is what we see in Figure 2.17, while waves at smaller depths will produce an ellipsoidal velocity profile. The ratio $V_{\varphi y}/V_{\varphi x}$ will define which velocity is more dominant, and this will depend on the depth of propagation.

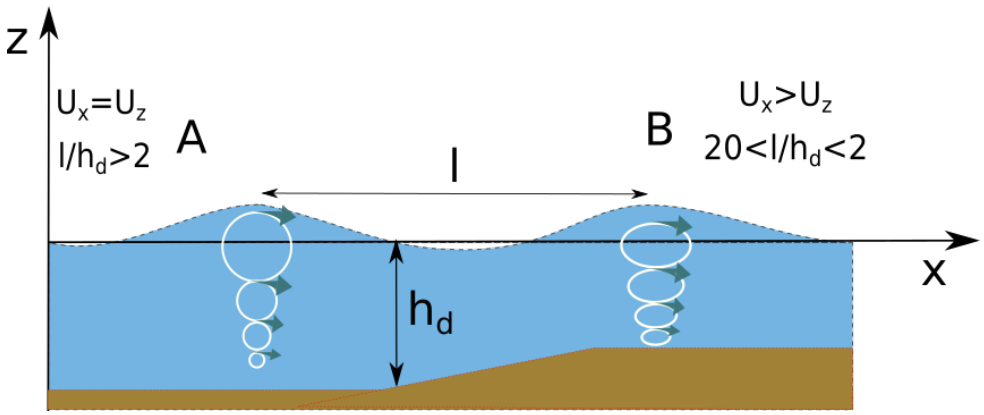

Figure 2.17: Velocity field trajectories of a wave in open ocean at section A, left, and shallower waters, right, at B. The field trajectories depend on the relationship λ/h_d.

For shallower regions, the velocity relationship will satisfy the relationship $V_{\varphi y}<V_{\varphi x}$. In general, wave systems with wavelengths short enough to not interact with the bottom will be deep water systems that will satisfy $V_{\varphi y}/V_{\varphi x}=1$. The opposite case will consist of large systems in the shallower region, which will satisfy $V_{\varphi y}/V_{\varphi x}<1$. Long wave systems have a different impact from the large amplitude systems that have been studied for extreme load cases [63], [64] or wave loads under non-low amplitude conditions [65]. Some values for swells that satisfy low amplitude and large length conditions are shown in Table 2.2.

Wavelength vs Wave height for linear swells wave conditions		
$\lambda\,(m)$	$H\,(m)$	$a=\frac{H*\lambda^2}{depth^3}$ at $\lambda\,(h_{70\,m})$
100	4	0.11
110	4.4	0.15
120	4.8	0.20
130	5.2	0.25
140	5.6	0.32
150	6	0.39
160	6.4	0.47
170	6.8	0.57
180	7.2	0.68
190	7.6	0.79
200	8	0.93

Table 2.2: Wavelength and wave height values from λ=100m to λ=200m and their Ursell number at a depth of 70m of a must be one order of magnitude lower than the unity to use Airy theory.

2.5 Wave propagation from the open sea into the continental shelf

Conditions that we mentioned on the velocities, linearity, and depth of the interaction will depend on the zone of wave propagation for any long swell system. As many weather systems are produced in remote areas of the ocean, the waves will propagate from open zones to the coast over large distances, as we mentioned. The propagation zones close to the continent will be dominated by the shelf physiography, and the shelf will modify the wave behaviour as the wave systems cross over it.

2.5.1 Shelf physiography and wave propagation

The ocean basin has average depths of $1000m$. However, as we get close to the lighter continent crust, it rises. The bathymetry profile will sharply increase its height near the continent. Larger waves crossing the ocean and propagating on the continental shelf will interact with the sea floor. The continental shelf areas can be divided into three principal sections, as shown in Figure 2.18: the continental rise, the continental slope, and the coastal shallow waters.

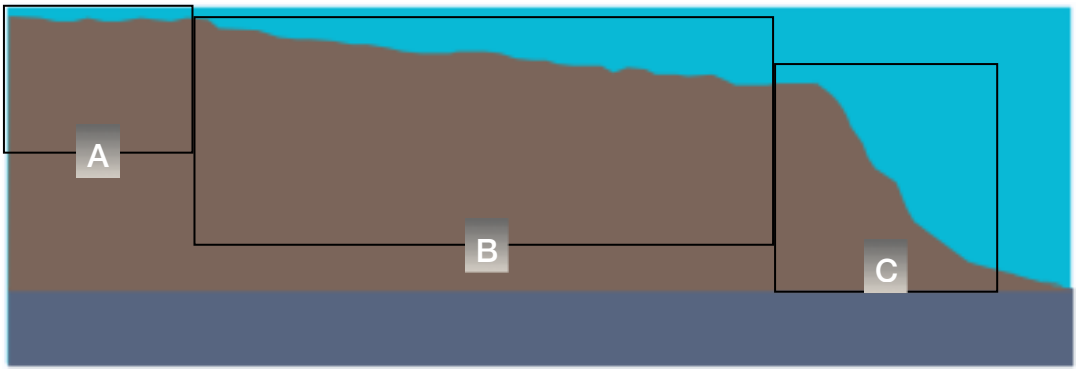

Figure 2.18. Bathymetry cut showing the open ocean basin and continental rise C, the continental slope B and the coastal shallow waters A.

It becomes evident that, for larger wavelengths, the seafloor interaction will become relevant. Shelf topography is relatively regular, decreasing its depth by $1.7m$ every $1km$ on average [66]; however, it has a

diverse set of geographical accidents and also magnifies tidal flows because of its shallow topography.

In the case of the tidal sites, most of the engineering efforts are constrained by the ocean's depth. Tidal sites are located near the sea shelf (zone A). As the technology matures, reducing the velocities for energy harvesting, the area of development for tidal energy will expand on the continental shelf. The expansion could move developers not only outside traditional sheltered straits but also deeper waters with lower velocities that are highly exposed to swell conditions. The continental shelf (zone A) has an average depth of 60m [67], extending to the shelf break on B with an average depth of 140m [66]. Any tidal system installed in zones A to B would be sensible to wave systems with periods T>11s. As wave systems longer than T>14s are a normal occurrence, the increased kinetic energy variation near the seabed will be more important as the engineering effort moves further away from coastal areas. One physiographical characteristic that tidal turbines could face is the sudden change in bathymetry after a geographical rise.

2.5.2 Classical long wave propagation solution

Wave shoaling and bed friction are very well-known phenomena, but little attention has been given to analytical solutions to solve wave propagation as a function of its period under a wide range of depths. In coastal engineering, the explored solutions use assumptions such as shallower water depths, no vertical velocity components, and negligible amplitudes P_{wave}~$P_{surface}$.. The problem has been addressed before by Horace Lamb [68], modelling long waves in a canal of variable depth, as in Figure 2.19.

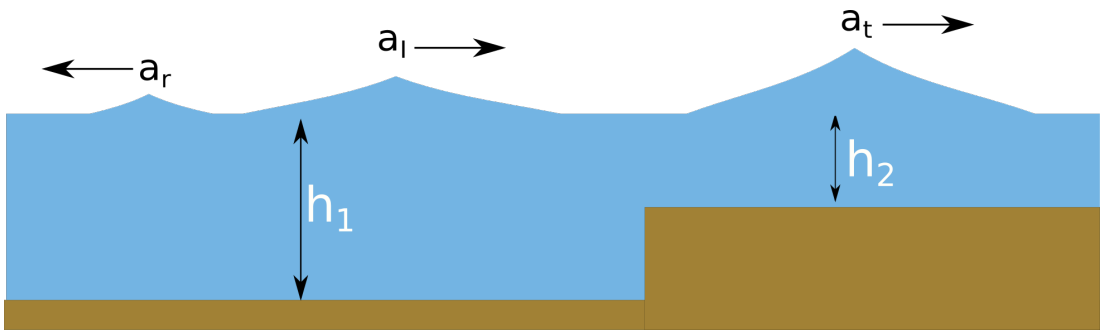

Figure 2.19: Lamb's model based on geometrical constraints. The model has constant breadth and two different depths, namely h_1 and h_2. The system defines the wave transmitted a_t and reflected a_r as part of the incident wave a_i.

The classical solution requires two conditions: small amplitude $a_i << \lambda$ and wavelengths larger than the depth at which a wave moves $\lambda >> h_d$. Lamb's formulation uses simple geometrical constraints, requiring one only to satisfy the surface continuity and low amplitude. Its solution is independent of the wave shape. The phenomenon modelled by Lamb is explained as a simple wave reflection where the wave moves through a canal with a different depth and the same breadth. Wave reflection and transmission in this model are non-elastic processes, bouncing back waves with the same frequency f and period T as the incident wave. The results of Lamb's coefficient of transmission and reflections are shown in Figure 2.20.

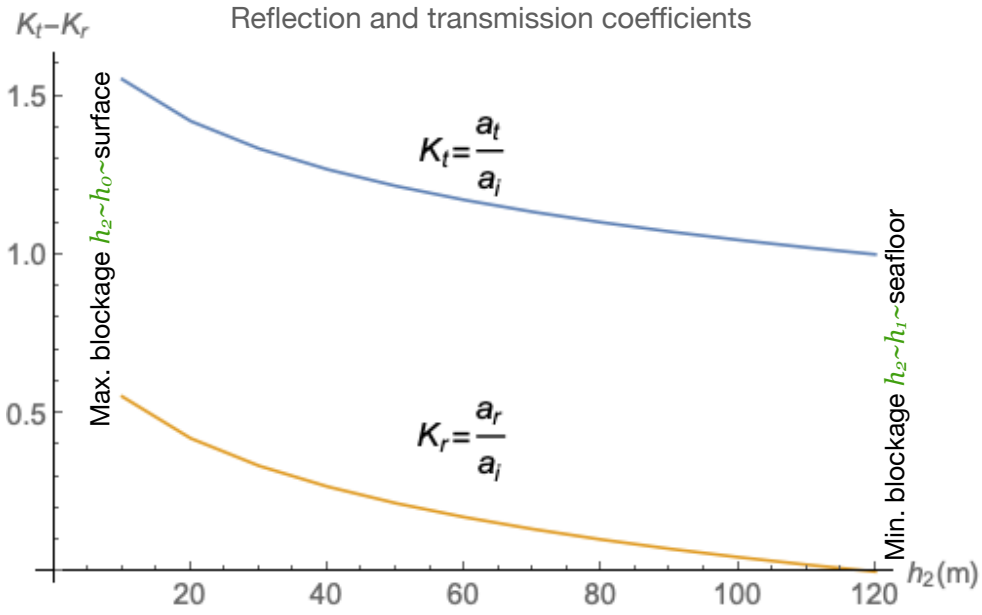

Figure 2.20: Lamb's model for a depth h_1=120m and a varying shelf depth h_2 from 120m to 10m. The terms K_r and K_t are named as the reflection and transmission coefficients respectively.

Mathematical formulations like Kreisel's [69] confirmed the mathematical behaviours of Lamb's model. Newman's model later confirmed that propagation holds not only for infinite-depth waters (h_d~∞) but also for finite-depth waters [70]. Newman's work also found that conditions of shallow depth only need to be satisfied for the transmitted wave. Newman's proposed model has been verified by authors like Miles [71], and the model shows successful agreements for a broad spectrum of waves on the transmission side and a 5% error in the transmission coefficient. Miles's work shows a proportional increase in wave amplitude depending on obstacle depth, meanwhile wave reflection is inversely proportional to it. The reflection coefficient however diverges as the depth ratio to wavelength increases. Lamb's formula and those derived by Newman and Miles have a theoretical relevance but might not be technically recommended as most tidal stream sites are located in deeper zones that break the condition under which Lamb's model is made $\lambda >> h_d$.

Later studies by Takano [72] and Mei and Black [73] consider higher complexity propagation on a finite length shelf. Takano's model agrees with Macagno [74], showing an increase in the amplitude over the obstacle. In Takano's studies, an increase in wave period appears to result in a larger wave transmission coefficient; however, his results lack a wider range of conditions and periods to be more conclusive.

Mei & Black also model Lamb's case and compare their results with the experimental data. Their method shows that the reflection coefficients and transmission coefficients vary depending on the wavenumber K and depth h_d. Mei & Black's studies are important as they cover a wider range of depth to wavelength ratios, but the results are only compared to a single case of obstacle depth. Another important study is Santos et al.'s [75], using different wave periods and different obstacle depths, showing the depth of obstacle immersion and wave amplitude dependence for waves with a larger set of propagation depths. These studies also show some limiting special cases, one of which is an obstacle with a small height K_r~O. Overall the variation of the coefficients in many studies shows a consistent behaviour of

wave amplitude variation. As the amplitude will define the strength of the velocity field and the change in the fluids pressure, it is an important characteristic to measure as any change in the amplitude will affect the loads felt by any underwater device at suitable depths.

2.5.3 Wave fission

Other important processes related to wave propagation are wave fission and harmonics. Fission of the incident waves has been found previously [60], wherein waves that cross an obstacle will split. The split will produce a main wave and a small train that follows behind. Massel addressed this phenomenon using a numerical model [76], and his simulations were compared to experimental data.

The results of wave fission are also supported by experiments conducted by Jolas [77] whose results show that wave transmission depends on the incident wave period, as pointed out by Macagno, a summary of Jolas results is shown in Table 2.3. This wave fission is also observed by experiments carried out by Szmitd under transitional water depths [78].

$T(s)$	K_r	K_t	$h_1\,(cm)$	$h_2\,(cm)$	$l\,(cm)$
0.816	0.04	0.910	31.2	20	100
0.910	0.177	0.877			
1.005	0.222	0.842			
1.104	0.110	0.850			

Table 2.3: Experiments carried by P. Jolas to measure wave transmission over a finite obstacle against wave period.

2.5.4 Experimentation and numerical modelling of wave propagation

A number of experiments and numerical simulations offer insight into the experiments carried out later in this thesis. The most important works for this PhD will be analysed and discussed in the next pages.

Newman's work analyses the transmission and reflection coefficients under a wave propagation from deep waters to transitional waters h_d/λ~0.146 and infinite deep water to shallow waters h_t/λ~0.0063. The work shows how the transmitted wave amplitude increases as the obstacle decrease in depth. Newman's work extends Lamb's assumption about wave propagation bas the depth of propagation for the incident waves includes $h_d=\infty$ and the solutions, even if not completely accurate for values $(kh)^{1/2}>0.5$ (where k is the wave number), follow the same behaviour predicted by Lamb as long the incident depth of transmission is infinite.

Newman's experimentation, however, is made in a depth regime that more resembles a tidal wave condition, which is far from swells with a moderate height. The experiment is also focused on an infinite shelf, so it does not explore the wave propagation after a limited seize obstacle.

The work carried out by Santos et al. used six different depths [15cm to 30cm] using an obstacle of 10cm height. Wave generation covered a period range of 0.5s to 5s, with the smallest possible wavelength (0.39cm), propagating from depth waters to transitional waters. Santos examines the relations between the depth of propagation, wave amplitude, and obstacle depth. His results show conclusively the same behaviour observed by Newman, with waves increasing their amplitude as the depth of immersion of the obstacle decreases. Santos also observes the generation of a secondary transmitted wave of limited amplitude, which in this case can be linked to wave fission and harmonic generation. Santos looks at how the transmitted amplitude increases depending on the amplitude of incidence, a result that, like Newman's, gives evidence about the importance of the wave amplitude, which Lamb's model does not take into account. Despite offering more evidence of a greater implication of the incident wave amplitude in the process of propagation, there is a lack of information regarding how the wave period might affect the amplitude of the wave transmitted. There is also a limitation in the experiments as the obstacle is maintained with a fixed length, thus it does not allow one to see possible effects on the propagation. This is because it is possible that larger obstacles could interact enough to

modify the wave shape or amplitude by inducing shoaling or other important mechanisms. The wave amplitude is also extremely large, with amplitudes larger than 10% of the tank's maximum depth which is not the case for our experiments.

Another important experimentation and modelling is Szmidt's, including wave propagation over a finite obstacle. Szmidt models the wave transmission and reflection components after a regular obstruction is placed in the path of the wave. The obstruction, regular in nature, resembles a block. Szmidt's incident waves move in transitional waters, at depth to wavelength ratios (h_d/λ) of [0.125-0.1]. The obstacles used by Szmidt have a constant depth of $0.24m$. In these cases, the propagation occurred on the theoretical limit for shallow waters at $h_d/\lambda=0.05$. Szmidt observed the generation of higher-order components which were not predicted by Lamb. The two cases modelled by Szmidt $\lambda=8h_d \; and \; \lambda=10h_d$ did not show a larger component than the main wave transmitted. He also showed that the main waves propagated for his experiments had a wave height equal to 1/6 of the tank depth, which reduces its application to wave phenomena close to the shore.

Szmidt's work introduces the high importance of non-linear effects in wave propagation. It is noted that the experiments introduce not only a non-linear interaction, which produces higher harmonics that are released into the upper stream, but also a possible relationship between the incident amplitude and the higher-order components. It is also important to take note of how in Lamb's theory the amplitude to wavelength relationship is $a/\lambda<<1$ s not true. How these conditions create higher components of waves and how this might interact with the wave amplitude and depth are explained further in experiments made by Massel and Ting et al [79]. Work done by Massel shows harmonics with larger amplitudes and an increase in wavelengths after the obstacle. Simulations and experimental data, when compared, appear to show that harmonics will not share the same phase, length, and period. It also shows an increase in an important energy transfer to the 2nd harmonic, as shown by the extreme increase in the amplitude of this

harmonic. Massel experiments also test the frequency dependence of this phenomenon for two different wave periods, however the depth to wavelength ratio of Massel's data for both periods in their cases is very similar, which might reduce how we can extrapolate Massel's observations to our case.

There are three main physical limitations in Massel's work. The first is in the places where wave measurements are taken. In this case, measurements were limited because they were only made before and after the obstacles. No observations are made on the wave propagation over the obstacle. Secondly, the incident waves propagate only from transitional waters to near shallow waters over the obstacle. In Massel's case, examples made in his work are focused on a water depth to wavelength ratio of (h_d/λ) over the obstacle of [0.065-0.14]. The larger wavelengths pushing against the barrier will increase the wave height, as predicted by Lamb. In this case, the amplitude of the incident wave will be important, which takes us to the third point. Massel's wave data also shows a ratio of amplitude and wavelength (a/λ) with a value closer to 1 for finite length obstacles, before the obstacle. His amplitudes are also far larger than the work done here. Massel's example of wave propagation over an infinite shelf considers a long wave propagating with amplitude to wavelength ratios 15 times larger than the largest wave considered in this thesis.

Another important experiment with useful information on wave propagation over obstacles with variable depth, width, and different periods is the one made by Ting et al [79]. Their experiment analyses harmonic generation and energy transfer from the main wave components to higher harmonics. The work carried out by Ting et al. explores harmonic generation by non-linear behaviour after waves interact with a regular breakwater, and it introduces the concepts used by Mason and Keulegan [80] and Mei and Unluata [81], where the energy transferred to the harmonics and their generation both depend on the Ursell number and the non-linearity to dispersion parameter $a_o h_s^2/\lambda_s$. In these cases, the incident wave energy shifts towards higher

harmonics as the number $a_o h_s/\lambda_s$ equals 4 [80]. According to studies carried out by Grue [82], harmonics after the obstacle can be equal to 60% of the incident wave amplitude. However, Grue's studies were carried out in situations where the waves transferred to very shallow depth waters with a maximum depth of h_d=5cm and a minimum wavelength of 1.05m which indicates a very small depth to wavelength ratio under the range of shallow waters h_d/λ<0.04.

In this case, not only is the depth of propagation different from the experiments carried out here, but the concepts introduced by them using the Ursell indicate that for a strong transmission of energy to occur to higher harmonics, the parameter $a_o h_s/\lambda_s$ should be closer to 4, meaning $a_o h_s$=4λ_s. This indicates very large amplitude for these cases as the product of both will necessarily be 4 times the wavelength propagation over the obstacle.

Very importantly, Ting et al. derive a formulation using a multivariable regression on experimental data. This formulation describes the ratio of the maximum amplitude of the second harmonic to the minimum amplitude of the first harmonic $\mathrm{a2_{max}/a1_{min}}$.The result is approximately equal to the Ursell number multiplied by 0.022. This definition allows one to obtain a possible reference to measure how the higher components can alter the transmitted wave after it is propagated over and after the obstacle. In this regression, the most important parameter is the obstacle to tank depth ratio h_s/h_d.

In general, all of these studies reveal important characteristics to take into account when modelling and experimenting with wave propagation over obstacles. One is the importance of the depth of propagation, the second is the importance of harmonics, and the third is the possibility of other factors influencing wave propagation over obstacles.

2.5.5 More complex bathymetry scenarios

Analysis of more complex bathymetry scenarios for wave transformation under an arbitrarily varying seabed has been described by Jung et al. [83]. This method divides the sea bed into sloped transitions that

need to be solved at each step. Cho's method has been used more recently to solve profiles with scouring trenches, and also by authors like Xie et al. [84] to solve K_r.

Solutions found by Xie and Cho converge with Lamb's formulation when the scour trenches are set to zero. Xie and Cho use the shallow water equations where the phenomena is dominated by the horizontal velocity. Xie and Cho's solutions can only be applied if the condition $V_{\varphi x} >> V_{\varphi y}$ is met, and these theoretical models can only be used in waters where the wavelength has a larger order of magnitude than the depth it propagates. Although a solution for K_t is possible, we are constrained by the water depth at depths useful for engineering applications.

Other complex scenarios to model 2nd order Stokes waves were proposed by Athanassoulis, and the solutions found have been coupled with non-linear waves [85] and [86]. Athanassoulis's model shows that wave transmission appears to depend on the incident wave frequency, a dependence similar to the one observed by Jolas and Macagno on linear theory. However, results of the 2nd order do not address waves moving from infinite-depth waters to transitional waters. The mentioned experiments and models lack a feature that is very important to wave propagation: the possible changes in the wave frequency, wavelength, and deeper waters.

2.5.6 Limitations of past experiments and models

The most important experiments from past authors briefly analysed in the last section provide a window into the conditions and variables to be measured in a more general experiment in order to observe and analyse wave propagation using a wider set. The limitations of the experiments are as follows:

1. Experiments and models working on shallow water theory to verify the conditions set by Lamb use shallow water wave conditions. These conditions are more suited to experiments and models that analyse waves near the shore, far away from the places suitable for tidal energy

devices. Two of these experiments are the ones made by Newman and Massel, with h_d/λ conditions [0.065-0.14] for Massel and [0.146, 0.0063] for Newman. These values are closer to the more extreme cases that will be analysed here.

2. Wave amplitudes in experiments such as the ones made by Santos et al. and Szmidt use waves with amplitudes of at least one order of magnitude larger than the amplitudes studied here. Waves in this case have a size of 10% of the tank depth for experiments run by Santos et al. and 16% for experiments run by Szmidt.

3. The experimental set-up is mostly done to analyse the amplitude of an infinite shelf or a single obstacle. In the case of experiments run by Santos et al., Newmann, and Szmidt, they use a single obstacle with a fixed length. This could obscure certain propagation characteristics derived from the obstacle length.

4. In the experiments carried out by Ting et al. and Massel, important information is provided about the creation of harmonics. In the case of Massel, limitations are not only presented by the lack of data on how important the length of an obstacle could be for wave propagation, but also the lack of information about measurements taken over the obstacle. Information related to how conditions over the obstacle could have an impact on the waves propagated afterwards is non-existent. In the work carried out by Ting et al., the harmonics are found to be linked to the wave amplitudes. However, the depth of propagation and transmission occurs in shallow water processes. Another limitation is presented by the importance of the wave amplitude to depth product to predict the energy transmission to high harmonics. The product of this value needs to be equal to or closer to 4 times the wavelength, meaning that wave amplitudes would necessarily need to be fairly large. Ting et al.

provide no information about waves with a smaller value, which can account for large regular waves with a softer amplitude in deeper waters.

The ranges explored by Newmann, Massel, Santos et al., Szmidt, and Ting et al. can be observed in the next table. If more than one depth is tested this is given a range, like [0.3-0.15], and the same if wave amplitudes cover a wide range of values.

Autor	Newmann	Santos et al.	K. Szmidt	Massel	Ting et al.
$h_d(m)$	0.6	0.3	0.6	0.3	0.275
$\lambda_{min}(m)$	0.2	0.39	4.8	1	1.31
$\lambda_{max}(m)$	10	8.57	6	1.5	2.19
$h_t(m)$	[0.037-0.15]	[0.2-0.05]]	0.24	[0.26-0.141]	[0.151-0.065]
$a_i(m)$	0.01	[0.02-0.12]	0.04	[0.0023-0.005]	[0.21-1.04]

Table 2.4: Table with the depth (h_d), maximum (λ_{max}) and minimum (λ_{min}) wavelengths, amplitudes (a_i), and depth of immersion (h_t) for the main experiments discussed in 2.5.4.

2.5.7 Wave velocity and wavelength change

Other important subjects on wave propagation that have not been addressed properly are wave frequency change, wave velocity shift, and wavelength change. Physical characteristic values like wavelength, period, and celerity will define cycles of variation on our hydraulic head and possible changes to the underwater velocity field, thus proving our wavelength is long enough at the transitional depth. Massel's [76] description of harmonics shows that after propagating over an obstacle, the fundamental component will have a different wavelength and phase from the incoming wave. As the wavelength is a function of the wave frequency, then a frequency change after propagation will have effects on the wavelength, period, and wave velocity. Very detailed research by Goring [87] shows discrepancies in the frequency propagated after a bathymetry rise using a scaled wave experiment.

Goring modelled tidal waves produced by tsunamis under linear conditions. The experimental campaign showed a consistent change in the frequency and wave velocity, as in Figure 2.21.

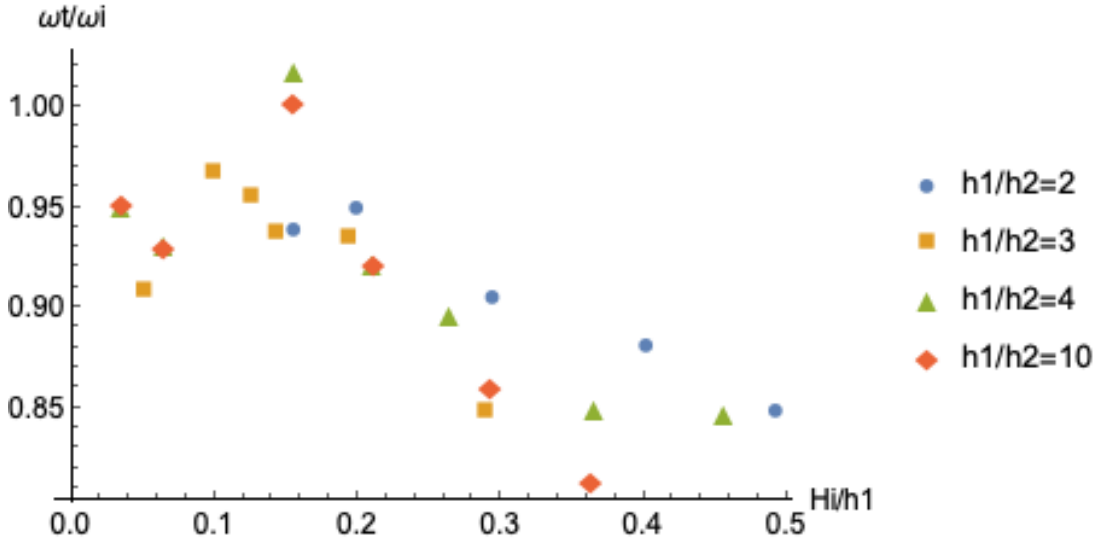

Figure 2.21: Experimental propagated frequency shift ratios ω_t/ω_i, as a function of depth before the obstacle h_1, after the obstacle h_2, and the incident wave height H_i.

Experiments designed by Goring address the conditions of tidal waves propagating over the continual shelf, where propagation occurs from deep-sea waters. The discrepancies between Lamb's theory and the experiments show that the depth ratio h_1/h_2 affects the transmitted angular frequency ω_t, where the depth ratio is defined as the depth before obstacle h_1 and after obstacle h_2. Values of the transmitted angular frequency were lower than the incoming wave frequency ω_i, and the results also appear to be affected by the incident wave amplitude. Despite the results obtained, the variation of ω_t against the wave height H shows a scattered behaviour.

Naghdi and Marshall addressed the wavelength change using a linearised solution for the wave equation [88]. The analytical solution found is proposed to be used for long waves at small amplitude. The formulation can be also reduced for shallow waters as in Goring's case. Naghdi and Marshall's formulation could explain what Goring observed. Their work predicts that wavelength will change depending on the depth at which the waves propagate. Their results differ in depths $\lambda > 20h_1$ and $\lambda > 2h_1$, showing a slight increase in the wavelength and then a decrease as $\lambda/h \to \infty$.

2.6 BEMT and the underwater velocity field

Because tidal turbines use hydrodynamic surfaces to capture the current stream velocity, converting that flow into mechanical work, modelling the mechanical output is necessary to calculate the flow interaction with the device. In order to simulate the effects of the fluid velocity over the tidal turbine rotor, mathematical models are required. Some models used require complex calculations and dedicated software to address this. A brief list of models standardised for research and development is given below:

- Lifting Line Theory
- RANS-BEM
- Blade resolved RANS
- Blade resolver LES
- CFD

The order of complexity and time to simulate the turbine increases in descendant order. One of the established methods to model turbines is the Blade Element Momentum Theory (BEMT). BEMT has been developed to include corrections for fluid losses [89] and synthetic turbulence [90]. BEMT solves systems at a higher velocity compared to other tools such as Computational Fluid Mechanics (CFD), producing reliable results despite showing an under-prediction of peak power according to studies done by Masters et al. [91]. Methods of high complexity like CFD can also be used to complement other faster methods like BEMT, using a combination of BEMT+CFD. BEMT theory can be divided into two sections: flow conservation energy analysis and flow dynamics structure interaction.

The first section analyses the quantity of energy that a flow exerts over a rotor on a tidal turbine, where the energy exerted must be equal to the energy loss of the fluid. The second part analyses how the flow captured by the rotor produces the torque and thrust on a tidal turbine due to the lift and drag forces over the airfoil. The method depends on the interaction of

the rotor with an incoming flow at speed U_∞, just as when the fluid passes and produces work it reduces its velocity [92], as shown in Figure 2.22.

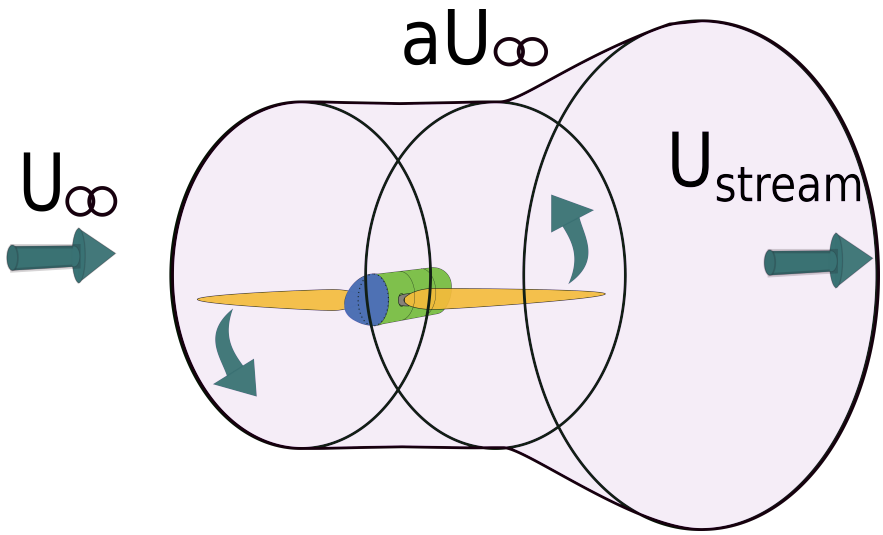

Figure 2.22: Diagram of the velocities at a BEMT model, here U∞ is the free stream velocity, a is the factor of reduction that depends on the energy absorbed by the rotor to produce mechanical work and U_{stream} is the velocity released after our turbine.

The velocity at the rotor will be reduced by an a factor, and then released. The flow released after the rotor interaction will expand its area. As the work produced by the rotor depends on the flow, any unsteady condition in the regime or an induced flow change in the velocity field will produce a change in its performance. Studies done by Nevalainen [46] and Masters et al. [91], have shown the turbine mechanical variation induced by the change in the inflow velocities. The change in the flow velocities was produced by waves. The relationship between the small differential of torque and thrust expressed in their works can be shown in equations 2.10 and 2.11. The relationship between the torque and thrust expressions is made by replacing the term U_∞ with expressions 2.5 to 2.9.

$$\frac{dF}{dr} = 4\pi\rho\left(U_\infty^2 a(1-a) + (b\Omega_r r)^2)r\right) \tag{2.10}$$

$$\frac{dT}{dr} = 4\pi\rho b(1-a)U_\infty + \Omega_r r^3 \tag{2.11}$$

The equations define the differential of the torque dF and thrust dT per a little section of the radius dr. A full description of the equations is given

in Chapter 5. The term U_∞ defines the stream velocity. Any change in U_∞ will produce a direct change in the differential torque and thrust, and the change in each blade will have an overall impact on the rotor. The work of Nevalanien [46] and Faoudot and Dahlhaug [43] has shown that waves have a clear impact on the loads experienced at tidal devices. The change in the loads is induced by the oscillation in the wave velocity. This can be expressed simply when we take the total underwater velocity U_∞ as a composition of the current velocity U_∞ and the wave velocity $G(x,z,t)$, as seen in equation 2.13.

$$U_\infty = U(z) + G(x, z, t) \tag{2.13}$$

As the wave velocity field depends on the wave amplitude a_i but is also a function of the frequency/period f/T, any change in these values will modify $V\varphi_x$ and $V\varphi_y$, and any change in the field will impact equations 2.10 and 2.11. Wave transformations due to bathymetry changes could have a direct impact on our torque and rotor, thus depending on the wavelength to be able to reach great depths. Large swells that are a normal phenomenon in the sea at T>11s will be able to interact with a tidal device.

2.7 Conclusions

The ocean is currently a viable source of vast renewable energy. In this area, technologies such as wave and tidal devices have become more mature. Despite advances, however, many challenges have arisen in the modelling techniques, device construction, and deployment. These challenges are connected to the sea being one of the toughest environments on the planet due to the continuously changing weather conditions and many other factors. These conditions will determine not only the feasibility of the project but also how the design constraints are met to withstand the forces that our devices will face in the ocean.

Waves are one of the main weather components in the sea and one of the main drivers behind unsteady forces felt by marine energy devices and,

in our case, tidal stream devices. The wave weather is strongly dominated by swell components across the ocean. Studies show 60% of the energy being carried by swells [48] and a weather dominance of more than 80% for the swell in both hemispheres [49]. Even if tidal devices are sheltered at suitable engineering depths that can reach 50m, the theory shows how wave spectrum components with larger periods can interact at depths larger than $100m$.

As the sea bottom where these swells move is not perfectly horizontal, they will interact with the different obstacles and profile changes under the sea. Wave propagation over these geographical constrains will cause a change in its parameters, such as the wave height. Studies have shown how larger waves interacting with regular topographic obstacles can modify the wave amplitude. One classical solution for tidal waves is the one found by Lamb [68] which shows how waves increase their height when moving to shallow waters in the cases where their length is larger than the propagation depth $\lambda >> h_d$. Newmann's work extended this model to cases where the incident depth is larger than the wavelength [70]. More recently Naghdi and Marshall offered a solution for finite depths, which is suitable for larger waves which are not tidal in nature and could be used to model larger wave components [88]. In Marshall and Naghdi's case, its solution includes a change in the wave frequency as it propagates to shallow waters where $ki_{ncident} \neq k_{propagated}$.

As turbines and other marine energy devices are deployed in the sea, geographical conditions might vary and possible local geographical constraints could become important. The possibility of large swell components reaching a turbine despite this device being sheltered against local wind waves could become an important factor to account for when looking at the device's lifecycle. Wave weather predictions could be different in the area if wave components behave differently under local constraints, such as changes in amplitudes or cycle loadings.

Due to these changes, it is important to know how the installation of our devices over or after a bathymetry will modify the forces felt by our turbine. The logical first step is an exploration of these other constraints to account for the mechanical response variation in the devices, which is part of a long chain of research on the factors that can impact marine energy design, deployments, and production.

3 Methodology

The study of wave propagation over obstacles, and how the change in the wave properties could affect a tidal stream device installed nearby, is explained in the next pages. The problem is complex, and so it is important to understand precisely every part of it. This section covers the subjects related to the mathematical model of the swell systems used and the proposed formulation. The methods used in the laboratory validation are described in Chapter 4, and a more detailed description and application of the methods to determine the sea weather conditions are detailed in Chapters 5 and 7.

The mathematical statement: The mathematical background is described as the long-wave theory for small amplitudes. Most of the theory used here falls into linear or weakly linear waves, where nonlinearities are small. The theory was treated this way, as the first approach to modelling radiating long swells from a distant wave field. The mathematical statements were used to derive an analytical solution that could model wave propagation over an obstacle. The model aimed to take into account the frequency shift observed in past studies [77], [87]. The solution found was compared to experiments carried out in a wave tank flume in Chapter 4.

Spatial and seasonal data processing: Spatial and seasonal data was used to gather precise information about sea weather data, including wave directionality, wave height, and wave occurrence. The work used data from buoy systems owned by several state agencies and research institutes in the USA. The data gathered was then processed, allowing us to obtain a general view of the wave weather in the area. Swell dominant conditions were isolated and applied to a nearby geographical position in Chapter 4.

Bathymetry analysis: Information about the seabed in the swell area location was fed into software processing tools to obtain a simplified model of the seabed. The required models retained the main features of the

underwater topography, and these models were later used for the site analysis, along with information about the desired tested position.

3.1 Wave properties

3.1.1 Wavelength in the open ocean under moderate current values: MacKeen and Fenton model

Waves are an oscillatory phenomenon of energy transmission. In the case of ocean waves, they can usually be divided using three methods. The first divides waves by their frequency and wavelength, which is a simple representation of the wave spectrum that relates to both variables. This can be seen in formulation 3.1 and Figure 3.1.

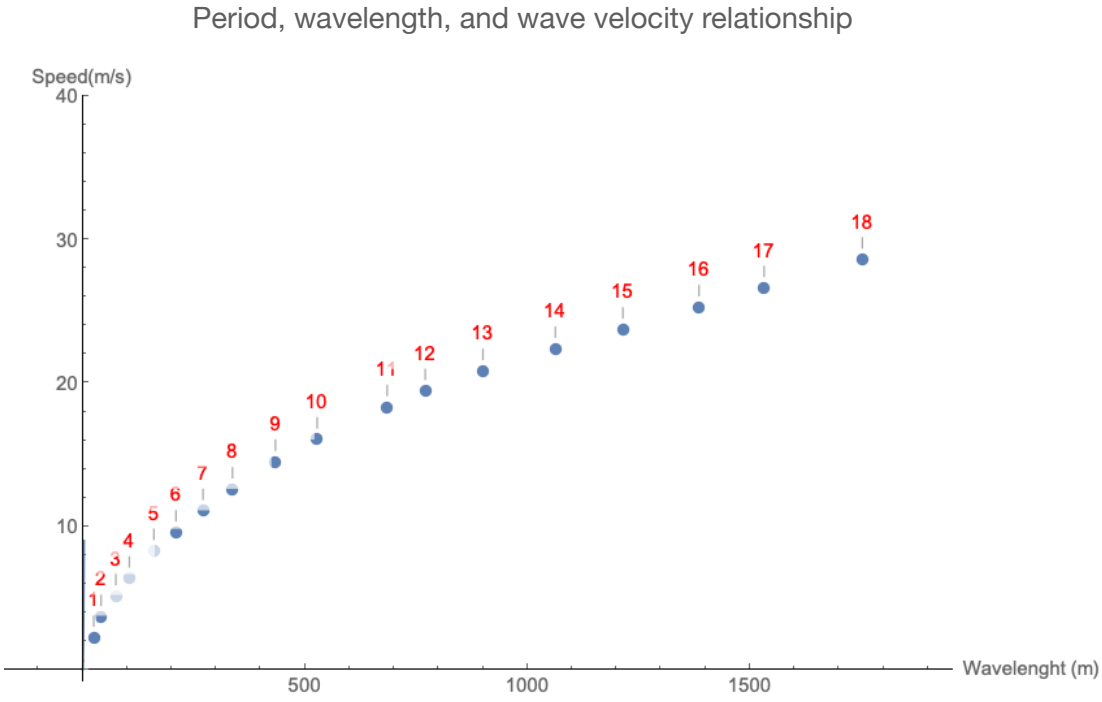

Figure 3.1: The relationship for frequency in red (T), wave speed, and wavelength (λ) for periods bigger than $1s$ using linear deep water wave theory.

$$\lambda = f(T) \,||\, \lambda = f(\tau) \tag{3.1}$$

$$\lambda = L_0 \left(Tanh \left[\frac{2\pi d}{L_0} \right]^{3/4} \right)^{2/3} \tag{3.2}$$

$$L_0 = \frac{gT^2}{2\pi} \tag{3.3}$$

The mathematical solution for this relationship depends on the solution of the wave equation for infinite depth waters. Solutions to describe wave behaviour have been improved during the last 70 years. A solution given by Fenton and Mackee [93] allows us to calculate wavelengths independently of the current and the amplitude. The solution proposed is seen in formulations 2.3 and 3.3. As with all solutions, this one depends on a physical range of applicability defined by the physical boundaries of the problem. Fenton and Mackee's solution has been compared to other formulations, and this comparison shows a good agreement with values with current velocities as high as 1/10 of the wave propagation velocity. As swells are long waves, the range of velocity shown can be approximated by the long wave theory in infinite deep waters. Infinite depths can be approximated in theory as $\lambda/h_d \sim 0$ and then $h_d \sim \infty$. The solution for this allows for swells over 6 to 7 seconds to have wavelength values valid for currents around $1.1 m/s$. The formulation is used in this work to calculate the wavelengths of open ocean incident waves in sites where long swells propagate, as large swells will have a larger range of applicability due to their faster propagation velocity.

3.1.2 Wavelength in deep waters and transitional waters: The long wave model

As waves move from the deep ocean to the coast they will enter shallow waters. The second method to classify waves uses the open ocean wavelength and its wave field of penetration into the water column. For this method, the ratio between the wavelength and the depth of propagation is used to divide waves being propagated. Waves with larger wavelengths will reach a greater depth equal to half the wavelength at depth waters. By the same token, shorter waves will reach only depths near the ocean surface. This relationship has implications for the wave velocity component. This

formulation is useful as a mixed wave spectrum on the surface will likely have long swell waves and shorter local wind waves. The regions defined by this method are shown in Figure 3.2. Open ocean regions are divided into A (deep waters), B (transitional waters), and C (shallow waters).

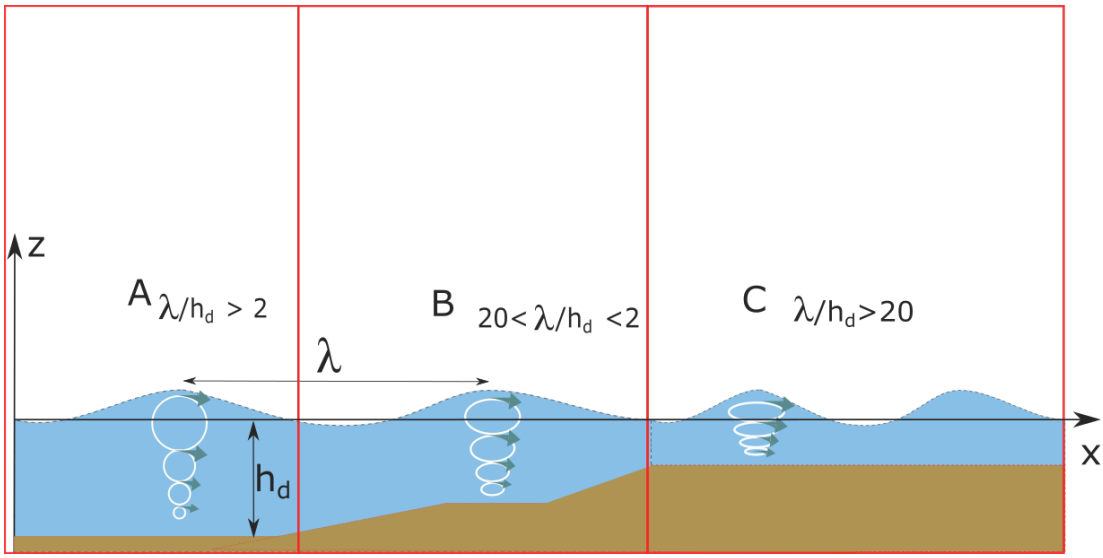

Figure 3.2: Division of the wave theories depending on the depth of field penetration: A, deep water theory, B, transitional water theory, and C, shallow water theory. Symbols h_d showing the depth, the velocity components paths, and the wavelength "λ".

It is known that as the wavelength reaches shallower waters, their wavelength value from equation 3.2 will be shorter than the original one. Due to the shallower region of propagation, the lengths of the swells after reaching the shallower waters will need an iterative correction given by equation 3.4. The formulation found by Fenton and Mackee can be used as a starting value for the iteration process, and the starting value can then be applied to equation 3.4, shown below for long swells at $\lambda/h_d<2$. This correction is needed as long waves will present a velocity profile where the horizontal component x will be larger than the vertical y component.

$$\lambda = \frac{g}{2\pi} T^2 Tanh\left(\frac{2\pi d}{\lambda}\right) \qquad 3.4$$

The corrected wavelength and the wavelength depth relationship follow the relationship expressed in formulation 3.5, where the indexes i and t refer to the incident and transmitted regions.

$$[\lambda_{Ti}(h_{di}) > \lambda_{Tt}(h_{dt})] \Longleftrightarrow [h_{di} > h_{dt}] \quad 3.5$$

3.1.3 Wavelength in deep waters and transitional waters: The Stokes model and Stokes expansion

The Stokes expansion method relates each type of wave to the theory that can be used to study its properties. This method of division is commonly used to subdivide the wave spectrum into linear waves, and any Stokes order theory as in Figure 3.3. The method uses the wave non-dimensional height, in equation 3.6, and non-dimensional period values, in equation 3.7. The values are used to determine the theory that can be applied to this wave. This method allows us to divide the wave spectrum easily, find the mathematical theory that could be used to model the wave properties, and divide the wave spectrum.

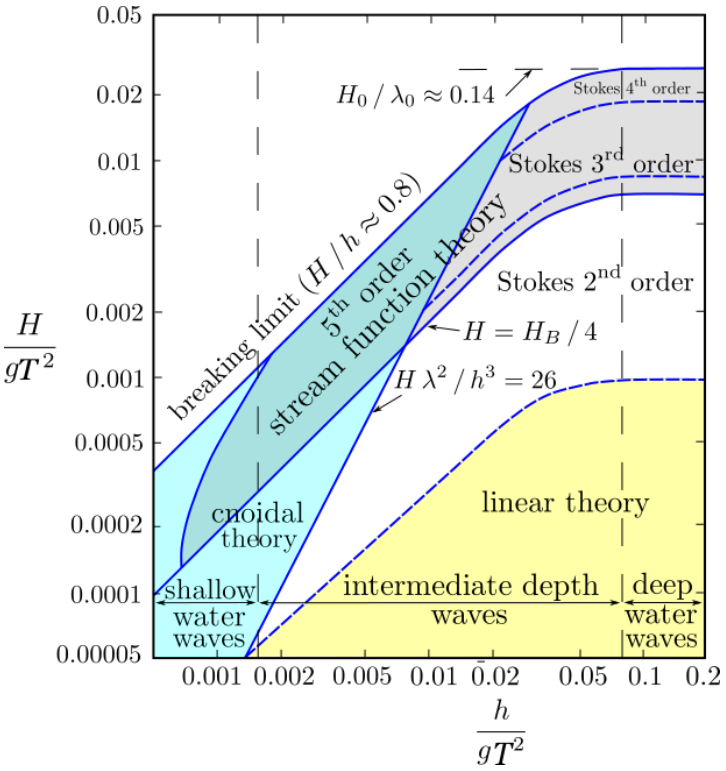

Figure 3.3: Division of wave using the non-dimensional values in equations 5.3 and 6.3. Image from Le Méhauté [94]. H referred to the wave height, λ to the wavelength and indexes ₀, and B to the depth water conditions and the breaking limit.

$$y = \frac{2a}{gf^2} \tag{3.6}$$

$$x = \frac{h_d}{gf^2} \tag{3.7}$$

3.1.4 Long wave swells and their mathematical formulation: The long linear wave theory and the Ursell number

After leaving the storm systems, wave swells will lose energy due to turbulence, wave to wave interaction, currents, and other phenomena. The amplitude decay will make swells behave like low amplitude wave systems, and this decay will happen far away from the storm generating these systems. Given the proper conditions of propagation, these systems can be easily modelled using Airy theory as long they do not propagate on shallow waters. The conditions necessary for this to apply are that given any wavelength, this must be two orders of magnitude larger than the amplitude. Since swells can have lengths over $200m$ and amplitudes of $2m$, these conditions are easily satisfied.

The general problem for a long wave moving in a volume of water with infinite depth can be described theoretically by equations 3.8 to 3.12.

$$\frac{\partial^2 \varphi}{\partial x^2} + \frac{\partial^2 \varphi}{\partial z^2} = 0 \tag{3.8}$$

$$w - \frac{\partial \varphi}{\partial z} = cte \tag{3.9}$$

$$\frac{\partial \eta}{\partial t} + u\frac{\partial \eta}{\partial x} = w \tag{3.10}$$

$$\frac{p}{\rho} + \frac{\partial \varphi}{\partial t} + \frac{1}{2}\left(u^2 + v^2\right) + gz = cte \tag{3.11}$$

$$\varphi = G(x, y, z, t) \tag{3.12}$$

There is no complete solution for the problem stated by equation 3.8 in all conditions. However, if we look at the swell linear case we can relate the conditions that make them linear wave systems. If wave systems above

T=8s can reach an order larger than 1x10²m, then any wave with amplitudes lower than linear wave theory at 2m will make the term $u(\partial\eta/\partial x)$ of equation 9.3 vanish, as we see in equation 12.3 and Figure 3.4.

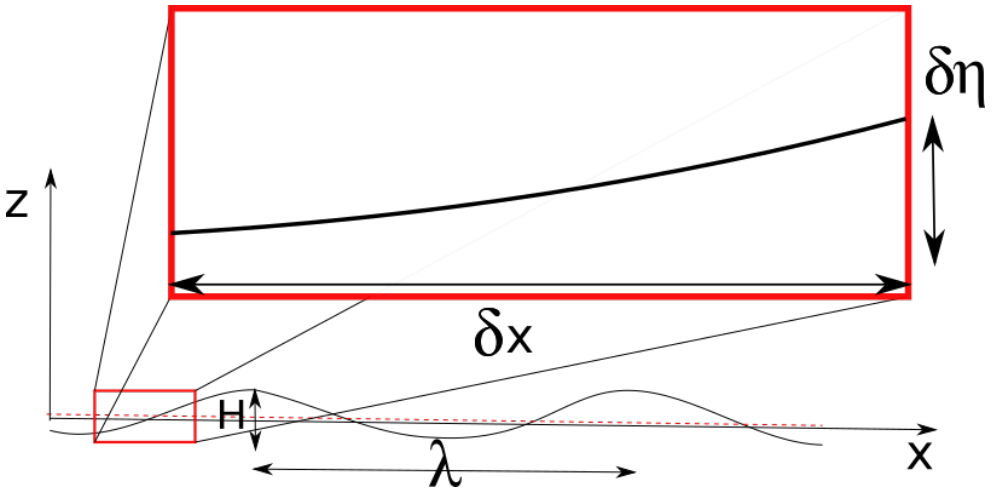

Figure 3.4: Increase in amplitude at a given increase of wavelength, as δx<1, then δη<<1.

$$\frac{\partial\eta}{\partial x} = \frac{\Delta\alpha}{\Delta\lambda} \to 0 \qquad 3.13$$

Equation 3.10 shows us that the balance of forces at the surface depends on the water velocities too. However, the wave velocities are found if we derive the function in equation 3.12 using the variables x and z, meaning we will obtain the velocities, as seen in equations 3.14 and 3.15.

$$\frac{d\varphi\left(x,y,z,t\right)}{dx} = V_{\varphi x} \qquad 3.14$$

$$\frac{d\varphi\left(x,y,z,t\right)}{dz} = V_{\varphi z} \qquad 3.15$$

The function φ is also called ‘the potential function’. The function expresses the amplitude time variation in time and space. As any swell with a small amplitude will likely behave as in equation 3.13, then the ratio of change expressed in equation 3.13 is smaller than the unity. The expressions u^2 and v^2, after satisfying the small amplitude conditions, can be approximated to be smaller than 1, which results in equations 3.16 and 3.17.

$$\frac{\partial \varphi}{\partial x_i} = \frac{\Delta a(x,z,t) \to 0}{\Delta \lambda \to 0} \ll 1 \quad 3.16$$

$$\left(\frac{\partial \varphi}{\partial x_i}\right)^2 = {V_{\varphi i}}^2 \to 0 \quad 3.17$$

The classical boundary condition at the bottom is taken, which states that there is no wave velocity at depth $z=h_d$. The constant in equation 3.9 is 0. This will leave us with a linear wave system in equations 3.18 to 3.21.

$$\frac{\partial^2 \varphi}{\partial x^2} + \frac{\partial^2 \varphi}{\partial z^2} = 0 \quad 3.18$$

$$\frac{\partial \varphi}{\partial z} = 0 \quad 3.19$$

$$\frac{\partial \eta}{\partial t} = w \quad 3.20$$

$$\frac{\partial \varphi}{\partial t} + gz = 0 \quad 3.21$$

Equation 3.12 expresses that we search for a solution that depends on variables (x,y,z,t), as we take the velocity and change to y as constant, so the function φ must be only dependent on (x,z,t). The solution for this system is known for deep waters and transitional-shallow waters when under the conditions stated, such as small amplitude conditions or $\eta(z)/\lambda \sim 0$, where the amplitude must be smaller than the wave wavelength or $\eta(z) << \lambda$. As mentioned before, this means that wavelengths must be in orders of Nx10^2 and amplitudes in the order of less than 5x10^0. The solution to the linearised equation of the system is known and shown in equation 3.22.

$$\varphi(x,z,t) = \omega\alpha \left(\frac{Cosh[k*(d+z)]}{Sinh(k*d)}\right) Cos[(\omega*t)+(k*x)] \quad 3.22$$

Another useful parameter with which to calculate the applicability of wave theories under low amplitude circumstances is shown in Equation 3.23, a parameter known as the Ursell number.

$$U_{ursell} = \frac{H\lambda^2}{\delta^3} \tag{3.23}$$

The Ursell number relates the depth at which a wave moves, its amplitude, and wavelength. If the Ursell number is smaller than 100 then the linear theory can be used, as the non-linearities of the wave system are small and irregular crests are not important. If any swell system satisfies the conditions of low amplitude and the Ursell number [59], as in the dimensional requirements of Figure 3.3, then it can be treated as a fairly linear wave. Figure 3.5 and Table 3.1 show the relationship for several swells using the Ursell and Fenton formulations.

$T(s)$	Max $H(m)$	Depth h_d (m)
20	3.55	281
19	3.2	252
18	2.8	225
17	2.5	200
16	2.2	175
15	1.9	153
14	1.65	131
13	1.4	112
12	1.2	94
11	1	78
10	0.8	63

Table 3.1. Values for long swells at infinite depths that satisfy the Ursell condition of linearity.

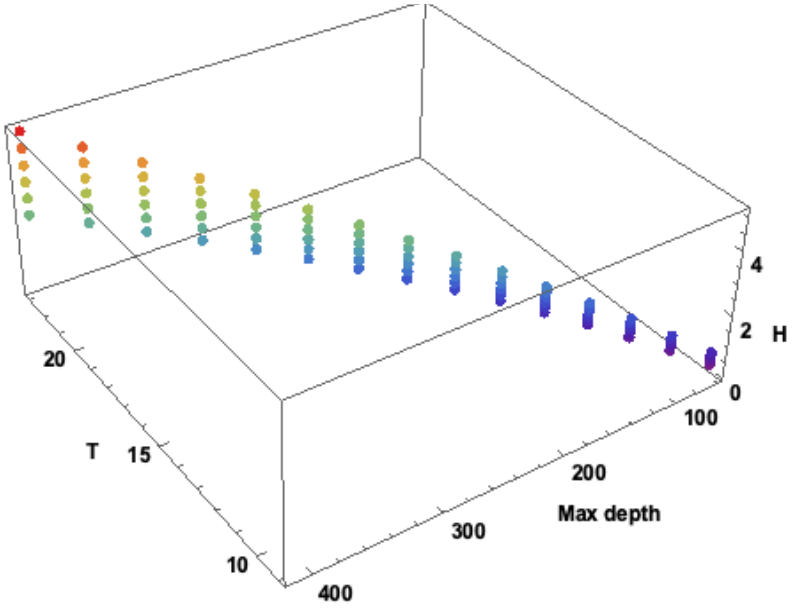

Figure 3.5: Values for different long swells that can satisfy the Ursell equation in the open ocean.

3.1.5 Open sea conditions

An open sea environment offers special conditions for the solution. The term related to the hyperbolic functions in equation 3.22 can be rewritten, as in equation 3.24.

$$\varphi(x,z,t) = \omega\alpha\left(e^{kz}\frac{1+e^{-2k(z+h)}}{1+e^{-2kz}}\right)Cos[(\omega * t)+(k * x)] \qquad 3.24$$

If we consider that the average depth of open ocean basins is $5000m$ at the central point and $3800m$ at the continental borders [67], then the exponential ratio can be approximated as 1 at large depths. Large depth conditions occur when depths are several orders bigger than z in equation 3.25. The function that satisfies equations 3.18 to 3.21 in the open ocean is 3.26.

$$h \to 1x10^{3} \therefore \frac{1+e^{-2k(z+h)}}{1+e^{-2kz}} \to 1 \qquad 3.25$$

$$\varphi(x,z,t) = \omega\alpha e^{kz} Cos[(\omega * t) + (k * x)] \tag{3.26}$$

The expression 3.26 tells us how a linear wave like a swell system behaves when travelling across the ocean. Here the velocities can be obtained as derivates of φ in its components, which is shown in equations 3.27 and 3.28, where the z component must add a term if the waves are under a constant current U that varies with the depth z.

$$V_{\varphi z} = \frac{\omega a}{k} e^{kz} Cos[(w * t) + (k * x)] + U(z) \tag{3.27}$$

$$V_{\varphi x} = \frac{\omega a}{k} e^{kz} Sin[(w * t) + (k * x)] \tag{3.28}$$

The velocities will decay to near zero at half the wave system wavelength. These trajectories are approximately circular if we neglect a small contribution from the Stokes drift. The trajectories and the velocities tell us that a linear swell like systems will have velocities in x and y balanced and with a phase displacement of $a\pi/2$ as in equation 3.29.

$$V_{\varphi x}(x,z,t) = V_{\varphi y}\left(x, z, t \pm \frac{\alpha\pi}{2}\right) \tag{3.29}$$

3.1.6 Transitional water depths or continental shelf conditions

After entering the continental shelf, propagated waves will exhibit a transitional depth behaviour. This change in the wave properties can be expressed by the wave equation in 3.22. However the depth difference will modify the potential equation, and velocities are then expressed by the modified derivates of φ, as in equations 3.30 and 3.31.

$$V_{\varphi x}(x,t) = \omega\alpha \left(\frac{Cosh[k * (d+z)]}{Sinh(k * d)}\right) Sin[(\omega * t) + (k * x)] \tag{3.30}$$

$$V_{\varphi z}(x,t) = \omega\alpha \left(\frac{Sinh[k * (d+z)]}{Sinh(k * d)}\right) Cos[(\omega * t) + (k * x)] \tag{3.31}$$

Wave interaction in these regions will reach the bottom of the seabed and then its trajectory profile will be ellipsoidal. The main difference will be not only the particle trajectories, but the velocity component $V_{\varphi x}$ will be the principal component as the $V_{\varphi y}$ component will vanish, $z \sim h_d$. This can be seen as the $Sinh$ term and the $Cosh$ term converge to values such as one and zero as in equations 3.32 and 3.33.

$$V_{\varphi z} = \frac{\omega a}{k} e^{kz} Cos[(w * t) + (k * x)] \tag{3.32}$$

$$V_{\varphi x} = \frac{\omega a}{k} e^{kz} Sin[(w * t) + (k * x)] + U(z) \tag{3.33}$$

The velocities in the open sea are directly proportional to each other, which implies that for a swell like system with low amplitude propagation $V_{\varphi x} \sim V_{\varphi y}$, the velocity field is also conservative. This means there will not be variation as long there is no energy dissipation or this dissipation is minimal. We can see the behaviour of the ratio of the velocities mentioned for the open sea waves and the transitional waves in Figures 3.6 and 3.7 below. The ratio of both will tell us how much kinetic energy will penetrate the velocity field below the ocean surface.

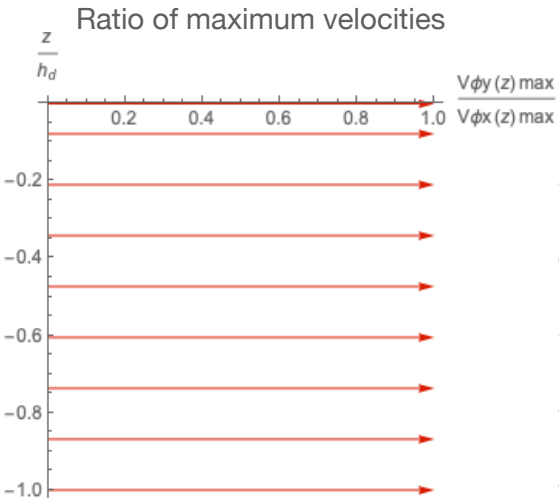

Figure 3.6: Velocity field ratio of maximum velocities for an open sea linear wave.

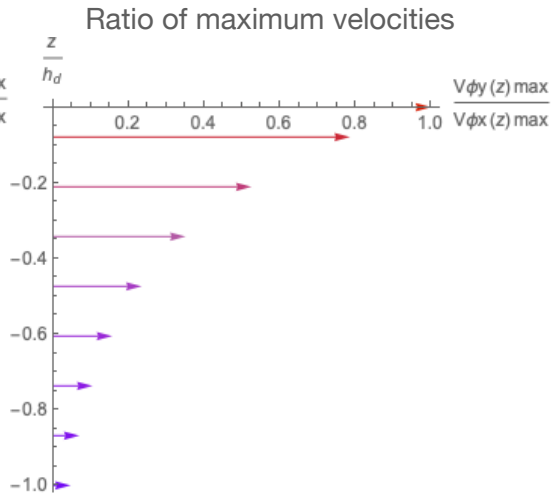

Figure 3.7: Velocity field ratio of maximum velocities for linear waves at transitional waters.

3.1.7 The energy carried by a wave

The energy of any fluid that is set in motion is expressed as the sum of potential, kinetic, thermal, or chemical energy. Variation in the fluid energy is given by the gradient on equation 3.34, as in [32]. The equation represents the balance of a fluid moving across the sea basin. In this case, the change in velocity of the fluid must be equal to the change in the thermodynamic energy and the potential energy of the fluid.

$$\frac{\partial \overline{V}}{\partial t} + \left(\overline{V} \bullet \bigtriangledown\right) \overline{V} = - dw + g \qquad 3.34$$

As swell systems propagate around the globe, the zone of propagation can vary drastically in its temperature. Generating swell systems in the Antarctic/Artic can reach temperatures lower than 0 degrees, and they will later move to zones of tropical seas with temperatures above 20 degrees at the sea surface.

As density and energy play an important role in the fluid energy exchange, the term dw could be important for its propagation on a macro scale. However, swells under relatively local circumstances of propagation will not have any important thermal exchange. If we neglect the terms related to thermal and chemical gradients, then dw ~0 in equation 3.34. After neglecting the term dw we obtain the energy balance in equation 3.35.

$$dw = (Tds = 0) + Vdp \therefore \frac{\partial \overline{V}}{\partial t} + \left(\overline{V} \bullet \bigtriangledown\right) \overline{V} = - Vdp + g \qquad 3.35$$

The partial derivate of the velocity vectors defined by equations 3.28 and 3.29 is zero, and this relationship then gives us equation 3.36.

$$\frac{\partial \overline{V}}{\partial t} = 0 \therefore \left(\overline{V} \bullet \bigtriangledown\right) \overline{V} = - Vdp + g \qquad 3.36$$

The equation 3.36 can be rewritten as a new expression using the cross product rule of vector calculus. The obtained simplification allows us to rewrite it using a rotational term for the velocity; however, if the fluid is

governed by a potential function as in equation 3.12, then we obtain equation 3.37.

$$\frac{1}{2} \bigtriangledown \overline{V}^2 - \left(\overline{V} \times \bigtriangledown\right) \overline{V} = - Vdp + g \tag{3.37}$$

We can now say that the cross product is zero, and then express the velocity that is the volume as a unit of mass between the sea density in equation 3.38.

$$\left(\overline{V} \times \bigtriangledown\right) \overline{V} = 0 \therefore \frac{1}{2} \bigtriangledown \overline{V}^2 = - \frac{dp}{\rho} + g \tag{3.38}$$

Then we multiply by the density on both sides and we remain sure that the change in gravity due to the column oscillation is small. Equation 3.38 converts into 3.39, taking into account that the pressure change depends on the amplitude variation.

$$\frac{1}{2} \bigtriangledown \rho \overline{V}^2 = - \rho g z \tag{3.39}$$

Equation 3.39 tells us that, for a defined wave system, by the properties of equations 3.18 to 3.21, under open ocean conditions where λ<2a, with maximum height expressed in Figure 3.5 and Table 3.1, and following the limits of small amplitude and local changes in propagation with a minimum exchange of energy, our wave can be regarded as an exchange between its potential and kinetic energy. To obtain the whole energy of the long wave particles moving, we must integrate into the column from the wave mean depth h_d and later through the whole wavelength λ as in equations 3.40 and 3.41.

$$\int_0^{h_d} \int_\lambda^0 \frac{1}{2} \bigtriangledown \rho \overline{V}^2 dx dz = \int_0^{h_d} \int_\lambda^0 - \rho g z dx dz \tag{3.40}$$

$$\int_0^{h_d} \int_\lambda^0 \frac{1}{2} \bigtriangledown \rho \overline{V}^2 dx dz + \int_0^{h_d} \int_\lambda^0 \rho g z dx dz = 0 \tag{3.41}$$

As both equations are reciprocal, we obtain 3.42.

$$E[\varphi(x,z,t)]_{Total} = E[\varphi(x,z,t)]_{pot} + E[\varphi(x,z,t)]_{kin} \quad 3.42$$

It is necessary to say that as waves move through a basin beyond 4000km [51] there is little attenuation. This means energy is conserved if it does not interact with other ocean phenomena. Other phenomena that can cause wave energy to change in its propagation are diffraction and shoaling. These energy exchanges can be disregarded, if we assume the propagation of the local wave over a distance x incurs a very minimal energy loss. Then the wave at the locality of propagation on large scales is considered a conservative energy phenomenon.

3.2 Wave propagation after obstacles

Waves propagate radially from the point of origin, be that a storm system or an earthquake. After leaving the open sea basin where conditions are h_d>>λ that give rise to equation 3.24, they will change its physical properties as we have mentioned before. These changes will produce a variation in the wave characteristics, as they propagate over the shelf and obstacles. Over the next pages, the theory behind this interaction will be developed. Some analytical formulations will be reviewed and also their range of application. The formulations will be used to propose a new analytical formulation to model wave propagation over an obstacle from depth waters to transitional waters.

3.2.1 Long wave propagation after a seabed level change under non-variant frequency

If long waves that satisfy conditions $\lambda>>h_b$, $\lambda>>a$, the Ursell number, and equations 3.40 to 3.42, they can be modelled as linear swells. Linear long swell like waves can be modelled using Lamb formulation [68], wherein waves propagate perpendicularly to an obstacle through a canal of fixed width. The canal proposed by Lamb has a constant width b, without radial

spreading [$\Delta s=\Delta r\theta$]~0 or interaction with the walls. Waves will cross a section at $x=o$ with an abrupt depth change, as $h_d<\lambda$, also $\Delta h<\lambda$. We can see this in Figure 3.8.

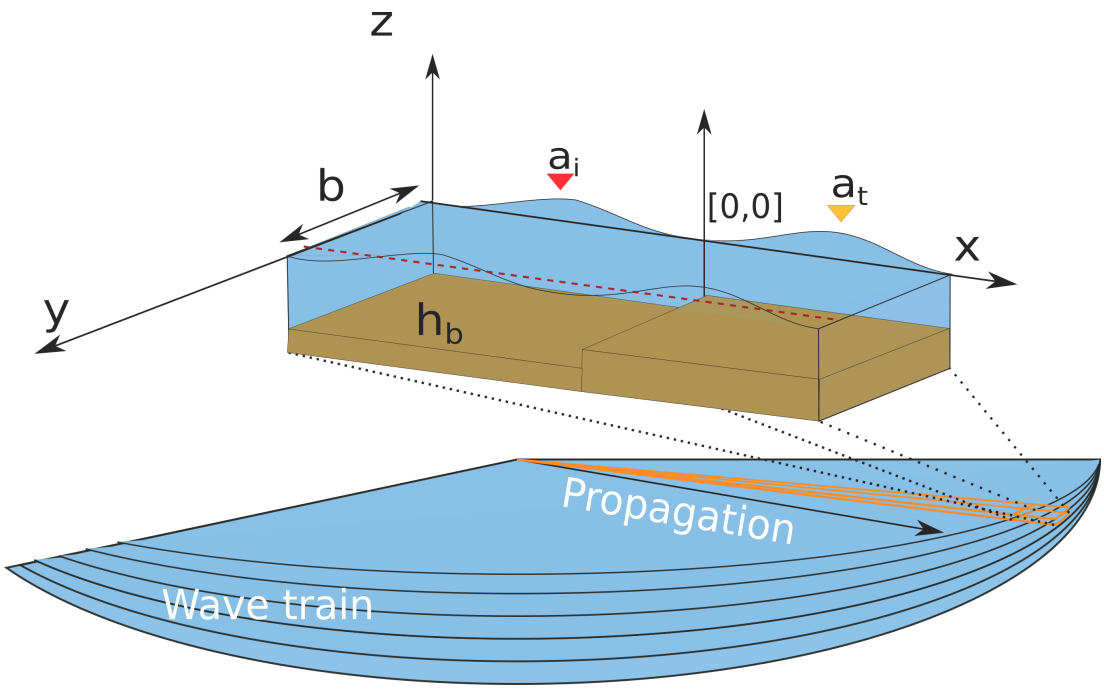

Figure 3.8: Model proposed by Lamb to study wave propagation after crossing a regular obstacle. Here a_i and a_t are the reflected and incident wave amplitudes.

The conditions imposed by $\lambda>>h_b$ state that only very large wave systems can use this formulation, and the wavelengths of these wave systems will be two orders of magnitude larger than the shelf mean depth. Using these conditions, we can reduce the wave solution to a simple system as in equation 3.43.

$$\varphi_i(x,z,t)+\varphi_t(x,z,t)+\varphi_r(x,z,t)_r=0 \qquad 3.43$$

The system depicts three long waves, one travelling from [-∞, 0], φ_i, a reflected wave from [0, -∞],φ_r, and a transmitted one from [0, ∞]φ_t. Without loss of generality, we can say that the solution for the three waves is shown in equation 3.43. The wave amplitude z is a function of x and t *in* 3.44.

$$z=f\left(t-\frac{x}{c}\right) \qquad 3.44$$

From equation 3.43 we can conclude that three solutions are needed, one for a reflected wave f_1, a transmitted wave f_2, and an incident wave f_3, as in equation 3.44. Those solutions must satisfy that the wave amplitude is the same at x, y=[*0*, *0*].

$$f_1\left(t-\frac{x}{c_1}\right)+f_2\left(t-\frac{x}{c_2}\right)=f_3\left(t-\frac{x}{c_3}\right) \tag{3.44}$$

The solutions have certain restrictions. On the right side, we only have incident waves at very long distances from the obstacle. Meanwhile, on the left side, we only have waves radiating to the shallower region. Another important aspect of this formulation is that continuity of the fluid surface needs to suffice at x=0 for the fluid. The continuity must also satisfy geometrical constraints as in equation 3.45; constraints of the continuity are: the depth where the waves propagate h_n, the canal breadth b_n and the wave's phase velocities c_n.

$$\frac{gb_1h_1}{c_1}f_1\left(t-\frac{x}{c_1}\right)-\frac{gb_2h_2}{c_2}f_2\left(t-\frac{x}{c_2}\right)=\frac{gb_3h_3}{c_3}f_3\left(t-\frac{x}{c_3}\right) \tag{3.45}$$

The term c_n is the wave celerity and by combining equations 3.44 and 3.45 Lamb's solution is then obtained, as we see below in equations 3.46 and 3.47 and plotted in Figure 2.21 in Chapter 2.

$$K_r=\frac{1-(h_2/h_1)^{(1/2)}}{1+(h_2/h_1)^{(1/2)}} \tag{3.46}$$

$$K_t=\frac{2}{1+(h_2/h_1)^{(1/2)}} \tag{3.47}$$

The generality of the solution found by Lamb also tells us that the wave energy will be split into a transmitted and an incident wave energy. If we look again at equation 3.43 and then we use Lamb's assumption, we get equation 3.48.

$$E\varphi_i(x,z,t)-E\varphi_r(x,z,t)_r=E\varphi_t(x,z,t) \tag{3.48}$$

Wave energy is frequency-dependent, so a split in the overall energy due to the obstacle/wave interaction indicates that frequency must not be the same for both the propagated and the reflected wave. Lamb's statements expressed by equations 3.46 and 3.47 are however frequency independent. As T_{shift}~0 the formulation shows some inconsistencies that have been observed by several authors, as mentioned in Chapter 2.

3.2.2 Long wave propagation after an uneven seabed level change under non-variant frequency at finite depth

Lamb addresses wave transmission under regular obstacles, but bathymetry in open sea can be more complex. Obstacles range from rocks of a few metres, jumps of several dozens of metres, and sudden walls of more than hundreds of metres that cover the ocean floor. The result of this is an intricate system of wave reflections and transmissions from the ocean basin to the coast. Solutions for bathymetric anomalies under long-wave and shallow water conditions are known and these methods are based on the solution of the equations under shallow water conditions. The proposed system that has been addressed by Xie et al. [84], Bender [95], and Jung et al. [83] uses solutions of the shallow water equation, as seen in Figure 3.9 and equations 3.48 to 3.50.

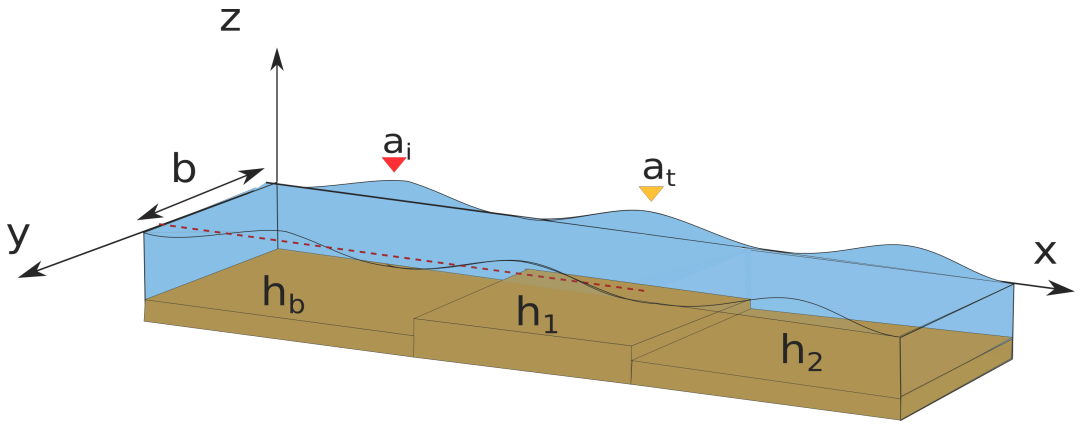

Figure 3.9: Wave propagation model using shallow water equations. The sea bottom is split into regions with depths h_b, h_1, and h_2.

$$z_1 = a_d e^{ik_1 x} + a_{r1} e^{ik_1 x} \qquad 3.48$$

$$z_2 = a_{t1}e^{ik_2x} + a_{r2}e^{ik_2x} \tag{3.49}$$

$$z_3 = a_{t2}e^{ik_3x} \tag{3.50}$$

In this method, if we assume a solution in the form of equation 3.12, which is a general form of a solution, the amplitudes a_d, a_{r1}, a_{t1}, a_{r2}, and a_{t2} are the amplitudes of the incident wave a_d, and the transmitted and reflected waves through the basin. Then we have a system of n equations that must be satisfied, as with Lamb's continuity at the jumps. The system of equations can be expressed as a matrix system. The solution that depends on the obstacle shape is shown in equation 3.51 by Xie.

$$Kr = \left(\frac{(s_{21} - s_{01})^2 + \frac{1}{2}(1 - s_{01}^2)((1 - s_{21}^2))(1 - Cos2\theta)}{(s_{21} + s_{01})^2 + \frac{1}{2}(1 - s_{01}^2)((1 - s_{21}^2))(1 - Cos2\theta)} \right)^{1/2} \tag{3.51}$$

In this scenario h_d=h_0, s_{21}=$(h_2/h_1)^{1/2}$, s_{10}=$(h_0/h_1)^{1/2}$, and θ=$2s_{01}\pi N$ (N=obstacle length/λ). The method has been tested analytically only for limits on which depths range from 20-60 times λ, and values like this restrict its application for wave periods below $19s$ in waters not larger than $30m$. However, numerical studies by Dean [96] and Bender [95] suggest a relatively good agreement in ranges with shorter wavelengths as λ<$9.42h_d$. The suggested values put Lamb's formulation in a transitional water regime. To obtain the expression for the transmitted wave, we take the conservation of energy. This expression comes from the continuity relationship in the Lamb formulation. The surface must stay continuous around the bathymetry jump on any obstacle. We assume the reflection near the x=0 jump is inelastic so energy is conserved. From the energy conservation for the wave system energy, we have equation 3.52.

$$E[\varphi_i]_{kin} + E[\varphi_i]_{pot} = \left(E[\varphi_r]_{kin} + E[\varphi_r]_{pot}\right) + \left(E[\varphi_t]_{kin} + E[\varphi_t]_{pot}\right) \tag{3.52}$$

The solution is simple as we only require the same assumption made by Lamb, Cho, and Xie that the amplitude does not depend on the frequency. The formulation implies then that k_i~k_r~k_t. We require losses to

be minimal so that the energy flux is conserved. The transmitted wave energy must be the remainder of this energy exchange. Then, we know the Laplacian of the potential must be zero after and before the obstacle, at least outside the locality of the jump discontinuity, as in equation 3.53.

$$\bigtriangledown \bullet \varphi^2 = 0 \;\&\; E[\varphi]_{kin} = \frac{1}{2}\rho \bigtriangledown \bullet \varphi^2 \therefore \oint E[\varphi]_{kin} = 0 \qquad 3.53$$

Using this simple relationship we can conclude that at the jump zone the energy disregarding dissipation effects must be conserved, and then the solution for the transmission must be equation 3.54.

$$E[\varphi]_{pot} = \rho g z \;\&\; z = A_n e^{ik_i x} \therefore Re[e^{ik_r x} - Kr \bullet e^{ik_n x}] = Re[Kt \bullet e^{ik_t x}] \qquad 3.54$$

The solution tells us that the wave transmitted must be smaller than our incident wave, and this condition is given if no change in frequency is allowed. However, the frequency problem is still missing as propagation around the jump is regarded as frequency invariant.

3.2.3 Long wave propagation after a seabed level change under variant frequency in shallow and transitional waters

As Goring and other authors have shown, even in cases where the characteristics are given by wavelengths larger than the propagation depth $\lambda >> h$, a shallow-water basin, as in $\lambda/h > 20$, and amplitudes $a << \lambda$, a frequency change is presented. Frequency change after propagation could arise due to several factors such as energy losses after transmission, border-shelf interaction, non-elastic collision against the shelf, or other mechanisms of the abrupt change of depth. These mechanisms will modify the energy of the wave transmitted, as Naghdi and Marshall suggest [88]. The Naghdi and Marshall's formulation uses an Eulerian reference frame. As the solution using Eulerian theory requires a moving frame of reference, the frame is given by functions defined under the basis vectors e_{1i}, e_{2j}, and e_{3k}. The main theory behind the fluid model and physical terms can be found in

Green and Marshall's earliest works [97-77], where every part of the fluid is defined by a layer that moves tangentially to the sea bottom. The layers that move cause the wave oscillations that are defined by their velocity in any of the main directions (e_{1i}=x, e_{2j}=y, e_{3k}=z). The model can be seen in Figure 3.10.

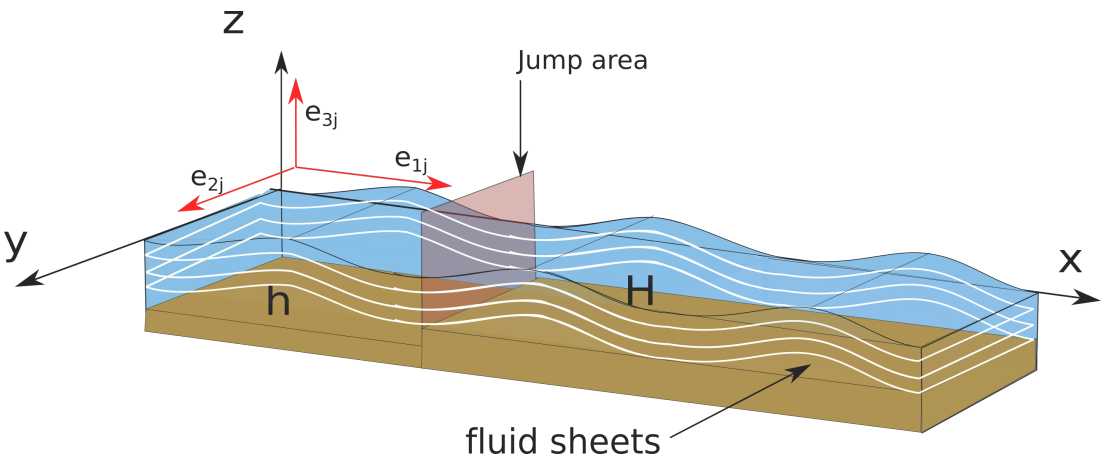

Figure 3.10: Green and Marshall's model based on the directed fluid sheets theory. The fluid is divided on individual sheets that have associated vectors e_{nj} for each direction.

In the Eulerian representation, every function of the velocity is related to a vector in the direction of this velocity, and then our system consisting of a function f that varies on (x,z,t) can be represented as a function consisting of three vectors. The formulation that models this can be seen in equation 3.55.

$$V\varphi = w_0 + w_1 Cosh[a(z+h)] + w_2 Sinh[a(z+h)] \qquad 3.55$$

Here the functions w_0, w_1, and w_2, as defined by Green and Naghdi ,are functions in the form of $\varphi(x,z,t)$, and these functions from the Lagrangian theory are used to derive the small-amplitude long-wave equations on infinite and finite depth. Solutions are related to the ones in equations 3.8 to 3.12. As we can see, our hyperbolic functions are the same as in classical Linear theory. The advantage of this system is that it can be defined for non-linear water waves. In the Eulerian system for directed fluid sheets the hyperbolic functions depend on z and the depth they move in

$h=h_d$. Then our wave amplitude is defined by $z=B(x,z,t)$, and thus our swell height ratio to jump depth ratio is small, $Hs/H\sim0$. Then $z+h=(B(x,z,t)-h+h)\sim0$. The velocity can be defined as below for the directed fluid sheets theory derived from Naghdi and Green, shown in equation 3.56.

$$V_{\varphi} = w_0 + w_1(z+h) \tag{3.56}$$

The relationship in equation 3.56 comes from the small amplitude requirement as in Lamb and others. However, it extends its application to arbitrary depths. The conditions for the jump are similar to those in Lamb's and Naghdi and Green's formulations, so they must satisfy that the wave surface must not break at the discontinuity. This is assumed because if it happens it will also break the small amplitude, suggesting that our wave entered shallow waters. The other conditions are that the force exerted at the jump must be different from 0 and the derivate of the function must be at least analytical at the locality from both sides. The expressions for this are shown below.

$$\varphi'_{x+\to jump} = \varphi'_{x-\to jump} \tag{3.57}$$

$$\frac{w_{11}Sinh[a(z+h)]}{k}_{x+\to jump} = \frac{w_{11}Sinh[a(z+h)]}{k}_{x-\to jump} \tag{3.58}$$

$$F_{jump} \neq 0 \tag{3.59}$$

The first condition is in Lamb's continuity, where the wave system passing the step must be continuous and not break at the surface in equation 3.57. This condition also states that the fluid must be conserved as it passes over the step. The solution for the wavenumber of the wave train's propagation over the obstacle can be seen in equation 3.60, as obtained by Naghdi and Marshall.

$$k_2 = \left(\frac{h k_1^2}{H\left(1 + \frac{1}{3}k_1^2h^2 - \frac{1}{3}k_1^2hH\right)} \right)^{1/2} \tag{3.60}$$

This solution satisfies for terms that are, as we said earlier, k_1h_1~0 or k_2H_2~0. Another useful relationship for this case is that the wave numbers are related as follows in equation 3.61.

$$k_1 Tanh[k_1 h] = k_2 Tanh[k_2 H] \qquad 3.61$$

The decomposition says that any x value greater than 0.9 at $Sinh$ and 0.5 at $Cosh$ will have more than 10% deviation from using just the kH value. We can then calculate that at operational depths between 70m to 50m our wave height is limited under this theory to β=0.5m. The limit can be a long swell with high dissipation from the open sea but amplitudes for shorter wavelengths offer a very limited range of application. Given conditions for kh<0.5 in equation 3.61, our wavenumber depends on the obstacle depth ratio. For waters where the wavelength is extremely high with periods between 19s to 20s at depths of 50m to 30m, we can reduce the denominator as kh^{n}~*0.* The overall value of the denominator is *H(1 +*γ*)* where γ*~0* the wavenumber relationship is given by equation 3.62.

$$k_2 = k_1 \left(h/H\right)^{1/2} \qquad 3.62$$

Equation 3.60 suggests that the wavelength will increase in some cases depending on the wavelength and the depth ratio values defined by γ. The relationship is known to hold locally mathematically, but has not been subjected to more precise experimental tests to the author's knowledge. However, we can see that wavelength will increase after the jump. The increase will occur for values ranging from 1/10 of the original depth to 1.4 times the original depth. The depth ratio for this sudden increase to occur places the waves into transitional to deep waters systems. This can be seen in Figure 3.11 and Table 3.2 where values for the incident wavelength value are in the range k_1=[π/3 , 4π], and initial depth h_d=h..

The characteristic wave amplitudes in the order of 1x10^{-1} make Naghdi and Marshall's formulation limited for a big part of the wave spectrum, since waves with smaller lengths need very small amplitudes. As

ocean waves can retain the linearity at higher values of wave amplitude and propagation from deep waters to transitional is not addressed, the next pages explain a simple analytical formulation to address this.

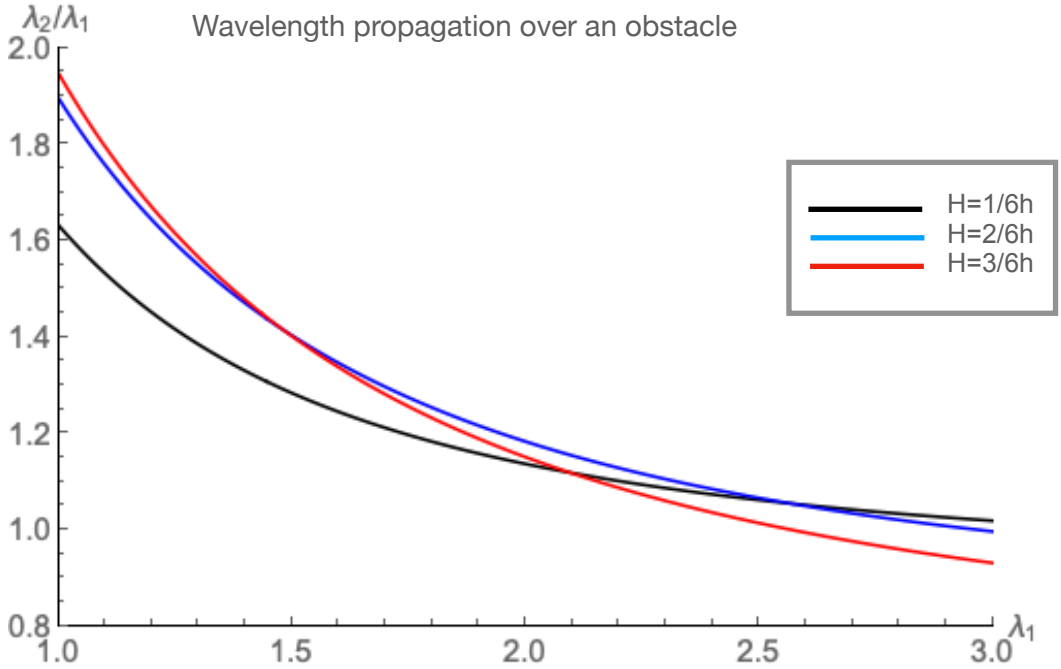

Figure 3.11: Variation of the transmitted wavelength ratio λ_2/λ_1 depending on the obstacle obstruction and the incident wavenumber k_1.

λ_1(m)	λ_2/λ_1 H=1/6h	λ_2/λ_1 H=2/6h	λ_2/λ_1 H=3/6h
1	1.6	1.9	1.9
1.5	1.28	1.4	1.4
2	1.13	1.18	1.14
2.5	1.06	1.06	1
3.0	1	1	0.93

Table 3.2. Values for the wavelength transmission using equation 3.60.

3.2.4 Long wave propagation after a seabed level change under variant frequency from deep waters

We must address the physical problem of long wave propagation from the open sea to the continental shelf to understand the possible effects

on engineering structures installed near bathymetric jumps. The previous solutions developed by several authors work in relatively shallow waters, so a solution to the problem requires an approximation for the propagation in cases where the wave transmits from depths $\lambda/h_d<2$ to $\lambda/h_d>2$. As engineering devices will be installed at $\lambda/h_d>20$, one needs a formulation addressing these depths that is able to describe the frequency and wavelength shift. To address this problem we start with the wave equation in open waters where again $H<<\lambda$ must hold or $H\sim1\text{x}10^0$ for $\lambda\sim1\text{x}10^2$ in the orders of magnitude. We also require continuity at the surface, energy, and mass conservation, as in equations 3.63, 3.64, and 3.65 below.

$$[\eta_i + \eta_r]_{x\to 0^+} = [\eta_t]_{x\to 0^-} \tag{3.63}$$

$$E[\varphi_i]_{kin} + E[\varphi_i]_{pot} = \left(E[\varphi_r]_{kin} + E[\varphi_r]_{pot}\right) + \left(E[\varphi_t]_{kin} + E[\varphi_t]_{pot}\right) \tag{3.64}$$

$$\varphi_i(x,y,z,t) - \varphi_r(x,y,z,t) = \varphi_t(x,y,z,t) \tag{3.65}$$

Now we take an energy balance approach. We know the total energy of the wave system, disregarding losses, must be a sum of the wave kinetic energy and the wave potential energy in equation 3.66.

$$E[\varphi]_{kin} = \frac{1}{2}\rho \bigtriangledown \bullet \varphi^2 \wedge E[\varphi_{pot}] = \eta(z) g\rho \therefore E[\varphi] = \oint E[\varphi]_{kin} + \oint E[\varphi]_{pot} \tag{3.66}$$

If the energy is equally distributed and losses are minimal, we can define an integral to apply the energy balance. We assume the length of the interval is $\Delta x<\lambda$ and $\Delta t<T$, and during this interval length the energy must be conserved at any two points in the same fluid streamline. The streamlines that pass through two fluid layers points, (x_1, z_1, t_1) and (x_2, z_2, t_2), must have the total same energy. Given any oscillating wave, the fluid particles over the fluid surface and the different sheets that compose the fluid continuum can be described as lines. The lines will behave as individual formulations for a wave moving in a chord. Every part of the fluid will oscillate at the function that defines the wave equation that we have described as having solutions as equations 3.22 and 3.24. The fluid lines oscillate at conditions given by low amplitude and infinite depth on the incident side, and low amplitude and

finite depth on the transmitted side. If the same particles also satisfy the linear conditions, thus proving the Ursell number is small enough, they can be regarded as linear. Given these conditions, they will also satisfy the energy equation, 3.64. The physical formulation can be seen in Figure 3.12, and the energy then can be regarded as having the expressions for kinetic and potential energy as in equation 3.67, where terms are integrated around an indefinite volume V, where dV is the total derivate around the wave contour from z=[$\lambda/2$, 0], x=[0, λ].

$$E[\varphi] = \frac{1}{2}\rho \oint \nabla \bullet \varphi^2 dV + \oint \eta(z) g \rho dV \qquad 3.67$$

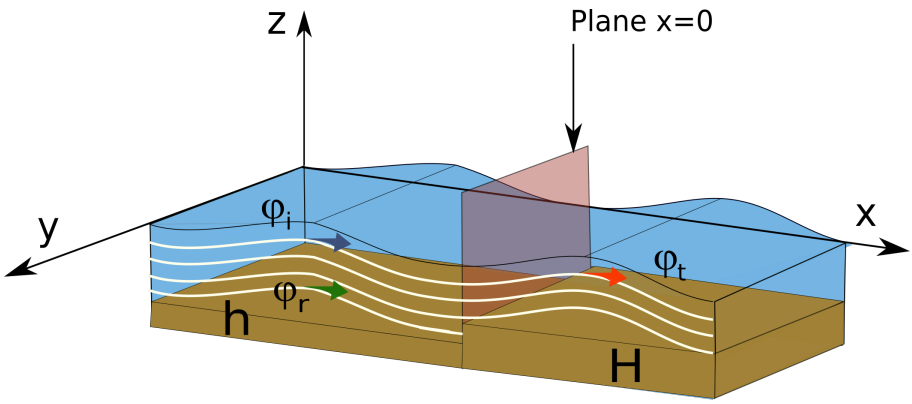

Figure 3.12: Model proposed for wave transmission under variant frequency and arbitrary obstacle length. Here the functions φ_n define the wave function for n={ i, r, t } that are the respective incident, reflected, and transmitted waves, here h_d=H.

For a stream of fluid oscillating from the negative side of the plane x the contained energy is the same, and the energy between a maximum potential and kinetic energy are both equal, as in equation 3.68, for the total wave energy.

$$\oint \nabla \bullet \varphi^2 dV = \oint \eta(z) g \rho dV \qquad 3.68$$

As it must suffice for the two arbitrary points in the stream, we can express any stream energy as equation 3.69.

$$\nabla \bullet \varphi^2 = \eta(z) g \rho \qquad 3.69$$

We also know that the total energy of the incident wave must be equal to the transmitted wave energy and the reflected wave energy as in equation 3.64, with no dissipation processes given by possible vortexes and turbulence at the border of the shelf or obstacle. This relationship is expressed in equation 3.70.

$$E[\varphi_i] = \frac{1}{2}\rho \bigtriangledown \bullet \varphi_r{}^2 + \eta_r(z) g\rho + \frac{1}{2}\rho \bigtriangledown \bullet \varphi_t{}^2 + \eta_t(z) g\rho \qquad 3.70$$

We know by the mass conservation that the fluid transmitting energy to $x \rightarrow \infty$ is the area between $z=[0, h_b]$; meanwhile, the area from $z=[h_b, \lambda/2]$ is the fluid energy that bounces back. This can be seen in equations 3.71 and 3.72.

$$E[\varphi_t] = \oint_{h_b}^{0} \eta_i(z) g\rho \, dV + \oint_{h_b}^{0} \bigtriangledown \bullet \varphi_i^2 dV \qquad 3.71$$

$$E[\varphi_r] = \oint_{\lambda/2}^{h_b} \eta_i(z) g\rho \, dV + \oint_{\lambda/2}^{h_b} \bigtriangledown \bullet \varphi_i^2 dV \qquad 3.72$$

The index refers to the incident wave, as the energy of the propagated wave will be calculated using the incident total energy we mentioned. This is, regardless, just an approximation that can only be sustained under small amplitudes at large wavelengths as we mentioned before. The diagram of the system can be seen in Figure 3.13 at next page.

We know that the potential energy is equal to the kinetic energy in a wave with almost no dissipation, so energy is equally distributed between the three waves. Then the total energy of the three waves for each streamline satisfies all the wave positions after the jump. We can express the total energy as the energy of each streamline as in equations 3.73 to 3.75, where $\beta_n=(a*g)/w$, $\tau_n=e^{kz}Cos(kx-wt)$ and $n=i,r,t$.

$$\oint_{\lambda/2}^{0} E[\varphi_i]_{kin} = \oint_{\lambda/2}^{h_b} E[\varphi_r]_{kin} + \oint_{h_b}^{0} E[\varphi_t]_{kin} \qquad 3.73$$

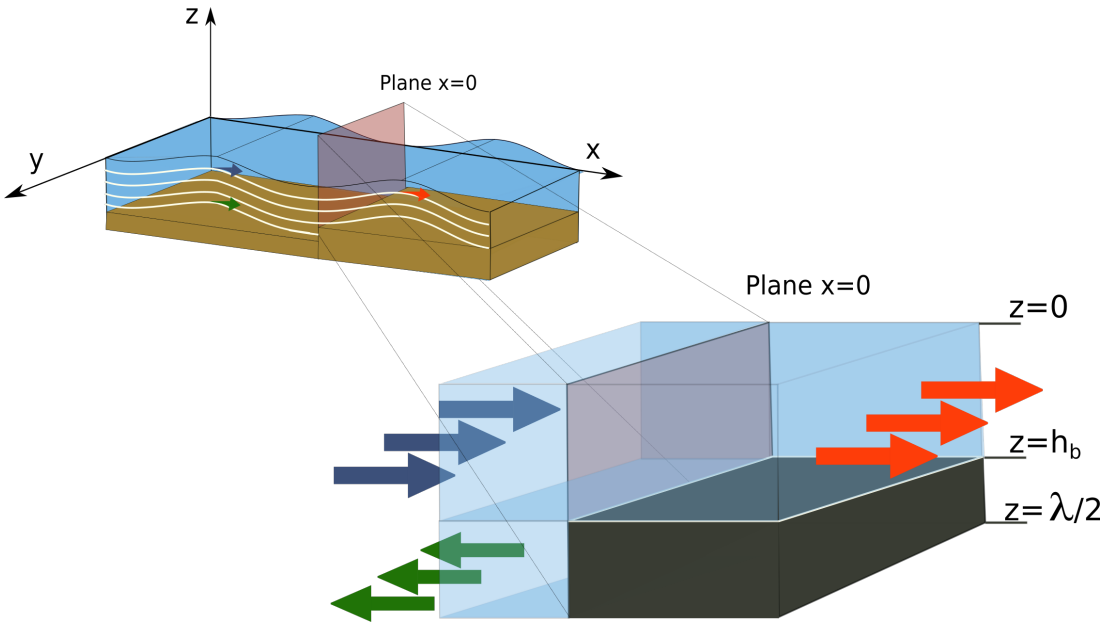

Figure 3.13: Model proposed to calculate the wavelength transmission of a wave propagating over a regular obstacle. Arrows show the energy flow of the incident (blue), reflected (green), and transmitted (red) wave trains interacting at plane x=o.

$$\frac{\lambda_n}{h_d} < 2 \therefore \int_{\lambda_n/2}^{0} E[\varphi_n]_{kin} = \int_{\lambda_n/2}^{0} \frac{a_n g}{2\omega_n} \rho \bigtriangledown \left(e^{k_n z} Cos(k_n x - \omega_n t)\right)^2 \quad 3.74$$

$$\int_{\lambda/2}^{0} \frac{\beta_i}{2} \rho \bigtriangledown^2 \tau_i = \int_{h_b}^{0} \frac{\beta_t}{2} \rho \bigtriangledown^2 \tau_t + \int_{\lambda/2}^{0} \frac{\beta_r}{2} \rho \bigtriangledown^2 \tau_r \quad 3.75$$

If we take the next steps, we integrate along the depths of each fluid mass that is transmitting energy, and we consider that the reflected wave energy is equal to the wave energy flow that is obstructed below the obstacle, and thus calculate the integrals assuming continuity at the surface, we get equation 3.76.

$$a_i{}^2 e^{2k_i(s_i - h_b)} = a_t{}^2 e^{2k_t(s_t - h_b)} \quad 3.76$$

As we know s_t and s_i are just the surfaces of our waves at s=0, changing the integration limits will give us the same relationship. But now h_b

is positive, the difference is just the depth below, the solution to which gives the next relationship for our wavelength in equation 3.77.

$$\lambda_t = \frac{-4\pi h_b}{ln(a_i/a_t)^2 - (4\pi h_b/\lambda_i)} \quad 3.77$$

We can recognise the term a_i/a_t as the inverse of the relationship for the transmitted wave amplitude, as found by Lamb [68], Naghdi and Marshall, [88] and the extreme cases for Xie et al. [84]. We need to infer a wave amplitude as a starting point to obtain an iterative method and, for this, we use the Naghdi and Marshall theorem on wave transmitted amplitude for non-linear waves at an arbitrary depth. Then we get equations 3.78 and 3.79 and k_t calculated from the Naghdi-Marshall or Lamb formulation.

$$K_t = \frac{A_t}{A_i} \quad 3.78$$

$$\lambda_t = \frac{-4\pi h_b}{ln(1/K_t)^2 - (4\pi h_b/\lambda_i)} \quad 3.79$$

As we can deduce from the expression, the wavelength change depends on the amplitude transmitted, as K_t~1 then λ_i~λ_t. The expression relates a potential energy property as the amplitude with a kinetic energy property as the wavelength. The formulation found shows that the term $ln(1/K_t^2)$ will define the wavelength, and as A_t grows larger the ratio of $1/K_t^2$ will decrease, thus making the ln a larger negative number. Larger values of a_t will make the denominator larger, and this will decrease the transmitted wavelength.

3.3 Model Limitations and Applicability

The model presented here consists of simple geometrical constraints, trying to find an approximate close solution to the problem of wave propagation. However, the model presents some characteristics that limit its

application; the model limitations are physical, mathematical, and also methodological.

3.3.1 Mathematical limitations

The expression derived here in 3.79 can not be solved by itself, requiring a value for the transmission coefficient or the transmitted amplitude. In this case, our function f depends on K_t, h_b and λ_i, where only h_b and λ_i. can be known.

Here K_t should be calculated using the Lamb or Naghdi-Marshall formulation. To calculate K_t the function g from equation 3.47 the solution for Naghdi-Marshall needs to be used. After this, the solution can be used in 3.79. The solutions for K_t, and our model have a condition that does not coincide, which is for Lamb and Naghdi-Marshall $\lambda << h_b$ and for the model presented here $\lambda > h_b$. However, the studies carried out by Newman probe that these solutions could work when the incident wave depth is larger or $h_b \rightarrow \infty$, and it is possible that the solutions of our formulation diverge as the incident depth grows.

Another limitation of the model is related to the depth of propagation and the assumption of linearity for the transmitted wave. As the depth of propagation is reduced $h_b \rightarrow 0$, the wave amplitude should grow and then the linear theory would not apply for the transmitted wave. In this case, as K_t increases, the formulation would not work and then it is limited to small transmitted waves. The limit for this is not proven in this thesis.

3.3.2 Modelling assumptions

The model specifically addresses a single wave transmitted and a single wave reflected. As is reported from other experiments, such as K. Szmidt's, the production of harmonics can start at relatively large depth to wavelength ratios in transitional water depths $(h_d/\lambda)=1/8$.

It is expected that as the ratio of immersion (difference between the obstacle depth and the propagation depth) decreases, harmonics will

increase their size, as observed by Tin C. et al. As the model and experiments do not take into account the possibility of harmonics, it is probable that amplitudes could be contaminated with large harmonics of different frequencies as the obstacle depth decreases $h_t \rightarrow 0$. As problems related to waves propagating in shallow waters are expected, the experiments and model will work with depth to wavelength ratios above those used by other experiments. To conclude, if they are important for the modelled waves, the parameter obtained by Tin C. et al. will be used in each case.

Another important limitation is the apparition of eddies in the corners of the obstacles, as reported by Takano. The eddies will dissipate energy, making the energy conservation assumption null, and might introduce other non-linear mechanisms which are not explored in this work. In the model ,another process that could be important is the relative length of the obstacle due to shoaling, which is assumed to be negligible for the experiments in Chapter 4. However, it is known that large obstacles will likely cause more bed friction and, in expectation of this, a series of experiments with a variable obstacle length were also run.

3.3.3 Model applicability

The model applicability depends on three key assumptions made:

1. Incident waves move from depth waters $h_d/\lambda=\infty$ to finite depth waters $h_t/\lambda>1/2h_d$ but no shallow water conditions $\lambda<(1/20)h_d$. In this case, the models of Lamb and Naghdi-Marshall had been proven to work when incident waves move from deeper to finite depth waters, but only with obstacles under relatively shallow waters. The models and experiments analysed here, do not work with larger depth and wavelength ratios, leaving the range $h_t/\lambda=[1/2\text{-}1/7]$ unexplored. As the wave dynamics conditions change when moving to deeper waters, the conditions for propagation are explored in our model and further experiments.

2. Waves modelled here do not present harmonics with a large energy shift (amplitude peak) after the wave propagates. This is derived from the depth of submergence (h_t/h_d) as explored by Ting et al. In this case ratio of (h_t/h_d) it is large enough.

3. Waves have a small amplitude after and before the obstacle, so they can satisfy the linear wave equation, before and after the obstacle. In these cases, the transmitted wave can not grow extremely large. It is possible that certain ratios of K_t will not comply with the proposed model.

3.3.4 Model improvements

The model presented here is not a complex numerical model, and despite its simplicity can offer fast solutions within a valid range of depths and wavelengths. Some advantages compared to the models of Lamb or Belibassakis and Athanassoulis are:

- It is faster and easy to implement in code than the finite depth water methods used by the authors [83], [84], [85] and [86].
- It provides an analytical solution for cases which can suit normal operational conditions for devices in the open ocean. These conditions include depths of interest for marine energy applications while covering normal wave weather conditions. Others models only apply to tidal waves and near shore conditions.
- The solution does not depend on the wave order or shape as long the physical conditions remain valid.

3.4 Wave properties after propagating over an obstacle

In the last two sections, we reviewed the range of applicability. We also developed some important formulations that can be used to describe its propagation under certain conditions, and also its mathematical background, which will be used to study how the waves propagate after a sudden change of bathymetry. These changes must resemble jumps on the seabed and the wave systems will resemble long swell waves. The main

changes in the wave parameters will be in amplitude and frequency, both of which will have several impacts on the forces and loads that our devices will be subjected to under the sea surface. In the case of the tidal turbines, it is expected that the change in the fluid field velocities, will have an overall effect on the hydrodynamic performance of the fluid capturing structures. The effects of changed properties will be addressed in the next paragraphs, as well as the range of applicability for the wave amplitude change theories.3.4.1 Wave theories and their range of applicability depending on their wavelength. Lamb's model, and those of Jung et al., Xie et al., and others, predict a change in the wave amplitude depending on the jump height ratio. All models under relatively low amplitude conditions show that regimes will depend on the depth of propagation. As with Lamb and Xie et al., the ratio of wavelength/depth where the model is proposed to have validity is around 0.3, according to Newman's results. The value of this ratio defines our operational depths in shallow waters. Depth values could range from $40m$ to $30m$, for wavelengths above $500m$. The results of these theories could only be applied effectively to very large swells with wavelengths larger than 1/6 of the depth. Results by Naghdi-Marshall extend this to transitional waters. In our case, using energy conservation, we can propose a range where it can hold as long as the wavelength is shorter than the depth before the obstacle. The range is shown in Figure 3.14.

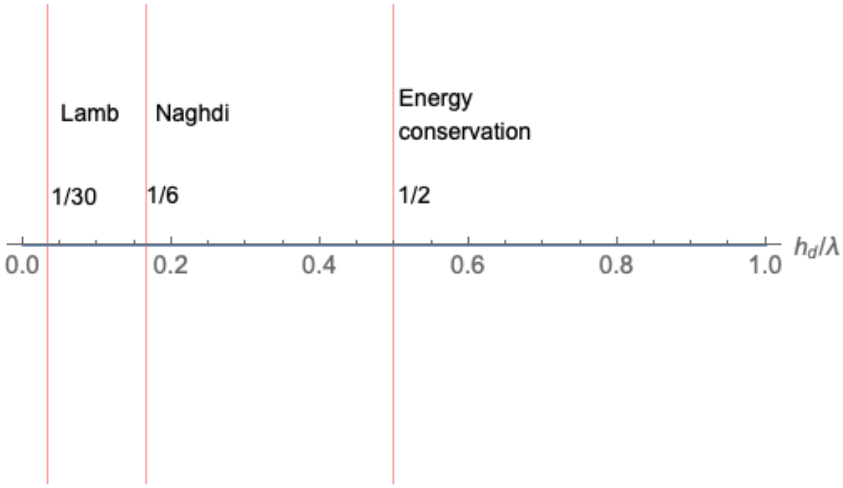

Figure 3.14: Proposed range of applicability for the wave theories according to their wavelength to depth ratio.

In the case of the Nahgdi-Marshall formulations and the energy balance model, both are independent of the wave shape.

3.4.1 Wave frequency and wavelength changes

Operational circumstances can change if we place our turbine after or above a bathymetry rise. As cyclical load magnitudes will depend on the amplitude magnitude, then wave loads will increase proportionally after propagating over the obstacle. The increase in the loads and forces is expressed in equations 3.80 and 3.81.

$$F = m\,a \;\therefore F_{induced} = \rho \frac{\partial^2 \varphi}{\partial n^2} \tag{3.80}$$

$$F_{induced} = \rho A \frac{\partial^2 \varphi'}{\partial n^2} \tag{3.81}$$

As such, the function defining the potential for the waves will be a function of w and k as in equation 3.82 and then at conditions where variant frequency applies. Here, φ' is also a function dependent on variables (x,y,z) and also its angular frequency w and wavenumber k. Then the velocity and force oscillation will be as in equations 3.82 and 3.83.

$$F_{induced} = \rho A \frac{\partial^2 \varphi'(\omega, k)}{\partial n^2} \tag{3.82}$$

$$V_{induced} = \frac{\partial \varphi(\omega, k)}{\partial n} \tag{3.83}$$

The solutions will define the periodicity and strength of cyclical loads and their impact on the device torque and thrust. In the case of transitional waters for the Naghdi-Marshall model and the energy formulation proposed here, a wavelength increase is given at transitional/deep-water depths. A suggested relationship between the wavelengths and theories is shown below in Figure 3.15.

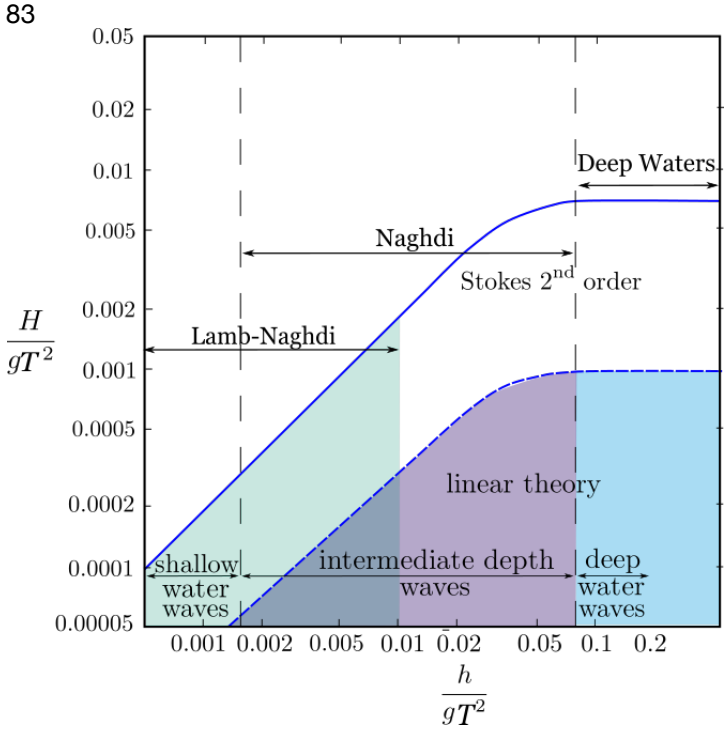

Figure 3.15: Diagram of water wave theories and proposed theories for wavelength change after wave propagation over an obstacle, based on the work of Le Méhauté.

3.4.2 Wave induced velocities

The wave velocity field will be sensitive to the amplitude change, as the wave formulation states that the amplitude will be the scaling factor of the velocity, as in equation 3.84. Here $V_{\varphi n}$ is the element n of the velocity field, namely x or y, and m is the amplitude component of the incident, reflected or transmitted wave.

$$V_{\varphi n} = A_m f(x, z, t, w, k) \tag{3.84}$$

The orbital velocities are directly proportional to the amplitude. Under normal conditions for short-wavelengths below $100m$, operational sites will be only affected by the deeper field providing the rotor is close to the central part of the canal. Waves with larger amplitudes and longer wavelengths will have a bigger effect on the field below.

Depending on the wave effect after wave trains encounter an obstacle, these might produce second-order waves after increasing amplitude, or produce transitional water waves after altering wavelength. Wave velocity, as we stated, is proportional to the amplitude and its cyclical variation is given by

the frequency of the wave. Any change to both quantities will have a direct impact on the velocity field below. As amplitude increases in some ranges of the theory, this will increase the wave velocity field proportionally to its value. Sudden rises in the seabed might produce a higher velocity flow at the upper end of the wave field. For a given situation where the frequency changes, the wave velocity fluctuation will increase or decrease its ratio of orbital acceleration. This will affect the angular frequency transmitted w_t, as seen in formulation 3.85.

$$\omega = \frac{2\pi}{T} \wedge T_i \neq T_t \therefore \Delta t\omega_i \neq \Delta t\omega_t \qquad 3.85$$

As the waves propagating over an obstacle will modify their frequency after propagation, the values after the obstacle will define the new loading cycle as this one will depend on the propagated frequency.

3.5 Ocean wave weather

To analyse the possible effects in a real open ocean site, it is necessary to acquire wave data to analyse the conditions for a sea state. As the sea is composed of a wide range of wave frequencies, it is necessary to discern between highly wind-wave dominant seas and swell-dominated seas. Wind-dominated sea states will be defined by higher orders of non-linear terms, which will result in steeper waves that can not be represented using linear theory or 2nd order. In general, steeper waves will need a higher order of Stokes and higher orders can not be modelled as a linear succession of the solutions. As being able to represent the waves in form $\varphi=\varphi_1+\varphi_2+\ldots\varphi_n$ is a necessary condition, this will break mathematical assumptions for our energy balance equation.

3.5.1 Buckley relationship for swell dominant seas

The swell height relationship offers a method by which to divide the sea into a wind dominant sea or a wind wave dominant spectrum, and

Buckley's formulation [98] can be used here. Buckley's algorithm and equation are given by empirical relationships derived from data gathered by the NOAA (National Oceanic Atmospheric Administration). These algorithms take into account the energy of the wave spectrum, the periods that compose the spectrum, and the dominant wave height. The formulation is shown in equations 3.86, 3.87, and 3.88. The significant wave height H_s in a sea state is calculated from the mean value of all wave heights for the larger 1/3 of wave amplitudes. The value f_p is the peak frequency on the spectrum and SwH is the swell height.

$$x = e^{3.3ln(f_p)} \quad 3.86$$

$$x_{val} = x/1000 \quad 3.87$$

$$H_s > x_{val} \wedge SwH \geq H_s \therefore H = SwH \quad 3.88$$

The algorithm states that, for a given sea state with a continuum spectrum, there exists a cut frequency f_c that divides swell frequencies and wind wave frequencies. The wind wave and the swell wave frequencies have separate peaks of energy, f_{pw} for wind waves and f_{ps} for swell waves. If the value given in equation 3.65 is equal to or lower than the wave height and the swell height is equal to or higher than H_s in the swell spectrum, then the spectrum of this condition will be a swell-dominated sea. The swell must necessarily be larger than wind waves and the value of WWH (wind waves height) must be lower than the values of the swell to represent a swell-dominated sea state.

3.5.2 Swell and wind wave spectrum division

The wave spectrum is made up of constituents or a broad range of wave trains with different frequencies f_m, as the spectrum is considered a continuum. The full energy of the frequencies range can be expressed as the integral from m=1 to n. As the energy spectrum is the integral of the frequencies, they can be decomposed on a discrete sum Δf as seen in

Figure 3.16. The continuous range of this discretisation of the analogue wave signal forms the spectrum function, as given by equation 3.89.

$$f = \sum_{m=1}^{n} f_m \tag{3.89}$$

The decomposition of the spectrum is given by function G, and the function takes the spectrum in the domain of the time and makes it a discrete sum. The constraints given to our swells for linearity allow us to recognise that as the function describing $\varphi(x,z,t)$ is linear, it can be decomposed in a sum of solutions using G. As a linear or weakly non-linear swell satisfies this, any train of swells can be superimposed. The function G is the Fourier transform and this decomposition of the spectrum is given as in equation 3.89. The discretisation of the wave signal allows us to obtain the different frequency components, where lower frequencies will be related to swells.

$$G[f(t)] = \Sigma f(\tau) \tag{3.90}$$

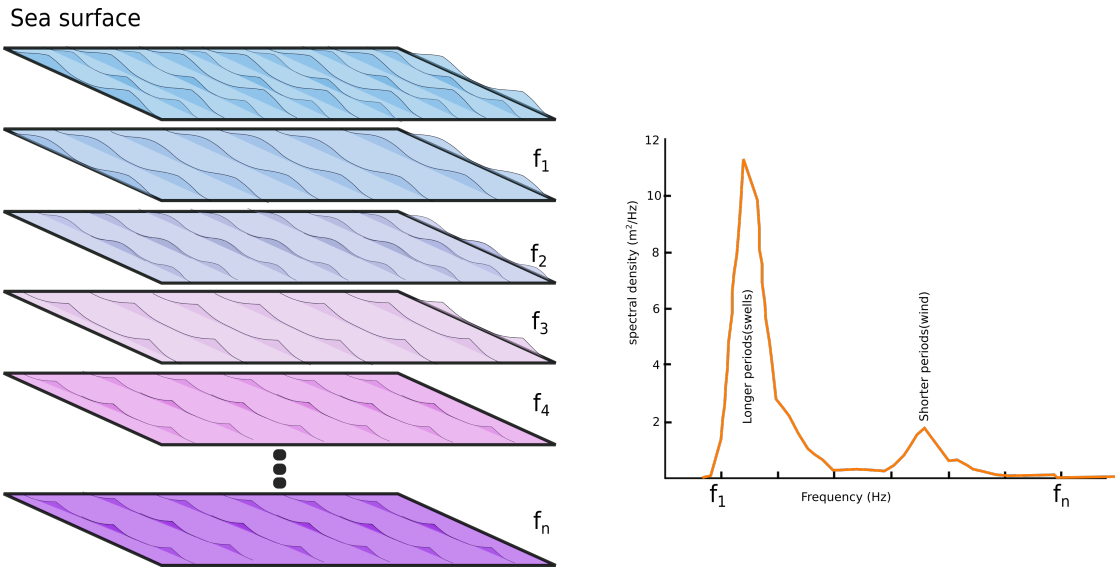

Figure 3.16: Division of the sea spectrum by its components is performed using Fourier analysis. The components for a lower frequency are the constituents of the swells propagating on the sea.

We have established that a wave spectrum is a continuum, as wave systems will cross the sea in a radial direction to a focal point as in Figure

3.16. Each section of the radial spectrum has a different peak frequency given by the wave systems that integrate that frequency, as in Figure 3.17.

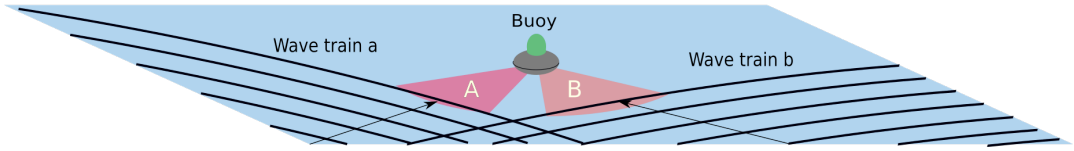

Figure 3.17: The different wave trains at different radial sections [A,B...Z]=$\Delta\theta_n$ will produce different spectrums $f=\Sigma f_n$ for each section $\Delta\theta_n$, depending on the incident direction.

To find the swell frequency for each section, as shown by equations 3.89 and 3.90 in the given sea data, a partitioning method has to be used. The method used by NOAA [99-79] and the WMO (World Meteorological Organisation) is based on the work of Gerling [100-80] and improved by Gilhousen [101-81]. This method is used to estimate the wave weather in the data used from the NDBC buoys. Wave buoys discretise the spectrum into ranges of values [f_1-f_n], and for each radial range, the spectra per square metre are calculated. To decompose the spectrum in a radial direction the given G is the directional Fourier transform over the range of $\Delta\theta$ as in equation 3.91.

$$\int_{\theta_f}^{\theta_i} \eta(t)d\theta = \int_{\theta_f}^{\theta_i} [\eta_0 + \sum_{j=1}^{n} a_j Sin(j\omega_(0)t + \varphi_j)]d\theta \qquad 3.19$$

The results for equation 3.91 will be the components of the spectrum, which will be divided into several $\Delta\theta$ angles from 0 to 360º. The transform function in equation 3.90 allows us to obtain the diverse spectrums, which will be used to calculate the energy of every $\Delta\theta$. The formulation allows us to recognise the main direction of wave incidence, and then a spectrum division is used to distinguish between swell dominant or wind-driven states. To know the state, the steepness E must be calculated, which is defined as the wave height to wavelength ratio for each frequency, as in equation 3.92.

$$E(f) = \frac{H_s(f)}{\lambda(f)} \tag{3.92}$$

The significant wave height H_s and the length λ of each wave train can be approximated as a function called momentum, as in equation 3.93.

$$E(f) = \frac{8\pi m_2(f)}{g(m_0(f))^{1/2}} \tag{3.93}$$

The ratio assumes that swells will have a lower amplitude due to decay after a wide sea propagation, and then wave swell steepness will be lower at lower frequencies (higher periods). Waves with higher periods and high amplitudes show behaviour that indicates that the weather system of origin must be close to the recording buoy. A typical wave spectrum will show two peaks as in Figure 3.17. The wave height where the separation of spectrum occurs between both peaks is calculated using a ratio of discrete integrals defined in equation 3.94.

$$m_n(f) = \int_{f_1}^{f_m} f^n s(f) df \tag{3.94}$$

The frequency separation will be calculated in equation 3.95 where C is an empirical constant and f_x is the frequency and the maximum energy at a certain steepness ratio, as defined in equations 3.92 and 3.93.

$$f_s = C f_x \tag{3.95}$$

The values of the frequency cut will depend on the steepness, as larger amplitudes will indicate an active sea, while lower indicate a swell dominant state. The result applied to the NOAA data sets divides the sea spectrum conditions that define a sea state.

3.5.3 Spectrum for a fully developed sea condition and fetch-dependent conditions

Division of the swell and wind waves at any given point in the sea is given by the use of empirical formulations. Two widely used spectrum

representations are the Pierson-Moskowitz spectrum [102-82] for a fully developed sea and the Jonswap spectrum [103-83] for wave growth over a limited fetch. Formulations can be seen in formulas 3.96 and 3.97, respectively.

$$S(f) = \frac{ag^2}{(2\pi f)^5} exp\left(-\beta \left(f_0/f\right)^4\right) \quad 3.96$$

$$S(f) = \frac{ag^2}{(2\pi f)^5} exp\left(-\beta_j \left(f_0/f\right)^4\right)\gamma^r \quad 3.97$$

Both formulations are used to create an approximate representation of the sea spectrum components as a continuous function f_n. The Pierson-Moskowitz spectrum assumes the sea has reached an equilibrium with the winds, meanwhile the Jonswapp spectrum relates the energy of the wind with the distance it blows continuously. In both sea states, β, r, γ, and β_j are empirical constants and quantities derived from the measured data. Both formulations depend on the modal frequency f_o and their equilibrium with the wind. The formulations express that for a continuous wind blowing, a maximum frequency will be developed and the modal frequency will define the spectral maximum. The use of these modal frequencies to discard possible local induced long waves is explained more broadly in Chapter 7.

3.5.4 Swell directionality detection and propagation

The direction of incidence for the wave propagation is given by the directional Fourier transform. To detect the angle of the incident swells, a method using the recorded data from buoy stations was proposed. The method uses the buoy systems in the geographical area chosen. The method will be briefly explained here and expanded in Chapter 7. The method divides the incident waves into a discrete range of degrees on each buoy, using the directional spectrum data given by the used NOAA systems. The systems calculate the wave steepness and the conditions for a swell or a wind-dominated sea. Different buoy systems are used to detect the main

angle of swell incidence and its main frequency. The frequency and wavelength are then used to calculate the propagation velocity of the swell events, and the velocity is used to calculate the time that it takes for the system to propagate between two buoy systems using equation 3.98. If conditions are met then a swell state is said to occur at the local area of propagation. We assume that the swell front developed at a distance where the arc of propagation is wide, and then the arc can be approximated as $Sin(\theta) \sim \theta$, as depicted in Figure 3.18.

$$\Delta t_{n-m} = Distance \bullet (f_n * \lambda_{f_n}) \qquad 3.98$$

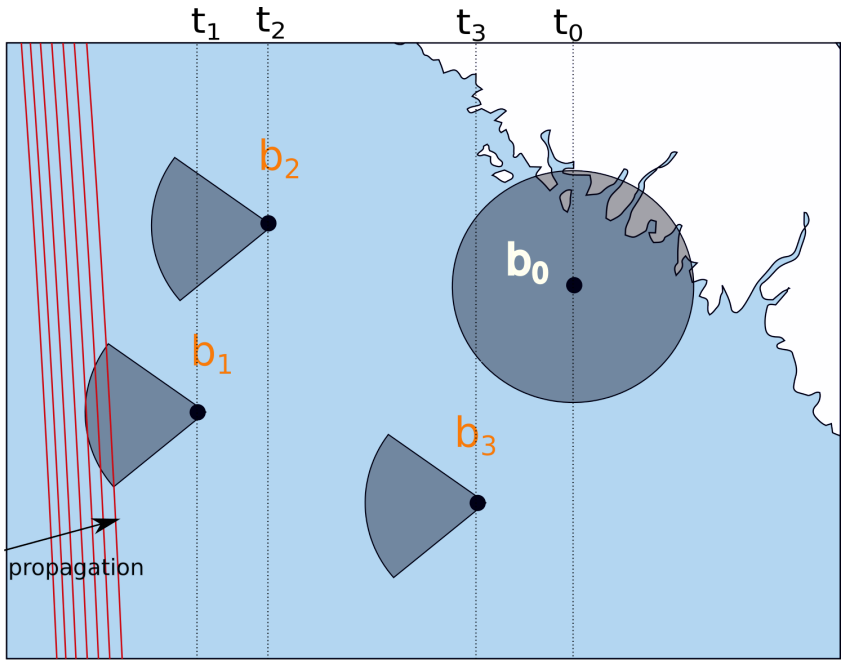

Figure 3.18: Arrival of the wave train propagating to the buoy system. The time of arrival for each one is given by equation 3.96.

To identify the swells on each buoy system, the data recorded by the systems are divided into $\Delta\theta$ pieces. The method of division for the incident swells is explained in section 3.4.2. The angle $\Delta\theta$ at which every incident wave belongs is given by the directional Fourier transform, as shown below in equation 3.97. The spectrum S here is a function of the frequencies f composing the sea state, and the angle range θ being measured.

$$S(f,\theta) = \frac{a_0}{2} + \sum_{n=1}^{2} [a_n Cos(n\theta) + b_n Sin(n\theta)] \quad 3.99$$

The coefficients a_0, a_n, and b_n are the amplitudes of our spectrum with an incidence direction θ. With this formulation we can get the direction of the energy spectrum for a given period as θ_1 and its main component θ_2. The values for both are shown in equations 3.100 and 3.101.

$$\theta_1 = Tan^{-1}(b_1/a_1) \quad 3.100$$

$$\theta_2 = \frac{1}{2} Tan^{-1}(b_2/a_2) \quad 3.101$$

To identify the wave trains that satisfy our swell conditions to be processed, the arrival time and the propagation direction of the wave systems are analysed. The process required an algorithm using the data from the buoy systems in order to relate the swells propagating between a group of two or more buoy systems. The algorithm used can be seen in Figure 3.19.

Figure 3.19: Algorithm method to search for wave swell dominant conditions in two places using directional buoys and the wave directional energy spectrum.

3.6 Seabed Bathymetry

To study swell propagation over large bathymetry changes, a description of the sea bottom topography is needed. A section of the seabed was digitised to search for large-scale changes of bathymetry in a coastal-tidal exposed area. The digitised version of the bottom surface was used to simulate a possible tidal turbine site. The turbine simulated was placed before and after the bathymetry change. The data retrieved to digitise the sea floor consisted of a set of s (x,y,z) data points defined by equation 3.102.

$$Surface = (x, y, h(x, y)) \tag{3.102}$$

The set of points represents the latitude x, longitude y in a map projection, and the elevation in the seabed h as a function of (x,y). As such elevation is an average of the real physical depth, its fidelity depends on the bathymetric type of survey, so an area with high resolution data was chosen. The processed data retained the general main characteristics of the area. The sea elevation was averaged from the points of acquisition using a polynomial fitting technique on QGIS™. The points representing coordinates on a form $P(x,y,z)$ allowed us to obtain a fitted function f for the points (x,y,z) on each point P_n of a mapped surface A. The function used is a simple linear approximation between a P_n to P_{n+1}. The representation of the process to convert the points to a surface is shown below in Figure 3.20.

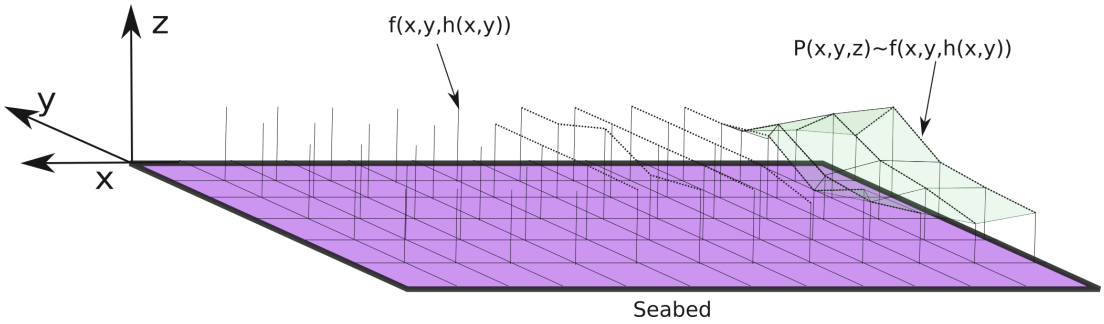

Figure 3.20: Technique to fit polynomial functions to reconstruct the seabed level.

The data files were processed to obtain a 2D elevation profile of the seabed, obtained using a bathymetry cut of the area in the main direction of swell incidence. The swell incidence was detected using the method described in section 3.4.4.

3.7 Sensitivity analysis

The study of the turbine includes a sensitivity analysis case. The study analysed how the different parameters that intervene in the turbine model can facet the mechanical performance, in this case, the torque a thrust of the machine. The study follows the procedure given by Nevalainen [36].

The sensitivity analysis is a method used to detect how the input variables of a model can affect their output and how the changes in the variables affect the changes in the output. The analysis is similar to the concept of the rate of change for multivariable derivates. In this case, the results of the changes in the derivates are used to calculate the importance of the changes of each variable $X=\{x_1,x_2,x_3...x_n\}$ in the main function F when the output value Y changes.

The Morrison method of sensitivity analysis is a one step at a time method, where each variable from the vector X is increased or decreased by a fixed amount to detect the changes in the vector Y, as shown in 3.103.

$$F(x_1, x_2, \delta x_3 \dots x_n) = \delta Y \tag{3.103}$$

In our case, the vector X that contains the variables x_1 to x_n is composed of parameters that define a sea state. The parameters for a sea state in this work are the wave period, the wave height, the current, and the depth, as shown in 3.104.

$$x_1 = T, x_2 = H, x_3 = v_c, x_4 = h_d \tag{3.104}$$

The output Y is then composed of the torque and thrust of the machine which is affected by these changes in the input parameters, as shown in 3.105.

$$F(T, H, (\delta v_c + v_c), h_d) = Y; Y = y_1, y_2 \quad 3.105$$

Here y_1 and y_2 are different from the base case where the value of Y is Y_o and the values for all variables in X do not have any variation from a predefined starting value.

As all changes in the variables will produce different outputs in Y, a significantly large enough set of outputs Y_n can produce a statistically significant data set to analyse how the change in X affects the change of Y. The method established by M. D. Morris [104] uses randomisation of the space in n dimensions that are defined by the input variables. The input variables are then increased one by one.

The elemental change is calculated as the difference after and before the change, divided by the change in the variable, as shown in 3.106.

$$EE = \frac{F(T, H, (\delta v_c + v_c), h_d) - F(T, H, v_c, h_d)}{\delta v_c} \quad 3.105$$

For each trajectory, R_i is composed of individual changes of the initial variables in the array X, one change at a time, as shown in Figure 3.21. Values in equations 3.106 to 3.108 are calculated, where R is the number of trajectories in the nth dimensional space defined by the set of variables that define the changes of Y in the model, with i as the trajectory number.

$$\mu_i = \sum_{r=1}^{R} \frac{EE_i(X)}{R} \quad 3.106$$

$$\mu_i{}^* = \sum_{r=1}^{R} \left| \frac{EE_i(X)}{R} \right| \quad 3.107$$

$$\sigma_i = \sqrt{\sum_{r=1}^{R} \frac{(EE_i(X) - \mu_i)^2}{R}} \quad 3.108$$

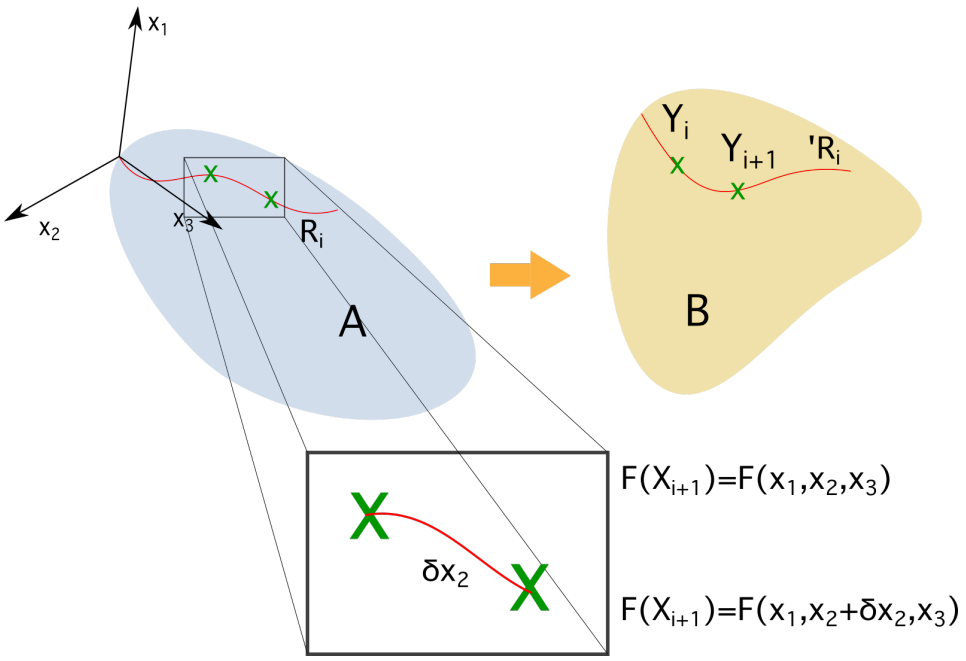

Figure 3.21: Trajectory Ri defined in space A and composed by variables x_1, x_2 and x_3. The evaluation of F on each point of A, following the trajectory along individual changes or δ of each x_n, producing a response of the model in B, following another trajectory 'Ri. The values in B are the results of F that correspond to the vector with values Y.

The results of this analysis are compared with Nevalainen where wave components are steeper and no wave propagating over an obstacle exists. This is explained in greater detail in Chapter 6.

3.8 Conclusions

Mathematically speaking, wave solutions have been solved for long linear waves of arbitrary amplitude since the 19th century and the work of Airy. However, the Airy model covers only waves of small amplitude $\lambda >> a$ in arbitrary depths h_d. Airy's model depends on the depth of propagation and wavelength. Steeper swell systems will require a different approach as the model breaks when the wave steepness grows. Stokes waves of higher order can model shorter and steeper swell systems. If we wish to model wave propagation over obstacles using larger depths, the solutions need to be able to satisfy the next points:

- Finite depth propagation where the wavelength λ is not excessively larger than the sea depth h_d.
- Shape independence, to model steeper swell systems, including second-order waves.
- Frequency variant, where the possible shape of the wave after propagation is also a function of the frequency variation after it propagates.

The non-variant frequency problem has been solved for shallow waters by Lamb [68] and, more importantly, some frequency variant solutions have been derived for arbitrary and finite depths by Marshall and Naghdi [88]. Other authors have solved the problem using complex solutions involving matrix solutions and Bessel series, like Cho and Jung [83], Xie et al. [84], and Belibassakis-Athanassoulis [85]. Despite many actual wave models predicting the wave shape, velocities, and propagation, the problem of wave propagation after an obstacle has been addressed in very complex solutions that might incur a large computational time, except for the solutions found by Naghdi and Marshall.

The frequency variant case is important for finite depth where Lamb's linear theory applies partially. Experiments carried out by several authors show how even in the case of linear propagation conditions like the ones stated by Lamb, frequency it is an important variable. Insightful observations on the wave propagation and changes in its properties come from detailed experimental works carried out by Goring [68] and Newman [55] which show clear frequency effects. As theories explore complex solutions or very simple linear cases, a simple approximation of an analytical and close solution is reworked here. The formulation uses the same physical arguments made by Lamb and Naghdi-Marshall, and the work proposes a function defining change in the wave properties after propagating abruptly over an obstacle.

The followed hypothesis is that the energy of the incident wave, the transmitted wave, and the reflected wave are almost linear and the energy dissipation is almost non-existent. Keeping this in mind, the changes in the

wave properties such as the amplitude and the depth of propagation should approximate the changes in the wave period and velocity change. The formulation does not take into account the wave shape, so any wave profile whose steepness is moderate could suffice for this approximation. This solution is later explored, along with Naghdi and Marshall, using an experimental facility in Chapter 5. These will be used to model a case where a tidal turbine sits after a regular bathymetry obstacle which modifies the parameters of the incident wave.

The simulation includes these formulations, including a sensitivity analysis case and a wave weather analysis of a section in the Pacific to simulate a tidal turbine deployment, discussed in Chapters 6 and 7.

4 Experimental methods and measurements

The models addressed by previous authors mentioned in Chapters 2 and 3 have been validated through experimental testing by those mentioned in sections 2.5.2 to 2.5.5. However, the experiments cover propagation depths which are outside the scope of this thesis. The results of the aforementioned tests have been published and effects related to the wave of propagation over other parameters, rather than the amplitude, have also been explored by Goring. The results are limited to the frequency behaviour and the possible relationship this has with the obstacle depth and the incident wave height. The next pages examine the possibility of measuring the length of a wave trough to trough and the velocity of the peak by searching for anomalies that link changes in the wave frequency to the depth ratio, as described by Goring.

The experimentation proposed here is used to model typical long waves with low amplitudes, arriving on the coast from deep waters. These wave systems will enter the continental shelf from deep waters and will move eventually to transitional depths, propagating over obstacles and changing the hydrodynamic conditions underwater as the wave parameters change over and after the obstacle. The modelled wave systems are chosen to resemble swells, which are wave trains that can be expressed as linear wave systems, according to the propositions found in Chapter 3. The waves also had to comply with the conditions such as wavelengths λ large enough compared to their amplitude a.

4.1 Introduction

The validation of a model requires experimentation and simulation. This is one of the most important steps in validating how well designed a model is and ascertaining whether it is able to retain the main behaviours that arise from it and predict our system properties.

An important part of this thesis was devoted to describing how long waves with low amplitude resembling swells behave on their approach to the coast after propagating over an obstacle. Works analysed here and previously published on long wave propagation to the coast show consistent results, but also a gap in the knowledge for deeper water regimes and other possible changes that can arise in the propagated wave, which are not related to their amplitude alone. To analyse this gap, an experiment was designed to test the theoretical assumptions made in Chapter 3, in the conditions which have not been covered by past experiments, and also validate previous analytical models explored by other authors and our own predictions.

This section is divided into the experimentation background, the methods and tools used in the experiment, and the procedure used to analyse the data. It is worth noting that special interest was given to other measurements apart from the wave amplitude, including possible anomalies in the wave as it propagates over the obstacle that could be observed in changes related to its shape (trough to trough) or speed decrease related to the propagation in shallow waters. The methods explained here were used to take measurements and to compare the Lamb and Naghdi-Marshall theories of wave propagation. These theories also included the formulation proposed here.

4.1.1 Experimental background

The particular experimental approach taken in this work was chosen to fill the gap in past experimentation procedures on wave propagation at larger depths. Studies reviewed include the works of Goring [87], Bendykowska [105], Newmann [70], Santos et al. [60], Ting et al. [79], Massel [76], K. Szmidt [78], and Charland [106]. Most of these works are focused on two main points: the long wave propagation case as $\lambda >> h_t$ or cases where $h_t/\lambda < 1/8$, and amplitude measurement. However, these experiments are more suited to describing extremely large waves or extremely shallow water cases. However, as Naghdi-Marshall [69] pointed

out, some of the models can describe fairly well a swell system on transitional waters under finite depths $k(depth)<\lambda$. A table with a brief description of the experimental conditions used by these authors is shown in Table 4.1. In this table, the next variables are shown:

1) Maximum and minimum wavelength tested λ,.
2) The minimum and maximum wave height H.
3) The minimum and maximum obstacle depth.
4) The minimum and maximum submergence ratio h_t/h_d.
5) The maximum and minimum Ursell number as defined by Ting et al., defines the possibility of energy being transmitted to higher harmonics.

The first variable helps to visualise the depth regime of each experiment by comparing it to the 4th column. The second one is the maximum and minimum wave height, which can tell us the wave steepness. The third and last row are related to studies by Ting et al. and indicate the possibility of a strong energy transfer to higher harmonics.

The authors include, in some cases, finite and infinite steps. Authors with a * indicate experiments where the data comes from a finite step obstacle. Experiments without a * only use an infinite shelf.

	$\lambda(m)$	$H\,(cm)$	$h_t\,(cm)$	h_t/h_d	a=0.022Ur
Newman	0.5-10	N/A	3.8-15.2	0.063-0.25	N/A
Szmidt*	4.8-6	4-10	24	0.4	a<0.0005
Massel*	1-1.57	0.5	14.1-26	0.47-0.86	a<0.0005
Ting et. al *	1.81-1.34	0.42-3.78	21-12.4	0.45-0.76	0.039-0.095
Goring	6.26	0.8-1.9	9.46-19.32	0.37-0.73	a<0.008
Charland*	2.62	10-20	150	0.5	a<0.0005

Table 4.1: Experiments on wave propagation over an obstacle. If variables present an NA it means the variable was not reported.

Most of the aforementioned studies are focused on the predictability of the reflected and transmitted wave coefficients, as defined by Lamb,

which also occur in regimes of shallow waters, or transitional waters but under very shallow depths, as mentioned in Chapter 3. It is also noticeable how only Ting et al. and Goring have larger values of a which defines a large transmission of energy to higher harmonics, despite Goring's experiments being conducted on a solitary wave. A very low number is observed also in the experiments of Szmidt, which observe the creation of small waves with very low amplitudes compared to the original wave train.

If we look at the importance of wave amplitude prediction, this can help to predict wave breaking and a wave height increase. The wave height will also help to calculate the pressure field below the water system and its increase will produce severe sea weather for any device installed near the sea surface. The amplitude increase also introduces severe vertical acceleration and velocity components which are proportional to the wave height, as expressed in Chapter 3. An aspect to take into account which was not considered here is the possibility of non-linear interactions such as vortices and turbulence over the obstacle. However, past experiments show good relationships between the experiments and the models, despite these non-linear interactions.

To measure the changes induced on a wave by obstacles (as it propagates over them), sensors are placed into the tank to measure the change in the elevation of the tank surface. Measurements are made without obstacles to characterise the wave propagation in the tank, and later obstacles are introduced to measure the changes produced by the underwater obstruction. Wave probes are installed, semi-submerged along the main length of the tank, parallel to the wave propagating, to measure the change in the water surface. The main length refers to the length defined as that covering the distance from the wave maker to the beach.

Measurements for these experiments are done in three locations:

1) Before the obstruction or obstacle, measuring the incident wave height.
2) Over the obstacle, measuring the obstacle wave interaction.
3) After the obstacle, measuring the waves after the obstacle.

The typical array for these experiments is shown in Figure 4.1.

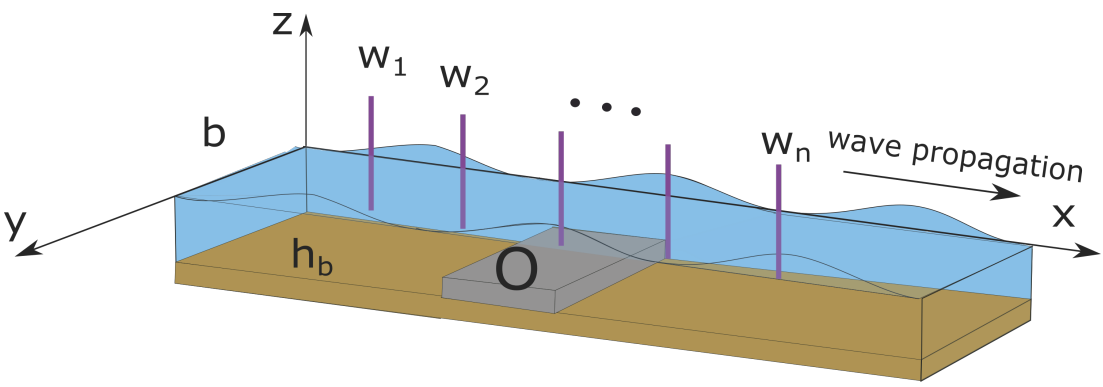

Figure 4.1: Figure showing the typical physical arrangement for wave propagation over an obstacle. The obstacle O can be finite or infinite as its length extends to the end of the wave flume. Sets of n wave probes w_1 to w_n are placed to measure the wave propagation inside.

A set of typical challenges encountered in the process of experimentation is the creation of small harmonics after the obstacle. As pointed out by Takano [72], these harmonics are normally observed in coastal conditions after swells arriving from the open sea propagate over sandbanks. As these harmonics have shorter periods and low amplitudes they have little impact on the wave transmitted after the obstacle. The harmonics measurement requires enough length for them to spread due to the wave dispersion process. Other processes include the creation of eddies at the corners of the obstacle. Due to the flow that attaches to the obstacle, the eddies and turbulence produced are then propagated after the wave passes the underwater obstacle and they are a source of energy loss that is usually not accounted for in theories due to the complex modelling they demand.

All analysed experiments have used relatively shallow waters and very long waves on conditions $h_d(depth) << \lambda$. Experiments also are limited to measuring the wave amplitudes as these are the characteristics which can be more easily extracted from the recorded data. However, it is possible that other changes or anomalies could be detected in the waves by measuring their velocity or wavelength as they propagate over and after the obstacle.

These anomalies could be related to conditions such as the obstacle length or depth, but more exploration is needed. Part of these explorations seek to follow the model addressed by Naghdi and Marshall where the wave number of the transmitted wave or k_2 depends on the incident wave number k_1, the incident depth h_d, and the upstream depth h_t. Some of these anomalies are reported in shallow water propagation by Newmann and Goring for fairly long waves $h_d<<\lambda$. The anomalies observed by Goring which are not conclusive appear to show a relationship between the wave amplitude, the obstacle depth, and the angular frequency of the transmitted wave.

An important common characteristic of past studies is that propagation conditions for these long waves emerge from regimes where the depth is closer to shallow waters and extreme cases of depth where the water waves will more closely resemble a tsunami.

4.1.2 Proposed experimental characteristics

Experiments on wave propagation are focused on methods for shallow waters. These methods are more suited to tidal waves and wave breakers and the two more important variables that constrain these methods are the depth to wavelength ratio and the wave amplitude to wavelength ratio, as well as the Froude and Reynolds numbers.

Froude and Reynolds scaling

Two important factors to take into account to scale our experiment are the Reynolds number and the Froude number. However, due to practical considerations, it is impossible to keep the Reynolds number similarity. The Reynolds number is defined in equation 4.1.

$$Re = \frac{uL}{\nu} \tag{4.1}$$

As ν, which is the nematic viscosity, is the ratio of the density per the dynamic viscosity, it is the same for both. The similarity between the real phenomenon (Re_r) and Re of the scaled model (Re_m) must be the same

Re_r=Re_m and it is reduced to u_rL_r=u_mL_m. As our characteristic length in an open flow channel is defined by the area of the channel divided by the wetted surface, in our tank this is reduced to equation 4.2 below:

$$L_m = \frac{(depth_{tank})(width_{tank})}{2(depth_{tank}) + width_{tank}} \tag{4.2}$$

This gives us a value of approximately 0.34. If we decide to scale our depth to 40m depth, we obtain a value of L_r~66.06L_m. In this case, the velocity of the waves in the scaled depth of 40m depth must be u_r~0.01513u_m, which is not feasible. In this case, we must assume the Reynolds similarity cannot be obtained and then possible effects related to turbulence would not be the same, reducing the accuracy of the simple formulation obtained to relate the wavelength and amplitude propagation in section 3. However, these differences are not accounted for in this work. The Froude number is defined in equation 4.3.

$$Fr = \frac{u}{\sqrt{gL}} \tag{4.3}$$

The Froude number represents the ratio of the inertia forces to the gravity forces on the wave. Again in this case, the length L represents the characteristic length and this is the hydraulic ratio which was defined in equation 4.2. As gravity is the same in both the real-world model and the scaled-down version, then the relationship between both Froude numbers, F_r and F_m, is reduced in equation 4.4.

$$\frac{u_r}{\sqrt{L_r}} = \frac{u_m}{\sqrt{L_m}} \tag{4.4}$$

In this case, again we can simply solve for the velocity of the waves moving in the real-world model, as in equation 4.5.

$$u_r = u_m\sqrt{\frac{L_r}{L_m}} \tag{4.5}$$

As we know L_r=66.06L_m, we can approximate the quantity as 0.123. This allows us to have a parameter to compare the wave trains used in the wave tank with the simulations that are presented in later chapters.

Water depth and wavelength conditions

Methods for shallow water conditions are suited to the Lamb theory where transmitted waves have no frequency change and where the vertical velocity and acceleration can be disregarded. In these conditions, variables like the wavelength-depth ratio can be defined as $\lambda >> h_d$. Meanwhile, the velocity components obey the relationship $V_{\varphi x} >> V_{\varphi y}$. These conditions are however far from applicable to our experiments, as we mentioned before. Wave amplitudes should suffice $a << \lambda$ for these shallow-water cases.

Regarding our depths, these differ from the methods used by other authors. Useful depths for tidal and wave energy engineering focus on accessible areas in the continental shelf at depths ranging from $40m\ to$ $100m$. Under these depths, formulations like the one proposed and Naghdi-Marshall could have better results. These two analytic models are compared in the next chapters. Under the depth conditions mentioned before, $40m < h_d < 100m$ wave periods in the range of $22s > T > 7s$ can approximately satisfy the finite water depth and infinite water depth conditions for both models.

If our tank depth can be defined as h_d, then our wavelengths during the experiments must be kept in the range of $2h_d > \lambda > 20h_d$. The periods were set accordingly to satisfy the wavelength conditions, depending on the wave period used in the wave tank.

As other authors have worked with experiments in transitional waters, where the wavelength to depth ratio is closer to shallow water (which can be defined simply as $\lambda \rightarrow 20h_d$), our experiments work in the range $2h_d > \lambda > 10h_d$. As the wavelength, in this case, depends on the period or $\lambda = f(T)$, there is only one value of T to produce every λ in the desired range. The dispersion relationship for both second-order water depths and the first-order is defined by equations 4.1 and 4.2.

$$\omega^2 = gk \tag{4.6}$$

$$\omega^2 = gk + \sum_{n=2}^{m} O_n (ka)^2 \tag{4.7}$$

The dispersion relationship remains the same as we reduce the term that follows the higher orders in equation 4.7 to 0, and then the formulation becomes the typical dispersion relationship for linear waves. The dispersion relationship relates the wave period to its respective wavelength, and this formulation has two expressions in our experimental range. The dispersion expression will apply for deep waters and the larger depths of transitional waters. Then, theoretically, we can find the wavelengths using linear theory given by equations 4.8 and 4.9, for deep waters and transitional waters respectively.

$$\lambda = \frac{g}{2\pi}T^2 \tag{4.8}$$

$$\lambda = \frac{g}{2\pi}T^2 Tanh\left[\frac{2\pi h_d}{\lambda}\right] \tag{4.9}$$

The wavelength size in transitional waters will be defined by the term $Tanh[\theta]$ where θ is not an angle but the value of $2\pi h_d/\lambda$. If this value is close to $\theta \sim \pi/2$, the wavelength will be similar in size to the deep water scenario, with a deviation of less than 10% of its real value, as $Tanh[\theta] \sim 0.91$. We can, with this result, theoretically assume the wavelengths will have a value closer to wave propagation in deep waters, even for some of our transitional water cases. However, the scaling of the water depth is still an important issue as shown by Noble et al. [107]. An incorrect scaling of the depth, if the depth is taken as infinite, can lead to errors in the range of ±30% in wave parameters such as the wavelength/celerity and steepness. Because of this, to calculate the wavelengths to depth ratio both equations 4.8 and 4.9 are used.

The wave amplitudes in our case must be bounded by the relationships $H\lambda^2/h^3 = 26$ and $H = H_B/4$, from Figure 3.3 of Chapter 3, where H_B is the wave breaking limit. To maintain the waves below these values the total wave height, which is two times the amplitude, was kept below $2cm$. The amplitudes in this case also satisfy the condition for which $a << \lambda$.

Under these defined ranges it is possible to examine the amplitude evolution for linear and second-order Stokes waves of certain amplitude a,

propagating over an obstacle, and to measure possible anomalies in their wavelength and velocity.

The conditions for this experiment were chosen to not only maintain the theoretically established constraints for wave propagation but also to depict real swell conditions in the open sea at suitable depths of study for possible engineering purposes. The differences in the approach we took for this experiment are that obstacles will vary not only in their depth but also in their length, as wave trains will encounter not only jumps in the seabed but sudden obstacles like sandbanks or local geographical rises.

The last observation is important as waves were not only measured at the locality after the jump but also after they propagated over it. The changes associated with propagation again into deeper waters were also observed in this work, but not modelled as the approach will require a longer process of study and modelling. The approach to the waves produced also differs from most experiments, as past studies covered solitary waves that can be modelled with different types of theory depending on their shape. The solitary wave modelling could hide certain possible effects due to the wave trough.

Experimentation also differed as it was carried out using a set of wave trains, whereas in real sea conditions wave trains are continuous and will occur continuously. Wave trains produced were long enough to have at least three complete waves and carefully chosen to not be affected by reflections from the wave tank beach.

4.2 Methods and Materials

This project was assisted by the Department of Naval Architecture and Ocean Marine Engineering (NAOME) and the fabrication of the obstacle by the workshop technicians in the laboratories of the Department of Mechanical and Aerospace Engineering (MAE). The experiments were carried out in a wave flume tank, for which instrumentation was provided by NAOME. Tests were set to analyse and characterise possible tank effects that could alter our measurements, such as reflections, noise of natural

vibrations, the best wave probe placement, and correct wave dimensions. This was to characterise the available and proposed models and also the simulated long wave sea characteristics. These methods and materials are shown in the next pages.

4.2.1 Materials

The installations used for the experimentations consisted of a wave tank with a longitude of 21.6m and a width of 1.6m. A set of four-wave probes were used to track the waves. The wave probe number was limited by the number of ports that could be used at the provided amplifier.

Wave probes and wave tank

The wave probes were connected using jacketed cables carrying the analogue signal to our wave amplifier. The amplifier converted our low power signal into a higher value.

The system is also protected against external noise due to the cable's construction. The amplifier was then connected to a Data Acquisition System (DAQ) system. The data gathered by the system was fed into a PC and software processing tools to be recorded.

The wave tank characteristics respective to the wave generation type, measures, and capability are shown in Table 4.2. Meanwhile, a drawing of the side view, front view, and upper view of the tank can be seen in Figure 4.3.

Wave tank type	Depth h_d	Width	Length	Wavemaker type	Wave type capability
Wave flume.	Variable from 0.3m to 0.65m.	1.6m	21.6m, 0.6 m beach length.	Flap type, driven by belt, and motor.	Regular and Irregular wave trains

Table 4.2: The Henry Dyer wave flume tank main characteristics, part of NAOME.

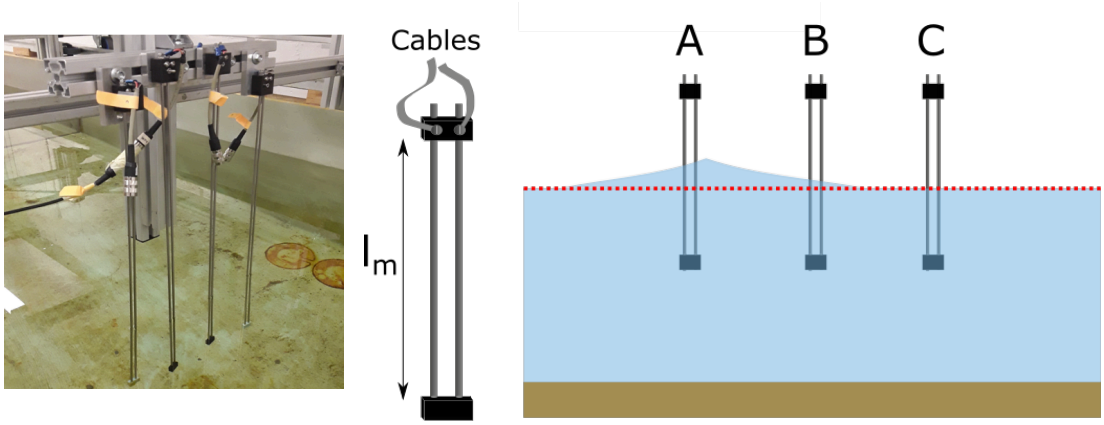

Figure 4.2: Wave probes used in the tank, left, and wave probe placement, right. The wave probes have an effective length of l_m. Wave probes used had a major sensitivity at $l_m/2$, so they were half submerged in the tank. The picture shows the initial tests for calibration of the wave probes by measuring the voltage signal vs the four probes' immersion depth.

The wave probes used were a resistive type, made of twin wires of the same length. The working mechanism that allows the wave probes to measure the surface change is the change in conductivity between both wires. As the value of the conductivity is affected by the water level, any variation in time will be recorded as $y=G(t)$, as shown by equation 4.10.

$$Voltage \propto a h_{water} \tag{4.10}$$

Wave probes were placed inside using the tank structure, as seen in Figure 4.2. The wave probe's main characteristics can be found in Table 4.3.

Wave probe type	length l_m.	Voltage output	Effective length of measurement	Connetor type/Cable type
Resistive twin wire.	$100cm$.	0-$5V$	$200mm$	BNC/Jacketed

Table 4.3: Table with values of the wave probes' main characteristics.

In equation 4.4 the value a is a constant to be determined by calibration, meanwhile h_{water} is the water level covering our wave probe. The wave probes were known to be sensitive to temperature, as the laboratory installation lacked any temperature control. Re-calibration had to be done

every time the wave tank temperature changed drastically. Methods used for probe calibration are explained in the next paragraphs.

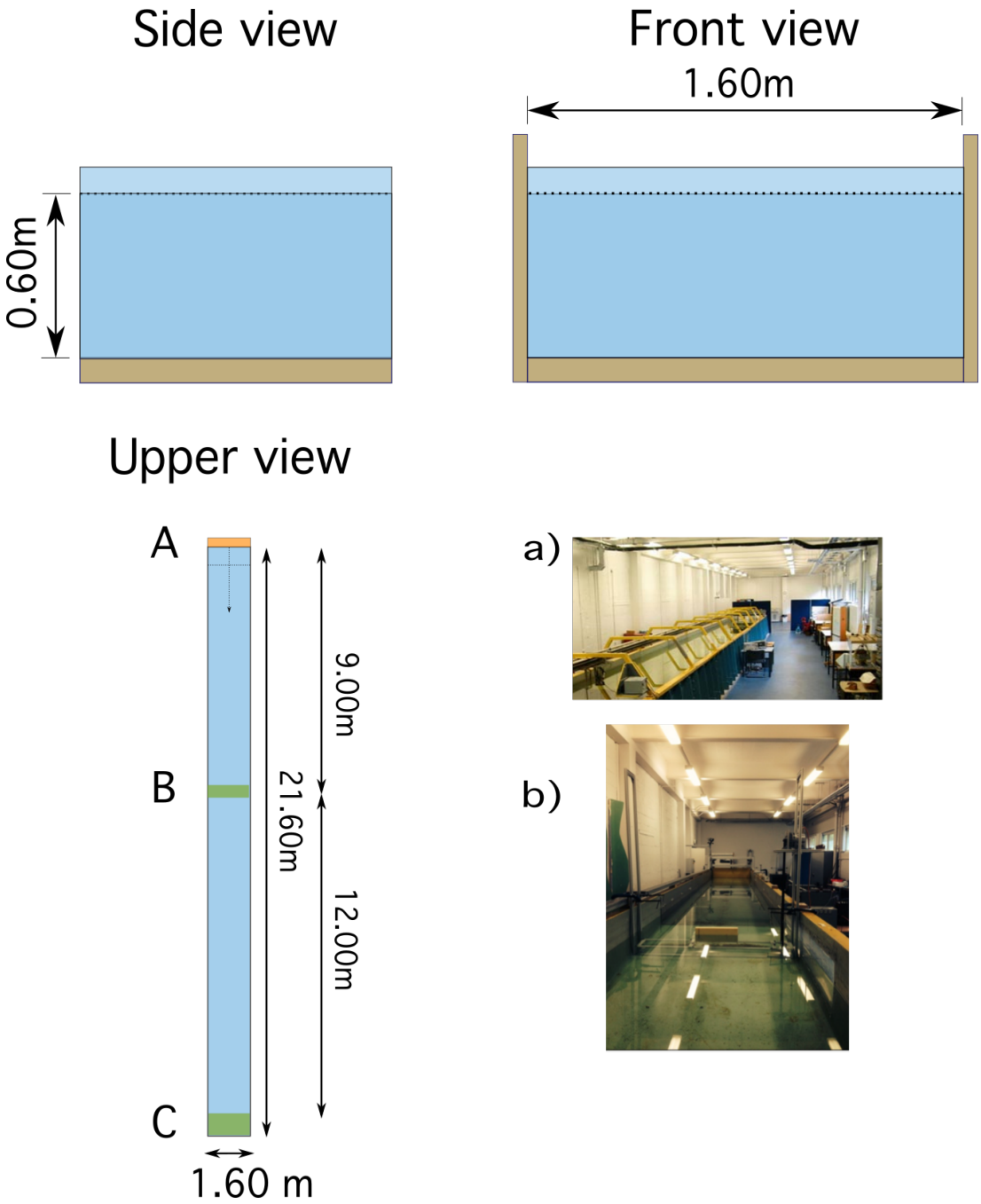

Figure 4.3: Experimental tank views with its main dimensions: a) shows the main length of the tank [108] and b) a view along the main length inside the tank [109]. The green area in the middle is the zone where the obstacle is placed, the orange area is the position of the wave maker, and the lower green area is the position of the beach.

The wave tank itself is now decommissioned and was designed by NAOME. The tank can vary in depth from 0.6m to 0.3m. The wave paddle

has a maximum aperture of 40º and a hinge depth of 0.6m. With this data, a plot of the maximum wave height in the period range [0.1s-5s] at a maximum aperture is produced for depths [0.03m, 0.06m]. The plot limited by a tank height of 0.65m is below. The tank's high frequency limit is 0.2hz.

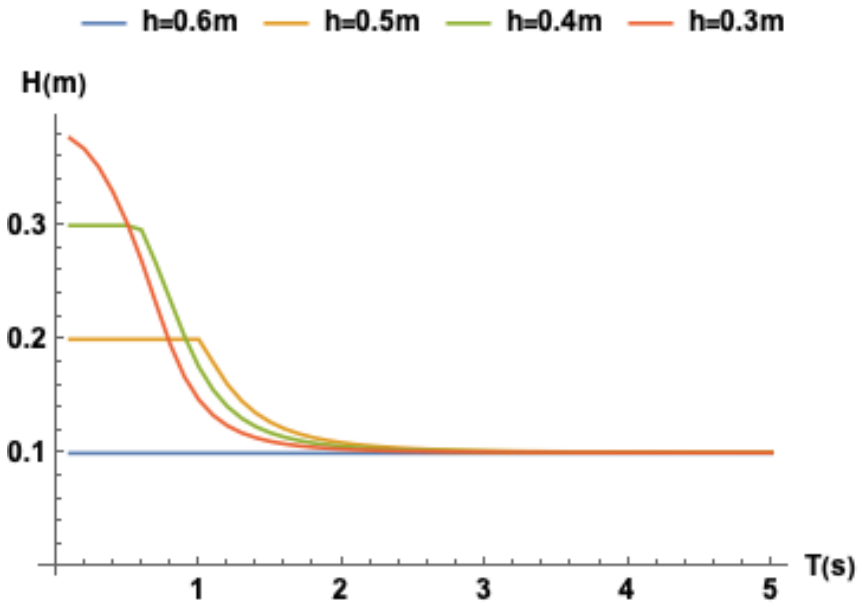

Figure 4.4: Plot showing the maximum wave height that can be achieved at different depths in the Wavemaker, following the procedure given by C. J Galvin [110].

Wave probe calibration

The wave probes were calibrated using a pre-marked rod of 1m in length, with incisions every 2.5cm. The tank had a metal bar with a rail mechanism, allowing the wave probe to move in a vertical motion on the water surface. The movement allowed us to change the immersion, as shown in Figure 4.5.

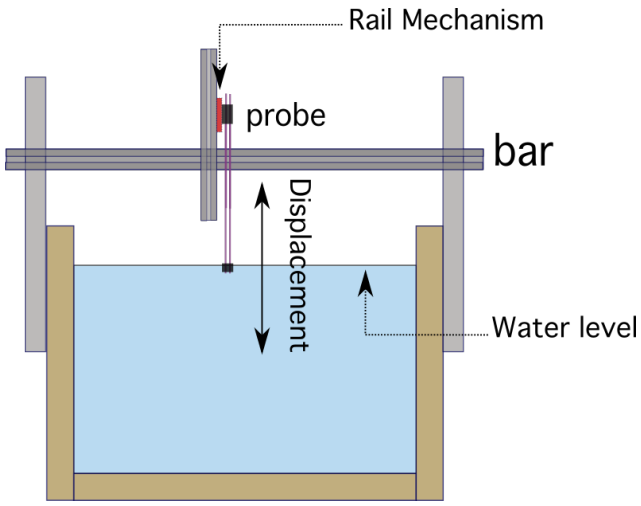

Figure 4.5: Figure showing the configuration to calibrate our wave probes. The rail mechanism in the vertical bar (red rectangle) allows the probe to move up and down fixed lengths. The movement was used to calibrate our wave probe, measuring the depth of immersion vs the voltage.

The probes were moved up and down and the voltage was measured to obtain a transfer function, as suggested by MARINET [111].

As the wave probe voltage varies depending on the immersion level of the probe, the immersion was changed to produce several readings of voltage and create a voltage vs depth function which was later transferred to the wave recording software. The steps for this are below:

1. The wave probe was attached to the rail mechanism and the wave recording software was turned on.
2. After verifying that any possible disturbance produced by placing the wave probe had disappeared, the wave probe's first recording was taken as level 0.
3. The wave probe was moved down 5cm following the incisions made in the rail. After disturbances generated by moving the wave probe disappeared, a second recording was taken, now by moving the wave probe another 5cm down (10cm in total).
4. The procedure was repeated until the wave probe moved 50cm or 11 measurements.
5. Measurements were repeated in the opposite direction by moving them up 50cm by 5cm at a time. This was to check for possible hysteresis.
6. The values of immersion were plotted against the voltage recordings (voltage vs immersion).
7. A transfer function defining the immersion vs voltage was then created.
8. Measurements to check the calibration of the four wave probes were taken. These measurements consisted of mounting the four-wave probes in the metal bar. The probes were moved up and down the water surface and the displacement recorded was measured against the displacement marked in the rail.

9. If measurements of the 4 wave probes were consistent and the deviation was small, they were mounted along the main length of the tank to start the measurement procedure.

A plot of one of the transfer functions produced by the calibration and its fitted function can be seen in Figure 4.6. In general, the wave probes provide a very good way to measure the water elevation produced by the wave maker and have a resolution of $\pm 0.1mm$. Data was very linear and almost no hysteresis was detected.

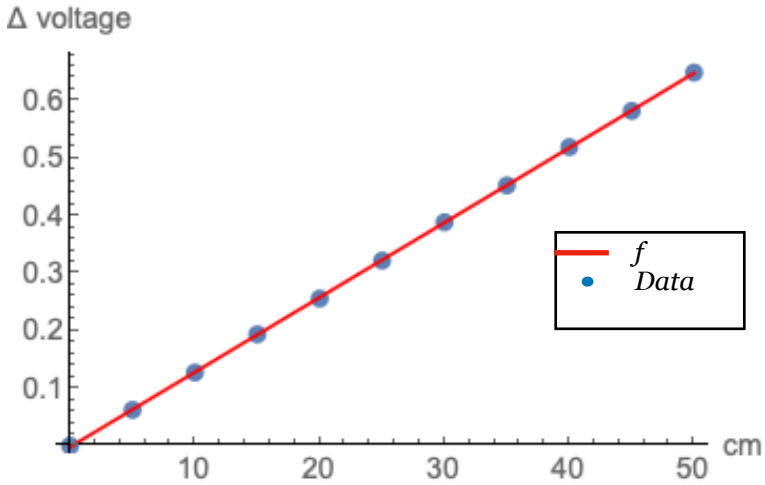

Figure 4.6: Plot of calibration process in blue dots and fitted function f in red.

Data acquisition system and sampling software

A data acquisition (DAQ) system was used to relay the data from wave probes to the computer system. The system is a CED 1401 A2D converter with 16 analogue input channels and a $12bit$ resolution. The DAQ system was connected along a system amplifier to compensate for the low voltage variation produced by the analogue wave probe signal. The system had 4 ports used for analogue entries and it was able to sample at a $100Hz$ rate. The software used to relay data after amplification and acquisition was CED Spike2, which allows multiple input channels to be acquired in real-time from our DAQ-amplifier system and also allows us to control the rate of sampling. The set of tools used for capturing the data and preprocessing consisted of Spike2 and scripts are written for Wolfram Language™ and can be exported easily into Python. Spike2 allowed us to import raw data from

the ports and then convert them into arrays of $.txt$ files, the files were later analysed using Wolfram Language. Laboratory control software made by NAOME was used to control and set up the wave maker characteristics at the desired period and wave height.

Obstacles

To characterise a bathymetry rise on the seabed in the given depths of the wave tank, a set of obstacles was fabricated. These obstacles were geometrically regular in nature and designed to resemble a sudden blockage in the wave train path. The range for the wave blockage r=h_d/o_h where o_h is the obstacle height was chosen as r=[1/6, 2/6, 1/2] depth. To ensure that obstacles remained at the bottom, aluminium was used to build the surface due to its higher density and its easy machining properties. Obstacles were made hollow to allow water to fill them and nullify any buoyancy that could lead them to rise over the bottom of the tank. As the tank depth could be modified from 0.65m to 0.3m a fixed depth of 0.6m was chosen, which allowed us to have 5cm free for wave amplitudes and 5cm extra for the tank's upper border. The operational depth of 0.6m meant we designed the obstacles as blocks of 0.1m height, then the obstacles could be stacked over one another to obtain the desired blockage ratio. Figure 4.7 depicts individual obstacle dimensions.

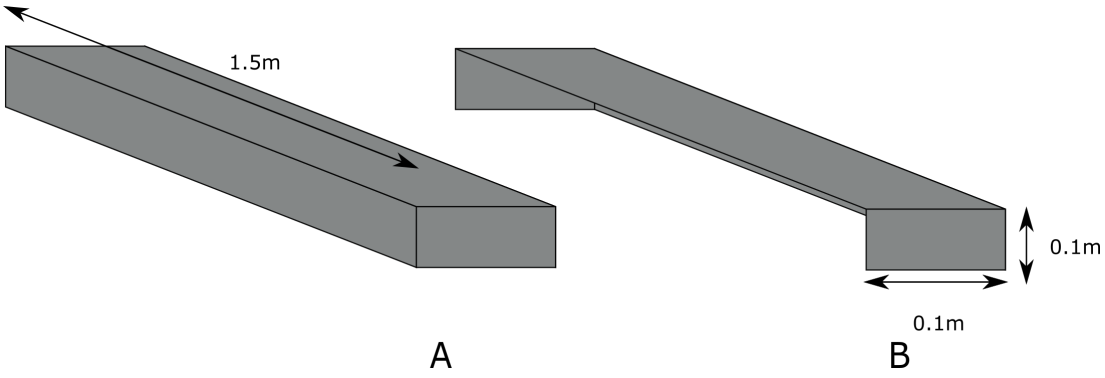

Figure 4.7: The obstacles with main dimensions: 1.5m width, 0.1m length, and 0.1 m height. Obstacles were 10cm smaller than the tank main width to allow correct placement.

4.2.2 Methods

Wave shape and properties can be described using theories that range from Airy theory to Cnoidal theory, Boussinesq equations, or the Stokes expansion method. All wave theories available are approximated solutions for the wave equation given a different set of scales for the wave parameters such as amplitude and wavelength, or physical properties like field velocities or shape. Waves modelled here used the first-order and second-order Stokes, which will be described in more detail in Chapter 6 using the linear equations derived in Chapter 3. Both formulations describe the wave shape and its properties using the wave steepness parameter H/λ, and the depth of propagation h_d. The two parameters were chosen along with the wavelength to depth relationship h_d/λ to produce the necessary waves with the desired scaled properties to simulate long swells in transitional and deep waters.

Scaling process

As the depth of our tank was set at h=0.6m, calculations were made for the waves to satisfy the linear and 2nd order theory. The calculations use the non-dimensional depth and height as defined in Chapter 3. The results in Table 4.4 show the necessary period and wavelength for waves in the tank.

T	x	T	λ	$\lambda/2$ to h_d
$T7=(h/gx_i)^{1/2}$	0.02	1.74	2.34	$\lambda/2 => h_d$
$T6$	0.028	1.47	1.7	$\lambda/2 > h_d$
$T5$	0.039	1.25	1.22	$\lambda/2 > h_d$
$T4$	0.049	1.11	0.97	$\lambda/2 > h_d$
$T3$	0.059	1.0	0.8	$\lambda/2 > h_d$
$T2$	0.074	0.9	0.64	$\lambda/2 \sim h_d$
$T1=(h/gx_s)^{1/2}$	0.093	0.81	0.51	$\lambda/2 < h_d$

Table 4.4: Values of wavelength λ against depth h_d and its non-dimensional depth x for our experimental range x_i to x_s.

As the set of waves that could cover this is large, a small subset of the waves was chosen with periods T=[1.7s,1.5s,1.2s,1.1s,1.0s,0.9s,0.8s] to obtain every non-dimensional depth (x) as can be shown in Table 4.5.

$T(s)$	1.7	1.5	1.2	1.1	1.0	0.9	0.8
x	0.021	0.031	0.042	0.05	0.061	0.075	0.095

Table 4.5: Non-dimensional depth values for a tank of 0.6m depth.

The conditions given by these relationships need to be corrected as wavelength can be different depending on the depth at which waves move, as explained in Chapter 2. Using the wavelength period relationship for deep waters for $T1$ to $T2$ and the transitional water theory for $T3$ to $T7$ to minimise an incorrect wavelength to depth ratio, as mentioned by Noble et al., Table 4.6 is obtained.

T(s)	1.7	1.4	1.2	1.1	1.0	0.9	0.8
Approximated λ (m)	3.5	2.71	2.1	1.8	1.5	1.2	1
Depth regime at h_d=0.6m	Upper T.	Upper T.	Upper T.	Upper T.	Upper T.	Deep Waters	Depp waters

Table 4.6: Approximated wavelength for each wave period, where Upper T. is the upper section of the transitional water spectrum for wave propagation at intermediate water depths x>0.02.

The values obtained in Table 4.6 will be scaled accordingly, as in Noble R. D, et al, using the equations below.

$$T_{Tank} = T_{Site}\sqrt{Ef} \tag{4.11}$$

$$h_{Tank} = h_{Site}Ef \tag{4.12}$$

$$\lambda_{Tank} = \lambda_{Site}Ef \tag{4.13}$$

In these three equations, Ef is the scaling factor defined by L_r and L_m from equation 4.1. These values will be used in Chapter 6.

Using Table 4.6 we can calculate the wave height to produce wave trains of 1st and 2nd order. The order is given by the non-dimensional relationship in equation 4.4 of Chapter 3. If we choose our wave height as

H=1±0.5cm, we can then calculate the range of waves using the non-dimensional parameters and obtain the range of the waves in Figure 4.8.

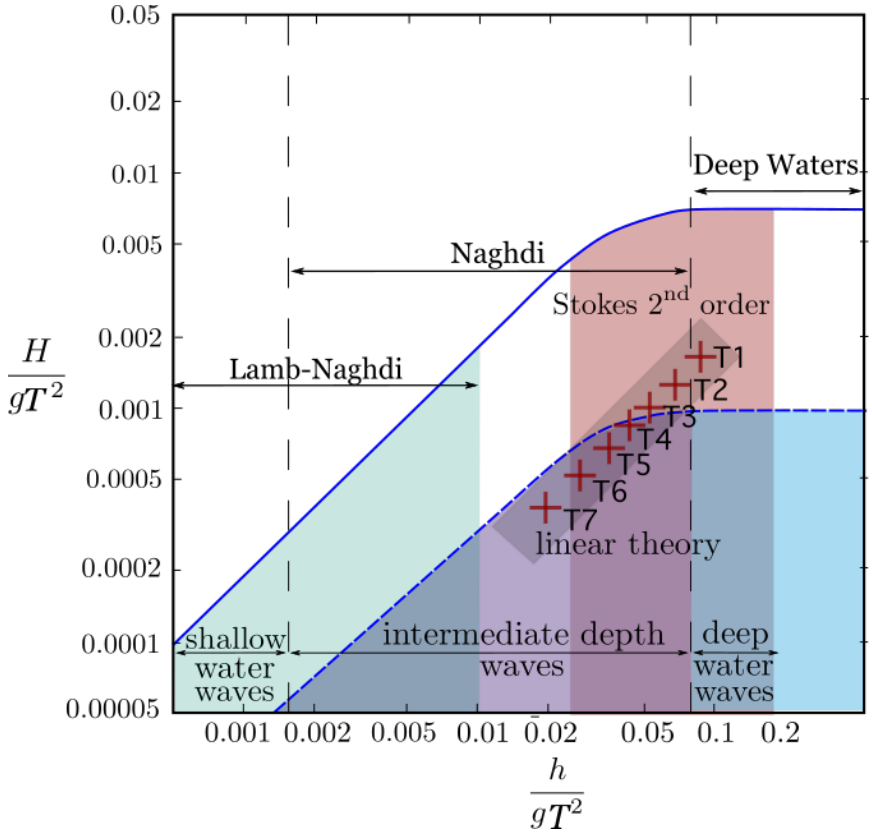

Figure 4.8: Periods chosen using the non-dimensional quantities and ranges of the dimension order of our tank capabilities from T1 to T7. The red band is the initial assumptions made for our experiments. The figure is based on the work of Le Méhauté.

Waves generation and wave reflection

The number of waves produced for each wave train varies depending on the wavelength and wave celerity. Our wave tank had an available length of 21.6m with 21m being its effective length due to the last 0.6m providing a beach. The tank beach did not have any mechanism to absorb the incident waves. The effects of lacking any dissipation mechanisms meant our waves were reflected and caused interference with the incoming wave trains. Due to the constraints on the wave reflections, the number of waves that can be measured without the overlap of both wave systems is limited to the wave velocity and the available tank length. To obtain the number of waves that could be produced without reflections interfering from the tank, we used the dispersion relationship and wave velocity. Velocity values for the fastest and longest wave trains were used to calculate an upper boundary for the time

of propagation between the wave-maker and the wave beach. The propagation time was measured using the fastest and longest wave available, $T7$. The values for the longest and fastest wave belong to $T7$=1.7s, and a value known here as the upper boundary value was used as a superior limit for the wave propagation time. The upper boundary ensured that, as long wave trains were slower than the bigger period wave, reflections from the wave tank beach would not interact with the incident waves. The values for the upper boundary and the different wave velocities and times for reflections to be present in the wave tank are shown in Table 4.7.

$T(s)$ [$T7$-$T1$]	1.7	1.4	1.2	1.1	1.0	0.9	0.8
Approximated C (m/s)	**2.0**	1.93	1.75	1.63	1.54	1.33	1.25
Time (s) to reach the beach at C and return to point x=7m	**14**	14.5	16	17.1	14	21	22.4

Table 4.7: Approximated propagation velocities for each wave period, where the upper boundary velocity was marked in bold font and belongs to the values at $T7$.

Wave trains produced showed that the upper boundary for the longer waves was around v=2m/s ($T7$ and $T6$). A point to place a wave probe at 7m from the wave maker will take 14s to detect reflections using the configuration shown in Figure 4.9. Several experimental run-ups included measures of non-dimensional height y. Observations made and data gathered concluded that wave height could be not controlled precisely, as shown in Figure 4.10, for each test without any obstacle.

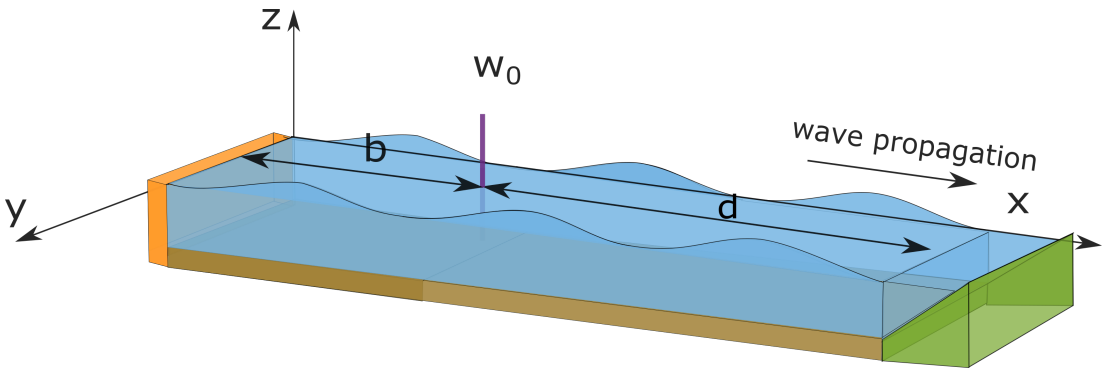

Figure 4.9: Wave reflection time was tested using the fastest and longest waves at T=1.7s, and the wave probe was placed at distance b=7m from the wave maker. The distance from the wave probe to the beach mid depth is d=14m.

As the non-dimensional height y was necessary for the conditions in Figure 4.5 to satisfy the experimentation needs, then the wave height only needs to be H<1±0.5cm for the smaller period. This limit however increases for larger waves as long as H<<λ. For the wave height, we were limited by the height between the tank border and the tank surface which was equal to 10cm using a depth of 60cm.

The paddle did not have any control to stop at a determined position, because of this pre-calibration procedures to detect the wave height generated show a wider range of values for larger periods T6 and T7 as shown in Figure 4.6. This was probably related to the angle of aperture of the wave maker, as the first waves would not be able to capture the full power if the flap was not in the correct position. However, measurements for shorter periods show a smaller variation on their wave height.

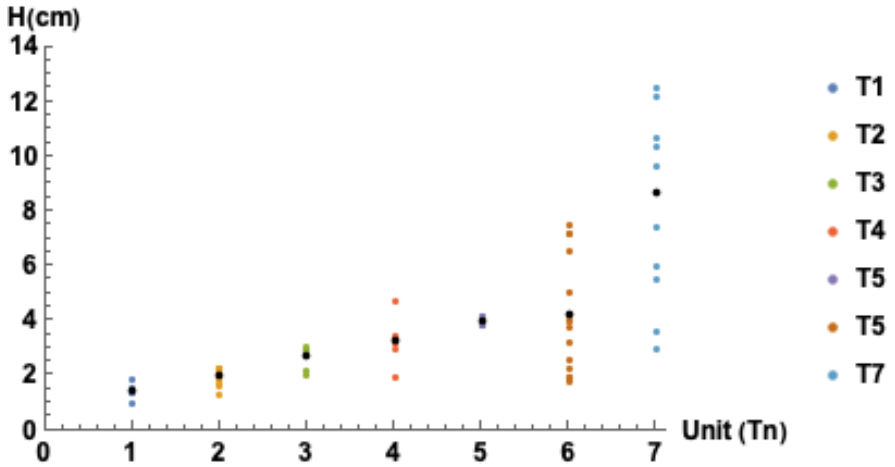

Figure 4.10: Wave height variability for different testing periods, T1 to T7 as shown in Table 4.7. Black markers represent the mean wave height.

As the limit is lower, concerns about the possibility of capillarity forces on the shape and form of the waves were taken into account. For this a minus wavelength was taken into account with a value of 1m length. The formula for the wave subjected to gravity and capillarity forces in equation 4.14 was then used to derive the ratio of gravity to capillary forces on a lower boundary at T1.

$$\omega^2 = |k| \left[\left(\frac{\sigma}{\rho' + \rho} \right) k^2 + \left(\frac{\rho' - \rho}{\rho' + \rho} \right) g \right] \qquad 4.14$$

Equation 4.6 value used the higher value of the water surface tension σ and the air and water at cold temperatures densities ρ and ρ‘ respectively. Capillarity forces, in the worst-case scenario, will only be around 3% of the total at our wave trains. The ratio of the forces indicates that at small amplitudes our waves will still hold for the non-dimensional values chosen because they depend on the gravitational component. In order to measure the wave reflection interference in the tank, wave recordings were made with the configuration shown in Figure 4.6.

The measurements taken for higher periods allow us to observe the wave reflection time, as recommended by experimental practice [90]. The reflection time allows us to obtain intervals of data acquisition. For this, wave trains of the frequencies $T6$ to $T7$ were tested to measure the time of reflection. The calculated values for the time of reflection were compared to the actual recorded reflection for all wave trains produced on the range $T6$ to $T7$. An example can be seen in an actual plot recording for periods $T7$=1.7s and $T6$=1.4s in Figure 4.11.

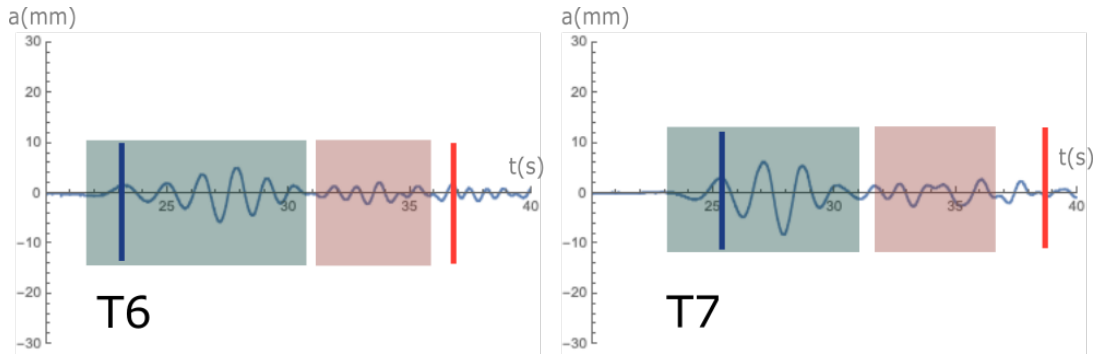

Figure 4.11: Recordings of wave trains T7 and T6 at 1.7s and 1.4s respectively, showing the reflected wave trains in red and the expected time of reflection as a red bar.

As the waves corresponding to $T7$=1.7s presented a faster propagation on the recordings than the calculated reflections, the recorded times were used to adjust the time that every experiment should allow for waves to propagate before reflecting. Careful measures were taken of each wave component on larger periods. The measurements took individual

waves (crest to trough) and analysed the time it took to propagate. The detections of each crest and its movement along the wave probes were used to calculate the propagation velocity of each of the wave trains with larger periods ($T7$) across the tank length l.

The velocity of propagation was then used to find the time for wave reflections approaching from the tank beach. This method allowed us to identify the frequency for each $T7$=1.7s wave train and calculate its actual velocity of arrival in Table 4.8.

$T7$=1.7s [f~0.58Hz]	
Approximate period T(s)	Approximate velocity of the main T component (m/s)
1.69	2.08
1.58	2.03
1.69	2.07
1.61	2.04
1.75	2.08
1.58	2.03

Table 4.8: Actual velocities of wave propagation according to its approximate measured peak frequency.

The methods used to capture characteristics such as the wavelength and the velocity were used to compare the generated period with the calculated one given the wave shape. The methods used are experimental and follow the procedure in 4.3.5. Such a method is not conclusive as the wave shape evolution will alter the calculated values. In these measurements, only waves with a very well-defined shape were taken and, despite this, for the measurements made with no obstacles, we saw only very small deviations in the periods of the fastest waves. The largest deviation in the period for this was below 9%. The deviation keeps our reflection time to around 14s, so this value was used as an upper boundary. The method using the wave shape to calculate and approximate wavelength detected small deviations for all periods, but they did not appear to be large

enough to affect our measurements. The result of this can be seen at the end of Chapter 5.

4.3 Experimental procedure

4.3.1 Wave probe placement

During the pre-testing and calibration, wave generation created a small wave train. This problem was occasioned by the wave tank, as the flap would vibrate after stopping. As the small waves were much shorter in length, velocity separated the desired larger waves from the small ones for any given T_n value, around a distance of x=5m. The observations made us place wave probes in positions x_1=7m, x_2=9m, and x_3=11m, and a fourth was added at x_0=2m to detect the incoming waves, as in Figure 4.12. The probe placement allows for the measurement of the waves along their trajectory, as suggested in ITCC recommended guidelines and procedures [112].

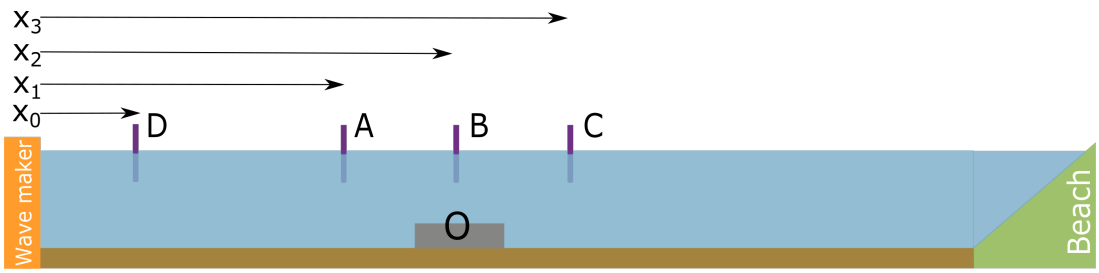

Figure 4.12: Wave probes were put at distances x_0=2m, x_1=7m, x_2=9m, and x_3=11m along the length of the tank. An obstacle was placed below wave probe B in the centre of the tank at 9.05m from the wave maker flap in orange.

As the wave probe located at 11m from the flap was at a distance d=10m from the tank beach, this gave us a length of 20m for wave reflections to arrive at the last wave probe installed in order to measure the propagation. As every wave lower than $T7$ has a velocity relationship v_{T7}<v_{Tn}, this allowed us to restrict the number of wave recordings that we made on the last wave probe C using the fastest the wave velocities of $T7$. The higher velocities averaging 2m/s, made us stop the measures of the

incident waves after 10s passed when the first detection in the last wave probe C was made.

4.3.2 Wave measurements

Wave amplitude: Wave amplitude was measured using the transfer functions found for each wave probe calibration. The wave probe is inserted inside the water at a mid-length of its size, and the value was taken as zero amplitude or water surface level. The changes on the level around the zero value were taken as the wave amplitudes as they propagated onto the tank. The magnitudes of the wave amplitudes were measured from the trough to the crest of each wave. To do this, the velocity of the wave crest was calculated as it moved, and the wave crest and its respective trough were followed on each next sensor.

Wave velocity: Wave probes are only able to measure the variation of the surface height in time $H(t)$, but the distance between each wave probe was fixed and this helped us to calculate the velocity. The velocity was calculated using the fixed distance between each wave probe that is equal to Δx=2m by using the v=$\Delta x/\Delta t$ relationship.

Wavelength: Wavelength was measured from the crest to the trough of each wave propagating in the tank. These measures were done by placing markers to identify the wave crests and through the recorded data.

Wave train series: Series were made to obtain the time between each measurement. The experiments suggested an estimated time ranging from 5min-2.5min for larger waves and 3min-2min for shorter ones. Measurements were done once the wave reflections in the tank were lower than the signal equivalent for an 1mm water height increase for each sensor. A recording can be seen in Figure 4.13.

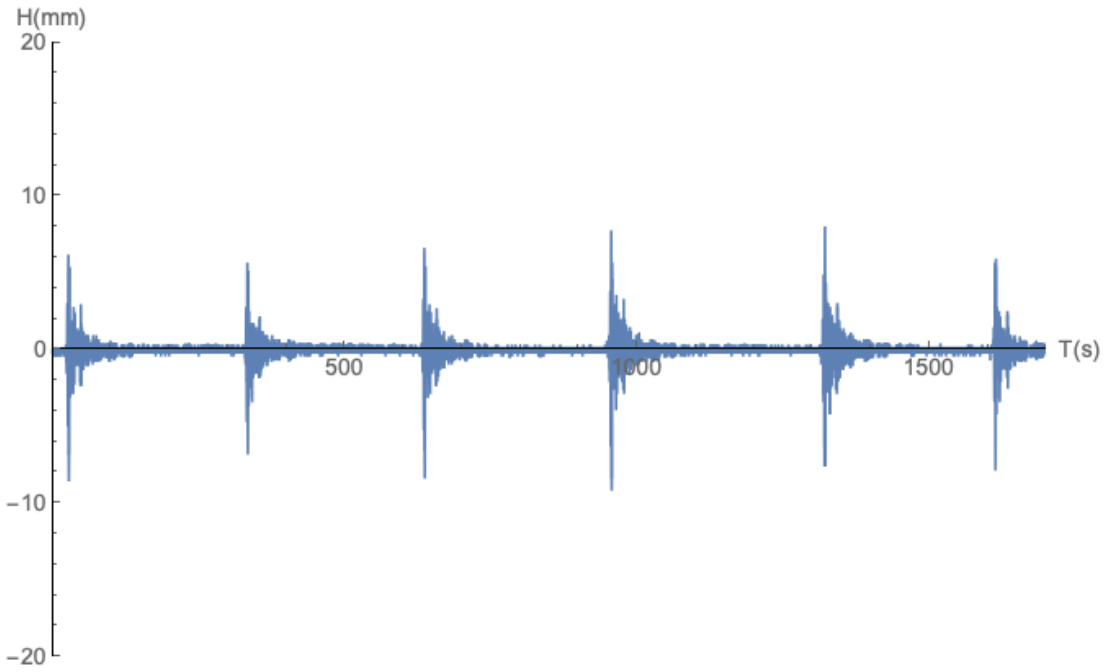

Figure 4.13: Wave recording showing wave trains and settling times between each test.

4.3.3 Experimental units and experimental arrangement

Obstacles were placed at the mid-point of the central wave probe B, at 9.05m from the wave-maker flap. To characterise the change in the blockage for incident waves, the obstacles were placed first to reduce the depth in the range from 1/6 to 1/2 of the actual tank depth. For the depth experiments, the length of the obstacle remained fixed. The second set of experiments included a change in the obstacle length using the same blockade ratio of 1/6 but modifying the obstacle length from l_i/l_{ts}=[1/3,2/3,1] where l_i is the individual obstacle length and l_{ts} the total length of the three obstacles, one after another. The experiments revealed that the wave tank's middle depth was narrower than the 1.6m specified, so much so that even our obstacles of 1.5m were able to fit.

Experiments were arranged to test every wave period range, from $T1$ to $T7$. Periodic revisions were made to recalibrate the wave probes every 3 to 4 hours of testing, thus searching for possible sensor deviations [113]. During the testing units to calibrate the tank, physical observations were made of the wave propagation. Observations using the experimental method to detect the wave shape concluded that the lower periods from $T1$ to $T3$ might have period values higher than expected. Values for these periods,

however, did not have a significantly large deviation to compromise our experiments, as shown in the results section. The deviations in the possible period can be related directly to the wave-maker startup process and our need to measure only the first wave trains.

Using the period, wave height data, and observations made, the experimental plan was devised to test wave propagation over an obstacle. The wave propagation to be tested consisted of an obstacle that changes its depth with a constant length and an obstacle that modifies its length at a constant depth. Both cases can be seen in Table 4.9. On the left are the experiments that change the depth of the obstacle, causing a blockade from 0 to 1/2 of the original depth using a constant obstacle length; on the right, experiments with a constant blockade of 1/6 of the original depth and obstacle lengths from 0.1m to 0.3m.

Change of depth			Change of length		
Depth h_d (m)	Blockade (h_i/h_d)	Obstacle length (m)	Depth h_d (m)	Obstacle length (m)	Blockade (h_i/h_d)
0.6	0	0.0	0.6	0.0	0
0.6	1/6	0.1	0.6	0.1	1/6
0.6	2/6	0.1	0.6	0.2	1/6
0.6	3/6	0.1	0.6	0.3	1/6

Table 4.9: Arrangement of the experiments for wave propagation after a change of depth and change of length of a regular obstacle placed at the bottom of the tank.

The wave tank testing was divided into two campaigns. The experiments for the 1st test campaign tested wave periods ranging from $T7$ to $T6$ and the 2nd covered periods $T5$ to $T1$. It was observed that the tank could not produce exactly 0.8 and 1.2 seconds, so the periods were modified, as shown in Table 4.10.

Due to the wave variability and deformation along the tank length, experimental units $T1$ to $T7$ were repeated 6 to 12 times. As the number of individual waves produced by each wave train was 3, this gave us a minimum of 18 waves for 6 repetitions to be measured. This number was chosen to maximise the number of waves that can be measured properly.

Campaign No 1	Change of blockade h_i/h_d at h_d=0.6m	Change of length $l_i(m)$	Wave conditions at h_d=0.6m
T7=1.7s T6=1.4s	0	0	Transitional waters
	1/6	0.1	
	2/6	0.2	
	3/6	0.3	
Campaign No 2	Change of blockade h_i/h_d at h_d=0.6m	Change of length $l_i(m)$	Wave conditions at h_d=0.6m
T5=1.25s T4=1.1s T3=1.0s	0	0	Transitional waters
	1/6	0.1	
	2/6	0.2	
	3/6	0.3	
T2=0.9s T1=0.83s	0	0	Deep waters
	1/6	0.1	
	2/6	0.2	
	3/6	0.3	

Table 4.10: Arrangement of experiments in two different campaigns and two different sets of wave conditions according to the scaling process. The period for the shortest time changed as the tank control did not allow one to measure a frequency of 1.25Hz=0.8s and 0.833Hz=1.2s.

The number of repetitions was chosen depending on the wave definition; longer waves produced a better-defined shape and had fewer small waves as the flap movement was more smooth. The shorter waves ranging from $T4$ to $T1$ required larger repetition numbers of 10 to 12. The shorter waves had a higher number of small waves and irregularities produced by the wave-maker at shorter periods, and a possible explanation for this is given in the next chapter.

4.3.4 Wave tank measurement procedure

The wave tank is equipped with two activation controls, one by software and one by manual. To avoid any incidental activation by software, the manual control was always non-active. The experimentation procedure

consisted first of the verification of the wave probes and their calibration. The process required measurement of a submersion length of 50cm in both the negative and positive z-direction.

The wave probes were re-calibrated if the measurements obtained had a deviation of more than 1mm in the 50cm length. The wave tank manual control was activated after this, and 2min to 5min was given to allow the small wave ripples caused by the wave probe immersion to vanish. After the control was started, obstacles were placed at the bottom of the tank and small weights were used to add some support. Next, wave probes [A, B, C] were verified to be installed at positions x_1=7m, x_2=9m, and x_3=11m respectively.

Experimental sampling rate: Wave probes by design had a sampling rate of 100Hz or 100 measurements per second. The sampling rate was left unaltered as the higher frequency to measure corresponded to 1.25Hz which is very low compared to our sampling rate and it is 40 times the minimum required by the Nyquist-Shanon theorem for the original wave signal, which is smaller than our set (T=0.8s). As proof of this, camping rates also detected smaller waveforms produced in the tank, as shown in Figure 4.14, caused by the wave-maker mechanism.

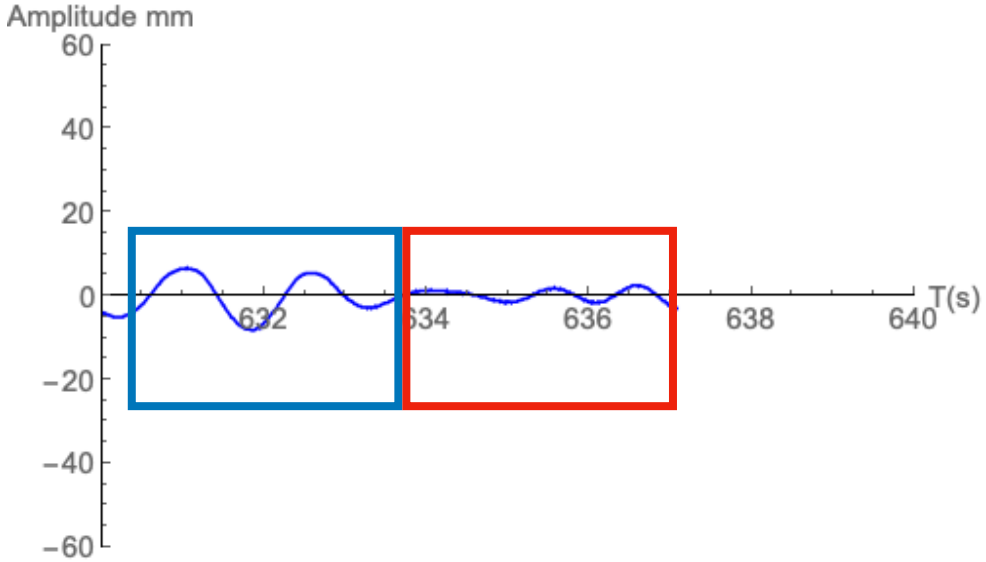

Figure 4.14: Small wave trains produced by the wave maker in red, after our main wave train in blue.

Recording procedure: Recordings and observations were made for each test to verify that the wave tank had no apparent ripples moving inside. Tests did not start until the noise was verified to be equivalent to $0.5mm$ in wave height. After verifying that only natural noise signals from the wave probes were present on the recordings, a small wave train was produced by just a few flap movements.

The wave-maker presented very irregular wave trains after a long period of inactivity; small wave trains were produced at the beginning of each experiment for a brief time period to avoid this. Once the wave-maker produced the first irregular wave train, the signal on each wave probe was tested and the process of producing the wave trains started. Wave trains were produced by moving the wave-maker flap 3 times. As the wave-maker does not have an automatic stop, one user had to give the signal to stop the wave-maker after the third complete flap. After the incident waves stopped, a time to stop the experiment Δt was taken until reflections disappeared and only the intermittent noise of the sensors was detected. Then the wave-maker was re-started to record another wave train. The process was repeated until all periods were completed.

4.3.5 Wave data processing

Data from the wave trains were pre-processed using Spike2. The software allowed us to feed each wave probe channel into the PC to produce $.txt$ files with the amplitude vs time values. The files were then processed using Wolfram for processing. Filters were applied to clean the signal from higher noise frequencies above $0.1Hz$. The waveforms were plotted for every experiment and the maximums and minimus of each wave train were extracted and used as control points to obtain the measurements of wave height, wave velocity between wave probes, and wavelength. This can be seen in Figure 4.15.

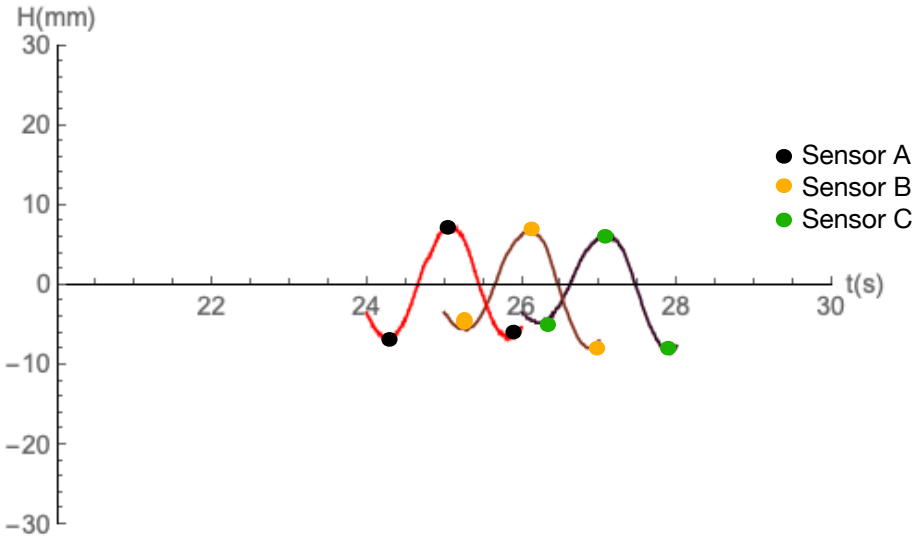

Figure 4.15: Control points to measure the wave development and properties.

4.3.6 Discrepancies in the wave peaks and troughs

As the instruments were able to measure the wave amplitude with a definition of 0.01s, small discrepancies in the values of the peaks and troughs appeared. The maximum or minimum values were spread over a Δx=Δt, as several time values had the same maximum value that defined the maximums or minimums. To address discrepancies in the wave crests and troughs, we averaged wave recording results that had more than one point defined as a maximum. The average was given around the central point of recorded values as local maximums or local minimums adjacent to the others. The value of t=x_{avg} was bounded by the maximum and minimum deviation of the x coordinate. Since the points adjacent are separated by 1*10^{-2}s, the deviation in the maximum/minimum was minimal.

4.3.7 Wave tank calibration

The wave tank was calibrated against the measurements made for no obstacles in the range of $T1$=0.83s to $T7$=1.7s. During this procedure, wave trains were produced to measure the relative changes in the waves due to the wave flume tank constraints and particular effects. Three particular

effects were addressed in the wave tank calibration: the amplitude change, the wavelength change, and the velocity change.

To calibrate the tank, wave trains without obstacles were produced. The amplitude, wavelength, and velocity changes were measured against their propagation in the tank. As we mentioned in the methods section 4.2.2, the calibration assumed that reflections from the beach arrived 14s after the first detected wave. The number of waves produced followed the observations made, this producing three completed flap movements. From the wave calibration records, it was observed that waves will be followed by a small irregular wave train. The distance of separation for these small wave trains was followed to understand how these wave trains could affect our measures. It was found that the small wave train will separate from the waves produced before our wave probe C, placed at 7m from the wave-maker. The wave probes then were installed at the already proposed distances of 7m, 9m, and 11m from the wave flap so the interference was minimal. No other important sources of waves able to obscure our recordings were observed, including reflections from walls.

Another important aspect was the calibration against the wave's natural shoaling, as it was expected that waves might reduce the wavelength and its speed if they propagate in transitional water depths. The wave periods subjected strongly to the wave shoaling were in the range $T4$ to $T7$. The measurements of the shoaling and velocity decay due to the wave's natural propagation over the bottom gave us the natural deviation caused by the wave tank, which was expected to be $\lambda > h_d$. The wave shoaling calculation and measurements can be observed in the data analysis section in Chapter 5.

The results of this analysis and the change in the wave properties and their propagation are presented in Chapter 5. These results are validated against the proposed and developed models in Chapter 3.

4.4 Experimental limitations

During the experiments, limitations and sources of uncertainty were observed. We can summarise these in four main categories:

- Energy to higher harmonics
- Irregular wave trains
- Vortex production
- Obstacle design

4.4.1 Energy transfer to higher harmonics

As was observed by Ting et al. [79] and Szmidt [78], harmonics would be produced after the waves propagate over the obstacle. According to the data obtained in experiments carried out by Ting et al. [79], discussed in Chapter 3, this energy transfer will be strong depending on the ratio of submergence, here defined as the ratio between the obstacle depth and the wave tank depth h_t/h_d and the variable defined es 0/022U_r, where U_r is the Ursell number. Mei and Unlata [88] also use the Ursell number as an indicator of the energy transferred to the 2nd harmonic. In their case, if the Ursell number is larger than 32.9, more than 25% of the wave energy is transferred to the second harmonic. The transfer will cause to harmonics grow as large as the original wave, near 60% of the original incident wave amplitude for Ting et al. and, in extreme cases like Massel's, the second harmonic can be larger than the first.

In all three cases, as reported by Ting et al., the depth of submergence plays an important role, as well as the depth of wave propagation and the incident amplitude. Because of this and in the interest of testing larger depths which are suitable for engineering purposes, depths were kept larger than those used by the past researchers and amplitudes were kept low, in an attempt to minimise these effects. A table with the ratios of wave propagation for this experiment and the number defined by Ting et al. can be seen below. The ratios of the maximum amplitude for the

2nd harmonic vs the wave transmitted amplitude are defined in equation 4.15.

$$\frac{a_{2max}}{a_{1min}} = \frac{H/2 * (\lambda_d)^2}{(h_d)^3} \quad 4.15$$

In equation 4.14 a_{2max} is the maximum measured amplitude of the second harmonic and a_{1min} is the minimum of the fundamental harmonic. Table 4.11 shows the maximum value for this ratio and also the Ursell number value, which might indicate a stronger transfer of energy to the higher harmonics, as defined by Mei and Ünlata [81].

Tank obstruction	$Max\ a_{2max}/a_{1min}$	$Max\ Ur$
1/6	0.1	4.5<<35.4
2/6	0.16	7.27<35.4
1/2	0.3	13.63<35.4

Table 4.11: Values of the maximum amplitude of the 2nd harmonic vs the fundamental harmonic for a wave propagating over an obstacle.

Table 4.11 shows that, for the last experiment, amplitudes for the 2nd harmonic could be at least 30% of the minimum height of the main component of the wave propagated over the obstacle. It is necessary to say that these values are very conservative as they assume our wave increases its height at least 2.5 times over the obstacle.

4.4.2 Vortex production

Vortex production has been reported by Ting an Kim [114] and it depends on the depth of submergence being stronger when waves pass over shallower obstacles. According to Ting and Kim, these vortexes will have an effect on the transmitted waves and in some cases will absorb 5% of the wave energy and flow separation will occur.

In these cases, models where waves do not lose energy due to

dissipation processes caused by the viscosity will only apply if the losses are small. It is then expected that, for the shallower obstacle cases tested here, dissipation could be a factor worth consideration.

4.4.3 Irregular wave trains

Only a few movements of the flap were allowed so reflections coming from the beach after the obstacle would not affect our measurements, which has an effect on the produced waves. The wave maker does not stop completely vertical and does not gain complete acceleration during the first movement. Because of the wave maker constrains the first flap movements produced waves with certain irregularities, making the first trough or amplitude more irregular than expected.

As this directly affected the characteristics we used to measure the wave (amplitude and trough), these variables have an associated uncertainty which was not defined due to the variability of the flap movement. Due to this, wavelength measures for the first waves were not as accurate as desired.

4.4.4 Obstacle design constrains

The obstacles in this experiment were designed as simple regular obstacles, instead of a long regular shelf. Experiments by Goring and Massel have two main differences.

1) They will present interaction with the bottom as the wave moves across the tank. This is because the wave will be in contact with the obstacle for a larger distance, causing shoaling. It is probable that any effect due to the obstacle's increased length is not properly observed here as wavelengths are kept larger than the obstacle's main length (the length perpendicular to the wave path). In these cases and other experiments with longer shelves, waves released after the obstacle can not be compared to the ones explored here, or the second set of experiments by Massel, Ting et al., and Kim.

2) The models considered here, such as by Marshall and Lamb, are proposed for long waves propagating over a single long obstacle. In these cases, these models do not take into account any other interaction with the obstacle after the wave rides over the first step. These models do not consider energy loss due to vortex interaction after the obstacle ends or how harmonics are produced and released after the obstacle. Despite measures being made after the obstacle, we expect limitations to the accuracy of the amplitude values after the obstacle.

4.5 Conclusions

Experiments carried out by authors like Goring [87], Bendykowska [105], Macagno [74], Newmann [70], Santos et al. [75], and Charland [106] show that, despite the good correlation between wave propagation theory, results show that physical parameters like the period and wavelength are affected by its propagation over an obstacle, parameters which are not accounted for in linear theory. Using these experiments as a base, an experiment was designed to explore different theories of wave propagation that could be used to enhance a tidal turbine simulation where wave propagation over an obstacle occurs, creating different conditions for the local wave weather after the obstacle. The experiment seeks to validate the models explored and proposed in Chapter 3 by Lamb [68], Marshall-Naghdi [88], and also the author's.

Methods to measure properties using tracking points of individual waves were used to derive their physical properties, such as the amplitudes, velocity of propagation, and wavelength. A certain degree of confidence is given to each property measured, given that the amplitude is easier to measure. Next is the velocity because it is measured by tracking the propagation in time of individual waves, while the wavelength is affected by the wave shape evolution and other possible effects.

A series of scripts that can be found in git/zenodo are included in Appendix section C.1. These scripts were done using Wolfram Language, and the code is also annexed in the same section at C.2.

The experiments were scaled to simulate swells with a moderate amplitude that move in transitional depth waters and from deep waters to a shallower regime in transitional depth waters. The swells were modelled after linear small-amplitude systems and second-order small-amplitude systems. The tests were divided into two campaigns that covered periods grouped from $T1$ to $T7$. The first campaign tested periods $T6$ and $T7$ and the second periods $T1$ to $T5$. For the experiment to measure the effects under the desired physical constraints of the formulations, the waves were calculated to have a range between $T1$~0.8s and $T7$=~1.7s. Meanwhile, amplitudes were calculated to be no larger than 1.5cm. Dimensionally, the conditions given prove that the wavelength values used are two orders of magnitude larger than the amplitudes, $O(\lambda)$ and $O(a^{-2})$, which complies with the conditions stated in Chapter 3 as $\lambda >> a$. It is important to notice that the periods were corrected afterwards as the wave maker could not produce frequencies for echo, so the period was equal to 0.8s and 1.2s.

The experiments were carried out in a wave flume tank with a depth of *0.6*m. *W*aves defined by the period groups $T1$ to $T7$ were propagated over a set of obstacles with two sets of arrangements:

Set 1: Wave propagation over an obstacle that changes its depth with a constant length.

Set 2: Wave propagation over an obstacle that changes its length with a constant depth.

The waves defined by the periods and amplitudes also cover propagation from deep waters to transitional waters ($\lambda_i/2 < h_d$) and upper transitional waters to transitional waters ($\lambda_i/2 \sim h_d \,||\, \lambda_i/2 < h_d$).

As we mentioned, the experimental design included the measurement of the amplitude, the wavelength and the wave velocity before, over, and

after propagation over the obstacles. The set of variables was chosen as most of previous experiments only measure the transmitted amplitude. The design also differs from other authors because the waves measured do not propagate in shallow waters but in transitional waters, since this regime would be useful for large swell components travelling to the shore.

5 Data analysis

The experiments presented in Chapter 4 are analysed here. This section shows their results and the main discussion is at the end of the chapter. The experimental analysis consists of four main sections.

The first is section 5.1 which analyses wave propagation across the wave tank and the measurements made for the amplitudes, the detected wavelengths, and the calculated velocity of each peak. Section 5.2 consists of the measurements made for the coefficient of transmission and its comparison to the theories of Lamb, Marshall and Naghdi. Section 5.4 offers insight into some anomalies and changes that occur in the detected wavelengths and the tracked velocities when an obstruction is placed in the tank. Finally, section 5.5 is a brief observation of changes that occur in steepness for shorter waves.

5.1 Wave propagation analysis

Measurements were done to test the wave generation, calibrate the wave maker, and also observe its mechanical performance. These tests were made without any obstacle in the wave flume tank. The experiments carried out covered the range of periods $T1$ to $T7$, and were made following the experimental arrangements mentioned in Chapter 4. The procedure analyses the evolution of the wave amplitudes for each wave, and also the changes in the amplitude and possible anomalies related to the wavelength and velocity propagating in the tank without any obstruction.

5.1.1 Wave velocity of propagation

Measurements for the wave propagation without obstacles were included in the wave tank calibration process. The repeatability of the experimental periods was tested, generating waves in the range $T1$ to $T7$ without obstacles, as mentioned in section 4.3.8. The system had a

limitation. The velocities measured at sensor A are indirectly calculated by measuring the wavelength against the desired period, due to our limit on the number of wave probes. Subsequent changes in the velocity after sensor A are more accurate as they were measured by calculating the time for the wave to travel the fixed distances between each of the wave probes. Because of the method used, the plots show apparent homoscedasticity and a wide spread, which can be related to four main sources.

1. The period is a fixed quantity and the ratio of the wavelength against the desired period is not completely exact. The first strokes of the flap do not always start at a perfectly horizontal position, hence the first waves would present a small deviation from the desired period.
2. The system to detect the wavelengths exaggerated the length of the first waves as the detection uses the wave shape. Detections of the first trough were exaggerated as the first trough merged with the undisturbed surface, making it hard to discern. A comparison of abnormal long deformed thoughts with a more defined one can be seen in Figure 5.1. This effect makes waves much larger than they appear.
3. Only waves with a defined wavelength were chosen by looking at the registered shapes to ensure that very long or deformed thoughts were not accounted for, resulting in a measurement which might appear biased. This was done to ensure no waveforms with very abnormal shapes were taken into account.
4. Waves were changing shape as they moved in the tank. Larger waves decreased their lengths and increased their size for conditions where $h<<\lambda/2$. Because of this, larger waves are smaller when they cross the last sensor C in Figure 5.11.

In general, the system to detect the wavelengths is less accurate than the one that follows the wave crests. The measurements of wavelengths and the velocity of propagation give useful insights into possible changes occurring

to the waves, but cannot be used as a substitute for the amplitudes which are easier to capture than the wavelengths due to possible small harmonics and irregular wave shapes.

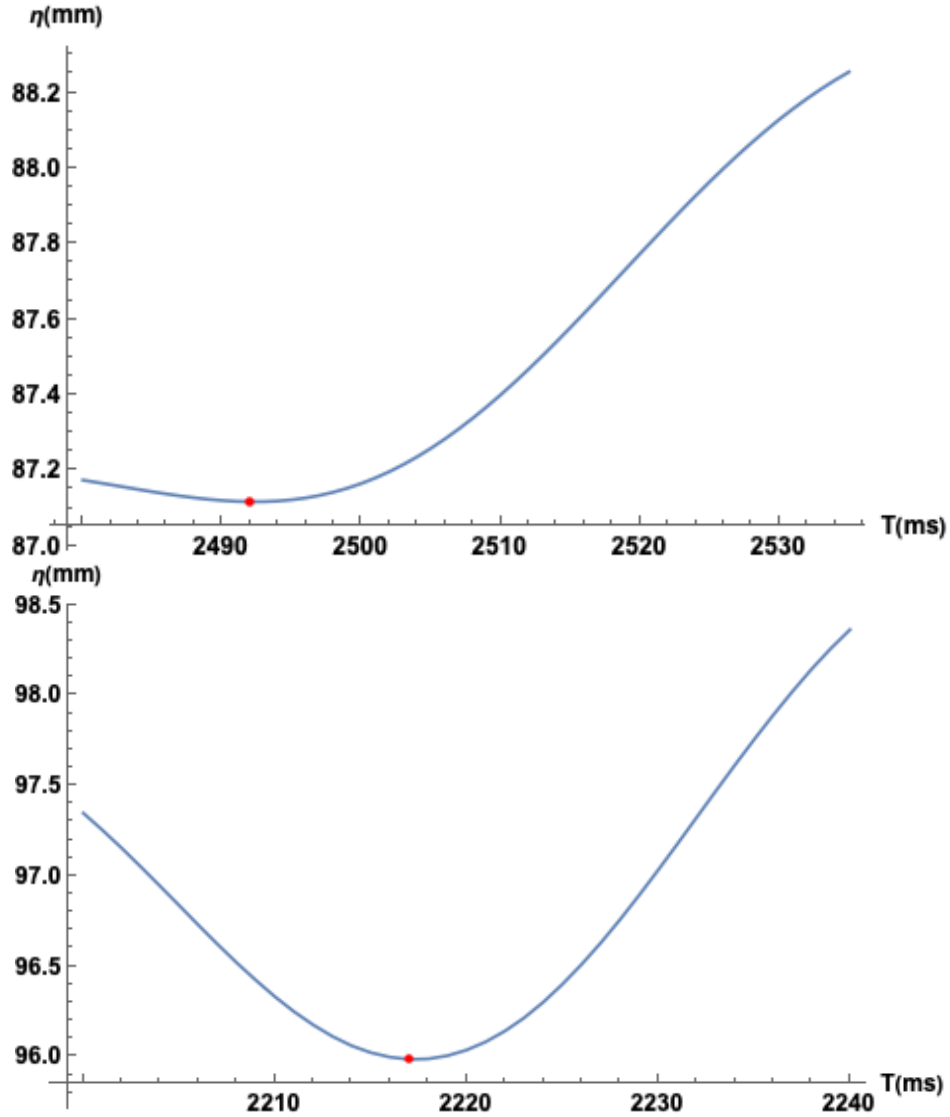

Figure 5.1: The first image shows a deformed trough, which was a normal occurrence following the wave shape. The lower part of the image shows a better defined wave shape. This variation usually made the wavelengths larger than expected.

The plot of the wave velocities is shown in Figure 5.2 for the first sensor A. The plot shows consistently larger velocities for many waves. This may be due to measuring the first waves which presented abnormal troughs. Velocities from sensors A to B and B to C can be seen in Figures 5.3 and 5.4.

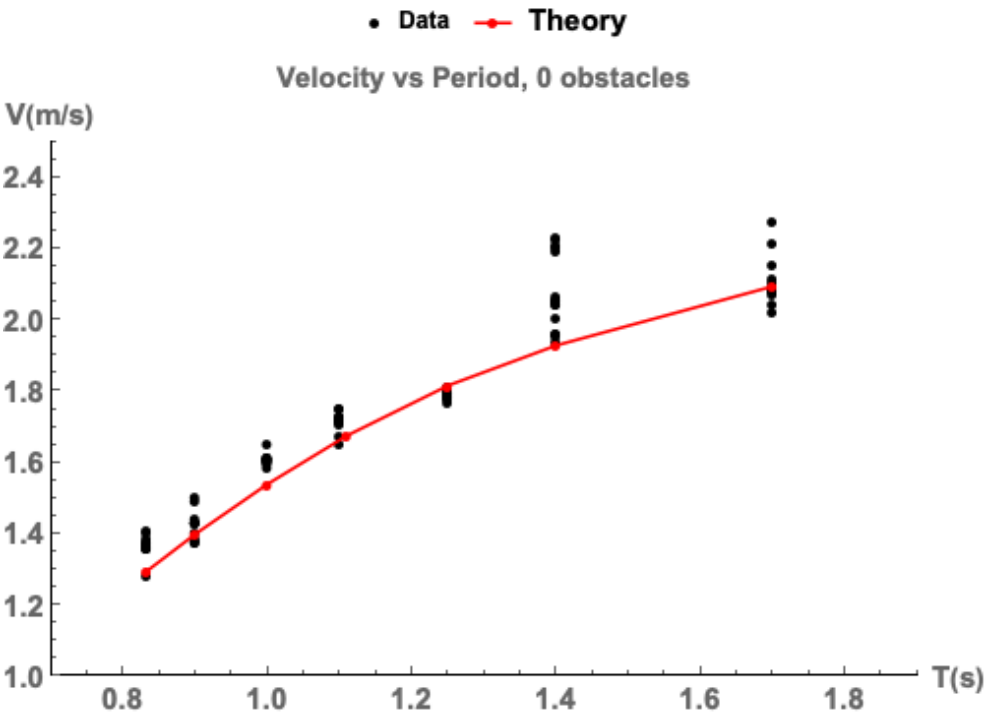

Figure 5.2: Approximated velocity of the generated waves, for the 7 periods proposed, as detected by the sensor at $7m$ from the wave maker.

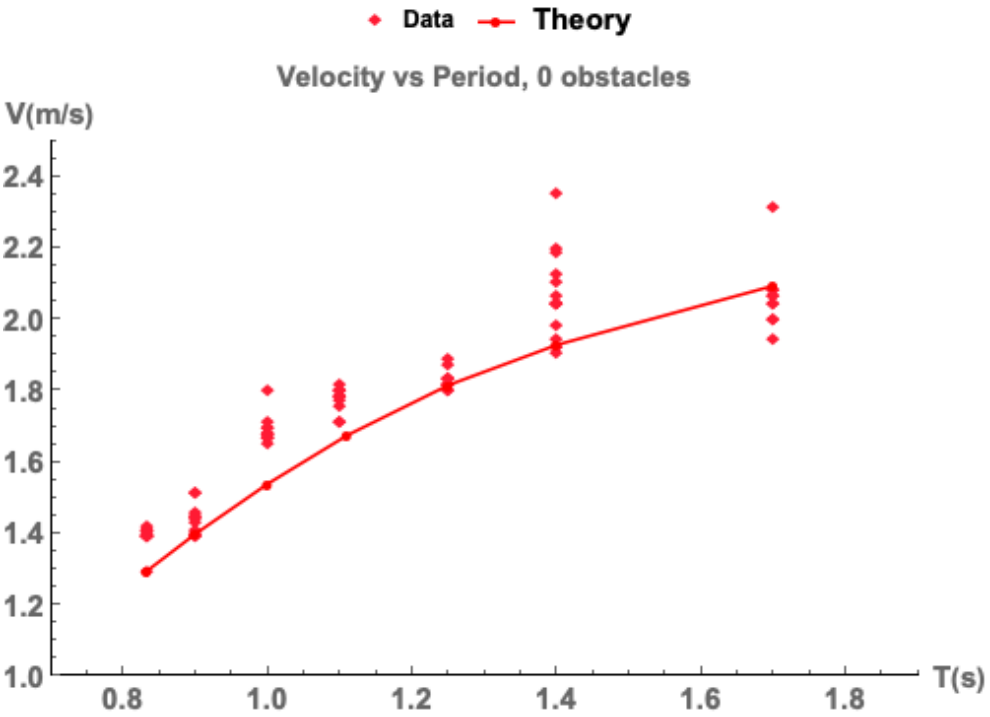

Figure 5.3: Approximated velocity of the waves generated for the 7 proposed periods, as detected by the sensor at $9m$ from the wave maker.

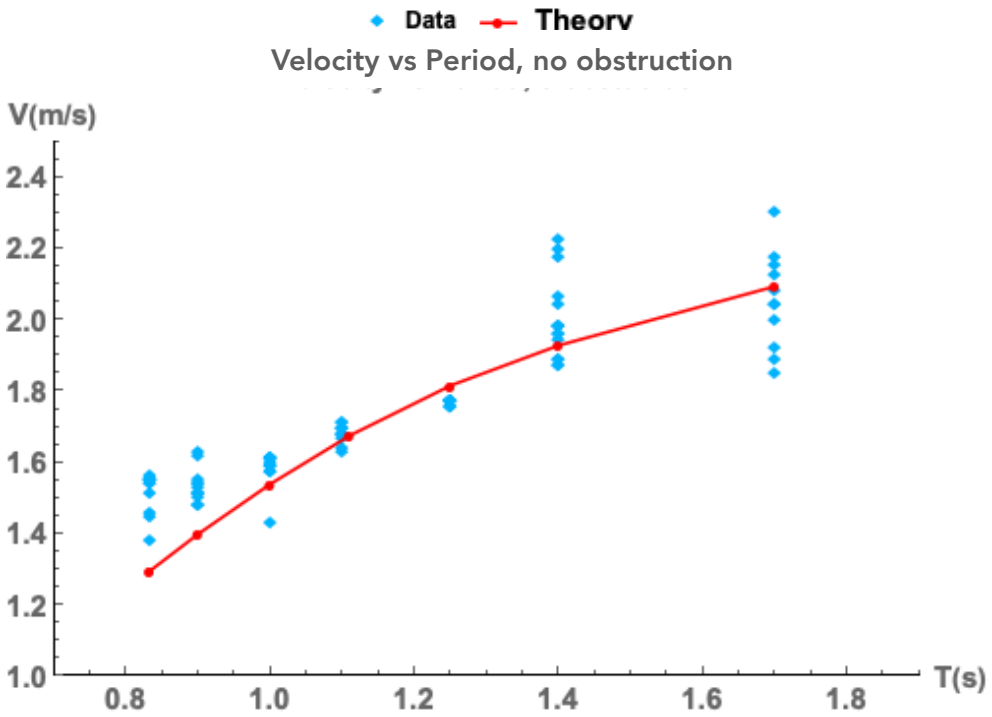

Figure 5.4: Approximated velocity for the wave trains generated for the 7 proposed periods, as detected by the last sensor at $11m$ from the wave maker.

If the period is calculated using the wavelength and plotted against the velocity, as in Figure 5.5, a more defined shape can be seen.

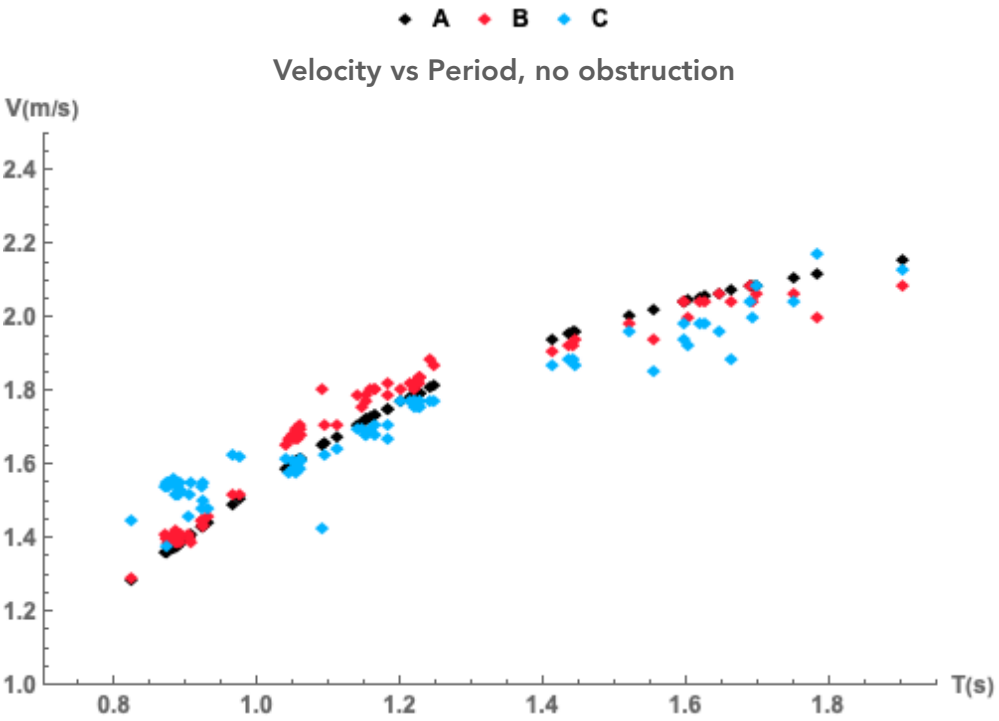

Figure 5.5: Velocity vs period for waves tested in the tank, in this case the variation presented horizontally for the waves tested. Sensors are C, B and A, positioned at $7m$, $9m$, and $11m$ from the wave maker.

In Figure 5.5 the data variation is shown horizontally. The data also shows a larger data scatter for larger wavelengths, as shown in Figures 5.6 to 5.7 for the first, second, and third sensors at $7m$, $9m$, and $11m$ respectively. The sensors also show how the evolution of wave shapes across the basin clearly does not allow us to define a constant wavelength, even at our shorter distances. Figure 5.6 shows that the mean value for the larger periods $T7$ appears smaller than for T6, which is inconsistent. This error appears to be linked to the definition of velocity for the first sensor, which is calculated using the measured wavelength.

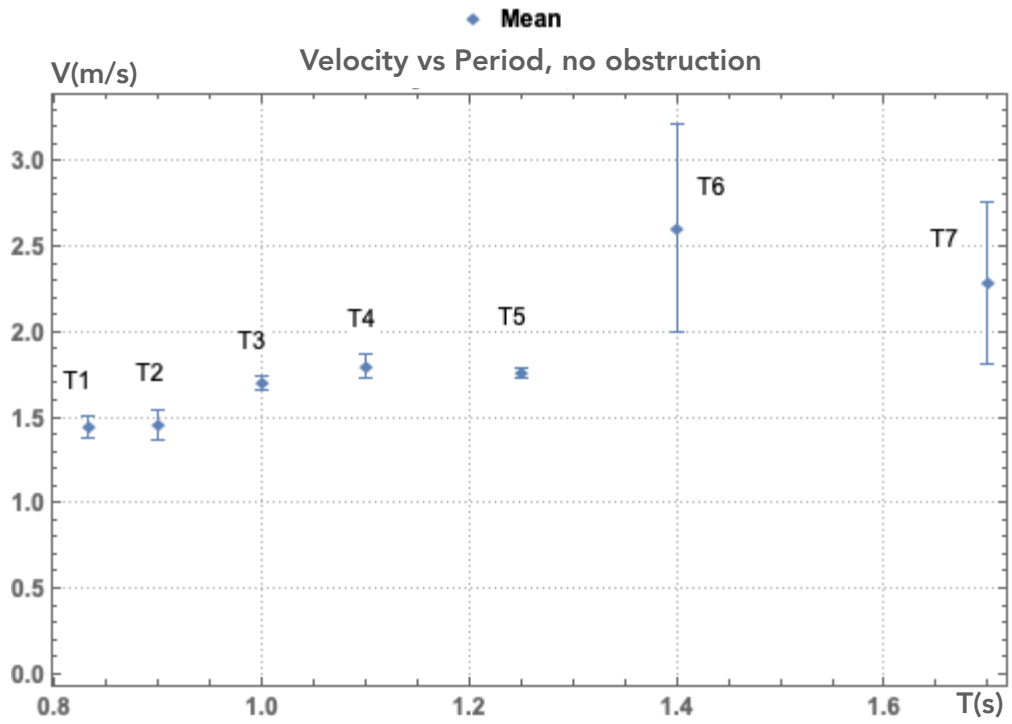

Figure 5.6: Velocity vs period for waves tested in the tank. In this case the data variation presented for the waves tested. For sensor A, which is located at $7m$ from the wave paddle, the definition of velocity is calculated using the wavelength detected by the software and the period of the wave.

In Figures 5.7 and 5.8, the velocity is calculated using the fixed distance between the wave probes and dividing by the recorded time from sensor A to B and then B to C.

The data in both figures 5.7 and 5.8 shows a decrease in the mean value for larger periods, $T7$ and $T6$, as might be expected and linked to shoaling. The figures also show an increase in the recorded velocity for the smaller periods, $T1$, as opposed to larger periods, $T5$.

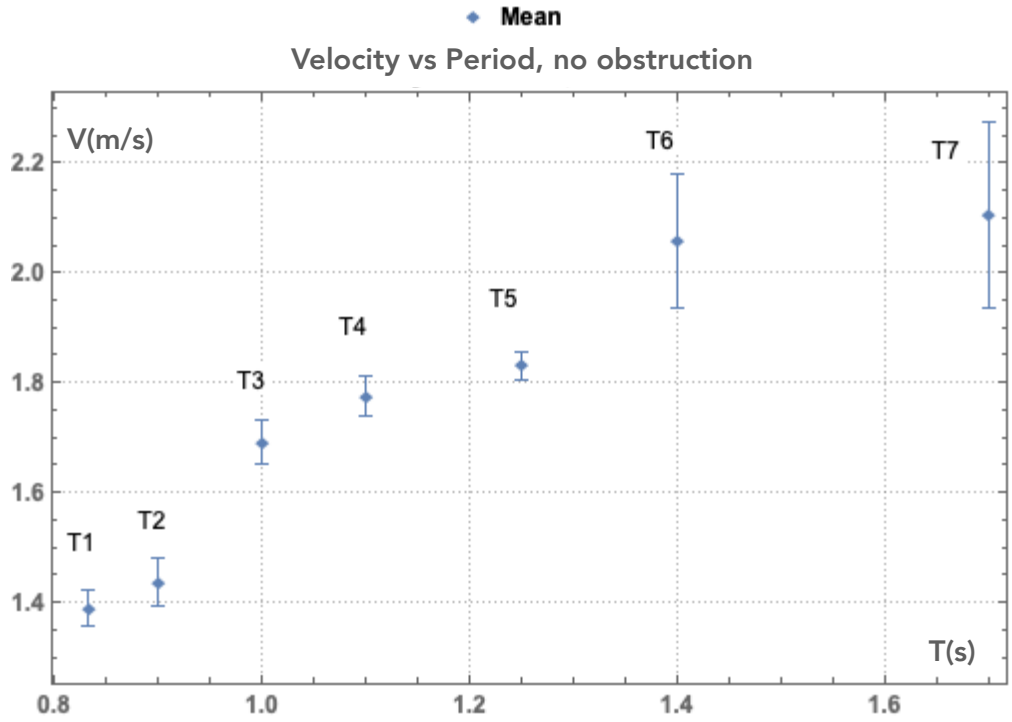

Figure 5.7: Velocity vs period for waves tested. In this case the data variation is presented for sensor B which is located at $9m$ from the wave paddle, and the velocity is calculated using the distance between the wave probes A and B.

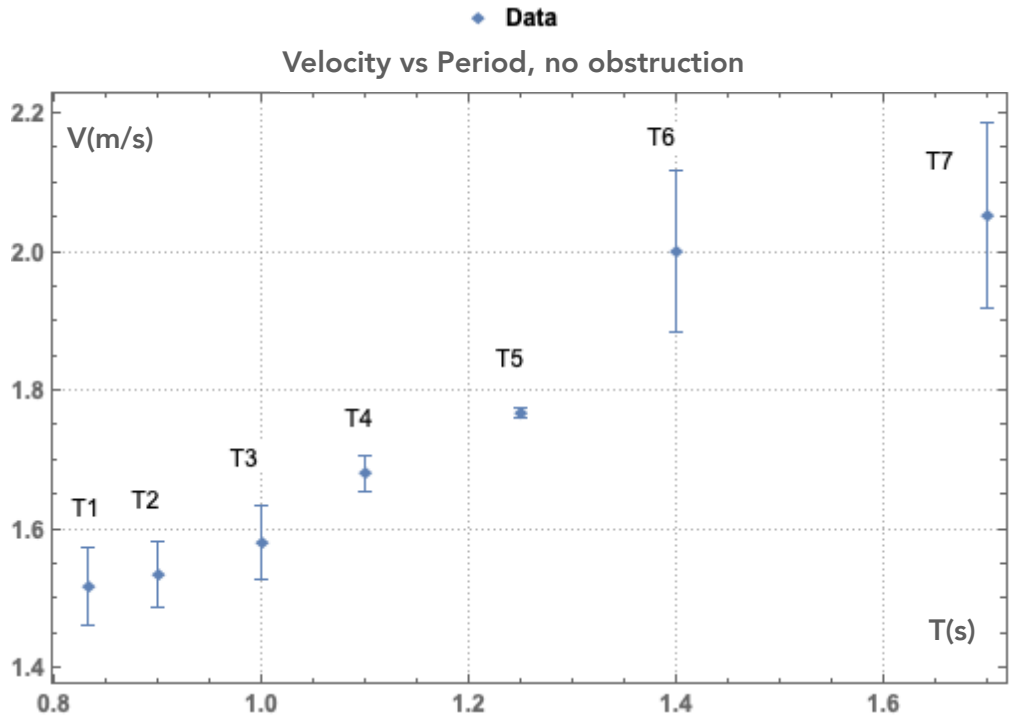

Figure 5.8: Velocity vs period for waves tested. In this case the data variation is presented for sensor C which is located at $11m$ from the wave paddle, and the velocity is calculated using the distance between the wave probes B and C.

5.1.2 Wavelength detection

Data used to characterise the wave velocity across the tank is used to measure the wavelengths for waves propagating from sensor A to sensor C.

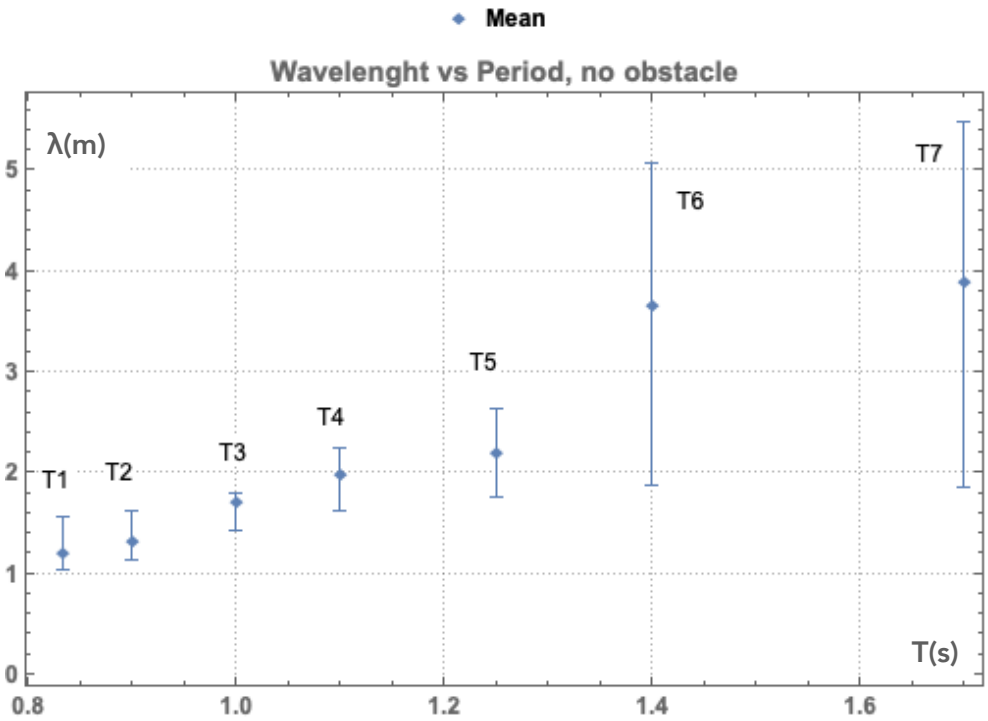

Figure 5.9: Wavelength vs period for waves tested in he ranges $T1$ to $T7$ at sensor A.

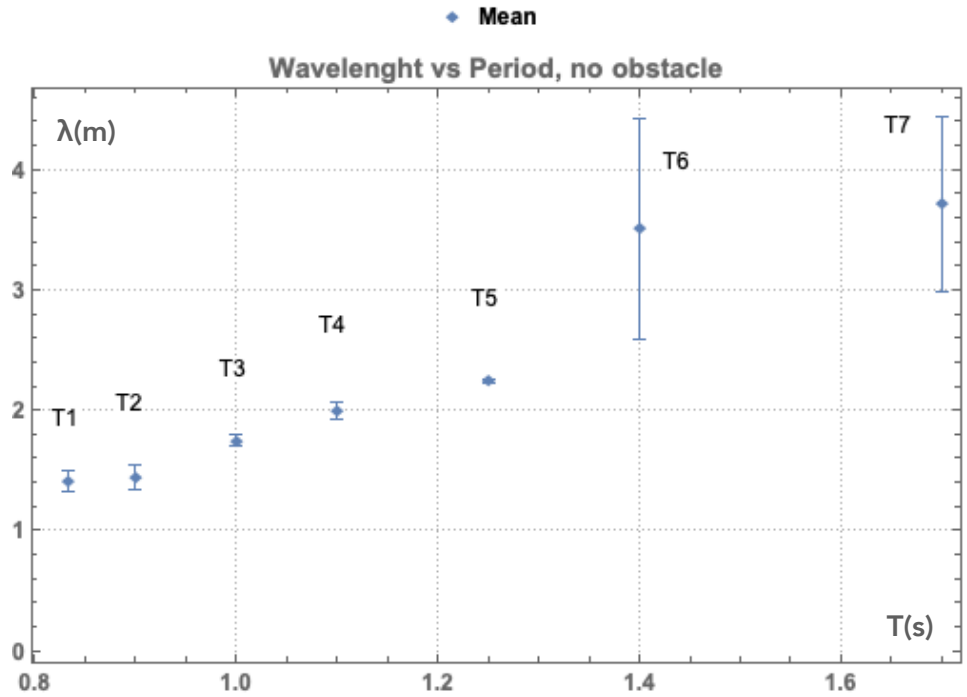

Figure 5.10: Wavelength vs period for waves tested in the ranges $T1$ to $T7$ at sensor B.

T(s)

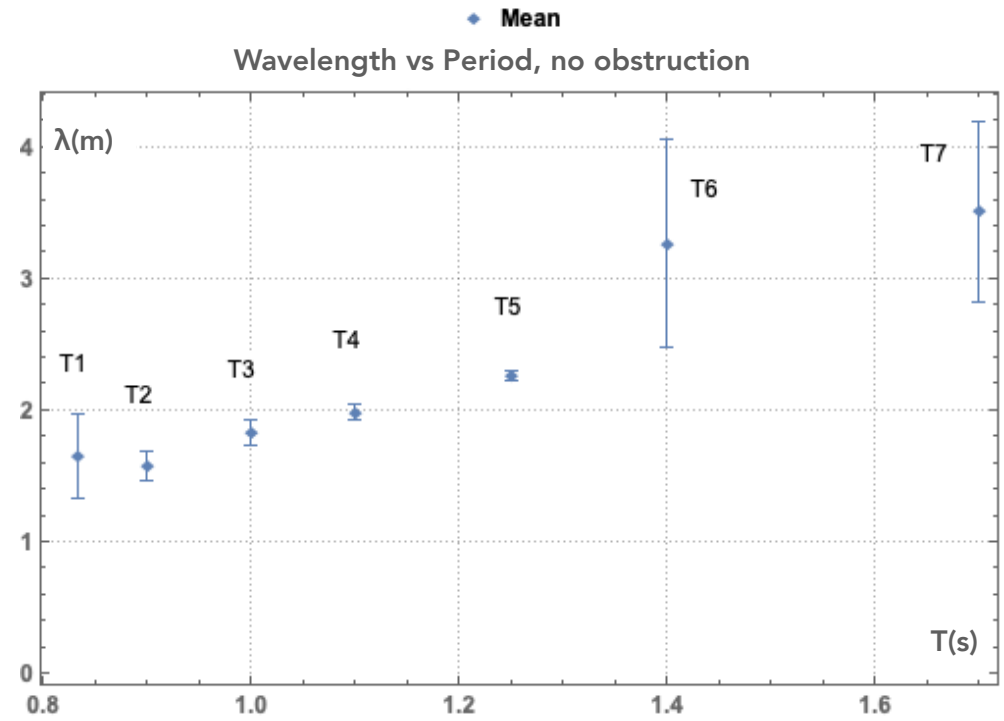

Figure 5.11: Wavelength vs period for waves tested in the ranges $T1$ to $T7$ at sensor C.

Data shows a consistent increase in the mean value for wavelength from $T1$ and $T2$ as shown in Table 5.1 and Figures 5.10 and 5.11.

A more detailed analysis of the amplitudes is provided in section 5.2.1. The data also shows a decrease in the wavelengths for larger periods in the range $T6$ to $T7$, but Figures 5.8 to 5.11 also show a larger scatter of the data for larger wavelengths. It is possible that these anomalies in the waves are linked to how the wavelengths are measured and to the wave maker mechanism. If the period is calculated using the measured wavelengths, Figure 5.12 is obtained.

T(s)

T(s)

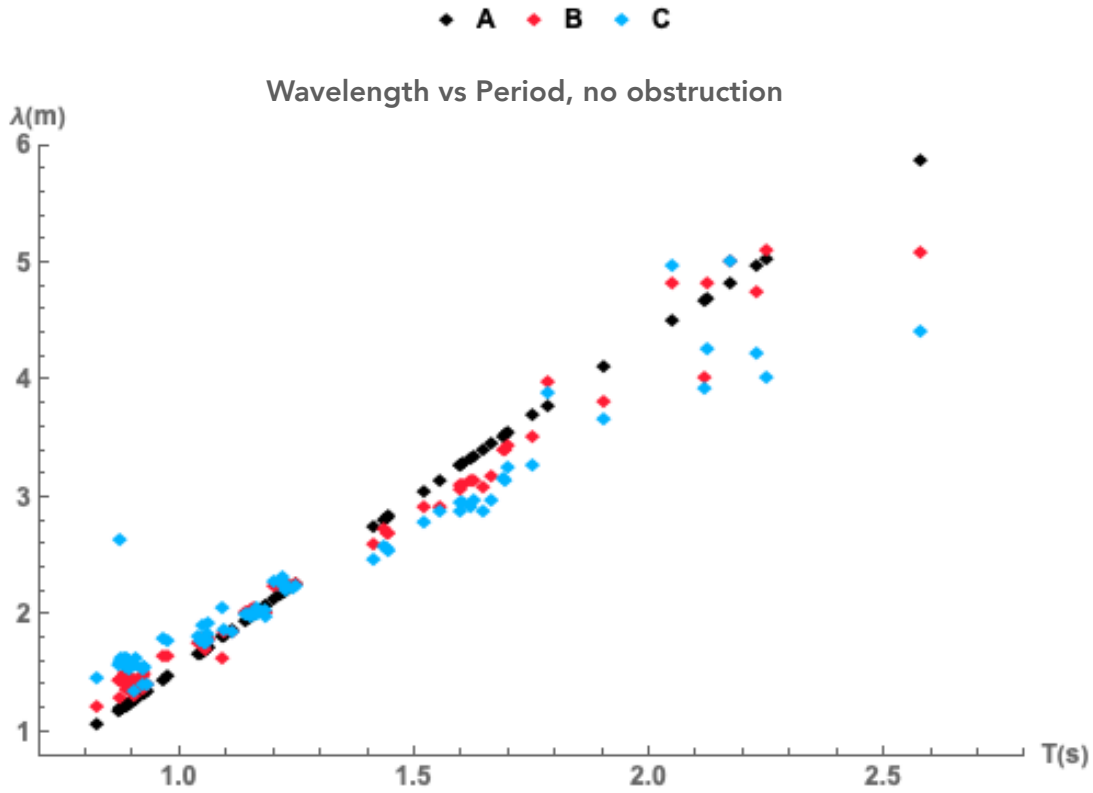

Figure 5.12: Wavelength vs period for waves tested in the tank. In this case the variation is presented horizontally for the waves tested. Sensors are C, B and A, positioned at $7m$, $9m$, and $11m$ from the wave maker.

The data in Figure 5.12 shows the detected wavelength, which is calculated by detecting the wave shape and subsequently used to calculate the period. It shows the variation observed in Figures 5.9 to 5.11 but in a horizontal manner as waves show wavelengths and periods higher or lower than the ones produced by the wave maker. The calculated wavelengths using the system to track the wave shapes increase the wavelength when abnormal waveforms are detected. Some extreme wavelengths reach lengths of $5m$, as seen in Table 5.1.

Table 5.1 shows the extreme wavelengths detected for a given desired period in the range T1 to T7 and the expected period calculated using the correspondent wave theory for deep waters or transitional waters, given by equation 3.3 or 3.4.

Period range	Expected $\lambda(m)$	Mean (m)	Max-Min λ (m)
$T1$	1.08	1.2	2.63/1.05
$T2$	1.25	1.31	1.78/1.22
$T3$	1.53	1.7	2.06/1.62
$T4$	1.82	1.97	2.07/1.81
$T5$	2.26	2.19	2.31/2.12
$T6$	2.70	3.64	5.09/2.46
$T7$	3.54	3.88	5.87/2.87

Table 5.1: Mean value, expected value, and maximum and minimum wavelengths detected for each period range.

Wave shoaling: It was expected that shoaling would occur for the larger waves. Length values for periods above $T3$ will show a consistent decrease in their value as they propagate across the tank, as Figure 5.13 shows.

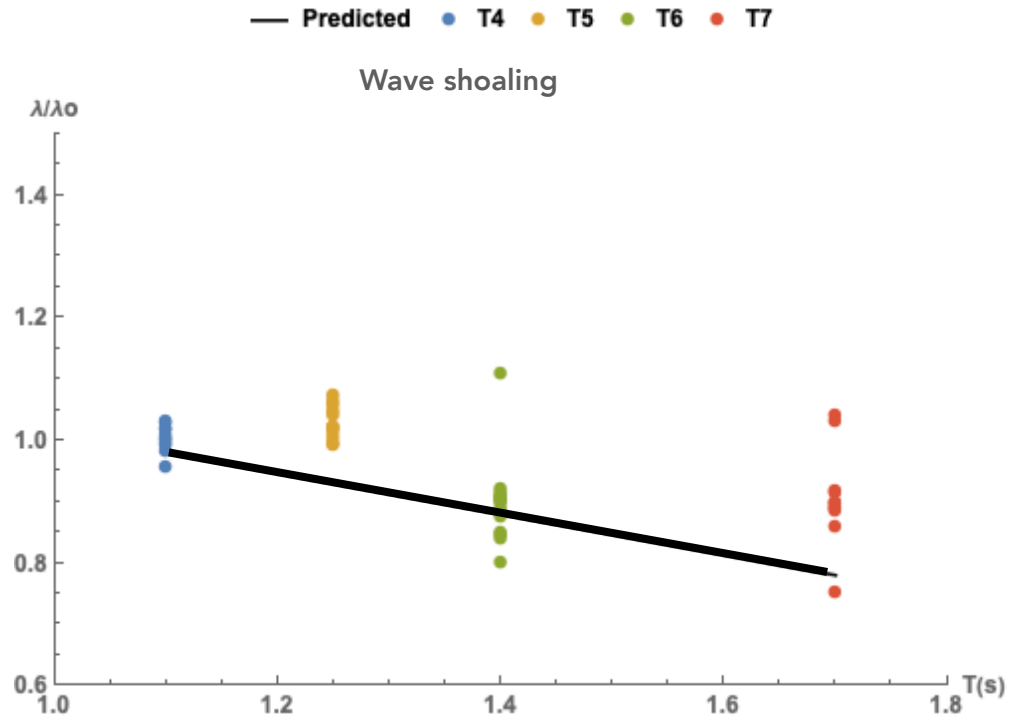

Figure 5.13: Wavelength ratio, where λo is the wavelength at sensor A=7m and λ is the wavelength at sensor C=11m for all waves in the period range $T4$ in blue to $T7$ in orange.

We expected larger periods to show larger deviation in their wavelengths, which was confirmed by the data shown in Figure 5.11. However, an increase is observed in some of the data for periods $T4$ and $T5$. Deviations

appear for periods $T6$ and $T7$, but the tendency is for them to have smaller wavelength values at the last sensor C than the first sensor A. The mean values for the data and their deviations are shown in Table 5.2. The data represents the ratio of the detected wavelength at sensor A and the detected wavelength at sensor C across a distance of four metres.

Period	$T4$	$T5$	$T6$	$T7$
Mean λ/λ_o	0.99	1.0	0.88	0.89
σ	0.018	0.033	0.077	0.086

Table 5.2: Wavelength decreases for larger periods where λ is significantly larger than two times the tank depth and its standard deviation.

5.2 Model validation and the coefficient of transmission

The models of Lamb, Marshall, and Naghdi are compared against experimental measurements of the waves propagating across the tank, made by obstructing the tank in the manner described in Chapter 4. The waves are measured before and over the obstacle, at $7m$ and $9m$ from the wave maker flap, respectively. Lamb's formulation has been proven to be able to capture wave propagation as long the incident depth is large, which suits our experiments. Meanwhile, the Marshall and Naghdi model works only for finite depths, capturing deeper propagation depths. The data will allow us to analyse the effects of wave propagation and shed light on the possible effects on a turbine deployment after a bathymetric rise.

5.2.1 Wave propagation over an obstacle with a constant length and variable depth

No tank obstruction

The first set of experiments, using the periods defined in Table 4.10, a depth of $0.6m$, and positioning the wave probes as described in Figure 4.9, is shown here. The wave evolution without obstructions is measured in this

section. The mean values and the standard deviation for the waves is shown in Figure 5.14, where data comes from wave probes A and B. The data shows the ratio of the wave height as defined in equation 5.1 for units $T1$ to $T7$, which is also the transmission coefficient as defined by Lamb or Kt when an obstacle is placed under probe B.

$$Ratio = \frac{H_B}{H_A} = Kt \tag{5.1}$$

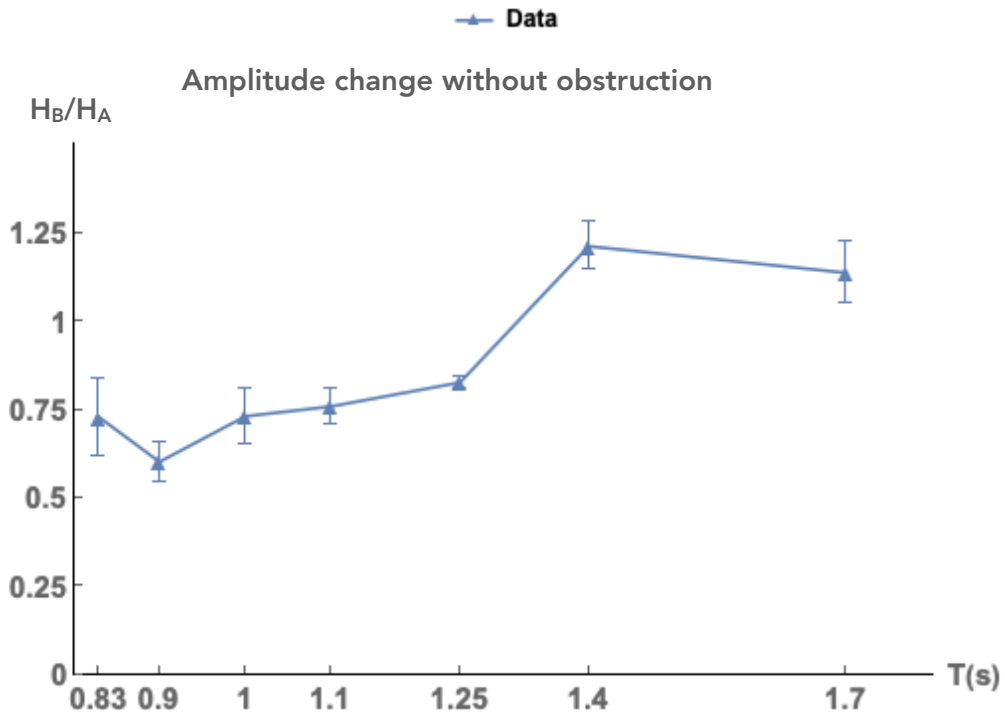

Figure 5.14: Mean wave height ratio defined as the ratio of sensor A and sensor B, and its standard deviation at $7m$ and $9m$ from the wave maker flap respectively.

The data is also shown in Table 5.3, in addition to the standard deviation.

Period	$T1$	$T2$	$T3$	$T4$	$T5$	$T6$	$T7$
H_B/H_A	0.73	0.60	0.73	0.75	0.82	1.21	1.13
σ	±0.11	±0.056	±0.078	±0.05	±0.015	±0.067	±0.087

Table 5.3: Mean wave height ratio and standard deviation, defined as the ratio of heights in sensor A and sensor B at 7m and 9m from the wave maker flap respectively.

It can be observed that, except for the waves tested in T1, the standard deviation is small, which gives us confidence about the measurements of the wave propagation. Data shows a consistent decrease in the wave height from sensor A to sensor B for all small periods, which corresponds to shorter wavelengths. Figure 5.15 shows the same behaviour as wave progress across the tank, but now at the position that corresponds to sensor C, 11m from the wave maker.

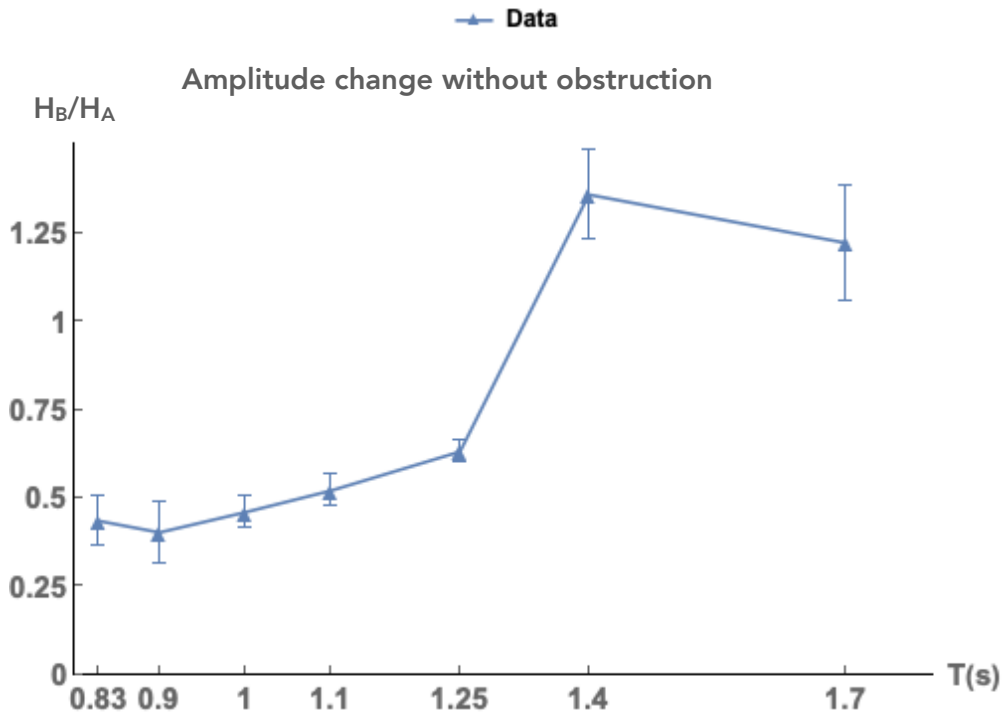

Figure 5.15: Mean wave height ratio defined as the ratio of sensor A and sensor C, and its standard deviation at 7m and 11m from the wave maker flap respectively.

In Figure 5.15, it is observed that for small periods with corresponding wavelengths shorter than 4 times the tank depth, the amplitude keeps decreasing. Meanwhile, larger waves in units T6 and T7 increase their amplitudes, which might be linked to the wave shoaling as is observed in Figure 5.12. The mechanism behind this larger increase in Figure 5.14 from 5.15 will be the compression of the larger wavelengths caused by the bed friction and the proportional increase in their heights. This can be observed by comparing Table 5.3 and Table 5.4.

Period	$T1$	$T2$	$T3$	$T4$	$T5$	$T6$	$T7$
H_C/H_A	0.43	0.40	0.46	0.52	0.63	1.35	1.22
σ	±0.069	±0.086	±0.045	±0.044	±0.03	±0.012	±0.161

Table 5.4: Mean wave height ratio defined as the ratio of sensor A and sensor C at 7m and 9m from the wave maker flap respectively and their standard deviation.

A comparison between the changes at sensors A to B and A to C can be seen in Table 5.5. The table shows the percentage of increase or decrease of the wave height ratios from A to B first ($7m$ to $9m$ from the wave maker) and then A to C ($9m$ to $11m$ from the wave maker).

Period	$T1$	$T2$	$T3$	$T4$	$T5$	$T6$	$T7$
H_B/H_A	-27%	-40%	-28%	-25%	-18%	21%	13%
H_C/H_A	-67%	-60%	-64%	-48%	-47%	35%	22%

Table 5.5: Decrease or increase in the mean wave height values from sensor A to B and A to C ($7m$ to 9m and $7m$ to $11m$ respectively).

Mean values with tank obstructions

Before addressing graphically the comparison between the theories of Lamb and Marshall-Naghdi and the experimental data, it will be helpful to pause to consider the summary of the mean values for all the experiments. Table 5.6 shows the mean values of the wave height ratios as defined by equation 5.1. The data includes the standard deviation for all experiments, with obstructions equal to 1/6, 2/6, and 1/2 in the tank's depth, measuring the wave height changes from wave probe A to wave probe B.

The data in Table 5.6 shows an increase in the wave height ratios as the obstruction increases for waves in the range $T1$ to $T5$, with the exception of $T3$. Data for larger waves show a poorly defined progression and it is scattered. An increase is observed with an obstruction of 1/6. When the obstruction of 2/6 of the original depth is placed in the tank for both larger periods $T6$ and $T7$, Kt is lower. Data for the obstruction of 2/6 of the

original depth, however, shows a larger variation, which could account for the sudden decrease.

Periods	$T1$	$T2$	$T3$	$T4$	$T5$	$T6$	$T7$
0	0.73±0.11	0.60±0.06	0.73±0.08	0.76±0.05	0.82±0.02	1.21±0.07	1.14±0.06
Kt(1/6)	0.60±0.16	0.63±0.13	0.83±0.33	0.86±0.09	0.84±0.02	1.31±0.07	1.22±0.15
Kt(2/6)	0.74±0.08	0.61±0.06	0.73±0.03	0.81±0.05	0.84±0.05	1.16±0.12	1.19±0.26
Kt(1/2)	0.76±0.05	0.62±0.07	0.71±0.04	0.95±0.07	0.87±0.02	1.20±0.08	1.21±0.08

Table 5.6: Data showing the mean coefficient of transmission Kt defined as the ratio of the wave heights. The data shows the mean value and the standard deviation for an obstruction in the wave tank of 1/6, 2/6, and 3/6 its original depth, defined here as 1/2, using a regular obstacle at 9m from the wave maker with a constant length.

Tank obstruction of 1/6 of the original depth

Measurements for when an obstacle obstructs 1/6 of the tank depth are shown in Figure 5.16. The image shows the increase of the transmission coefficient defined as the ratio of the transmitted amplitude, which can also be defined as the ratio of the wave heights, as in equation 5.1. The data shows a substantial increase in the wave height for larger periods $T6$ and $T7$ as Kt is greater than 1 (1.14 and 1.21 respectively). The shorter periods ($T1$ to $T5$) also show a slight increase in the amplitude compared to the experiments with no obstruction except for $T1$.

It is observed that large scattering in the data occurs at the shortest and largest period, the latter corresponding to the largest wavelength, which is the shallowest experiment for the obstruction of 1/6 of the original tank's depth. In the last case, it is possible that an increase in the energy transferred into the harmonics is causing this large scatter.

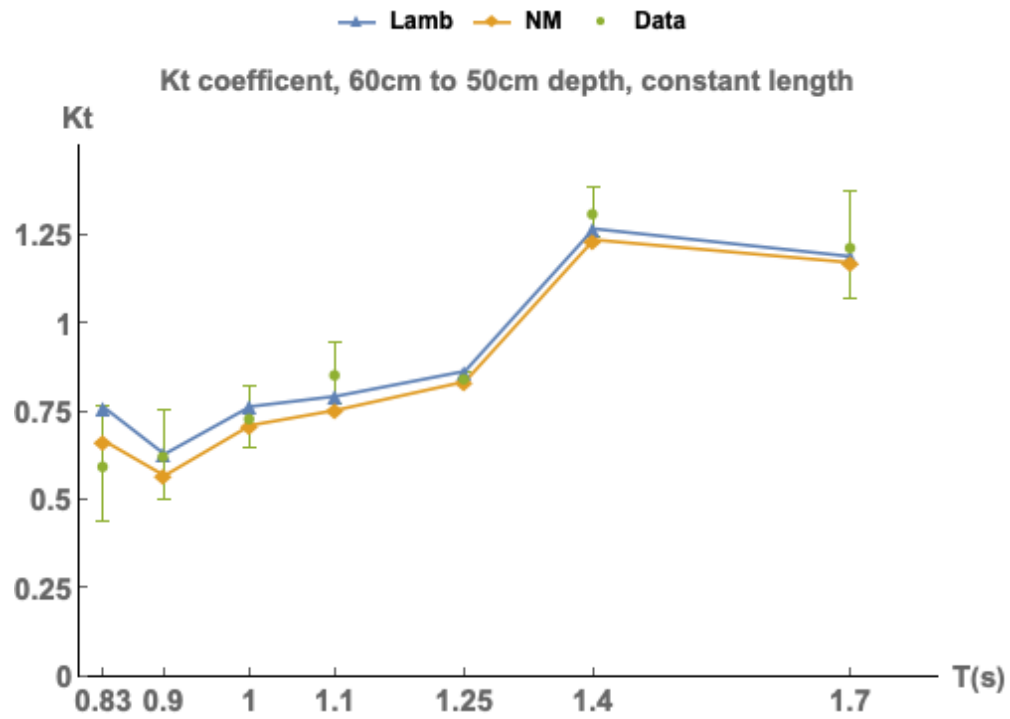

Figure 5.16: The wave height ratio Ht/Hi also defined as At/Ai=Kt for a wave propagating over an obstacle of 10cm height in a wave tank with 60cm water depth, keeping the length constant at 10cm.

Tank obstruction of 2/6 of the original depth

Wave height measurements using an obstruction of 2/6 of the tank's original depth show how the experimental data and predicted values for the Lamb and Naghdi and Marshall formulation maintain good agreement, as seen in Figure 5.17. However, it is observed that scatter in the data grows for the larger periods $T6$ and $T7$.

In this case, the periods show a larger data variation from the experiments without any obstruction, as shown in the standard deviation in Table 5.6. Again, $T7$ and $T6$ represent the largest waves, which are now at shallower waters compared to the previous experiment, with the obstruction of 1/6 of the original tank's depth. The periods and data scatter strengthen the idea of harmonics interfering with the wave measurements as the experiments move to shallower water regimes, even if these are kept at larger depths than those tested by past researchers. Lamb's theory starts to overpredict the values for the transmission coefficient Kt. However, it is

observed in Table 5.6 that all coefficients for this experiment are mostly bounded between being smaller than the case where there is an obstruction of 1/6 and larger than a wave propagating without any obstruction.

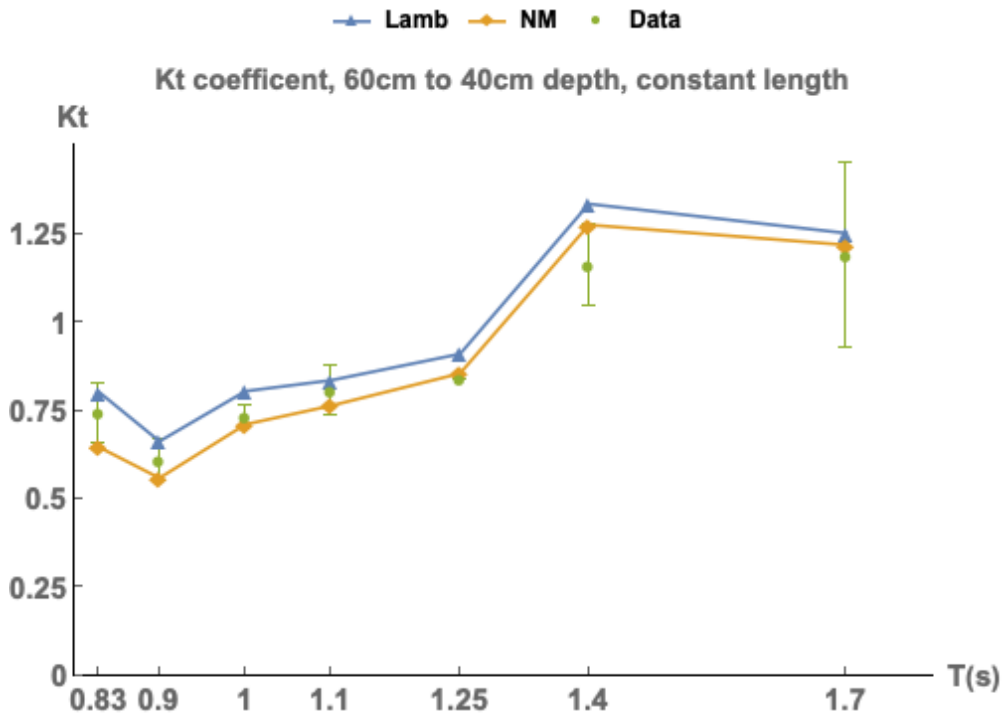

Figure 5.17: The wave height ratio Ht/Hi also defined as At/Ai=Kt for a wave propagating over an obstacle of 20cm height in a wave tank with 60cm water depth, keeping the length constant at 10cm.

Tank obstruction of 1/2 of the original depth

The last measurements for an obstacle with varying depth were made by obstructing half of its original depth. The tank obstruction is the largest for all experiments and, as is also shown in Table 5.6, the amplitudes for almost all periods suggest again an increase against the case without any obstruction, as shown in Figure 5.18. However, values do not follow a natural progression as the author expected. Mean values for all periods are not considerably larger than the values for obstruction of 1/6 of the tank's original depth, and the data scatter shows a smaller or similar range than the data for the obstruction of 1/6, seen in Table 5.6. The mean values are smaller for the largest periods using an obstruction of 2/6 of the original depth, which again will correspond with the larger wavelengths and

shallower cases where the depth ratios h/λ are 0.018 and 0.084 respectively. Further commentary on the possibility of harmonics, given the depth conditions for 2/6 and 1/2, is offered at the end of this chapter.

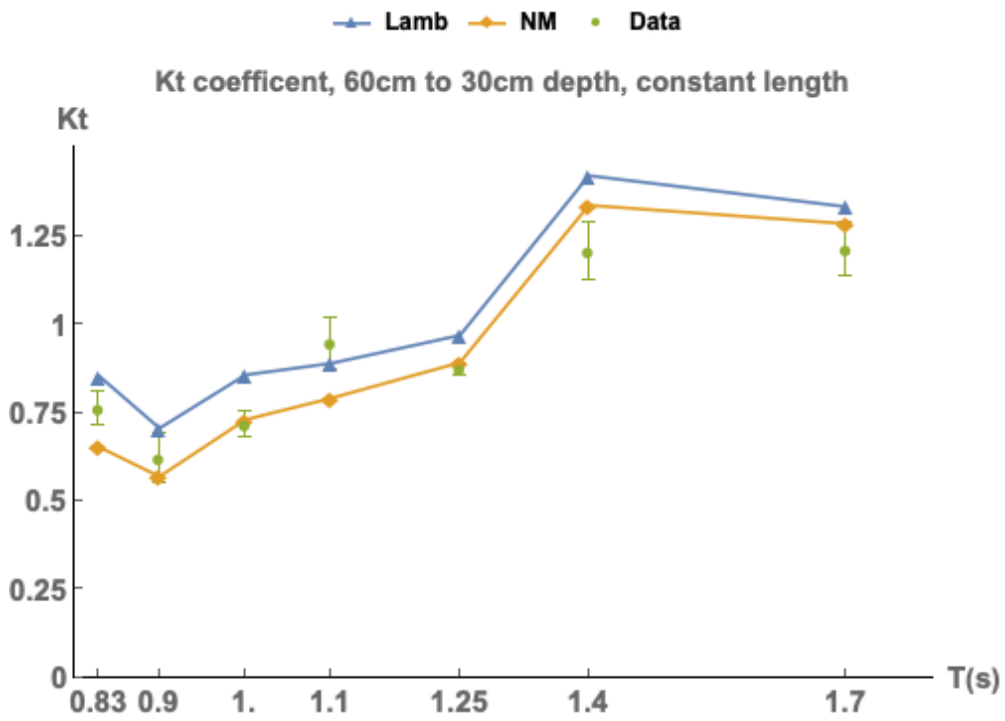

Figure 5.18: The wave height ratio Ht/Hi also defined as At/Ai=Kt for a wave propagating over an obstacle of 30cm height in a wave tank with 60cm water depth, keeping the length constant (10cm).

It is also observed that, as the experiment occurs at the shallower obstacle, higher harmonics might be presented, perhaps causing a large data variation, although the opposite might suggest otherwise.

5.2.2 Wave propagation over an obstacle with constant depth and variable length

Further experiments were made to try to capture the possible effects caused by changes in the obstacle length on the waves propagating over it. In these cases, the obstacle was kept at a constant depth of 50cm causing an obstruction of 1/6 of the original 60cm depth. The obstacle length changed from 10cm to 20cm and 30cm respectively.

The experiments try to capture the possible effects of the obstacle when its length, rather than its depth, changes.

The experiments follow the same arrangement described in Chapter 4. However a slight change was made, as the wave probes were positioned at the mid part of the obstacle length, placing them at 7.05m, 7.1m, and 7.15m (for lengths of 10cm, 20cm, and 30cm respectively). Measurements also include the wave heights at 11m from the wave maker, propagated after the obstruction. Tables 5.7 and 5.8 show the variation of the transmission coefficient over the obstruction and after the obstruction at 11m from the submerged obstacle. They offer a summary before the figures are introduced.

Table 5.7 shows the waves propagated after the obstacle. It is observed how most of the coefficients of transmission show a decrease in the wave amplitudes after the obstacle for periods in the range $T1$ to $T5$. However, the trend is not consistent for $T1$, which is the only wave that transitions from deep water to transitional waters over the obstacle.

Period	$T1$	$T2$	$T3$	$T4$	$T5$	$T6$	$T7$
0	0.44±0.07	0.40±0.09	0.46±0.05	0.52±0.04	0.63±0.03	1.36±0.13	1.22±0.16
Kt(1/6)	0.48±0.13	0.35±0.08	0.7±0.5	0.65±0.08	0.71±0.03	1.5±0.14	1.29±0.30
Kt(2/6)	0.6±0.9	0.3±0.04	0.40±0.01	0.5±0.04	0.5±0.05	1.53±0.13	1.40±0.18
Kt(1/2)	0.71±0.13	0.47±0.05	0.6±0.07	0.75±0.01	0.67±0.01	1.5±0.13	1.49±0.23

Table 5.7: Data showing the coefficient if transmission is defined as the ratio of the wave heights or the amplitudes by Lamb. The data shows the mean value and the standard deviation for an obstruction of 1/6 of the tank depth, meanwhile the length of the obstruction changes from 10cm to 20cm and finally 30cm and the case without any obstruction. The data corresponds to the waves propagated after the obstacle at 11m from the wave maker.

The values that contradict the decreasing trend in $T1$ for an obstacle with 20cm length or Kt(2/6) and 30cm length or Kt(1/2) also show a larger data variation, which is observed in Figures 5.17 and 5.18. In Table 5.8 it is also observed that, for an obstacle of twice the original length, values are lower than for an obstacle of three times the original depth in the case of periods in the range $T2$ to $T5$ which cover transitional waters. With smaller

wavelengths than $T6$ and $T7$, this reduction can be as large as 60% of the original value without an obstacle.

Period	$T1$	$T2$	$T3$	$T4$	$T5$	$T6$	$T7$
0	0.73±0.11	0.60±0.06	0.73±0.08	0.76±0.05	0.83±0.02	1.21±0.13	1.14±0.16
Kt(1/6)	0.60±0.16	0.63±0.13	0.83±0.33	0.86±0.09	0.84±0.2	1.31±0.07	1.22±0.15
Kt(2/6)	0.43±0.04	0.39±0.04	0.42±0.01	0.53±0.04	0.5±0.05	1.12±0.04	1.08±0.07
Kt(1/2)	0.75±0.1	0.67±0.04	0.72±0.07	0.93±0.02	0.82±0.02	1.24±0.04	1.40±0.08

Table 5.8: Data showing the coefficient if transmission is defined as the ratio of the wave heights or the amplitudes by Lamb. The data shows the mean value and the standard deviation for an obstruction of 1/6 of the tank depth, meanwhile the length of the obstruction changes from 10cm to 20cm and 30cm. The data corresponds to the waves propagated over the obstacle at 9m from the wave maker.

It is possible that waves tracked could have passed energy to higher harmonics and the amplitude of the original wave could have been greatly affected. However, the progression of all mean values remains the same comparing the waves without any obstacle in the first row of Tables 5.7 and 5.8, all waves from $T1$ to $T5$ show a smaller amplitude after the obstacle than over it, the contrary is true for all mean values of the waves in $T6$ to $T7$.

Tank obstruction of 1/6 of the original depth with a length of 20cm

For an obstruction with twice the original length, the transmission coefficients drop dramatically for the waves in the range of shorter periods $T1$ to $T5$. In some cases, the drop is almost 60% of the mean value for waves propagating without an obstacle. The drop does not present a large variation in the values, and the theory does not point to the dependence of the transmission coefficient on the obstacle length. Due to the values, no theory appears to follow the wave behaviour since none incorporates the obstacle length and transitional water depths, as shown in Figure 5.19 for waves over the obstacle. The waves released after the obstacle are shown in Figure 5.20 where a small increase in the mean values for the wave coefficients of transmission is observed.

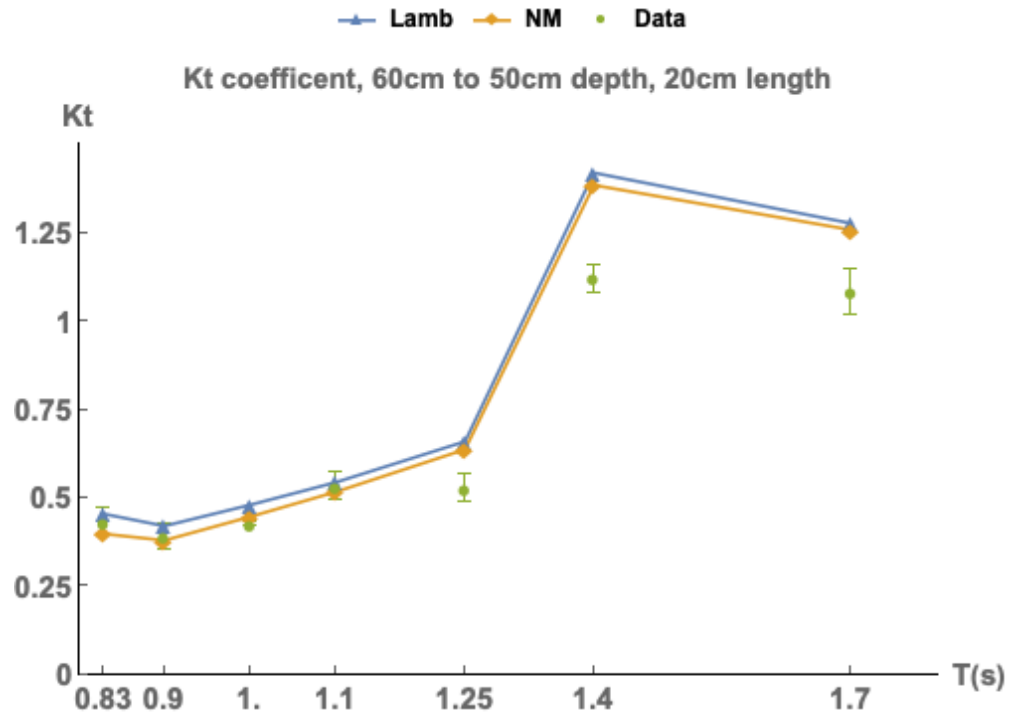

Figure 5.19: The mean wave height ratio Ht/Hi is also defined as At/Ai=Kt for a wave propagating over an obstacle of 10cm height in a wave tank with 60cm water depth, having a length of 20cm. This data collects mean values over the obstacle at 9m from the wave maker.

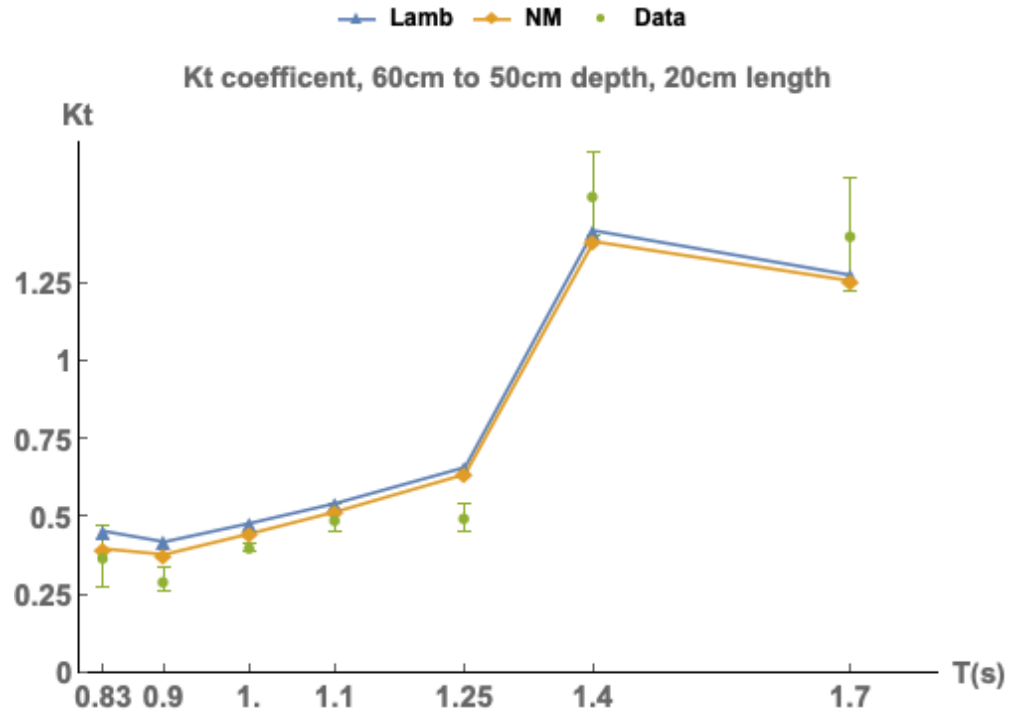

Figure 5.20: The mean wave height ratio Ht/Hi is also defined as At/Ai=Kt for a wave propagating over an obstacle of 10cm height in a wave tank with 60cm water depth, having a length of 20cm. This data collects mean values over the obstacle at 11m from the wave maker.

It could be expected mean values would be larger over the obstacle rather than after it, but this is not the case, as shown in Tables 5.7 and 5.8. In general, the data for an obstacle of twice the original length does not present a valuable conclusion as to how the length could change the coefficients of transmission, but it does shed light on a possible dependency on the wavelength, which is not addressed by other authors.

Theories predict a lower value for the transmission than was obtained experimentally after the obstacle, and the contrary is true over the obstacle for the larger waves in the period range $T6$ to $T7$.

Tank obstruction of 1/6 of the original depth with a length of 30cm

For our next case, the obstacle length was increased to 30cm and the depth over the obstacle was kept at 50cm. In both cases, the waves that are transmitted grow compared to the data for an obstacle that has a smaller length of 20cm for both sensors B and C, at 9m over the obstacle and 11m after the obstacle respectively.

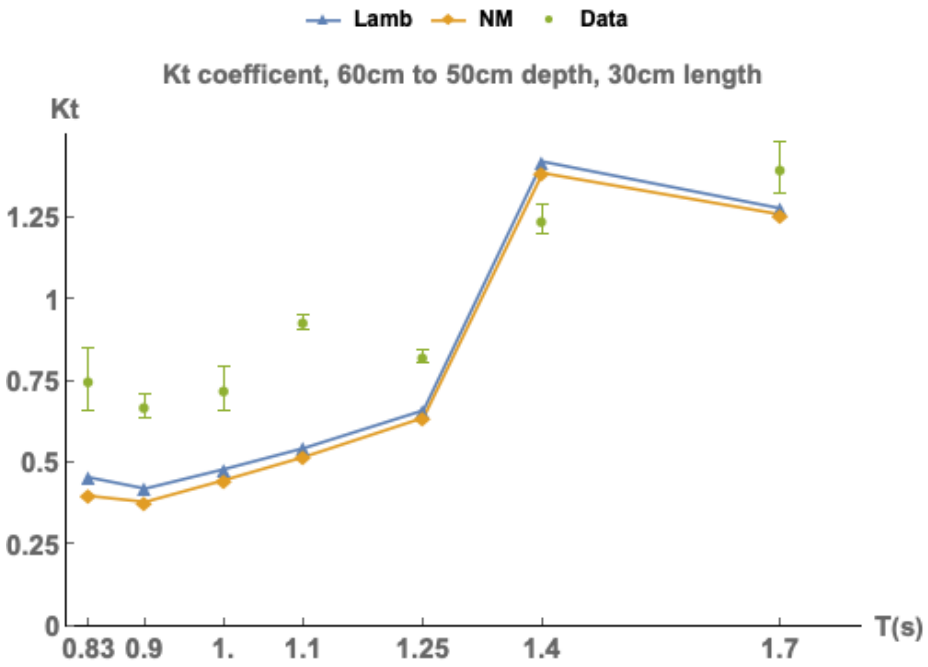

Figure 5.21: The mean wave height ratio Ht/Hi is also defined as $At/Ai{=}Kt$ for a wave propagating over an obstacle of 10cm height in a wave tank with 60cm water depth, having a length of 30cm. This data collects mean values over the obstacle at 9m from the wave maker.

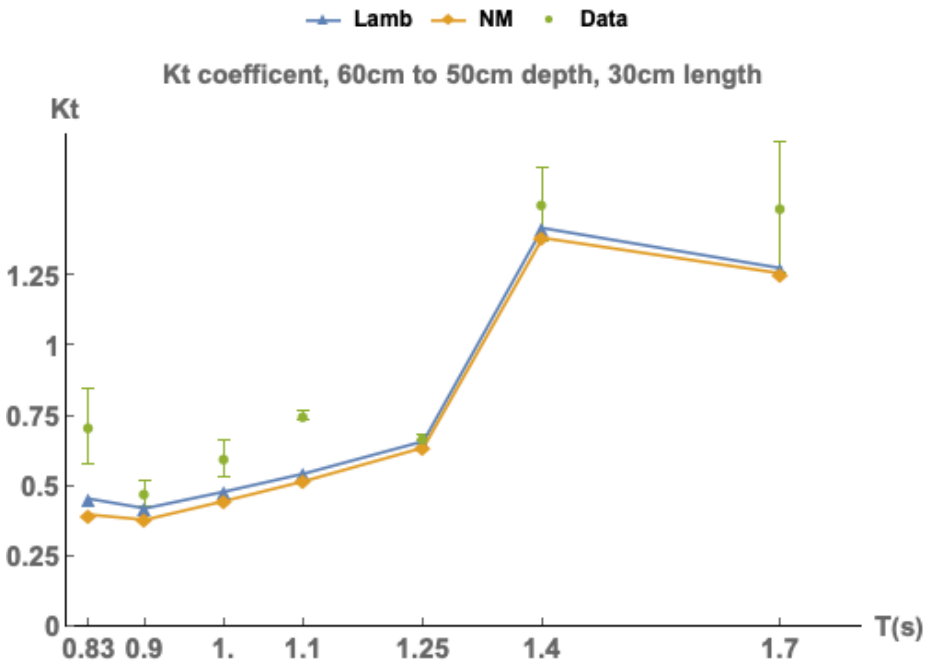

Figure 5.22: The mean wave height ratio Ht/Hi also defined as $At/Ai{=}Kt$ for a wave propagating over an obstacle of 10cm height in a wave tank with 60cm water depth, having a length of 30cm. This data collects mean values over the obstacle at 9m from the wave maker.

Observing the values in Figures 5.21 and 5.22, for an obstacle with 3 times the original length, waves crests offer scattered values when compared to expectations. In the plots of this section, a decrease in the coefficient for waves around the period $T2$ occurs. The behaviour does not appear in the models; however, it corresponds to the limit where the waves are large enough to interact with the bottom of the tank $\lambda/2{>}h$. It is probable the decrease and the depth-to-wavelength ratio are related. More experimentation on this transition between depth regimes might be needed to have a better-defined conclusion.

5.3 Wave velocity and wavelength anomalies

Just as the wave heights were followed, the respective wavelengths of each wave were measured. The method presented here can not substitute the amplitude measurement as abnormalities in the wave shapes will produce values with deviations that could be considerably different from the expected ones. The value, however, can help us to understand the

processes that waves go through after any obstruction and the possible effects this can have on the waves propagated over and after the obstacle, which in turn would affect any tidal device along the wave perturbation path.

No tank obstruction

The mean values for the approximate wavelength measurements and their deviation are shown in Table 5.9 for sensors A, B, and C at $7m$, $9m$, and $11m$ from the wave maker respectively. The data, including the standard deviation for each experimental unit from $T1$ to $T7$, shows how the wavelengths change from sensor A to sensor C. The evolution of the waves shows how waves in the range $T1$ to $T5$ increase their length as they propagate across the tank. If we observe this and relate it to the data presented in Tables 5.7 and 5.8 in the first row, which represents the amplitude propagation without an obstacle, it becomes evident that the mean value for amplitude decrease for waves in the range $T1$ to $T5$ is consistent with the detection of an increase in the wavelength of the waves for those same waves. As shown in Table 5.9, it is also noticeable how the increase in the waves' amplitudes as signalled by the mean values for the experiments in $T6$ and $T7$, and this is accompanied by a decrease in the wavelengths for the same waves from sensor A to C.

Unit	$\lambda(m)$, Sensor A	$\lambda(m)$, Sensor B	$\lambda(m)$, Sensor C
T1	1.2±0.05	1.4±0.09	1.62±0.32
T2	1.31±0.08	1.44±0.1	1.57±0.11
T3	1.7±0.03	1.74±0.04	1.83±0.09
T4	1.97±0.07	1.98±0.07	1.98±0.06
T5	2.19±0.03	2.24±0.01	2.25±0.03
T6	3.63±0.85	3.5±0.91	3.26±0.79
T7	3.88±0.8	3.71±0.72	3.5±0.68

Table 5.9: Mean values for the wavelength detected by the system and its standard deviation for experimental units $T1$ to $T7$. The sensors are located at A=$7m$, B=$9m$, and C=$11m$ from the wave maker respectively.

This suggests that any mechanism that would affect the wave propagation over the tank and does not transfer energy to higher harmonics would be observed in wave parameters, wavelength, and amplitude respectively. The data shows a higher standard deviation for the larger waves, the reason behind which is the existence of very large maximums and minimums.

The data in Table 5.10 that follows the wave crests and calculates the averaged velocity as the waves pass from sensor A to B and then B to C reveals how the waves evolve without any obstruction. Data shows how waves above units $T2$, reduce their velocity as they move along. This is significant as the waves between $T1$ and $T2$ have a mean value of $1.2m$ and $1.31m$. The wavelength data means this wave propagation occurs in deep waters or transitional waters with large depth. It is expected shoaling will occur for waves larger than $T2$, which is evident for all waves from $T3$ to $T7$. It also suggests very strongly that the larger changes in the wavelengths for the mean values in Table 5.11 in units $T1$ and $T2$ are related to this velocity change. The same can be observed for the waves from $T3$ to $T7$, where the decrease in velocity corresponds with the data for the wavelengths, as they decrease at the same time they are detected to slow down from sensor A to sensor B. However, data does not appear to follow the same progression for $T3$.

Unit	$V(m/s)$, sensor A-B	$V(m/s)$, sensor B-C
$T1$	1.38±0.03	1.51±0.05
$T2$	1.43±0.04	1.53±0.04
$T3$	1.69±0.04	1.58±0.5
$T4$	1.77±0.03	1.67±0.02
$T5$	1.83±0.02	1.76±0.01
$T6$	2.05±0.12	2.0±0.11
$T7$	2.10±0.16	2.05±0.13

Table 5.10: Averaged velocity between sensors A-B and B-C without any obstruction in the tank.

Tank obstruction of 1/6 of the original depth and constant length

The mean values for the changes in the wavelengths and the velocities are given in Tables 5.11 and 5.12. The data shows how the waves for the periods $T1$ to $T5$ deform in such a way that data shows an increase in the wavelength, but the same increase is detected without any obstacle. The comparison between the data with an obstacle shows how the mean value of the wavelength decreases as the waves cross the obstacle, which could be linked to wave deformation and compression.

The decrease can be observed when comparing the waves near or in deep water regimes such as in units $T1$ and $T2$. Without any obstruction, the waves appear to increase their lengths by 25% and 16% for $T1$ and $T2$ respectively. However, if an obstacle is placed in the tank, these values are reduced to 22% and 11% respectively, compared to Table 5.10. In general, for all experimental units, $T1$ to $T5$, lengths appear to decrease but larger waves appear to show changes of less than 5% with respect to the case without any obstacle.

Units	$\lambda(m)$, sensor A	$\lambda(m)$, sensor B	$\lambda(m)$, sensor C
$T1$	1.13±0.19	1.27±0.16	1.46±0.15
$T2$	1.31±0.17	1.40±0.11	1,48±0.1
$T3$	1.58±0.049	1.68±0.12	1.76±0.18
$T4$	1.82±0.053	1.89±0.07	1.96±0.08
$T5$	2.17±0.01	2.26±0.05	2.36±0.02
$T6$	3.48±0.7	3.2±0.64	2.83±0.49
$T7$	2.39±0.54	2.9±0.5	3.44±0.38

Table 5.11: Wavelengths detected by the system as the waves propagate on the tank. The detections were made at sensor A, sensor B, and sensor C, which are at $7m$, $9m$, and $11m$ respectively. This for an obstacle at $50cm$ depth and with $10cm$ length.

For larger wavelengths the case is different: values for the units $T6$ ad $T7$ show opposite behaviours. The system detects some extreme waves which mean for the experiments in $T6$ the detected wavelength decreases

by around 19% with a single obstruction, which is a larger value than the 11% without any obstruction. Values for $T7$ are the opposite, showing an apparent increase in their wavelengths. Table 5.12 shows data for the velocities which possess more uniform results. Following the individual crests, it shows a consistent increase in the velocity after the waves cross the obstacle. This is probably related to the waves entering deeper waters after crossing the obstacle.

Units	$v(m/s)$, sensor A-B	$v(m/s)$, sensor B-C
$T1$	1.3±0/2	1.45±0/07
$T2$	1.41±0/18	1.51±0.03
$T3$	1.58±0.03	1.6±0.06
$T4$	1.65±0.03	1.69±0.03
$T5$	1.80±0.02	1.81±0.01
$T6$	2.09±0.11	1.88±0.09
$T7$	1.21±0.07	1.96±0.1

Table 5.12: Velocity tracked by the system as the waves propagate in the tank. The detections were made at sensor A, sensor B, and sensor C, which are at $7m$, $9m$ and $11m$ respectively. This for an obstacle at 50cm depth and with $10cm$ length.

The data is more consistent than the approximated length of the waves, at least for waves with smaller wavelengths. Larger wavelengths, $T6$ and $T7$, show again a very large standard deviation, also in the cases with shallower depths. The graphical comparison between the wavelength calculated by the system while tracking the wave shape for an obstacle of $10cm$ length and a depth of $50cm$ and the experiment without obstruction is shown in Figures 5.22 and 5.23 for sensors B and C respectively.

For the waves passing over the obstruction in sensor B in Figure 5.23, lengths start to decrease slightly for very large wavelengths compared to the case without any obstruction, at least for waves with lengths larger than 4 times the tank depth. These waves correspond to waves in the units $T6$ and $T7$. The decrease in the large wavelengths shows a correlation with the increase in the mean value for the coefficient of transmission at sensor B in

Table 5.11. Implying a compression of the larger waves. Moreover, data showing abrupt decreases in the detected wavelength after the obstacle in Figure 5.24 can also be linked back to larger increases in the amplitude in the waves in Table 5.9 in larger periods.

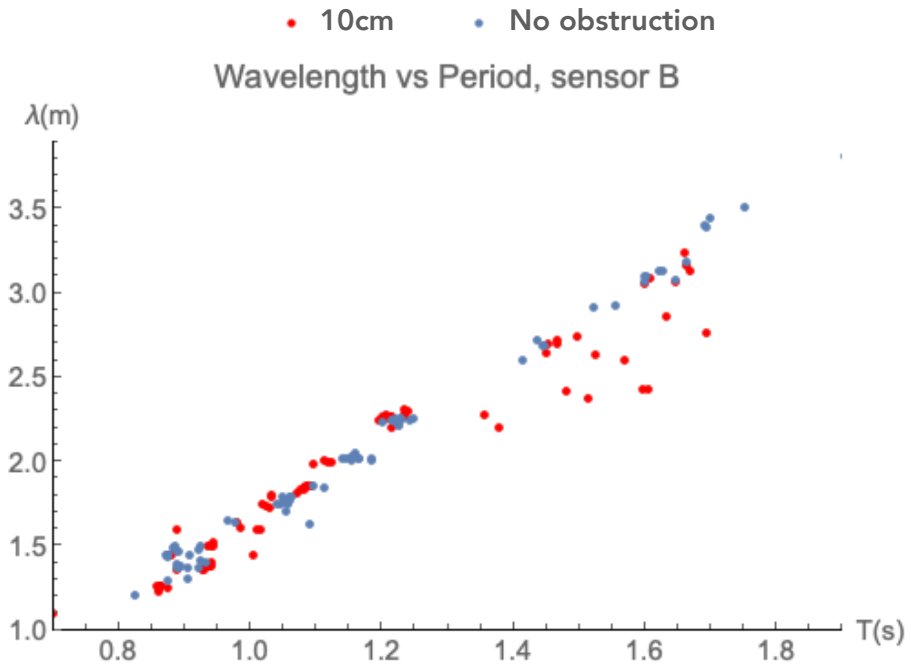

Figure 5.23: The detected wavelength for the waves tested using an obstruction of 10cm in both height and length and at 9m from the wave maker.

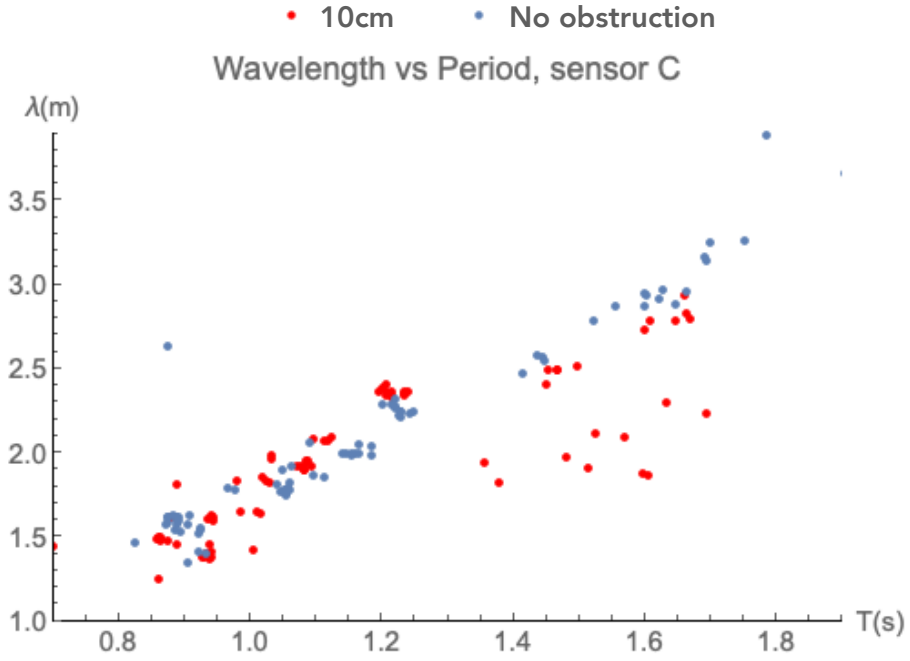

Figure 5.24: The detected wavelength for the waves tested using an obstruction of 10cm in both height and length and at 11m from the wave maker.

The comparison for the velocities shows the same trend in Figures 5.25 and 5.26 for sensors B and C respectively.

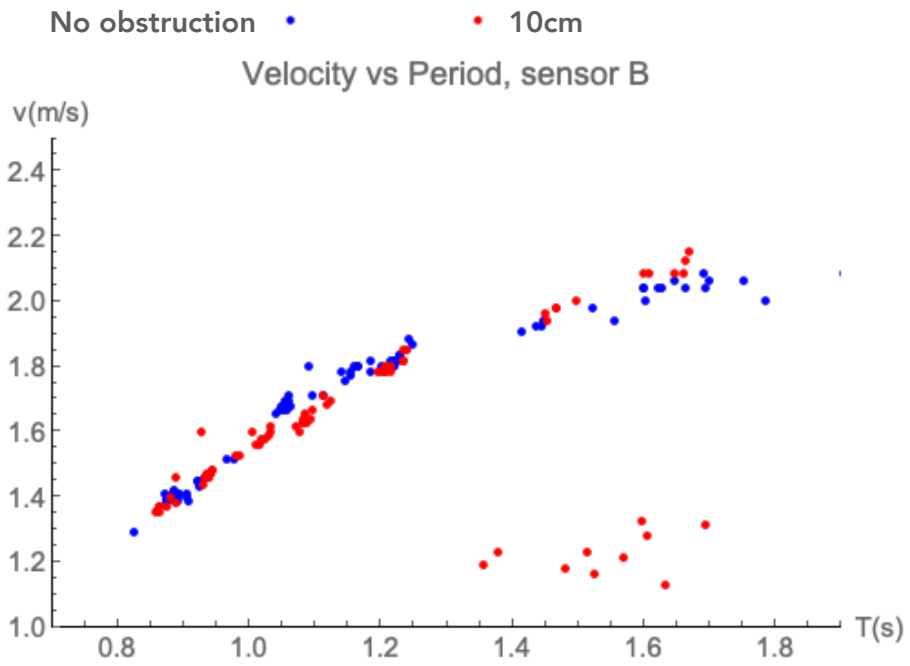

Figure 5.25: The tracked velocity for the waves tested using an obstruction of 10cm in both height and length and at 9m from the wave maker, in sensor B position.

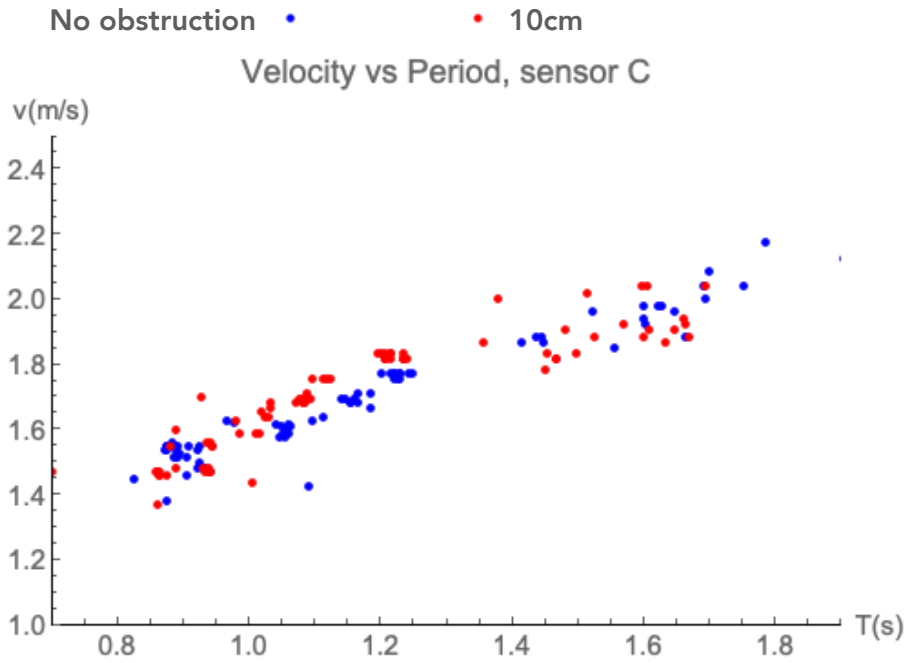

Figure 5.26: The tracked velocity for the waves tested using an obstruction of 10cm in both height and length, and at 11m from the wave maker, in sensor C position.

In sensor B several anomalies are detected with velocities lower than normal, by almost 40% in some cases. All of them belong to the range with

larger wavelengths and shallower propagation depths. This large deviation can be related to a failure in the sensor. The velocities tracked after the obstruction show a more consistent, less dispersed pattern. However, results show smaller velocities for waves in sensor C after the obstacle vs the case with an obstacle, which matches with the slightly smaller wavelengths for the waves in sensor C in Figure 5.23. If we look at Table 5.9 where the wave heights are shown, it also corresponds to an increase in the wave height. Figure 5.23 also shows that for waves below T=1.25s, which corresponds to T5, waves have a slight increase in the velocity between sensors B and C. It can be also observed how wavelengths appear to increase by the same length of the tank in Figure 5.24. This is observed for all but the shortest waves in the experiment.

A comparison of the wavelength predicted by the theory proposed here and that of Marshall and Naghdi is also shown in Figure 5.27.

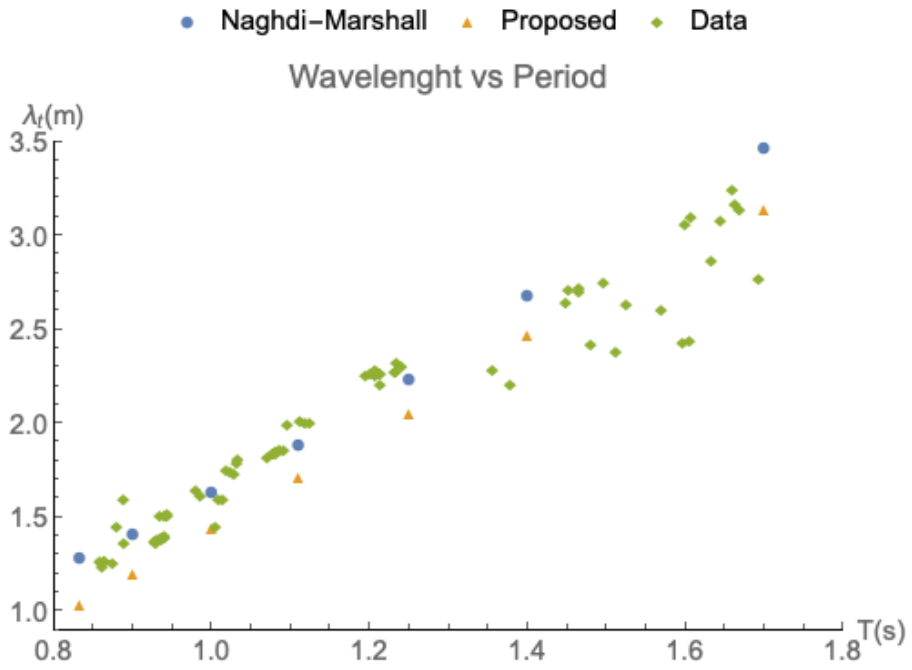

Figure 5.27: Comparison for the wavelengths predicted with the theory proposed, Naghdi-Marshall, and the experimental data.

This shows how the finite depth water theory, in blue, predicts values closer to the ones obtained in the experiment than the simpler formulation introduced in Chapter 3.

Tank obstruction of 2/6 and 1/2 of the original depth and constant length

The second and third round of experiments includes an obstruction of 2/6 and 1/2 of the original depth, leaving a depth over the obstacle of 40cm and 30cm respectively. The obstacle maintains the same length of 10cm in both cases. The mean values for the wavelength values as they propagate along the tank are given in the Appendix, section F. The plots of both experiments are shown here. The data for these experiments shows no sensible variation for the detected wavelengths over the obstacle at sensor B, over the obstruction. However, small increases in the detected length appear in Figure 5.28 for waves with shorter periods, in transitional water depths. The same happens for some waves in Figure 5.30 when the obstruction is half of the original depth.

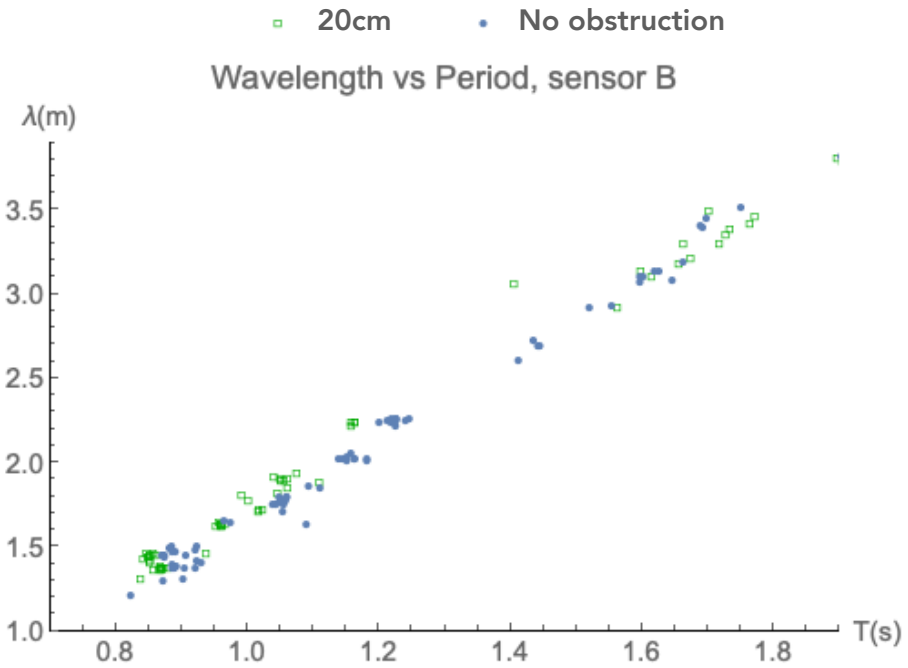

Figure 5.28: The detected wavelength for the waves tested using an obstruction of 20cm height and 10cm length at 9m from the wave maker, compared to a case without obstruction at sensor B, which corresponds to a depth of 60cm.

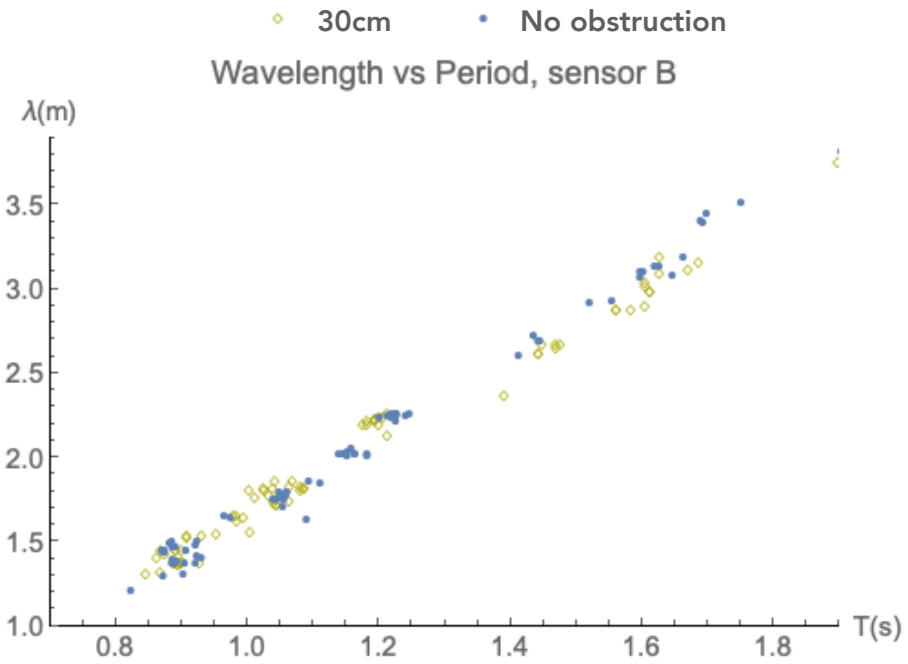

Figure 5.29: The detected wavelength for the waves tested using an obstruction of 30cm height and 10cm length at 9m from the wave maker. This is compared to a case without obstruction at sensor B, which corresponds to a depth of 60cm.

However, waves released after the obstruction in Figures 5.30 and 5.31 lengths of smaller waves increase in some cases more than 10%.

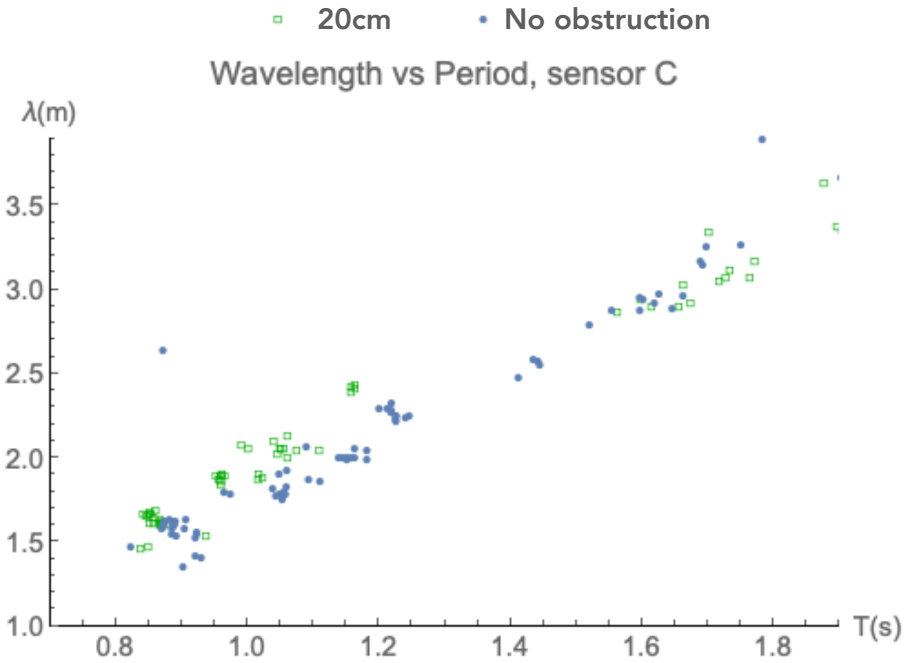

Figure 5.30: The detected wavelength for the waves tested using an obstruction of 20cm height and 10cm length at 11m from the wave maker. This is compared to a case without obstruction at sensor B, which corresponds to a depth of 60cm.

Fi
l=

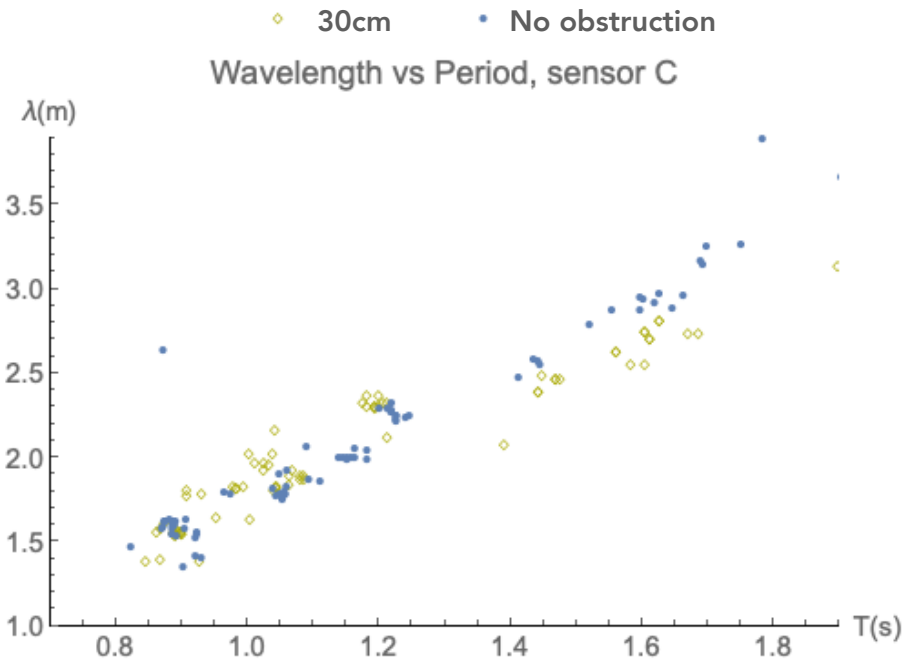

Figure 5.31: The detected wavelength for the waves tested using an obstruction of 30cm height and 10cm length at 11m from the wave maker. This is compared to a case without obstruction at sensor B, which corresponds to a depth of 60cm.

The disturbances created by the obstruction are more evident after they are released after the obstacle, as shown in Figure 5.32.

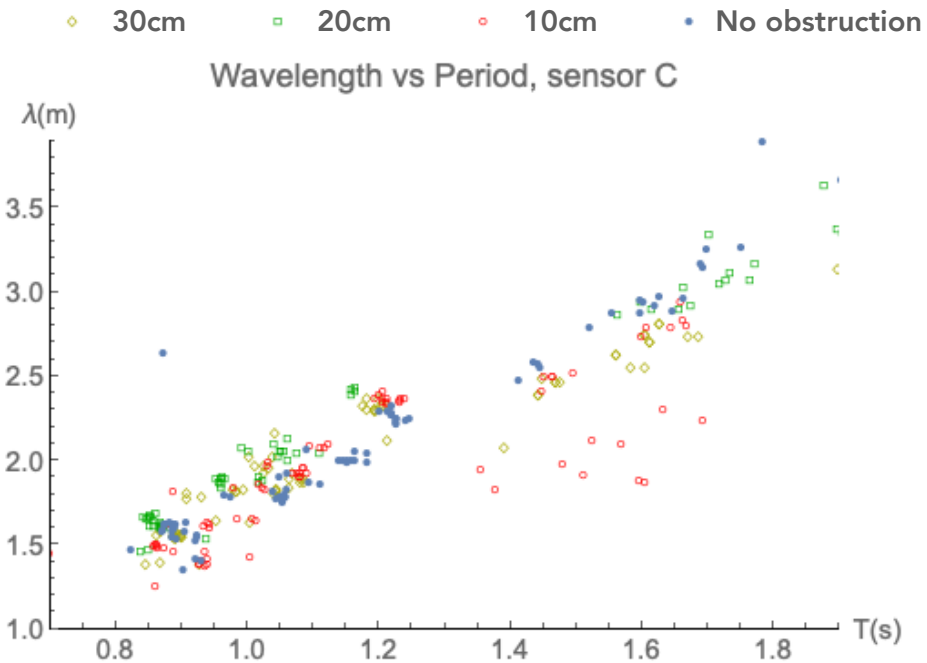

Figure 5.32: The detected wavelength for all the waves tested using an obstruction of 30cm-20cm-10cm height and 10cm length at 11m from the wave maker.

In the last figure, it is observed how for experiments with obstructions of 2/6 and 1/2 of the original tank depth, the length detected appears to increase after the obstacle. This is at least true for periods below 1.3s which correspond to experimental units $T1$ to $T5$. The difference between the detected lengths for obstructions of 2/6 and 1/2 of the tank's original depth has no more than 10% of variation from its mean value in Tables F.3 and F.4 in the Appendix, section F. The same is true for the length detected over the obstacle in Tables F.1 and F.2.

The tracked velocities are shown for the wave crests in Figure 5.33 for sensor B over the obstacle, and after the obstacle for sensor C in Figure 5.34. The results show all experiments as a general comparison. With the wavelengths for obstructions with 2/6 and 1/2 of the original depth, small changes are observed for shorter periods and larger periods in transitional depths, with waves slowing down compared to the case without any obstruction in blue, having 60cm depth at sensor B.

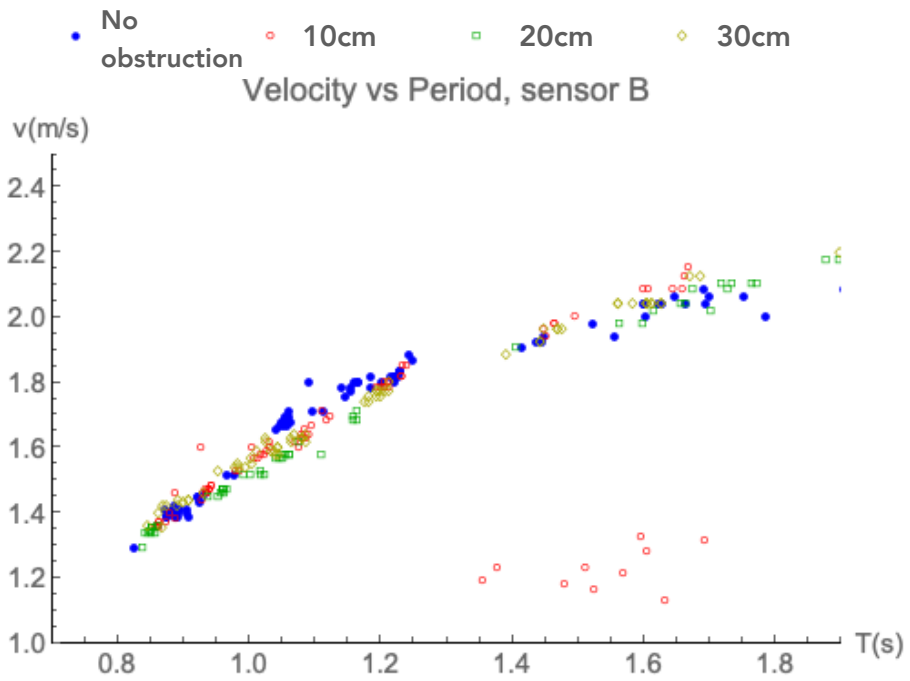

Figure 5.33: The tracked velocity for all the waves tested using an obstruction of 30cm, 20cm, 10cm height and 10cm length compared to a case without obstruction at a depth of 60cm on sensor B and 9m from the wave maker.

The variation is still small, with decreases no larger than 15% of the values compared to a case without obstruction in the most extreme values. However, waves released after the obstruction show a larger impact on the crests moving along the tank. Figure 5.34, showing the waves released after the obstruction, demonstrates how smaller waves appear to gain speed after they cross the obstacle. In some cases, this speed up is as large as 20% of the velocity for waves without any obstruction, for cases $T3$ to $T5$, which correspond to periods between 1.0s and 1.25s.

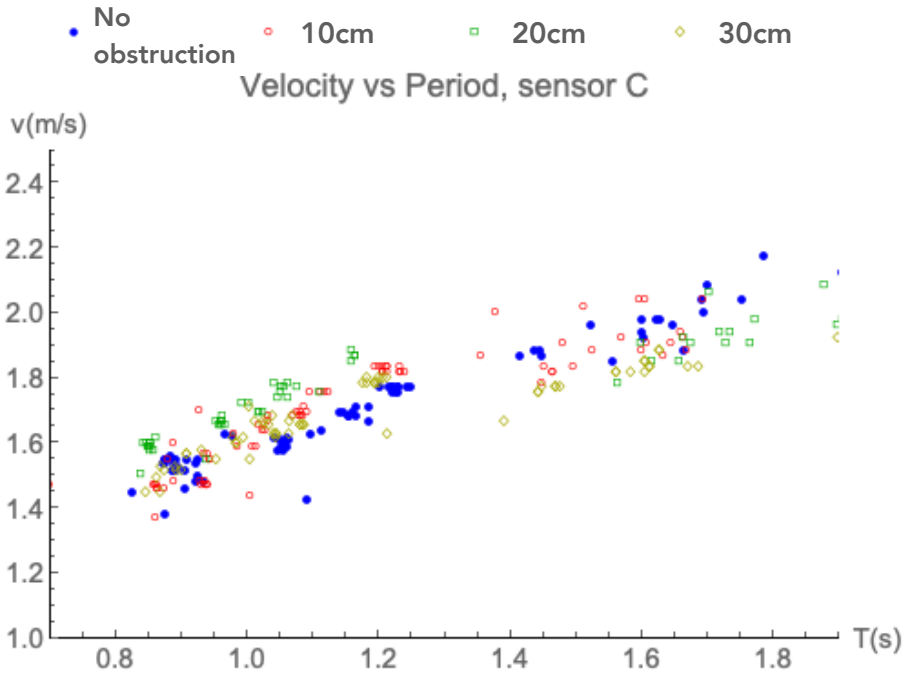

Figure 5.34: The tracked velocity for all the waves tested using an obstruction of 30cm, 20cm, 10cm height and 10cm length compared to a case without obstruction, with a depth of 60cm on sensor C and 11m from the wave maker.

The changes in the length of the waves are then compared to the theories of Naghdi and Marshall and the one proposed here in Figures 5.35 and 5.36, again for obstructions of 2/6 and 1/2 of the original tank depth.

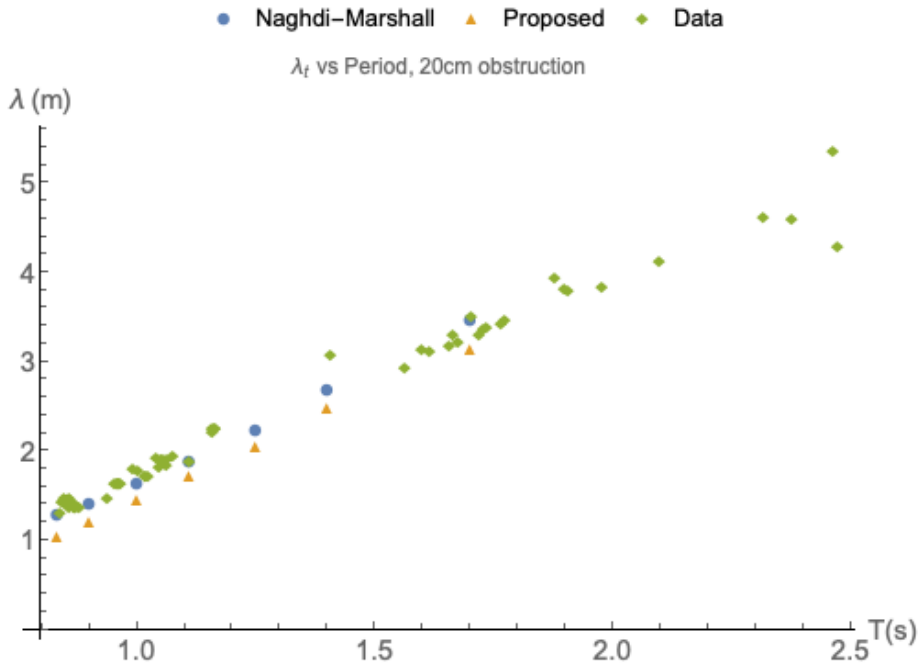

Figure 5.35: Length detected by the system for all waves after crossing an obstruction of 20cm height and 10cm length, compared to the formulation of Naghdi-Marshall and the one proposed here. Measurements are made by sensor B at 9m from the wave maker.

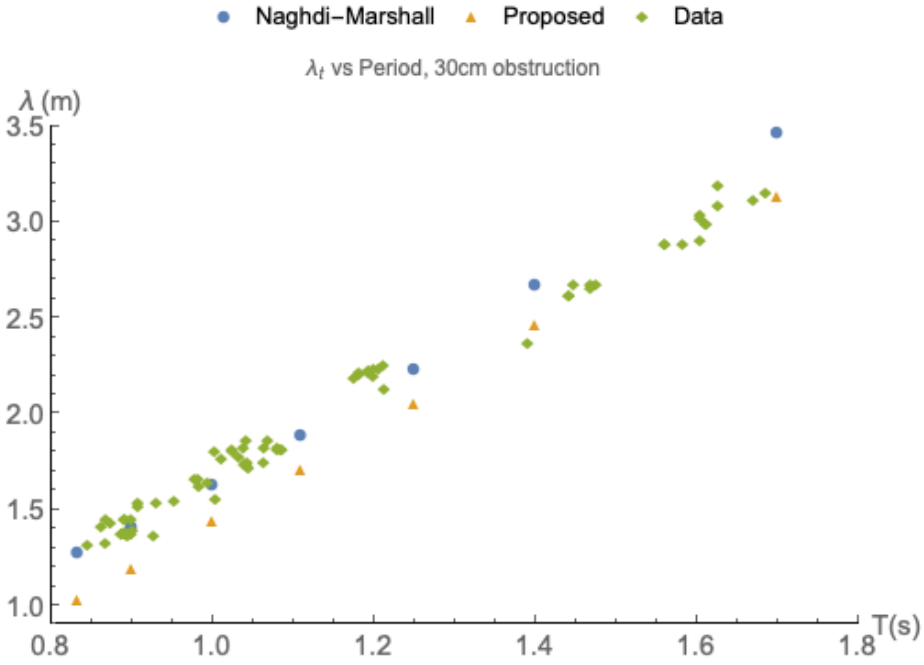

Figure 5.36: Length detected by the system for all waves after crossing an obstruction of 30cm height and 10cm length, compared to the formulation of Naghdi-Marshall and the one proposed here. Measurements are made by sensor B at 9m from the wave maker.

In both cases, the Naghdi and Marshall formulation offers a better result than the one proposed here. The finite depth equation, which uses a

more robust and complete mathematical theory than assumptions of linearity, appears to behave better for waves in units $T1$ to $T5$. Meanwhile, the formulation proposed would approach closer to the values as the length and period increase, leading to shallower water cases. This could be a result of the formulation using the simpler approach taken by Lamb, rather than a full linearisation of the finite depth water conditions in Naghdi and Marshall.

Tank obstruction of 1/6 of the original depth with a varying length

The last set of experiments where the length of the obstacle was altered to measure the wave properties after propagating over them are shown in the next figures. Neither Naghdi and Marshall or the theory proposed takes into account the length of the obstacle producing the obstruction and these measurements are not included in this section. However, the detected lengths and the tracked velocities of the crests as they move in the tank are shown here. Figures 5.37 and 5.38 show the effects of the obstructions in sensor B as they increase their length from $10cm$ to $30cm$, having a constant depth of $10cm$ or 1/6 of the original tank depth.

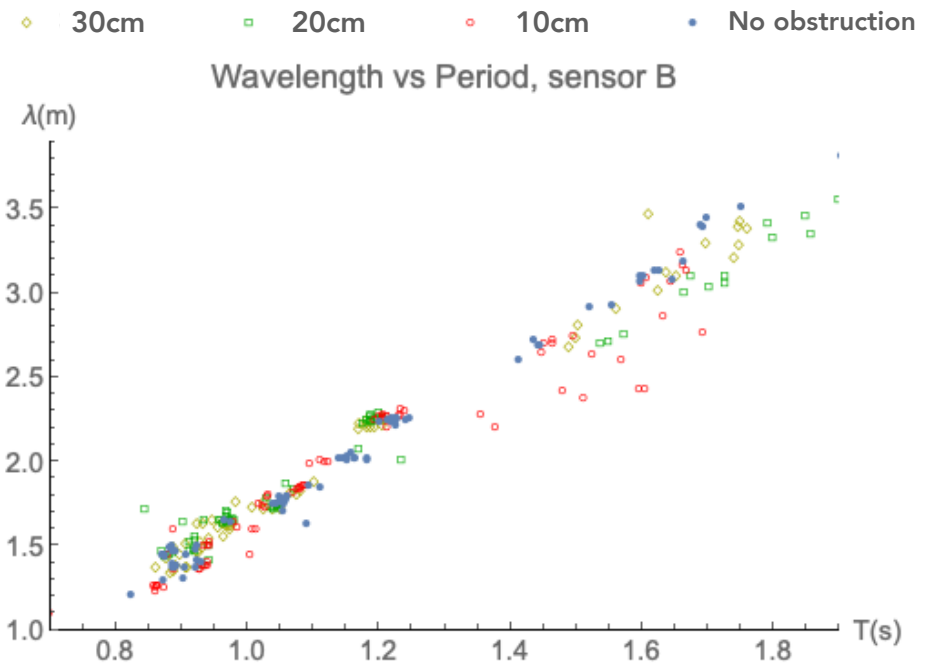

Figure 5.37: The detected wavelength for all the waves tested using an obstruction of an increasing length $10cm$ to $30cm$ and a height of $10cm$ at $9m$ from the wave maker.

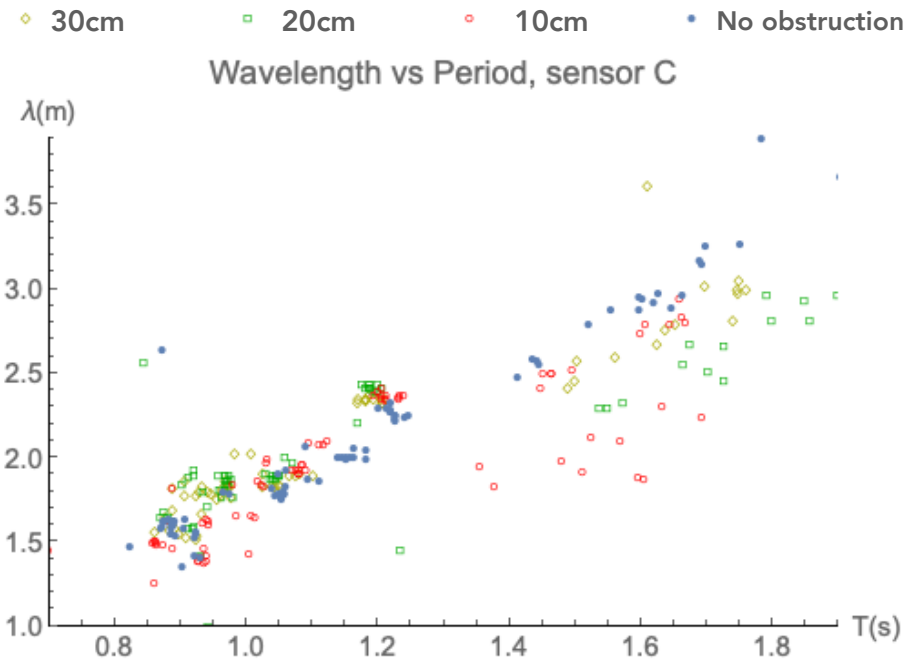

Figure 5.38: The detected wavelength for all the waves tested using an obstruction of an increasing length from 10cm to 30cm and height of 10cm at 11m from the wave maker.

The detected wavelengths for all waves tracked do not show a large change for small waves in units $T1$ to $T5$, however a stronger length deformation appears for larger waves when the obstacle length is 20cm. In the most extreme cases, this deformation reaches above 10% of the original value, if we observe values for the waves moving without any obstruction in Figure 5.38.

Length deformation is drastically increased for the obstruction of 20cm length, as shown in Figure 5.38. Here, the deformation for large waves on units $T6$ and $T7$ reaches 25% of the length measured without any obstruction. The origin of this mechanism is unknown, as the deformation caused by an obstacle of 30cm in length does not reach these higher values, with extreme cases around 10% of the original length for waves released after the obstacle. The effect is the same, however, causing a decrease in the detected length for larger waves in units $T6$ and $T7$. Changes for smaller waves in units $T1$ to $T5$ show an increase in their length for the waves

released after the obstacle, but no clear mechanism that links the length to the length deformation emerges.

Plots for the velocities are shown in Figures 5.39 and 5.40.

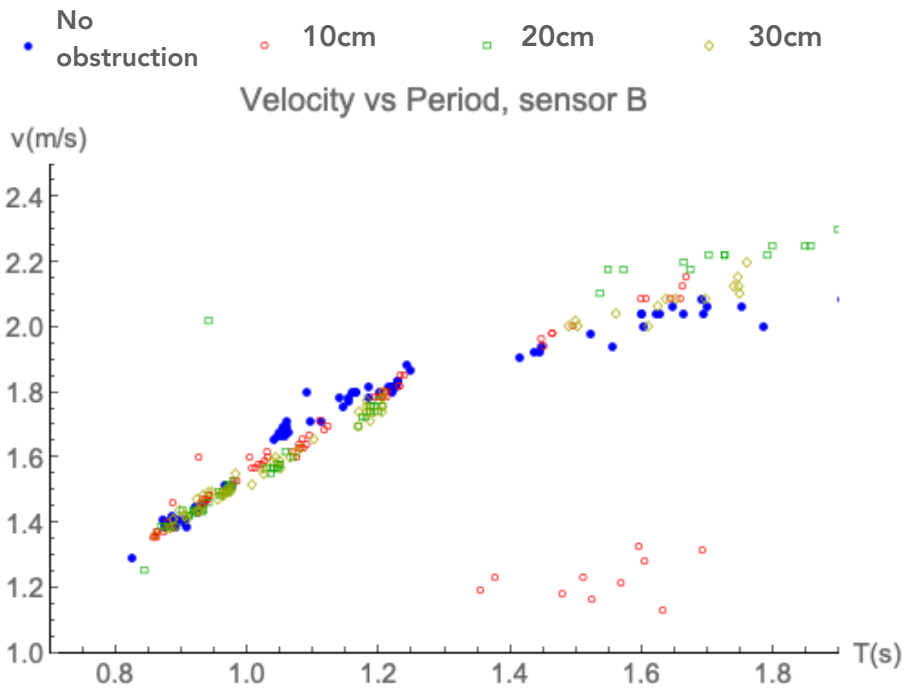

Figure 5.39: The tracked velocities for all the waves tested using an obstruction of an increasing length from 10cm to 30cm and a height of 10cm at 9.1m from the wave maker.

The tracked velocities for waves with shorter periods at the position of sensor B do not show a conclusive behaviour either. However, waves with larger periods on units $T6$ and $T7$ show a larger velocity while arriving at sensor B, which in this case is located at the centre of the obstruction of $20cm$ length. This is somewhat counterintuitive as the wavelengths show a deformation, indicating a decrease in length.

The waves released after the obstacle on the other side follow the pattern shown for the detected lengths when the obstruction has $20cm$ length in both the shorter and larger periods. Larger periods show a strong decrease in velocity in sensor C after waves arrive from sensor B. This can be linked to the amplitudes shown in Figure 5.18 where the wave amplitudes are sensibly higher than the ones over the obstacle in Figure 5.20 for this same experiment with a length of $20cm$.

The reason behind this strong effect for a specific length is unclear.

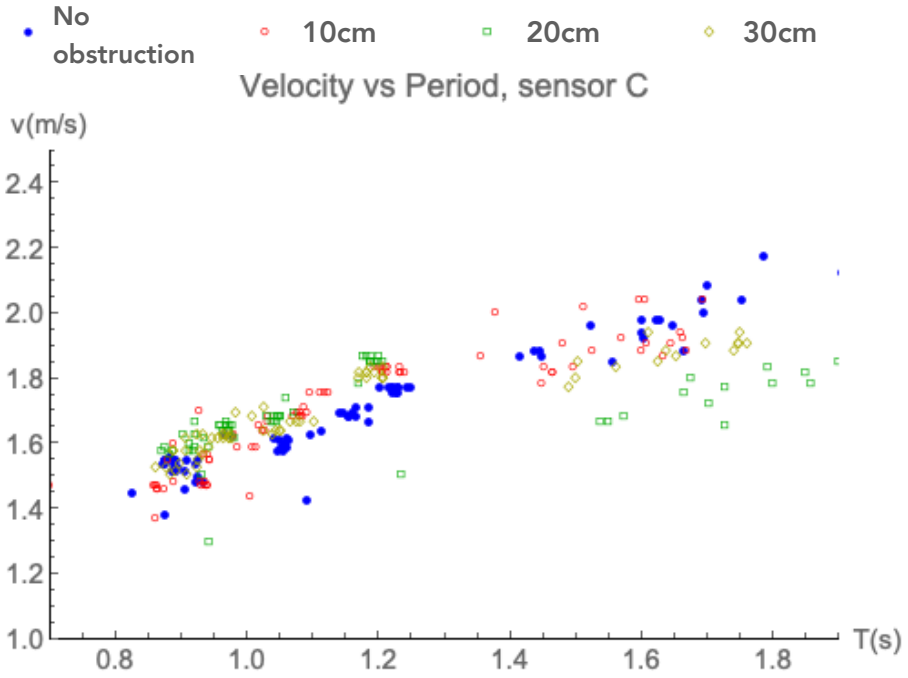

Figure 5.40: The tracked velocities for all the waves tested using an obstruction of an increasing length from 10cm to 30cm and height of 10cm at 9.1m from the wave maker.

5.4 Changes in the wave steepness

Another important effect on the wave parameters in the wave tank after propagating over the obstruction is their wave order. The first waves tested in the range of, *T*1 to *T*4, were all initially 2nd order waves.

When no obstacle is placed inside the tank, almost all waves from shorter periods reduce their steepness from 2nd order to 1st order (linear). When obstacles are inside the tank, the waves do not decay to first order. The most notable case is the obstruction of 1/6 of the original depth, where almost 60% of the waves remain in 2nd order for periods in $T2$ and 80% for unit $T1$. This effect only occurs for shorter periods and shorter obstacles. The reason behind this effect is unknown; however, this could be linked to the higher results of Kt for the waves in $T1$ and $T2$ and their depth of propagation in the tank.

5.6 Conclusions

Experiments were carried out to measure the wave propagation over an obstacle and also to validate the suggested formulations. The measured variables were: the wave amplitude, wavelength, and wave velocity of propagation. The experiments in this chapter show how wave frequency can affect the wave transmission as observed by Goring [87], Newmann [70], Jolas [77] and Macagno [74] appear also at wave propagation in deeper water regimes.

First, observation and experimental tests were conducted to observe the natural evolution of a wave train propagating inside the tank. The observations and measurements show an increase in the wave height for the largest waves in $T6$ and $T7$, while the contrary is observed for shorter waves in the range $T1$ to $T4$. The effect could be linked to the natural shoaling in the largest waves, with wavelengths 4 times larger than the depth of the tank. The wavelengths detected appear to react to this behaviour according to what could be expected. As in Figure 5.12, they appear to decrease their values for the largest waves, which then strengthens the idea behind the shoaling of the largest waves inside the tank. For the shortest waves, wavelengths detected appear to increase slightly also, which was not expected, but information for the waves moving inside the tank suggests that wavelength decrease or increase is inversely related to the amplitude of the wave as it moves in the tank, which is reasonable for larger wavelengths.

When obstacles are placed inside the tank, the waves show an increase in their coefficient of transmission for almost all tests, except for waves in the period range of $T3$, and some of the largest waves. The progression in their increase is not as regular as could be expected. It is very possible that this is due to nonlinearities, however the mean values in Table 5.5 show a clear tendency to larger amplitudes after waves propagate over the obstacle. In Table 5.5 it is also observed that for larger waves, $T4$ to $T7$, the increase in the coefficients Kt is stronger as the obstacle minimises its depth, as was observed by Goring [87] in shallower depth regimes. The

increase in the coefficient correlates again to the detected wavelengths in Figures 5.22 and 5.28 for an obstruction of 1/6 and 1/2 of the depth of the tank. This is weaker for an obstruction of 2/6 of the tank's depth in Figure 2.27. This also correlates with Table 5.5 where the Kt coefficient seems to have a weaker increase for the case of an obstruction of 2/6 of the depth of the tank. This relates directly to the formulation of Naghdi and Marshall and the one proposed here, where the transmitted amplitude is a function of the incident frequency as the wavelength is a function of the frequency itself through the dispersion relationship.

For the cases where the obstacle length varies and its depth is kept constant, the coefficient of transmission appears to increase to larger values than the ones where the depth decreases at a constant length. If we take the mean values, the increases in the coefficient of transmission for a variation in the depth of the obstruction do not increase their values more than 5% compared to waves where no obstacle is placed inside the tank. For waves where the obstacle is lower, but with an increase in the length, Kt increases to more than 10% in the most extreme cases in Table 5.6. for waves released after the obstacle. This indicates that the obstacle length might be a very important characteristic to take into account for waves propagating over sudden irregular topographies. An increase in Kt could be related to the increase in the interaction, as the length is larger than for the cases where the obstacle is shorter but shallower.

In general, changes in the wavelength and the velocities of propagation are observed over the obstacle, and larger waves decrease their length and slow down. This is predicted by Naghdi and Marshall theory as well as the formulation proposed here. This phenomenon is known in oceanography as waves crossing into shallower banks will slow down and modify their shape in the shallowest parts of the coast. These observations must however be corroborated using experiments designed specially for these measurements and reducing the errors caused by the wave maker as the detection of the lengths depends on the wave shape and sudden

deformities could result in anomalous values. In reality, amplitude is the best marker to measure.

The changes product of the wave propagation over an obstacle take our future discussion to the possibility of local disturbances in the wave weather that cannot be calculated from local measurements. These could induce changes in the loads felt by marine energy devices even if they are in the same geographical area.

The validation of the theories for wave propagation also shows a good agreement with Lamb and Naghdi and Marshall being closely accurate for the case of a single obstacle with limited length in Figure 5.16. However, the formulation of Naghdi and Marshall is more accurate in the two following cases where the depth of the obstruction increases in Figures 5.17 and 5.18.

The validation of the simple analytical formulation proposed here and the one proposed by Naghdi and Marshall (using the directed fluid sheet theory of Green and Marshall [97] to predict the changes in the incident-transmitted frequency through the changes of the wave number/wavelength) shows how the formulation for finite depths proposed by Naghdi and Marshall is more accurate for almost all cases of wave propagation. In general, the formulation proposed here appears to be more accurate for larger waves in the range $T6$ to $T7$ as shown in Figures 5.27, 5.35, and 5.36.

6 Wave propagation over an obstacle and its effects over a horizontal axis tidal turbine

The models used for tidal stream devices use wave models for transitional and deep waters. As established, the oscillations in the velocities caused by the waves at these depths will induce unsteady effects and time-varying forces over the tidal turbine. The unsteady effects will be transmitted to the blades and transmission will occur through its hydrodynamical interactions with the streamflow. The unsteady effect then will have a long-standing impact on the fatigue process of these tidal stream devices. Because any obstruction in the wave path will modify the wave shape and properties, as we saw in the last chapter, it is essential to know how these changes will affect the unsteady loads felt by the tidal turbine. Observations made in Chapter 4 show a slight increase in the wave height for waves in transitional waters. The increase in the amplitude will have a direct impact on the waves, as explained in Chapter 2. An increase in wave amplitude will lead to an increase in the velocity components and, as result, a direct effect on the turbine loads could be expected. The period shift suggested by the wavelength changes will also modify the load cycles.

Furthermore, changes in the velocity field as a result of an obstruction in the wave propagation path will lead to changes in the amplitudes and periods, which could in turn produce a different mechanical response for a tidal turbine. As these changes will occur only for larger waves that can reach the bottom, it is expected swells would be the main drivers behind these changes in the wave properties after the obstruction.

The apparent change in the incident wavelength λ_i, which is a function of the incident period T_i for the depths before the obstacle (x<0), shows a variation of less than 10% after the jump vicinity. We can say this is located x=0. This is explained in relationships 6.1 and 6.2 where λ_t and T_t are

the transmitted periods and transmitted wavelength respectively, x' is the distance after the jump, located at x=0, and σ is the distance after the jump.

$$\left(\lambda_i = f(T_i)_{x<0}\right) < \left(\lambda_t = f(T_t)_{x'}\right) \quad 6.1$$

$$x' = (x > 0) + \sigma \quad 6.2$$

Statements 1 and 2 simply express a distance range after the jump where the conditions discussed in Chapter 4 hold. This is because it is possible larger lengths will see more changes in the wave parameters as they propagate on a large shelf, mostly caused by bed friction. The distance at which this is valid is not explored here as the longest obstacle is approximately only 1/3 of the shortest wavelength for the shortest wave period. The distance σ it is not known but it is assumed to be shorter than λ.

if we look at the changes in the waves in Chapter 4, changes in the wavelength after crossing the obstacle and a variation in the amplitude will proportionally change the components of the wave velocity. The amplitude increase for the larger periods will increase in the horizontal velocity component after the obstruction. Meanwhile, a flow obstruction will change the total velocity component along the horizontal direction z, leading to different flow conditions and loading cycles.

In order to analyse the wave parameters following a regular bathymetric effect on a tidal turbine, two steps are taken.

1. A sensitivity analysis of the numerical model to changes in the period, wave height, depth, and current. The results are then compared to the Nevalainen et al. [36]. The main difference between this analysis and Nevalainen et al.'s is the wave weather, which is composed of a swell-dominated sea. This is in contrast to the mixed sea with steeper waves which corresponds to a wind-dominated sea and also the inclusion of a bathymetric obstruction in the wave propagation, which changes the wave height.

2. A comparison of the torque and thrust over the turbine rotor and a single blade and after the obstacle, taking some wave conditions that are scaled up from those tested in the wave tank.

In the next section and the introduction of the BEMT model, the turbine characteristics and the conditions used to conduct the sensitivity analysis and the simulation are explained in greater depth as their results.

6.1 Blade Element Moment Theory and its dependence on the velocity field

Nevalianen et al. [46] show how the waves' unsteady loads can impact the tidal turbine, affecting the eccentric forces at the shaft and bearing rings. The same loads of the waves will modify the harmonics presented on the axial thrust, as shown by Tantum et al. [45], thus impacting the blade fatigue [43]. It is then assumed that a change in the wave field properties, or the properties of the waves as they cross through some volume of water, will modify the impact on the same turbine characteristics through its mechanical performance. Tidal turbine mechanical performance depends on the hydrodynamics of the rotor and its interaction with changing velocity field U_∞. This will produce deviations in the rotational movements defined by the flows, which is shown in Figure 6.1.

The mechanics behind the transmission of movement to the rotor by the flow can be explained by the rotor-fluid interaction. The incident flow from the turbine's front, or U_∞, will be deflected by the blade in an upward direction, thus producing a reaction in the positive direction of the z-axis. The blade's rotational movement in the positive z-direction will cut the water flow and the upward movement will produce a secondary induced velocity flow U_I perpendicular to U_∞. The geometry requires that the overall velocity flow on the blade will be the geometrical addition of both flows. The apparent velocity of both is named U_A. The fluid velocity, U_A, will be responsible for the lift and drag properties of the turbine blades.

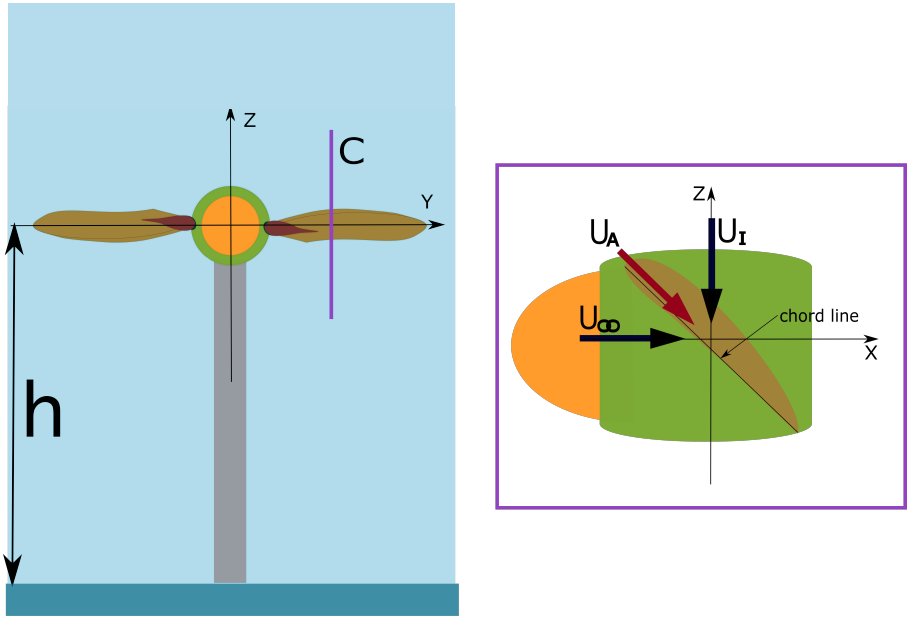

Figure 6.1: Image showing the turbine at a depth h with a cut C on the plane $Y=y_n$, left, and image of the cut, right, showing the velocities of the rotor in a steady state without waves. The right image shows the rotor velocity relationships: U_∞ is the free stream velocity, U_I the induced velocity, and U_A the apparent velocity, which is a result of both U_∞ and U_I.

The lift and drag forces are relevant because they are the main driver behind the turbine hydrodynamic properties. Low drag values in a rotor will decrease the resistance produced by our device to the induced rotary movement. As the turbine rotational velocity depends intrinsically on the flow velocity, the flow components will become important. The changes in the wave velocities will modify the blade's drag and lift, hence the changes in its components will be of significance. The most simple expression of the velocity components in the water column is shown below in equations 6.3 and 6.4. The expression $G(z)$ is a function that depends on the depth.

$$V_x = U_\infty \tag{6.3}$$

$$V_z = U_\infty G(z) \tag{6.4}$$

6.1.1 Torque and thrust of a tidal turbine rotor and their dependence on the wave velocity field using BEMT

The strength of the wave oscillations and their effects on the tidal turbine will depend, as explained in Chapter 2, on the depth at which the

turbine is deployed. The overall magnitude will also be proportional to the incident wave amplitude.

In this chapter, the type of the waves producing perturbations on the field are divided into the following categories:

a) Moderate waves with periods lower than 5s.

b) Moderate waves with periods lower than 7s and higher than 5s.

c) Large waves with periods over 7s.

Turbines facing wave weather conditions b and c will show moderate to large unsteady forces acting over its components at transitional depths, which will affect the mechanical torque and thrust. To explain how the waves and flow interact with the rotor torque and thrust, we need to explain the fluid-rotor interaction and the method known as BEMT.

The extended fluid-rotor system from Figure 1.2 in Chapter 1, describing the rotor interaction with the fluid flow, can also be seen below in Figure 6.2.

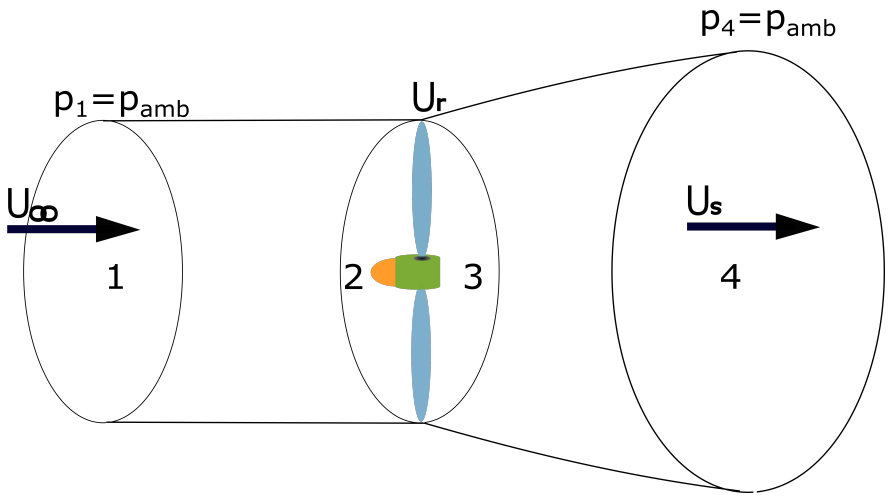

Figure 6.2: Relationship between the velocities in the BEMT formulation. $U_\infty = U(z)$ and its value corresponds to the stream velocity at a certain depth z, U_s being the wake velocity and U_r the velocity in the rotor area.

The figure shows that the stream velocities are also linked to the drop of pressure in the fluid stream. The system in Figure 6.2 can be analysed as an energy exchange by the flow-turbine system in 4 steps. The upstream

rotor's flow (1), the flow around the rotor (2-3), and the downstream rotor's flow (4). Physically, the flow will lose part of its incident velocity U_∞ and will be released to the stream as velocity U_s after the rotor interaction. Bernoulli's law states that equating conditions 1-2 and 3-4 allows us to equate conditions 1 to 4 in equation 6.5:

$$p_2 - p_3 = \frac{1}{2}\rho(U_\infty^2 - U_s^2) \tag{6.5}$$

The energy exchange is equal to the fluid velocity change across the area swept by the rotor A_r. The result of this is that equation 6.5 can be expressed as equation 6.6.

$$\triangle\, p = \frac{1}{2}\rho(U_\infty^2 - U_s^2) \tag{6.6}$$

The other mechanism of energy exchange is the mechanical work done by the rotor. The rotor's work must be equal to the mass flow passing through the rotor area per ξ. ξ is a value equal to the velocity loss of the fluid, as this is the vector for the energy exchange. We can say that the variable ξ is a factor a. In the rotor area, U_r must be lower than the incoming fluid velocity U_∞. Expressing this as (U_∞ - aU_∞), where our factor must necessarily be a<1, equation 6.7 is obtained.

$$U_r = U_\infty(1 - a) \tag{6.7}$$

Expressing the mass flow in the rotor we obtain equation 6.8.

$$\dot{m} = \rho U_r A_r \tag{6.8}$$

Since there must be a change in the momentum, this would be equal to the mass flow per the velocity change and equation 6.9 is obtained.

$$\Delta\dot{p} = \rho A_r U_r\left(U_\infty - U_s\right) \tag{6.9}$$

Substituting equation 6.7 into equation 6.9 and equating the change in the fluid momentum across the whole rotor to the energy loss, which is linked to a drop of pressure, we then obtain equation 6.10.

$$\frac{1}{2}\rho(U_\infty^2 - U_s^2)A_r = (U_\infty - U_s)\rho A_r U_\infty(1-a) \quad 6.10$$

For U_r to satisfy the relationship in 6.10, it must have a value U_r =(1-2a)U_∞. If we also express the turbine force as the drop in pressure around the rotor as F=(p_2-p_3)A_r, we can use it in expression 6.5 to obtain the turbine's thrust.

$$F_{tr} = 2\rho A_r U_\infty^2 a(1-a) \quad 6.11$$

If we add the rotational momentum of the turbine wake, the notion that A_r is the turbine's sweep area, and we also express the torque of an annular section of the rotor as in Nevalainen [46] and Masters et al. [89], we obtain expressions 6.12 and 6.13.

$$F_{tr} = \left(4\pi\rho U_\infty^2 a(1-a) + (b\Omega_r)^2)rdr\right) \quad 6.12$$

$$F_{tq} = \left(4\pi\rho U_\infty a(1-a)b\Omega_r r^2)\right) rdr \quad 6.13$$

The term Ω_r is the rotational velocity of the turbine and b is the second factor of the BEMT formulation, as defined in equation 6.14. The value w corresponds to the wake angular velocity in equations 6.12 and 6.13, where both are dependent on U_∞.

$$b = \left(\frac{w_s}{\Omega_r}\right) \quad 6.14$$

From Chapters 2 and 3, we know the U_∞=$G(x,y,z,t)$. The function $G(x,y,z,t)$ must be $U(z)$+$V_\varphi(x,y,z,t)$. As the width of the wave trains is assumed to be several magnitudes larger than the other dimensions, we know we can reduce it to $U(z)$+$V_\varphi(x,z,t)$. The functions that add the spatial and temporal variant fields are the wave velocity solutions of the wave equation. As the total rotor torque and thrust will depend on the power delivered by the flow U_∞, the components $V_\varphi(x,z,t)$ will affect it proportionally. The changes discussed in the experimentation section will define a function $V_\varphi(x,z,t)_i$ before the jump and $V_\varphi(x,z,t)_t$ after the jump.

6.1.2 Torque and thrust of a blade and its dependence on the wave velocity field using BEMT

The torque and thrust of the turbine will be equal to the torque and thrust produced by the blade's hydrodynamic responses. The blade hydrodynamics are defined by the incoming flow, as can be seen in Figure 6.1. The forces on the blades will induce drag and lift effects, the values of which depend on the blade shape design, also called the airfoil. The airfoil's geometry requires these forces to be components of the direction of rotation z and the direction of the incident flow U_∞.

In Figure 6.3 we can see the geometrical relationship between the flows and the lift and drag forces. U_r is the velocity at the rotor, but as we stated before, $U_r = U_\infty(1 - a)$. As U_i is aligned with the turbine rotor rotation, then it has the form $U_i = \Omega_r r(1 + b)$. The total velocity will then be $U_A = (U_r^2 + U_i^2)^{1/2}$. The drag and lift forces as shown in Figure 6.3 are caused by the flow, so from Figure 6.3 we can derivate equations 6.15 and 6.16. The angle can be defined by U_∞ and U_i as in equation 6.17, and the total flow will be then the sum of both, giving us equation 6.18.

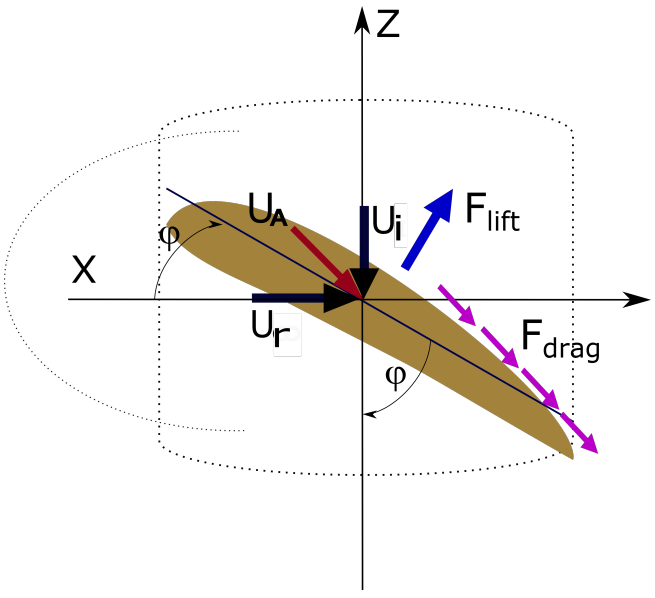

Figure 6.3: Figure showing the induced flow on the rotor rotational direction z and the incoming flow from the current on axis x. The plot has been rotated from figure 1.6.

$$\Sigma F_y = dLSin(\varphi) + dDCos(\varphi) \quad 6.15$$

$$\Sigma F_y = dLCos(\varphi) + dDSin(\varphi) \quad 6.16$$

$$\varphi = Tan^{-1}\frac{U_\infty(1-a)}{\Omega_r r(1-b)} \quad 6.17$$

$$U_A = \sqrt{\left(U_\infty(1-a)\right)^2 + \left(\Omega_r(1+b)\right)^2} \quad 6.18$$

The blade's induced forces in the radial direction (torque) and the forces in the flow direction (thrust) can be expressed in equations 6.19 and 6.20.

$$F_{tr} = B\frac{1}{2}\rho U_A^2 c(C_L Cos(\varphi) + C_D Sin(\varphi))dr \quad 6.19$$

$$F_{tq} = B\frac{1}{2}\rho U_A^2 c(C_L Sin(\varphi) + C_D Cos(\varphi))dr \quad 6.20$$

Here, the Drag and Lift coefficients can be defined as in equations 6.21 and 6.22. Here c is the chord of the blade (the distance from the trailing edge t to the nose of the profile) and L and D are the drag and Lift, where both coefficients are functions of the flow conditions [115].

$$C_l = \frac{L}{(1/2)\rho U_\infty^2 c} \quad 6.21$$

$$C_d = \frac{D}{(1/2)\rho U_\infty^2 c} \quad 6.22$$

The BEMT method equates the thrust and torque expressions for the blade with the overall thrust and torque on the rotor. If then we equate 6.12, 6.13, 19.6, and 20.6, we will obtain two expressions. The expressions are a system of equations with two unknown variables a and b. The equations that result from this can be seen in 6.21 and 6.22, as are also shown in Nevalanien's thesis.

$$\left(4\pi\rho U_\infty^2 a(1-a) + (b\Omega_r)^2)rdr\right) = B\frac{1}{2}\rho U_A^2 c(C_L Cos(\varphi) + C_D Sin(\varphi))dr \quad 6.21$$

$$\left(4\pi\rho U_\infty a(1-a)b\Omega_r r^2)\right) rdr = B\frac{1}{2}\rho U_A^2 c(C_L Sin(\varphi) + C_D Cos(\varphi))dr \quad 6.22$$

The unknowns, a and b, can be solved through iteration methods. However, the stream flow velocity U_∞ is also a function of time in presence of a wave system. As U_∞ is composed also of $G(x,z,t)$, the streamflow will be composed of two additional components, as in equation 6.23.

$$U_{\infty x} = U_{current} + V_{\varphi x} \tag{6.23}$$

The current flow will vary along with the depth of the site as a power function. This is modelled in this work as a 1/7 power law, and then the vertical change in the horizontal velocity will be defined as in equation 6.24.

$$U_{\infty z} = U_{\infty x}\left(\frac{z}{h}\right)^{1/7} + V_{\varphi z} \tag{6.24}$$

The results of inserting 6.21 and 6.22 into the tidal turbine rotor's torque and thrust expressions will result in an oscillatory rotor performance due to the change in the velocity inflow. We can see this in equations 6.25 and 6.26.

$$\left(4\pi\rho(U_{current} + V\varphi_x)^2 a(1-a) + (b\Omega_r)^2)rdr\right) = B\frac{1}{2}\rho U_A^2 c(C_L Cos(\varphi) + C_D Sin(\varphi))dr \tag{6.25}$$

$$\left(4\pi\rho(U_{current} + V\varphi_x)a(1-a)b\Omega_r r^2)\right) rdr = B\frac{1}{2}\rho U_A^2 c(C_L Sin(\varphi) + C_D Cos(\varphi))dr \tag{6.26}$$

The equations 6.25 and 6.26 describe the behaviour of a turbine deployed in the seabed below a depth h_d. If the depth is large enough to not allow local wind spectrums to interact with the tidal device $h_d > (\lambda/2)_{wind}$, then only large wave periods will cause a large oscillation in the torque and thrust below the wind wavelength limit.

6.2 Second order wave model for steeper low amplitude-long waves

The waves modelled here include terms for higher values of non-dimensional heights, hence they are steeper. Steeper waves have larger crests and at non-dimensional depths, reaching amplitude values of 1.5m

and 4.5m for the period ranges between T=7s and T=14s at depths of around 40m.

The experimental section in Chapter 4 and 5 included steeper waves which belong to 2nd order waves. Steeper waves like the ones described in the last paragraph have a higher amplitude. As the waves become steeper, they start to develop non-linear behaviours, also known as weak nonlinearities. To model waves with weak non-linearities, we use the expansion method from Stokes on a parameter called steepness. At this point, equations 7.6 to 11.6 from Chapter 3 are first transformed into non-dimensional equations. The process to transform the expression into dimensionless equations uses a set of transformations, which make every term of the wave equation non-dimensional, as in equations 6.27 to 6.32.

$$x' = xk \tag{6.27}$$

$$z' = zk \tag{6.28}$$

$$\eta' = \eta/a \tag{6.29}$$

$$t' = t/T \tag{6.30}$$

$$C' = \frac{cte}{ag} \tag{6.31}$$

$$\varphi'(x', y', z') = \varphi(xk, yk, zk)\frac{\sigma}{ag} \tag{6.32}$$

Inserting these new terms in the original equations, a product of the factors a and k will appear. The factorisation of the non-dimensional term, defined by the amplitude to wavelength ratio (ak), will modify our original wave equations. The result of this variable change produces a set of non-dimensional modified equations. The parameter, ak, is known as the wave steepness ε and it is used by Stokes in the power expansion model [116-93]. The modified equations can be seen below.

$$\frac{\partial^2\varphi'}{\partial x'^2} + \frac{\partial^2\varphi'}{\partial z'^2} = 0 \tag{6.33}$$

$$\frac{\partial\varphi'}{\partial z'} = 0 \tag{6.34}$$

$$\frac{\partial \eta'}{\partial t'} = Aw' \tag{6.35}$$

$$\frac{\partial \varphi'}{\partial t'} + gz' = C' \tag{6.36}$$

The terms can be expanded in a power series around ε, as in formulation 6.37.

$$\sum \varphi'(x', y', z') = \varphi'(x', y', z')^{(1)} + \varepsilon\varphi'(x', y', z')^{(2)} + +\varepsilon^2\varphi'(x', y', z')^{(3)} \ldots \tag{6.37}$$

The order of expression 6.37 is represented by the powers (1),(2),(3)… (n). The power expansion of the Taylor series needs to be applied to each term of equations 6.33 to 6.36. The produced terms with the same order $\varphi(x',y',z')^n$ are gathered together and the result is a set of equations that represent the steeper wave system. This formulation allows us to represent a steeper swell wave system, expressions for which are shown in equations 6.38 and 6.39:

$$\varphi_{2nd} = \varphi^1 + \varphi^2 \tag{6.38}$$

$$\eta_{2nd} = \eta^1 + \eta^2 \tag{6.39}$$

The terms φ^1 and η^1 are the already known solutions for the linear wave equation that allow us to model long swells on the x ranges chosen for $T7$ to $T4/T3$, while the new terms are the corrections to the linear theory. The corrections allow us to solve second-order Stokes waves. Solutions for these terms are shown below in equations 6.40, 6.41, and 6.42.

$$\varphi^2 = \frac{3ak}{8Coth[kh]}\left(Coth[kh]^2 - 1\right)^2 Cosh[2k(z+h)]Sin[2\theta] \tag{6.40}$$

$$\eta^2 = \frac{1}{4}Coth[kh]\left(3Coth[kh]^2 - 1\right)a^2 kCos[2\theta] \tag{6.41}$$

$$C = \frac{a^2 kg}{2Sinh[2kh]} \tag{6.42}$$

The term θ=(ωt+kx) is the argument of the wave equation as we know it. These terms were introduced in the model of the velocities to represent steeper waves, as in equations 6.43 and 6.44.

$$V_{\varphi z} = \frac{\partial \varphi^1}{\partial z} + \frac{\partial \varphi^2}{\partial z} + U(z) \quad 6.43$$

$$V_{\varphi x} = \frac{\partial \varphi^1}{\partial x} + \frac{\partial \varphi^2}{\partial x} \quad 6.44$$

These terms are then added to represent the flow velocities of second-order waves in our tidal turbine model. The complete terms are annexed in the Appendix, section F.

6.3 Analysis of the effects on a horizontal tidal turbine induced by waves before and after an obstruction

The conclusions from Chapter 5 and the expressions to model wave propagation over an obstacle are used to explore the effects a simplified bathymetry construction will have on the waves and how these changes will modify the forces felt by a tidal turbine

In order to do this, a set of conditions was established and a sensitivity analysis was carried out using the Morris method. The set of variables of study were two sea weather conditions and one geographical construction, with current flow and wave period being the two explored. The geographical constriction refers to an obstruction in the wave propagation, which represents a regular obstacle, as used in Chapter 5 for our experiments. The study seeks to capture changes in the mechanical performance of the turbine when these conditions change without any obstruction and when the waves are affected by an obstruction. This section is divided in the following manner:

- First and foremost, an explanation of the changes to the BEMT model and software used is given in 6.3.1.
- The scaling of the wave trains and the depth conditions are discussed in section 6.3.2.
- The tidal turbine dimensions and details are described in section 6.3.3.

- The Morris sensitivity method is explained in section 6.3.4.
- Results of the analysis are provided in 6.3.5.
- Simulations of a turbine using a scaled-up version of the waves and depths for a limited set of cases are made and results are shown in 6.3.6.

6.3.1 BEMT software

The software used to simulate the tidal turbine mechanical response was a modified version of the BEMT tool developed by the ESRU team at the University of Strathclyde, as documented in Nevalainen's thesis [46]. The in-house software is written in MATLAB™. The software solves the blade and rotor hydrodynamic properties to obtain the turbine's torque and thrust. The tool has been expanded and complemented to integrate several types of wave models and corrections. This software has been validated against experimental and CFD results, achieving good and consistent results produced by wave loads and rotor imbalances, as in Porter et al. [117-94] and Ordonez-Sanchez et al. [118], with some overestimation of forces.

The software capabilities include the solution of unsteady problems and mixed wave spectrums. The wave models that BEMT can solve linear waves in transitional waters and third and fifth-order Stokes waves. To obtain these solutions, the software solves equations 6.25 and 6.26 using an iterative method. The solutions then are applied to different annular sections of a tidal turbine rotor, and the results are integrated to obtain the torque and thrust. The software allows us to modify the current velocity and the blade design parameters, as well as to incorporate tip and hub corrections for the inflow-rotor interaction. Other software add-ons include a user-defined number of blades and variation in the turbine hub height, hub diameter, and blade length. The software runs an iterative process of optimisation based on multiple searches of points over a hyper-surface. Further detail on the BEMT tool is in [46], a link to the ESRU software website is in the Appendix section H.

Parts of this software had to be updated in order to calculate the mechanical torque and thrust of the turbine at suitable depths. Two additions were made:

1. The solutions for infinite depth waters $\lambda/h_d \to 0$ which we mention in Chapter 2.
2. The solutions for second-order Stokes waves.

The rationale for both additions is that the scaling process of the waves tested in Chapter 4 resulted in second-order waves for units $T1$-$T2$, meanwhile $T3$-$T7$ were escalated to linear long-wave swells. The conditions for simulation can be seen in Table 6.1.

Period (T_n)	Regime (adimensional parameters)	Depth
T1	2nd order Stokes	Deep waters
T2	2nd order Stokes	Deep waters
T3	2nd order Stokes/Linear theory	Deep/Transitional waters
T4	Linear theory/2nd order	Transitional waters
T5	Linear theory/2nd order	Transitional waters
T6	Linear theory/2nd order	Transitional waters
T7	Linear theory/2nd order	Transitional waters

Table 6.1: Wave regimes simulated at BEMT. Waves simulated are in the boundary between Airy (linear) and 2nd order Stokes.

The wave models we can simulate using BEMT are shown in Figure 6.4:

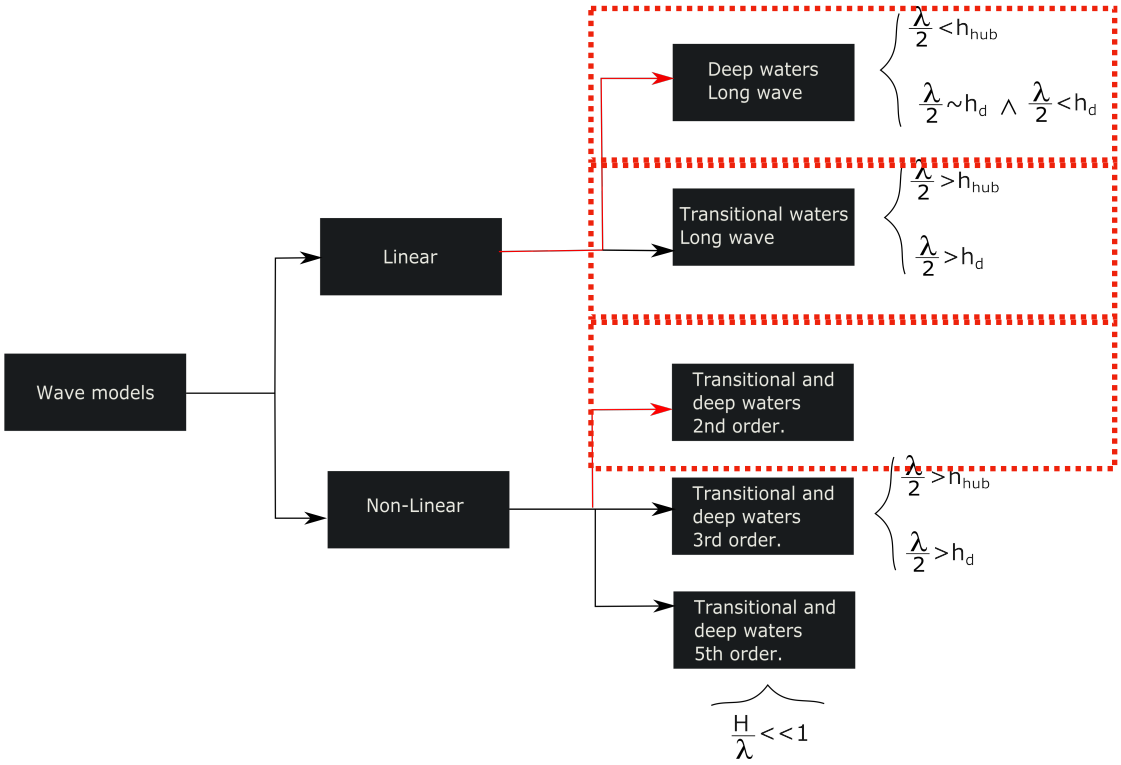

Figure 6.4: Diagram of the wave models added and modified to the BEMT software (in red) and those already developed by ESRU. The values of H and λ show the ranges for which each theory is valid.

6.3.2 Waves simulated

The waves tested in Chapter 4 were scaled up to satisfy the Froude number similarity. However, as we mentioned, the Reynolds cannot be satisfied due to physical constraints. Additionally, we could not discard that viscosity effects were larger in our tested waves in the tank because of their small amplitudes. In this case, the ratio of gravitational forces to viscous forces was compared, and both values are given by equations 6.48 and 6.49.

$$F_{grav} = \frac{p1 - p}{p + p1} g \tag{6.48}$$

$$F_{vis} = \frac{\sigma}{p + p1} k^2 \tag{6.49}$$

The values for the gravity to viscosity forces ratio are shown in Table 6.2. These allowed us to confirm that waves were purely gravitational where the ratio of both is small.

Periods T_n (s)	$C=F_{vis}/F_{grav}$
0.833	4.4%
0.9	3.7%
1.0	3.0%
1.1	2.4%
1.25	1.9%
1.4	1.5%
1.7	1%

Table 6.2: Percentage value of the gravity to viscosity ratios.

Secondly, the waves in the tank were scaled up comparing the Froude number for the waves in the tank. The Froude number was compared to waves scaled up using the non-dimensional depth and height, as given by Le Méhauté, which is shown in Table 6.3. Here, the depth was corrected to $42m$ instead of $40m$ when the Froude number was compared.

Wave tank, depth h=60cm			Simulated Model h=42m		
Period (s)	Height (cm)	Froude	Period (s)	Height (m)	Froude
0.833	1.5	0.535	6.97	0.4	0.534
0.9	1.5	0.576	7.54	0.6	0.576
1.0	1.5	0.634	8.37	0.7	0.631
1.1	1.5	0.685	9.3	0.8	0.686
1.25	1.5	0.748	10.5	0.9	0.742
1.4	1.5	0.796	11.73	1	0.786
1.7	1.5	0.860	14.1	1.1	0.843

Table 6.3: Froude number for waves in the tank and waves used in the simulation.

We also use the Ursell number with the suggested ranges of validity for the linear wave theory [59], as in equations 6.50 and 6.51. The wavelength here is calculated using the approximation made by Fenton [93].

$$linear \iff U_r < 40 \tag{6.50}$$

$$linear \iff \frac{H}{\lambda} < 0.04 \tag{6.51}$$

6.3.3 Tidal turbine and blade characteristics

The tidal turbine simulated is a horizontal axis tidal turbine, also known as HATT. The bottom of the channel where the turbine is placed has a depth of $42m$ which was found by scaling the Froude number values in Table 6.3.

The blade chosen for this simulation is the NRELs814 [119] owing to past studies conducted by Nevalainen and Barltrop [120] which tested the same airfoil using a BEMT model. Nevalainen tested the same blade under wave conditions similar to ours for the period range, current, and depths. Navalainen's works differ in the use of mixed wave weather with high amplitudes, rather than swell dominant weather. This in turn will allow us to compare his results partially. Nevalainen [46] reproduces the experiments made by Barltrop, which show how the BEMT tools used in this thesis can reproduce the forces over the individual blades of the rotor. The conditions tested by Nevalainen in B and Barltrop in C are shown in Table 6.4, along with the conditions in this work, A.

Test	T(s)	$H(m)$	$h_d(m)$	Theory	$U\infty(m/s)$	h_h(m)
A	6.97-14.1	0.4-1.1	42-28	1st-2nd	1.5-3.5	32-18
B	6-10	1-6	∞	1st	2.5-4	30-40
C	6-8	1.4-7	∞	1st	3.6	20

Table 6.4: Ocean weather used for the turbine simulations using the NRELs814 design under different weather cases. Here, h_h=h_{hub} which is the depth of the turbine's hub, and h_d is the sea depth before the wave propagates over the obstruction.

The other parameters (such as the diameter and tip-to-speed ratio) besides the airfoil differ from those used here because the aim of this study is to account for the variation caused by waves changing their physical parameters, rather than the turbine design or pitch changes due to misalignment. The general design parameters of the turbine are shown in Table 6.5.

Specification	Value
Blade profile	NREL S814
Turbine Depth (m)	42-28
Rotor radius (m)	8
Hub radius (m)	1.2
Blade number	3
Pitch angle	0
Twist distribution	[1]
Wave model used	Linear (1st order), 2nd order
Current time velocity profile	Linear shear current profile [46]
Distance between the seafloor and the hub (m)	10

Table 6.5: Characteristics of a tidal turbine modelled using BEMT.

The NRELs814 is considered a thick airfoil [119] which is suitable for stall-regulated operation and makes the rotors with this blade run at an approximate fixed speed when higher velocities are achieved without any geometry change. The physical model of the turbine was simulated to be at an initial depth of $42m$ depth, ranging to $28m$ in its shallower simulation.

The Reynolds number was given as constant. Despite this being incorrect, it is assumed to be negligible because the order of magnitude is approximately the same. In general, except for the shorter periods, the waves move in infinite waters in the simulations, instead of infinite depth waters as with the other authors. Also, the other authors use linear wave theory for their random case simulations, while the work presented here combines linear and 2nd order theory. An image depicting the height of the

turbine hub, the depth over the obstacle, and the depth before the obstacle is shown in Figure 6.5.

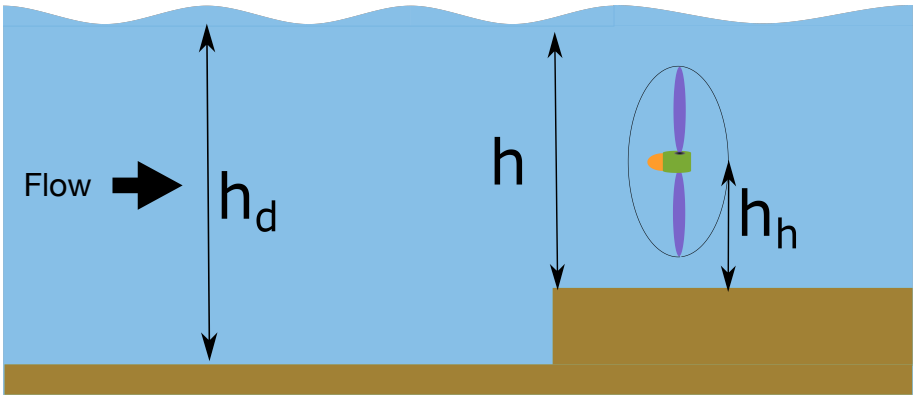

Figure 6.5: Principal depths for our tested model: h_d the seabed before the jump at 42m, h the obstacle depth variation, and $\mathrm{h_h}$ the hub height.

6.3.4 Sensitivity analysis

The blade NRELs814 and BEMT have been found to agree with enough confidence by authors like Masters et al., Nevalainen et al., and Barltrop et al. These cases and simulations have used sea condiments with active seas that present active wind-driven waves that are steeper. They have also simulated a flat seabed, without any particular irregularity that can modify the wave trains that propagate after or over the obstacle. The sensitivity analysis performed by Nevalainen et al. focuses particularly on the variation of the operational and design parameters of the turbine, as well as the sea weather. In our case, we focus on the analysis of a swell-dominated sea and a regular seabed that can modify the wave parameters.

As explained in Chapter 3, a sensitivity analysis is a method used to determine how the vacation of the input of a function can affect its output, which is also known as the uncertainty. In our case F which is our function corresponds to the BEMT model, which is composed of several other functions related to each other. The only way to ascertain the sensitivity is through a complex method known as the Morris method of sensitivity analysis [121], introduced byMorris in order to test and sample the importance of the inputs of a model. The Morris method is known as a global sensitivity analysis method as it samples all variables of a model F.

In the Morris method, all the parameters that can affect the output of the function F are changed to study how each one affects the output Y, which can be a vector of several outputs Y={y_1, y_2, …, y_n}. In this case, the inputs and outputs can be seen in Table 6.6.

Input variables X	Range	Output Y
x_1=T (s)	6.97-14.1	y_1=Torque
x_2=H (m)	0.4-1.1	
x_3=h,h_d (m)	42-28	y_2=Thrust
x_4=c (m/s^2)	1.5-3.5	

Table 6.6: Input variables and output values for the sensitivity analysis.

Unlike the work of Nevalainen et al, Barltrop et al, and Masters et al, in our case the wave height also varies depending on the depth of the obstacle. The wave height changes along with the size of the obstruction in the path of waves travelling to the coast in our model. This is done by using the formulation of Marshall and Naghdi and correcting the wavelengths as they move in waters of finite depth.

In order to measure the effects of the changes produced by each variable, a number of steps were taken according to the method.

- The range of the variables is divided into a fixed number of equally spaced sections, so the range [x_{min}-x_{max}] is now [x_{min}, x_{min}+$\Delta\chi$, x_{min}+2$\Delta\chi$, ..., $\Delta\chi$-x_{max}].
- A minimum set of simulations to iterate between each variable change is made, known as R.
- A set of random paths where each variable changes one at time during every iteration. These are the trajectories taken by our function F to obtain the values of Y as the vector of variables X changes. This can be seen in equation 6.52.

$$R_i = F(x_1, x_2, x_3, x_4) \rightarrow F(\delta x_1 + x_1, x_2, x_3, x_4) \rightarrow \ldots F(x_1, x_2, x_3, \delta x_4 + x_4) \qquad 6.52$$

Each result of the trajectories before and after the change of an individual variable, in this case δx_n, is divided by the change in the variable made to change from one point to another of the trajectory in equation 6.52. This ratio of the function at point Fa with variables Xa to Fb with variable Xb produces an elementary effect also known as EE. This effect is discussed in Chapter 3 and can be seen below, as described by Capolongo et al. [122].

$$EE = \frac{F(x_1, x_2, (x_3 + \delta x_3), x_4) - F(x_1, x_2, x_3, x_4)}{\delta x_3} \quad 6.52$$

The sum of the elementary changes will allow us to calculate the moments, which are related to the statistical distribution values of the central tendency of the model. The Morris Method of sensitivity calculates three moments:

- The sample moment μ_i is an average effect measure, where higher values suggest a main dominant contribution of the initial factor x to the responses in Y, and effects are expected to be linear. As their symbol suggests, as does the calculation method, this is related to the mean in statistics. The formula can be seen in equation 6.53. The response can also be monotonic, which means a Y variation proportionally to X but without a constant rate.

$$\mu_i = \frac{1}{R} \sum_{r=1}^{R} EE_i(X) \quad 6.53$$

- The sample moment μ_i^* is the total measure effect. In this case, which measures the total effect over the output Y independently of the response being negative or positive, the formula can be seen in equation 6.54. This moment accounts for the total effect of this factor to the response of the input.

$$\mu_i * = \frac{1}{R} \sum_{r=1}^{R} | EE_i(X) | \quad 6.54$$

- The third moment σ is used to calculate the non-linear interaction between each initial variable x_n to produce the output Y. The equation to calculate this can be seen in 6.55.

$$\sigma_i = \frac{1}{R-1}\sqrt{\sum_{r=1}^{R}(EE_i(X)-\mu)^2} \tag{6.55}$$

Here i is the individual elementary effect of the ith calculation on the trajectory R_i.

In order to produce random trajectories that move across the variable space, a matrix is made with dimensions k or $k+1$. Here, k corresponds to the length of the array input which contains the variables or $X=\{x_1, x_2, \ldots, x_n,\}$. This is 4 with H and h-hd, related by the equation of Naghdi and Marshall, giving a total set of 5 variables related to the sensitivity analysis.

The matrix to find the random paths is defined in equation 6.56:

$$A_s = J_{k+1}q^* + \frac{\delta}{2}[(2A - J_{k+1,k})D^* + J_{k+1,k}]P^* \tag{6.56}$$

- Here δ is the pre-defined division made to all variables in the ith space domain of the variables, which can be defined as Ω as in Nevalainen's work and which is a $4th$-dimensional space. The 4th variable is four variables linked by the Naghdi-Marshall relationship because the wave height H will vary depending on the wave number, which is period related (T), and the ratio of the depth before and after the obstacle (h, h_d).
- P^* is a permutation of the identity matrix.
- A is a triangular lower matrix with entries equal to one in the lower triangle.
- D^* is a diagonal matrix with entries randomly chosen to be -1 or 1, which allows the mapping of the input-output to have a decrease and increase of δ for each of the input variables in X.

- J_{k+1} is a matrix with values equal to 1 in all entries.
- $J_{k+1,k}$ is a matrix with elements that have the property of having only elements with a value equal to 1, one per column, but where the elements never share the same row.
- q^* is the vector with the initial values $X=\{x_{1\text{-}o}, x_{2\text{-}o}, \ldots, x_{n\text{-}o,}\}$ which are different for each trajectory in the Ω space. In our case, these values should be inside the range of the sampling space defined by Table 6.6. These values are also known as $X0$ and are defined in the Appendix, section H.

To run the sensitivity analysis, a relatively large sample of data is needed so that model F can be more accurately measured. In this case, Wentworth et al. [123] suggest using a division in the ith space of 20 and a sample of 50. In this case, R=50 corresponds to 250 experiments using 50 routes through Ω. As the parameters σ, μ, and μ^* represent measures of the response of F, the resulting plots can be roughly interpreted as displayed in Figure 6.6.

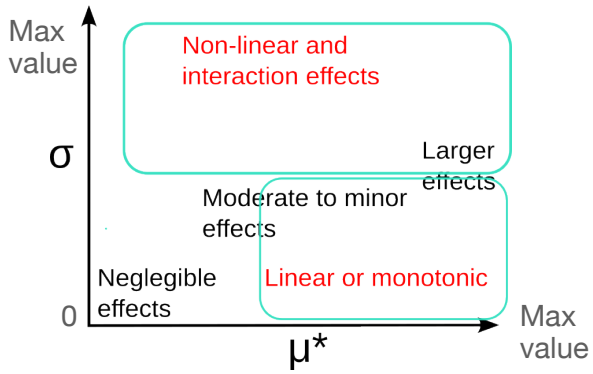

Figure 6.6: Graphical interpretation of the results for the sensitivity analysis using the Morris method, where μ^* and σ correspond to the values for each parameter in X.

6.3.5 Sensitivity analysis results

The results of the sensitivity analysis for an individual blade and the rotor of the turbine are shown in Figures 6.7 and 6.8 The x axis measures the parameter importance from 0 to 1, σ is the parameter value in the y axis.

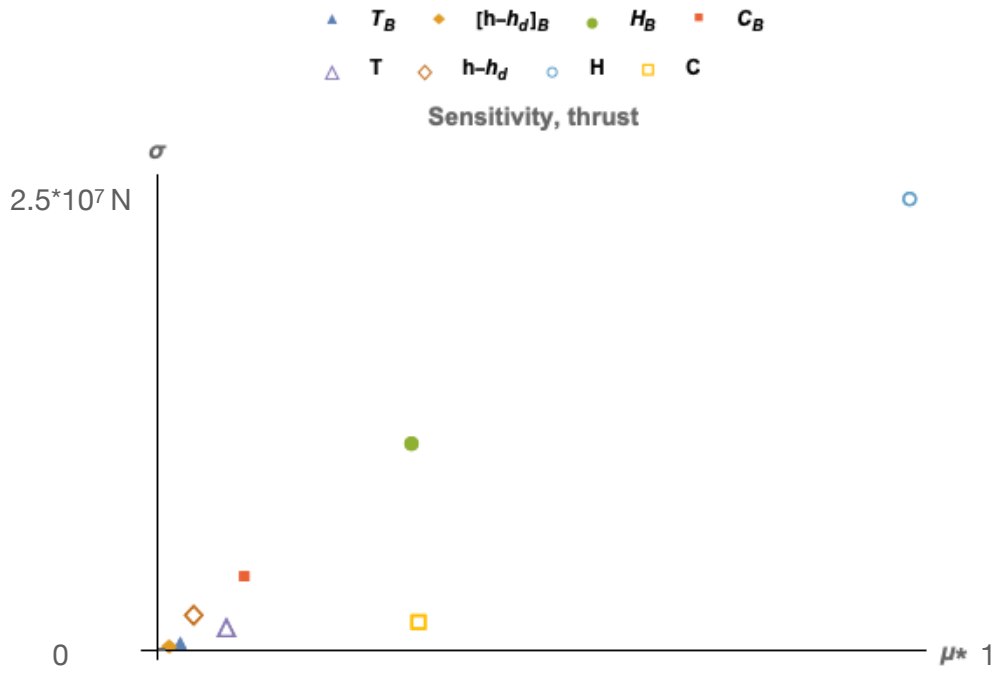

Figure 6.7: Results of the sensitivity analysis for the tidal turbine, values for the period, T, the wave height, H, the current, C, and the depth of immersion, h-h_d, exist in the range shown in Table 6.6. Letters with a subindex B refer to the blade results; those without refer to the total rotor results.

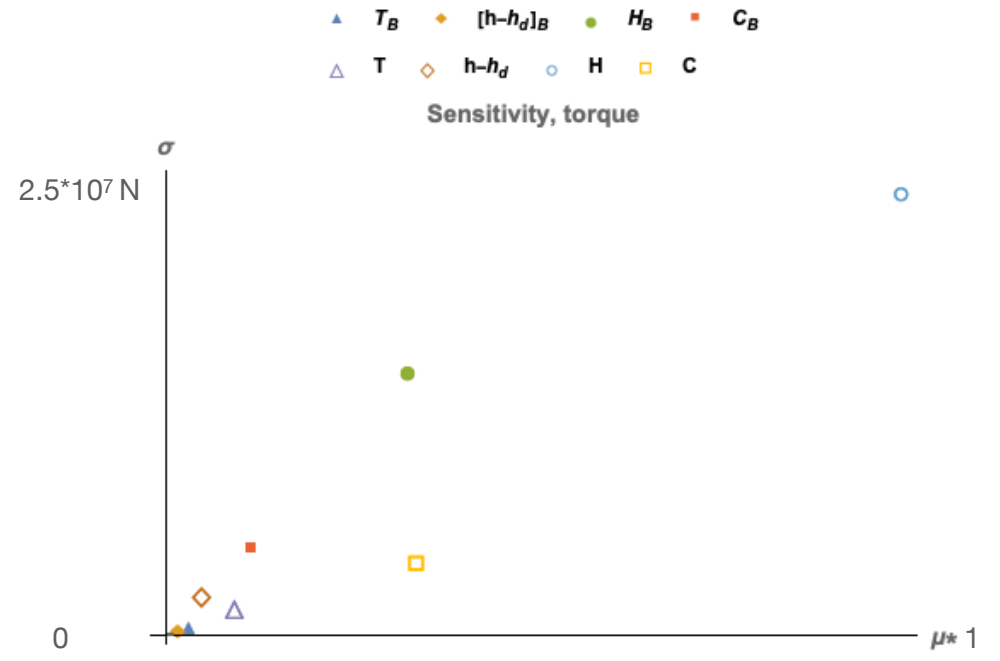

Figure 6.8: Results of the sensitivity analysis for the tidal turbine, values for the period, T, the wave height, H, the current, C, and the depth of immersion, h-h_d, exist in the range shown in Table 6.6. Letters with a subindex B refer to the blade results; those without refer to the total rotor results.

The result of the analysis are compared to Nevalainen's in Table 6.7. The comparison must be done with some limitations as the model tested by Nevalainen is the result of a mixed state with higher amplitudes, where the

measurements were made to detect events that represent a deviation from the mean thrust of the blade in most of his cases. In this work, we can only compare the mean thrust to the thrust of the turbine under swell conditions. For both the blade and the rotor, the values can be interpreted as in the table below.

Variables	Mixed state	Swell weather
Current, C	High effect, monotonic	Moderate effect, monotonic
Wave height, H	Low effect, non-linear	High effect, non-linear
Depth, h_d-h	Low effect, monotonic	Low effect, monotonic
Wave Period, T	Low effect, monotonic	Low effect, monotonic

Table 6.7: Category of the effects as detected by Nevalainen [36]-[46] and in this work.

There are some limitations in this comparison. The analysis corresponds to the same blade and it was performed under a range of conditions that overlap with the new test devised by Nevalainen et al and Barltrop et al. However, due to the sea weather conditions simulated for the numerical analysis, the magnitude is different. Values for the depth and period obtained by Nevalainen appear in the scale of $1x10^6$ Newtons, while the values obtained here are one order of magnitude lower in the scale of $1x10^5$ Newtons. Variables such as the depth and wave period, despite being equally low in Nevalainen's work, they are one order of magnitude lower in our case scenario.

The results are the contrary for the current and wave height. In our scenario, the sensitivity analysis shows a higher magnitude for the wave height and current, in some cases almost one order of magnitude larger than Nevalainen's case for the current. The total measured effect for Nevalainen's are in the order of $1x10^5$ N and in our case it has a total effect in the order of $1x10^6$ N. The results of the analysis show how the current and the wave height are the most important parameters in scenarios where the turbine sits in a relatively shallow part of the shelf and is exposed to swell dominant weather conditions.

For us, the turbine presents a high sensitivity to the wave height and a moderate to the current, contrary to Nevalainen. This is extremely important because the variation of the wave height caused by any geographical accident in the vicinity of our turbine will cause a large effect on the torque and thrust. However, as our wave height is limited to low step swell conditions, it is possible that waves with higher amplitudes in second-order will have an even higher effect on the tidal turbine torque and thrust.

It is also important to remember that in this analysis the limited obstacle size also produces a limited change in the wave height after the obstacle. However, as was pointed out by Ting et al. [79], an increase in the wave height and a reduced depth will likely cause energy transmission to higher harmonics. Since these harmonics are not addressed in this model, it is not possible to introduce higher amplitudes if wave fission and harmonics are not accounted for, which constitutes a limitation.

The study was also repeated for a single blade as in the case of Nevalainen, and the results show no variation. This was expected from the rotor case, as Nevalainen does not include the values for the total measured effect but he does include graphical information about the order of magnitude of the effects the wave weather has on the turbine thrust, they are compared in Table 6.8 below. The comparison between Nevalainen's case and the study made here tries to compare the magnitudes of each scenario because both scenarios differ in terms of sea weather conditions. The table shows the magnitudes in powers of 10 for the period, wave height, depth, and current. It is important to notice that mixed sea weather measures the standard thrust of the blade, which depends on the mixed sea weather conditions, while our case scenario maps a set of swell weather cases with a single dominant wave period.

Both the wave period and the depth have monotonic effect and have a low effect in both cases. However, the low sensitivity and monotonic behaviour in our model shows a larger order of magnitude which might be

linked to our turbine sitting in a shallower depth range between [34-20]m compared to [40-30]m in the mixed state case.

Variables	Mixed state, order of magnitude	Swell weather, order of magnitude
Current	$1x10^5$	$1x10^7$
Wave height	$1x10^5$	$1x10^7$
Depth	$1x10^4$	$1x10^6$
Wave period	$1x10^4$	$1x10^6$

Table 6.8: Order of magnitude of the effect parameter μ^* for the Mixed stated simulated by Navalianen's and our study using only swell components.

6.3.6 Simulation of the unsteady model with a change in depth and wave propagation

The set of conditions tested in the sensitivity analysis were chosen to model and simulate a tidal turbine. This enabled us to obtain the mechanical response of the rotor to compare the changes produced in the torque and thrust.

The case uses two different conditions each for depth and for current in each case. The depth conditions include a regular obstacle with a limited height which obstructs the wave path, so the wave propagates over the obstacle and then modifies its amplitude and period. To model this, the formulation of Naghdi and Marshall is again used. Several assumptions are made for this simulation.

- No turbulence is produced in the flow after the tidal current propagates over the obstacle and reaches the turbine.
- The geographical constraints are not large enough in the horizontal area to accelerate the flow considerably. On average, the velocity profile will therefore stay the same. This is convenient as it allows us to show only the variation caused by the wave change in height after it propagates over the obstacle. In reality, the flow will accelerate causing a higher velocity profile.

A possible solution to this is the integration of the flow profile across the constraint, using the velocity as a vector-valued function and then equating it to the output flow after the geographical constraints.

The cases evaluated are then compared to the same turbine when no obstruction constrains the wave propagation. The cases simulated using BEMT are shown below in Table 6.9.

Case	No obstruction	7 m obstruction	14m obstruction
Current (m/s), $C1$, $C2$	[1.9, 2.6]	[1.9, 2.6]	[1.9, 2.6]
Periods (s), $T1$, $T2$	[6.97, 14.1]	[6.97, 14.1]	[6.97, 14.1]
Heights (m), $H1$, $H2$	[1.2, 3.5]	[1.2, 3.5]	[1.2, 3.5]

Table 6.9: Conditions chosen to simulate a tidal turbine and obtain its mechanical response.

The corrections in the wave height for the obstruction can be seen in Table 6.10.

Case	No obstruction	7 m obstruction	14 m obstruction
Wave heights without correction (s)	[1.2, 3.5]	[1.2, 3.5]	[1.2, 3.5]
Wave height with corrections	[1.2, 3.5]	[1.0, 3.6]	[1.05, 3.8]

Table 6.10: Conditions chosen to simulate a tidal turbine and obtain its mechanical response.

The simulation compares the values of the torque and thrust of the rotor at different depths if the change in the wave parameters is not taken into account. It includes the changes in the wave as it propagates over the obstacle. The change in percentage in the total torque and thrust is also compared.

6.3.7 Simulation results

The torque and thrust are plotted for the two wave periods at the two different current velocities. First, the case where no model to compensate for the wave propagation is used, as shown in Table 6.10. This is done for a

turbine sitting first at 42m depth and then at 35m and 28m depth. The results are shown in Figure 6.9 below.

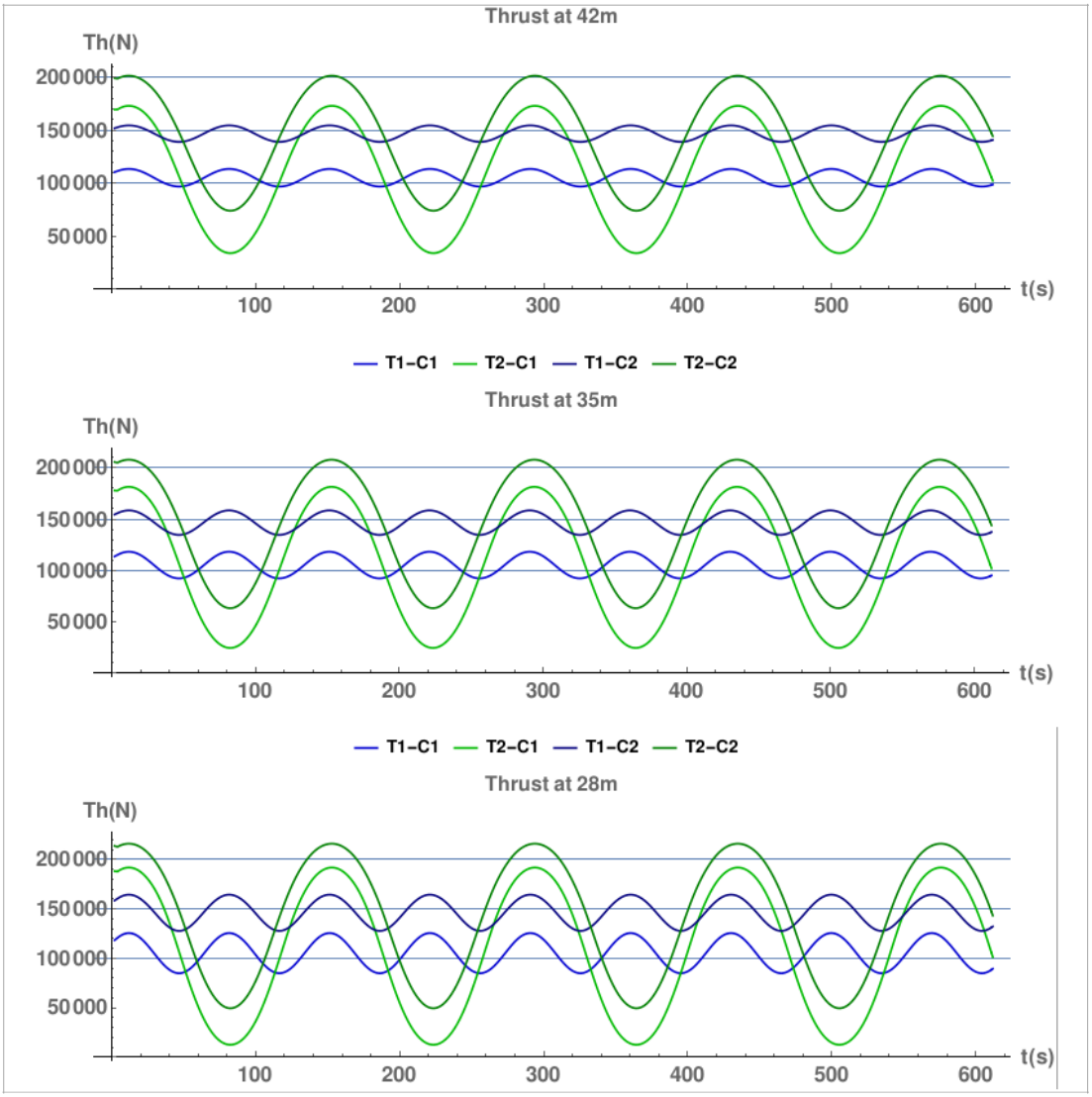

Figure 6.9: Thrust variation for a turbine sitting at a depth of 42m, over a sudden rise at 35m in green and sudden rise at 28m depth in blue (smaller oscillation). The values $T1$, $T2$, $C1$, and $C2$ correspond to the periods given in Table 6.9 where $T1$=6.97s, $T2$=14.1s, C1=1.9m/s, and C2=2.6m/s. The wave heights are $H1$=1.2 and $H2$=3.5m

The respective torque values for the same case can be found in Figure 6.10. The values follow a logical relationship. As the turbine moves into shallower regions from 42m to 28m depth, the increase in both torque and thrust values follows the increase of the current profile near the surface where the maximum velocity U_s is located for the power law. The results of

the simulations for changes in the wave parameters post-propagation over an obstacle occurs are shown in Figures 6.11 and 6.12 for the turbine torque.

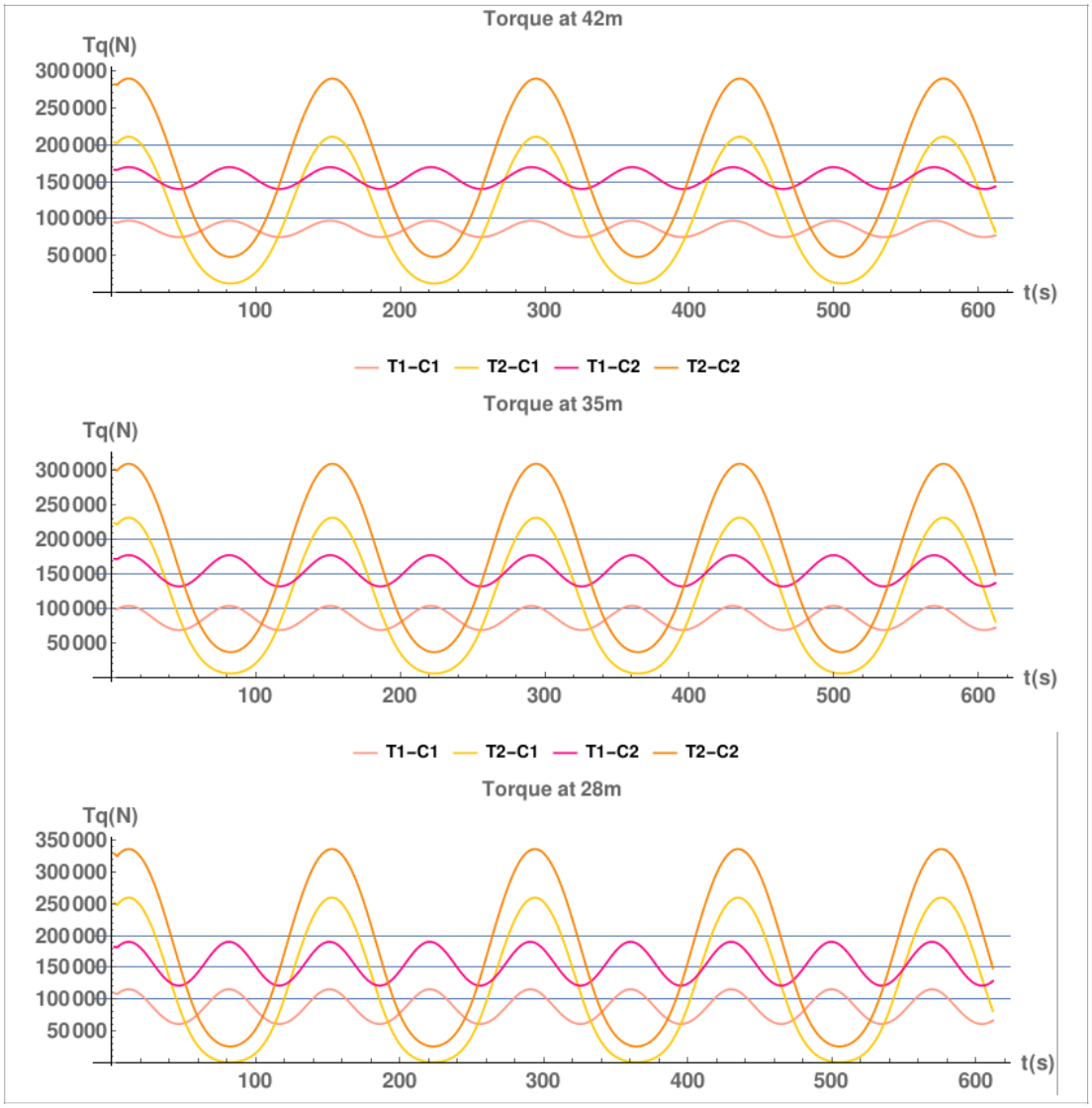

Figure 6.10: Torque variation for a turbine sitting at a depth of 42m, over a sudden rise at 35m in orange and over sudden rise at 28m depth in pink (smaller oscillation). The values $T1$, $T2$, $C1$, and $C2$ correspond to the periods given in Table 6.9 where $T1$=6.97s, $T2$=14.1s, C1=1.9m/s, and C2=2.6m/s. The wave heights are $H1$=1.2 and $H2$=3.5m.

Changes where the turbine sits over an obstacle at depth of 35m are small and, for this case, the model including wave propagation gives values that are so close to the model without any change that both plots technically overlap each other. However, this is not the case for the larger amplitude case at 28m depth, shown in Figure 6.13.

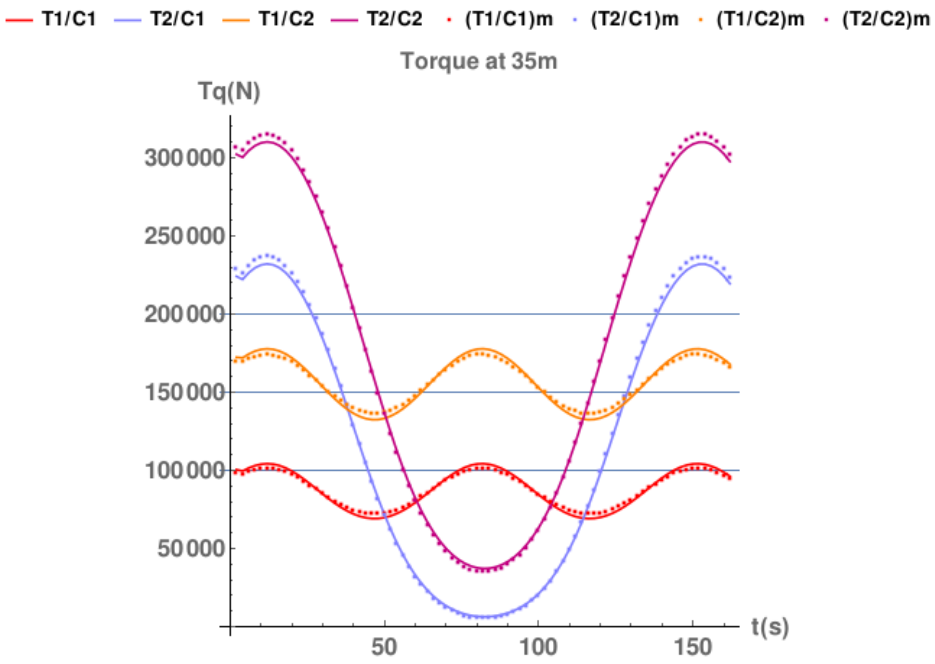

Figure 6.11: Variation of the torque over the obstacle for the model without the corrections and with the corrections (dotted) shows very little variation when the obstacle has a size of $7m$. The values $T1$, $T2$, $C1$, and $C2$ correspond to the periods given in Table 6.9 where $T1$=6.97s, $T2$=14.1s, $C1$=1.9m/s, and C2=2.6m/s. The wave heights are $H1$=1.2 and $H2$=3.5m.

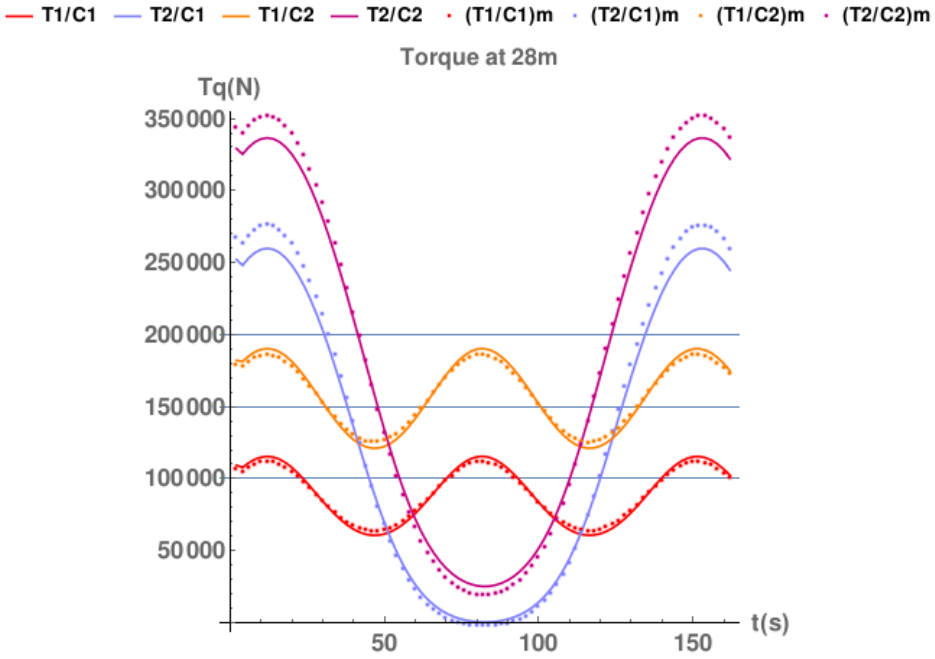

Figure 6.12: Variation of the torque over the obstacle for the model without the corrections in orange and with the corrections (dotted) showing an increase when the obstacle has a size of $14m$. The values $T1$, $T2$, $C1$, and $C2$ correspond to the periods given in Table 6.9 where $T1$=6.97s, $T2$=14.1s, $C1$=1.9m/s, and C2=2.6m/s. The wave heights are $H1$=1.2 and $H2$=3.5m.

It is evident from Figures 6.11 and 6.12 that obstacle size has a moderate influence on the torque variation because the larger the obstacle, the larger the resulting wave propagating over the obstacle. The effects are low for the thrust in Figures 6.13 and 6.14.

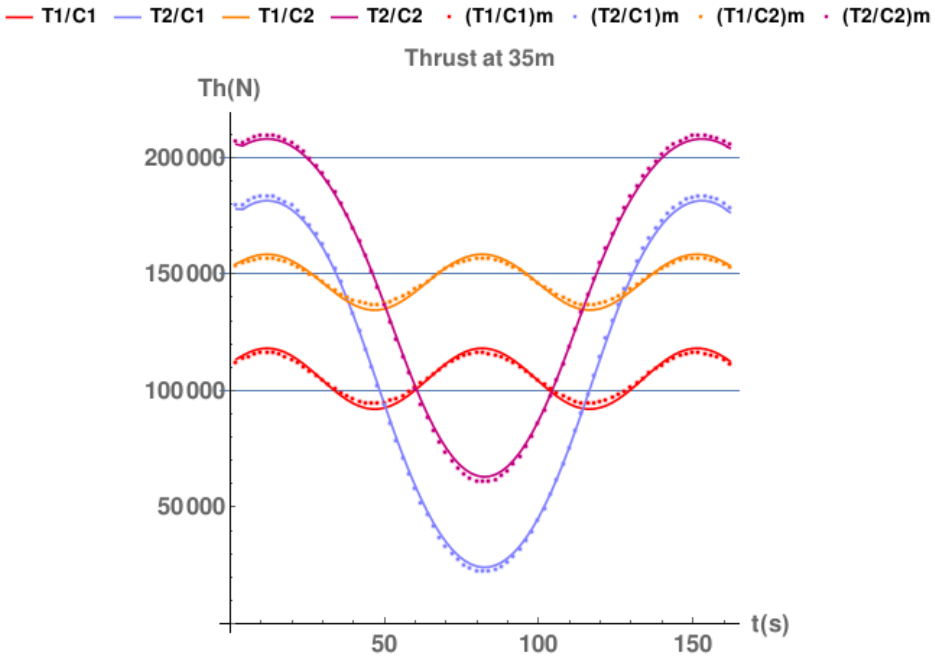

Figure 6.13: Variation of the thrust over the obstacle for the model without the corrections in blue and with the corrections (dotted) showing very little variation when the obstacle has a size of $7m$. The values $T1$, $T2$, $C1$, and $C2$ correspond to the periods given in Table 6.9 where $T1$=6.97s, $T2$=14.1s, C1=1.9m/s, and C2=2.6m/s. The wave heights are $H1$=1.2 and $H2$=3.5m.

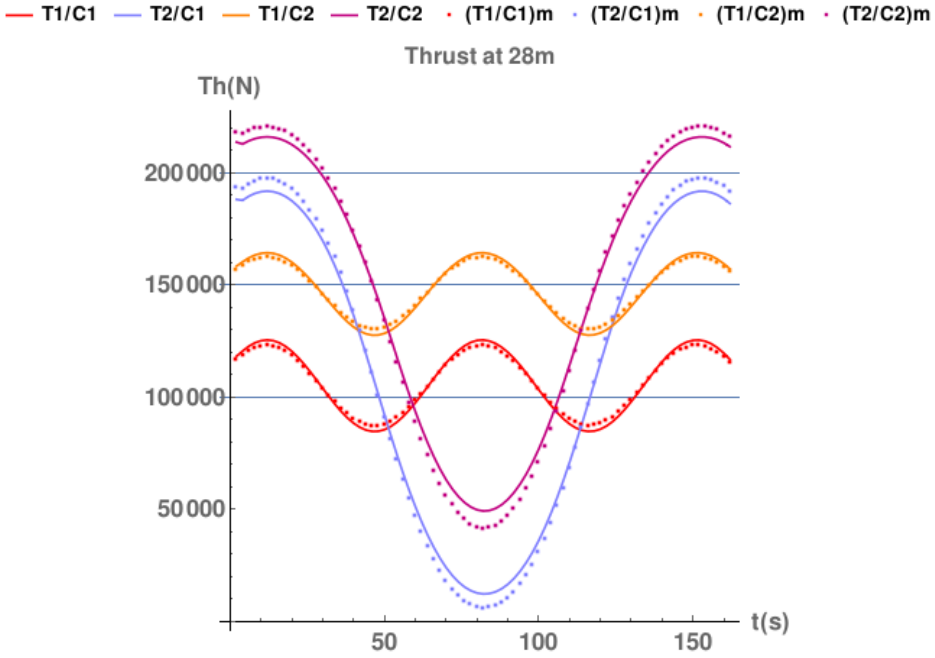

Figure 6.14: Variation of the thrust over the obstacle for the model without the corrections in orange and with the corrections (dotted) showing small variation when the obstacle has a size of $14m$. The values $T1$, $T2$, $C1$, and $C2$ correspond to the periods given in Table 6.9 where $T1$=6.97s, $T2$=14.1s, C1=1.9m/s, and C2=2.6m/s. The wave heights are $H1$=1.2 and $H2$=3.5m.

The changes in the wave height corresponds to an increase in the torque and thrust of the turbine. In this case, the increase of the wave height as a result of the obstacle size also appears to be monotonic. This means an increase in the obstacle size will directly affect the turbine mechanical response, but only larger heights will have a meaningful impact on the responses.

The wave height change shows a larger influence on the turbine torque, but all other values remain small. The influence of the wave height against the torque and thrust appears to confirm the sensitivity analysis where the wave height is the most important parameter for the swell. However, the height of the wave after the obstacle remains a function of the incident frequency and the obstruction. Changes are small, but the sensitivity to wave height is large and this will be observed in the case study in Chapter 7 where several wave weather conditions are tested.

The values for the changes in torque and thrust are shown in percentages in Table 6.11. Changes are measured against the models where no modification is made to the BEMT model to account for the wave propagation at depths of $35m$ and $28m$.

Case	Torque change in %, T1	Torque change in %, T2	Thrust change in %, T1	Thrust change in %, T2
$35m$	Less than 1%	Less than 1%	Less than 1%	Less than 1%
$28m$	Less than 2%	Less than 2%	Less than 2%	Less than 2%

Table 6.11: Change in total torque and thrust values as percentages, measured against the case where the model does not take into account the wave propagation over the obstacle.

Table 6.12 shows the changes in the percentage of torque and thrust due to swell conditions compared to the case where the turbine sits at $42m$ depth. This does not include the changes using the wave propagation as these are shown in Table 6.12. In Table 6.11, C1 and C2 are $1.9m/s$ and $2.6m/s$ respectively.

Case	Current	Torque change in %, T1	Torque change in %, T2	Thrust change in %, T1	Thrust change in %, T2
35m	$C1$	Less than 1%	5%	Less than 1%	Less than 1%
35m	$C2$	Less than 1%	2%	Less than 1%	Less than 1%
28m	$C1$	Less than 2%	10%	1%	1%
28m	$C2$	Less than 1%	5%	Less than 1%	Less than 2%

Table 6.12: Change in total torque and thrust values as percentages, measured against the case where the model does not take into account the wave propagation over the obstacle.

6.4 Conclusions

The wave formulations proposed in Chapter 3 and measured against experiments and results in Chapters 4 to 5 were coupled with the BEMT model. The model has been developed by the Department of Mechanical and Aerospace Engineering in the Energy Systems Research Unit in the University of Strathclyde and a detailed description can be found in Nevalainen's work [46]. The software allows us to calculate the changes in the torque and thrust of the blades of a tidal turbine. We used this model, a sensitivity analysis, and a simulation to obtain the mechanical response of the turbine to certain wave weather conditions. The key points of both are listed below.

Sensitivity analysis: The analysis uses the Morris method for sensitivity analysis to explore how four variables can affect the tidal turbine torque and thrust for the individual blade and the rotor. Its main points are to:

- Analyse how variables such as the wave height H, current V, depth of immersion, the obstacle h-h_d, and the period affect the BEMT model.
- Find which variables offer a lineal and monotonic influence and which are non-linear or interact with others.
- Observe how much influence the wave height has over the model compared to other sensitivity analyses by Nevalainen which take into account mixed-use weather.

Its results are as follows:

- The results show a large influence of the wave height parameter compared to other parameters such as the current, depth of immersion, and wave period. Wave height has a 200% times stronger effect over the turbine torque than the current. Meanwhile, for the thrust, the wave height effect is almost 300% times stronger than the effect caused by the current. The wave height appears to have a non-linear influence over the model.
- The second most important parameter influencing the mechanical response is the current, which is monotonic. The current has a three times larger effect compared to the depth of immersion or the wave period for the torque associated with the rotor. The current has a five times larger effect than the wave period or the depth of immersion, this is for an individual blade. The values for the thrust are similar, where the current has a three times larger effect than the period and the depth of immersion. The last parameters are the depth of immersion and the wave period.
- If we compare our study to the one made by Nevalainen, the current has the opposite effect. While for Nevalainen the current is the most important parameter for the mean thrust and it appears to be non-linear, in our case it appears to have a moderate and monotonic influence.

The simulation of the mechanical response of a tidal turbine torque sitting over a large obstruction from $42m$ depth to $28m$ depth and $42m$ depth to $35m$ depth offers the next results.

- The influence of the increase in the wave height after the obstacle has a negligible effect on the overall torque and thrust when compared against the model without any modification. However, this largely depends on the wave height. Larger wave heights have a large influence on the amplitudes of the torque and thrust variation.
- It is also evident that the current is the second parameter affecting the torque and thrust magnitudes of the turbine. In this case, the effect

appears to be an attenuation of the extreme values caused by the wave height.

It is important to note, in both the simulation and sensitivity analysis, our decision to keep the wave heights in linear order. It is assumed that larger waves with large periods would have a stronger interaction with the obstacle, causing them to increase their height and then increase the amplitude of the extreme values for the torque and thrust of the turbine. It is also important to note the limitation of the simulation in that the flow is kept constant after the obstacle. In a real case scenario where the magnitude of the obstacle is larger horizontally after a sudden bathymetry rise, the flow will be constrained and thus cause an increase in the flow for a turbine sitting at less depth.

7 Case scenario of a horizontal tidal stream turbine

Tidal turbines are exposed to a broad range of wave weather cases from active zones of wave-driven waves to swell zones. However, according to satellite data, in the southern and northern hemispheres more than 80% of the wave weather is dominated by swells [124]. In this chapter, the case of a tidal turbine exposed to swell dominant weather is analysed at a real geographical location using real wave and wind data. Geographical constrictions required in this case are related to the turbine deployment site, because this must occur near a bathymetry jump. The restrictions also cover a suitable depth of operation, which is on transitional depths inside the reachable domains on the continental shelf. This set of conditions aims to study how the change of the swell field propagating after the jump could play a major role in modifying the turbine loads in real conditions. Sharp bathymetry changes in the seabed will be what drives the wave field changes. This is an extension of the conditions studied theoretically in Chapter 3, experimentally in Chapters 4 and 5, and simulated in Chapter 6.

In this part of the thesis, these conditions are simulated using a real scenario where wave data is gathered and analysed to reproduce two meaningful cases where a tidal turbine is placed near the coast in a more open sea environment. The coast of California was chosen for our study. It is well known that sites with a regular high potential for tidal streams exist in the Pentland Firth, the British Channel, and the Bay of Fundy. These sites are also open to the sea conditions, at least in the case of the first two of the three sites, where swells come from the mid and north Atlantic crosses. However, the National Ocean Atmospheric Administration's (NOAA) instruments for measuring wave data and their rich data sets, which are verifiable from several sources, make this site ideal for gathering and analysing high-quality wave data.

The tidal resource in the area is strong, however, this resource is closer to the coast and concentrates near the golden gate area where the depth is shallower, limiting its application.

Current flows are strong in the Pentland Firth and the Bay of Fundy, where flows can reach 5m/s for the first case [8] and with a theoretical power available ranging from 0.01 GW to 1.9 GW depending on the number of turbines [8]. Meanwhile, the Bay of Fundy has a larger potential than the Pentland Firth, near 2.5 GW [125]. Tides are stronger inside SF Bay, but their power is lower compared to the Pentland Firth or the Bay of Fundy. The physiography of the place is different. Tidal flows accelerate closer to the coast near the bay area, where they can reach over $2m/s$ [126]. The power available according to the calculations is $2500MW$. The area is near a major urban centre which is an advantage. The geographical location could provide an easy connection to the shore.

7.1 Geographical characteristics

7.1.1 Onsite wave data acquisition and required parameters

Conditions that allow swells to interact with tidal devices suffice for wave weather in places like the west coast of the Pentland Firth, the English Channel, and many open sea places where swell wave trains are present in the summer and winter months. According to studies by Jiang and Chen [34], such areas are prone to 75% of swell probability, while vast sea areas called swell pools can have 80% of the swell dominance probability.

As swells can be determined by the wave height and the wave period, studies using altimeter satellites depict the swell-dominated areas [51], [124]. Other authors have also traced their propagation and dissipation process as in [60], [61], and [127], using the same satellite methods. The use of satellite data for these measurements has been consistent over the past 20 years. A parameter used to measure a wind-dominated sea is the wave age or $Wa,$ defined as the ratio of the wind speed at $10m$ over the sea

surface U_{10} and the mean wave speed C_m. Wave age values are high when the wind speed is larger and the phase of the waves shorter, which indicates an active sea and low swell energy. Data provided by satellite indicates that large swell pools are formed in the tropics as the swell radiates from the arctic and antarctic positions [34]. The zones of swell radiation show that the Pentland Firth, like the English Channel, can be affected by the North Atlantic swell, meanwhile the Pacific Basin is open to the south and north incidences. The data from satellite surveys show that swell incidence is a normal phenomenon in most of the oceans, making it important to quantify.

The data for sea observations and wave measurements to simulate a real tidal site and the swell conditions were taken from buoy systems. The properties of the waves modelled here required to have specific characteristics. The characteristics used to filter the required data were: directionality θ, time of acquisition t, dominant frequency DPD, and dominant wave height H_s. Wave directionality depends on the sampling of the wave field, which uses an array of three directional accelerometers. The specific need for directionality reduced our possible data sources. A search on the numerous systems active at sea with data availability was made, and the NOAA system was considered fit for this purpose.

The stations of the NOAA system are divided into two kinds of systems. The first are systems able to obtain directional wave data from specialised sensors and systems that derive this data from the onboard sensor analysis. The availability of the first systems is limited due to the use of dedicated sensors and different methods to process wave data. The second kind are more widespread due to their versatility in obtaining wave data after processing, making them the clear choice for this task. The widespread NOAA systems in the Pacific and Atlantic ocean basins that surround the USA coast can be seen next page in Figure 7.1.

The NOAA systems use the FFT (Fast Fourier transform), applied to the buoy movements, to obtain the wave spectrum measurements (with the directional Fourier analysis explained in Chapter 3). NOAA data provides a robust and proven method to measure the wave components at sea and its

system has been useful for calibrating altimeters from satellite measurements [128], [129].

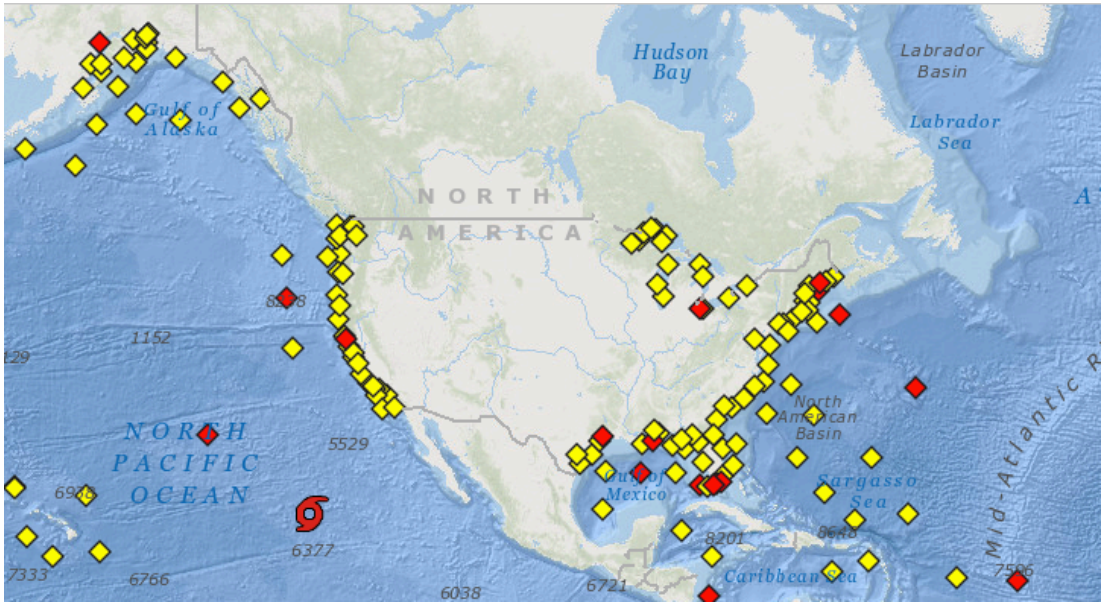

Figure 7.1: Systems managed by the NOAA under the NDBC program for the USA-Alaska and Caribbean area.

7.1.2 Onsite swell predominance

To test the modelled conditions, the site must have open to ocean waves. The US coasts provide a broad range of swell incidence that made them compatible with the NDBC data. As studies have shown, swell systems follow a great circle route. Wind systems in the Pacific and North Atlantic radiate swells throughout the year from their active areas of swell generation to the continental coasts [124]. Data on the swell dominance shows that the Pacific area of the USA offers a higher swell energy pool, like northwest Ireland and Scotland [128]. It is also noticed in the same studies that the calculated amplitude shows relatively low swell heights in the east Pacific Basin. The swell energy is also higher in the Pacific than in the Atlantic, which is probably related to the larger basin area being able to produce more powerful weather systems and larger fetch.

7.1.3 Continental shelf conditions

Due to the characteristics of the continental shelves, the conditions for wave propagation over long distances could change depending on the shelf length and geography. In general, there are two kinds of continental shelves. There are active shelves which are the result of geological activity like a sea plate moving below a continental plate, as in the Pacific. These shelves are short and offer a short distance of low depths for large wave systems like swells. The other kind of shelf is known as passive, which are submerged and produce large areas that can stand for hundreds of kilometres with shallow waters, one example being the European shelf containing the north sea. The type of shelf is important because their depth and length can constrain engineering deployments.

Long shelves resulting from passive continental margins can offer a longer range of wave propagation, while active ones will offer steeper and short changes. According to the most recent studies, dissipation of the swell appears to be stronger near the shore [130] and it is related to the sudden change of the seabed level across short lengths, as in [131]. Because of the bed friction, roughness, and changes in shorter distances, the buoy systems needed to be short distances from each other to reduce possible large fetch seabed effects. Due to the last requirement, the west Pacific coast was chosen as it possesses a large arrange of available systems and a short length of propagation for large wavelengths as $T(9s)=\lambda_i$ and $T(22s)=\lambda_s$. The propagation length on the shelf l_p ranges $l_{p=}[400\lambda_i\text{-}53\lambda_s]$ for shorter extensions, and $l_p=[700\lambda_i\text{-}100\lambda_s]$ for its larger areas.

7.2 Detection of the main direction of swell incidence into the coast

7.2.1 Swell incidence

The Pacific coast of the USA offers a wide angle of aperture for incident waves. The aperture angle is larger than 180º in most of the west

coastline and due to this swells are a common phenomenon in the area. Directional data of the most important swell trains in the Pacific has been recovered and analysed by Adams [35]. The analysed data shows that the main angle of incidence is located between 150º to 320º with an average between 295º to 200º. Here, the degrees are measured as 0 from the true north, using a system of magnetic sensors which is later corrected by measuring the magnetic north, the direction is positive clockwise. Considering the detailed studies by Adams, the decision to search for long swells in the range 180º-290º using the buoy system data was made. The search allows us to analyse the principal angle of swell incidence, and define the main direction of swell energy. The direction was used to detect the swells that will be modelled in our simulated deployment site. To detect the angle of incidence and the swell periods, a methodology was designed to search and compare the source of swells and their main spectral components. The method was divided into two steps. One was to search the main source of a swell using a deep water buoy system that can track incident swells from the Pacific; the second system, in transitional waters, was used to trace swell propagation over the angle of direction defined by the first system. The wind weather conditions were also compared to isolate distant swells from local wind-produced long wave systems.

7.2.2 Swell detection on the Pacific coast

The method to detect the main angle of incidence of the swell energy from the Pacific Basin into the USA coast was done by dividing the swell from the rest of the local waves in the buoy acquired data. The data analysed only the exposed areas to the open sea, by using a large temporal representative sample covering from January to December. The detection used a five-buoy system placed by the NOAA administration in deep waters to measure wave systems coming from long distances. The system coordinates and codes used can be seen next page in Table 7.1, and an image of the positions of the systems can be seen next page in Figure 7.2.

Buoy system	Coordinates
(A) 46089	45°55'29" **N** 125°46'17" **W**
(B) 46005	46°8'2" **N** 131°4'44" **W**
(C) 46002	42°36'42" **N** 130°32'12" **W**
(D) 46059	38°5'37" **N** 129°57'4" **W**
(E) 46047	32°24'13" **N** 119°30'22" **W**

Table 7.1: Buoy systems used for the yearly swell direction comparison.

The systems used in Figure 7.2 detect the angle of the main incidence using the wave energy directional spectrum as explained in Chapter 2.

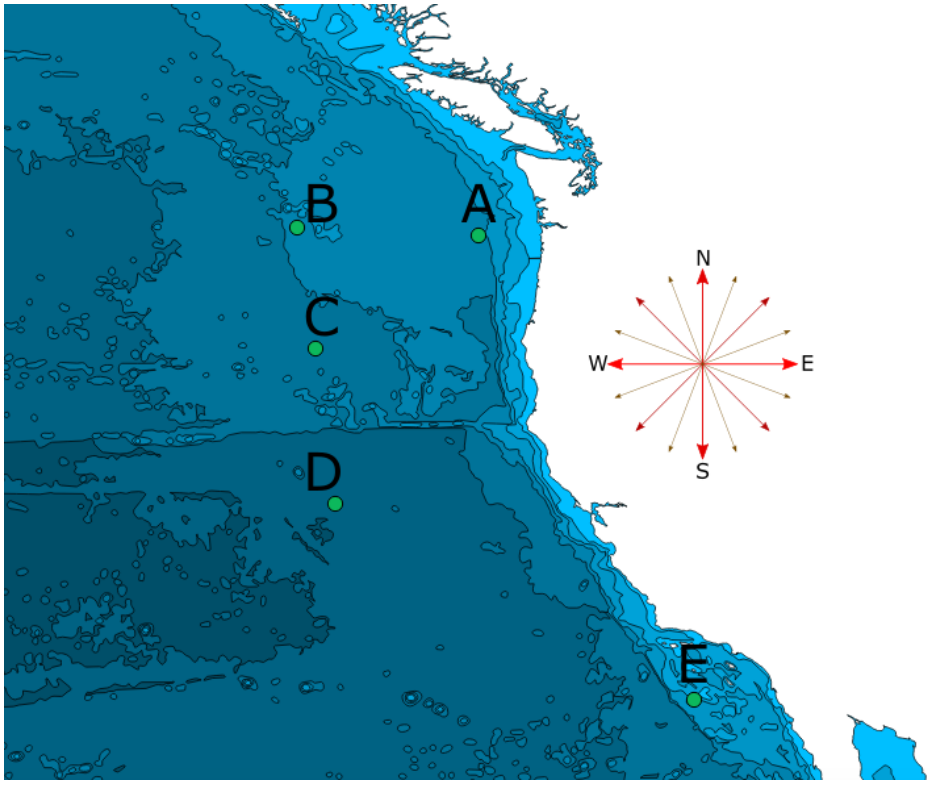

Figure 7.2: Buoy system used to detect the incident swell spectrum energy, buoys A to E are listed in Table 7.1.

The buoy systems A to E use the post-processing method explained in section 3.4.2 to divide the spectrum into discrete frequency units, Δf. The discretised spectrum has a period range of T= [2s-50s]. Discretised units of the spectrum are divided by their angle of incidence in degrees from 0º to 360º. The data gathered is organised in bands of Δ22.5^o aperture, using the NOAA standard notation for wave directional data.

The number and position of the systems were chosen to allow better detection of the swell energy incidence across the whole Pacific area. Their spatial disposition also ensures that any abnormal phenomena will not be replicated by the other systems. To ensure that local or nearby weather systems will not be listed in the incident swells, a method was designed to ensure that long waves that are locally produced will not interfere with our records. The method divided the wave spectrum into three parts by their frequencies. The first division used the possible maximum wave frequencies that the local winds could generate in a fully developed sea. The maximum frequency was calculated using the Pierson-Moskowitz modal frequency for continuous winds blowing over the sea surface. The second spectral division was made by calculating the maximum wave frequency that can be produced by local winds over a large distance in sustained conditions. The peak frequency was calculated using the modal frequency for the Jonswap spectrum. Wind data used in the calculations was retrieved from the buoys, and also the incident wave frequency. If the wind data results show larger periods than the locally recorded swells, the swell events under that period were discarded. The methods to calculate the frequencies for the locally produced wave systems are explained in the next sections.

7.2.3 Maximum frequencies for local wind-generated waves

The maximum wind-wave frequency was found using the relationship for the modal wave frequency. The value is calculated using the Pierson-Moskowitz spectrum relationship in equation 7.1.

$$f_w = \frac{g}{2\pi U_{10}} \tag{7.1}$$

The value f_w is the frequency at which the waves will travel as fast as the onsite wind, meaning that the sea has developed a speed similar to the zone winds. The value of the wind at the buoys was then used as a threshold value, and for any $f > f_w$ the waves were taken as local wind waves. The wind value was averaged from January to December, covering 4 years

or more of consistent data processed by the system. As the buoy systems wind measures use a mast at 3.4m over the surface, a correction was done using the wind shear stress formula as recommended by offshore wind engineering practice [132].

The corrections mentioned using the wind shear stress are shown in equation 7.2, where l_{rel} is the characteristic roughness of the ocean surface which is an average value of the height, cross-section, and space between the elements that populate an area. In the case of the ocean, it corresponds to the waves and acts as a statistical average of the roughness of the sea under certain conditions.

$$U_{10} = \frac{U_{ref} Ln[h_{10}/h_{rel}]}{Ln[h_{ref}/h_{rel}]} \qquad 7.2$$

The complete wind data and corrections are shown in Appendix section G.2.

7.2.4 Maximum frequencies for locally generated waves by winds blowing over a large fetch

The possibility of short swell systems produced near the buoys or at the coast was considered. Winds blowing from the coast could produce wave systems that could be filtered by their direction, while trade winds, seasonal winds, and near/local storms could produce large amplitude local swell systems that will be recorded by buoys. The possible long wave systems produced near the buoys were discarded, as was mentioned in section 7.2.2, by recording only the wave systems with periods larger than the modal frequencies produced by local winds. The difference from the Pierson-Moskowitz spectrum is that the wind must blow in a sustained way over a defined area around the buoy system. In this case, we consider the fetch as the maximum distance from the buoy to the coast or x. Just as for the Pierson-Moskowitz modal frequency, the Jonswap modal frequency or

f_m was used to exclude possible local long wave systems. The formula used to calculate the modal frequency can be seen in equation 7.3.

$$f_m = 3.5 x_a^{1/3} \tag{7.3}$$

The value x_a is the non-dimensional distance defined by equation 7.4, and f_m is the non-dimensional frequency as defined in equation 7.5.

$$x_a = \frac{xg}{U_{10}^2} \tag{7.4}$$

$$f_m = \frac{f U_{10}}{g} \tag{7.5}$$

Equations 3.7 to 5.7 allow us to calculate the threshold value for swells that could be produced by nearby weather systems each month. The fetch distance taken (x) for every buoy is shown in Table 7.2; the wind value U_{10} is the weighted mean of the larger wind standard deviation for the twelve months in each of the systems listed in Table 7.2. All these systems are able to process directional wave data.

Buoy	A	B	C	D	E
$\text{Distance}_{\text{aprox}}$	$138km$	$541km$	$495km$	$610km$	$180km$

Table 7.2: Minimum distance from the buoy system to the coast.

7.2.5 Results of the main direction of swell incidence

As the systems are sheltered from very large swells on the coastal side, the table of the aperture taken to swell systems at each buoy is shown in Table 7.3. The geographical angle of detection and the area used as a fetch to isolate waves generated by local winds is seen in Figure 7.3.

Buoy	A	B	C	D	E
θ_{aprox}	[75º-323º]	[134º-350º]	[128º-360º]	[110º-6º]	[126º-328º]

Table 7.3: Aperture for each system to the northern Pacific and southern Pacific swell.

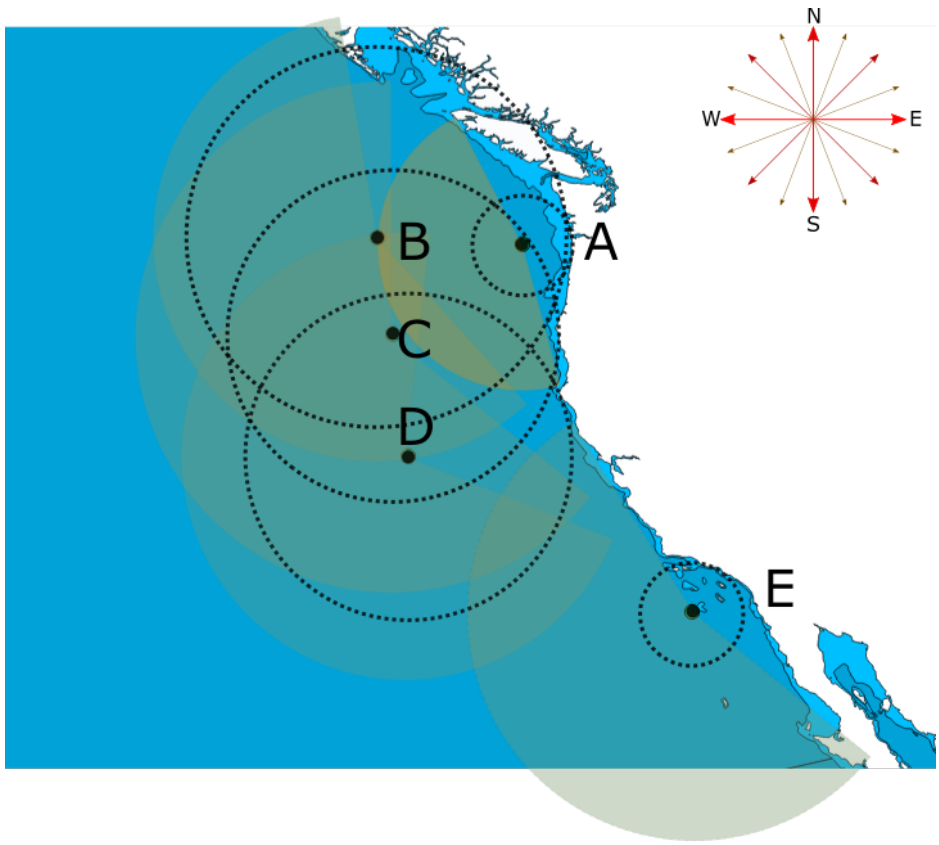

Figure 7.3: Zones delimited for the local wind waves produced at a close fetch in dotted lines and angle of aperture for the long range swell detection on yellow.

The data sets analysed correspond to the 2017 season. The higher percentages of detections depending on the incidence are shown in Table 7.4.

Buoy	%Total/Direction	%Total/Direction	%Total/Direction
A	27.8 (W)	20.2(WSW)	13.4(WNW)
B	30.5 (W)	16.7(SSW)	15.0(WNW)
C	27.6 (W)	23.0(WNW)	13.8(WSW)
D	31.7(WNW)	19.7(W)	14.2(NW)
E	23.6(NW)	19.7(WNW)	10(W)

Table 7.4: Main directions of incidence for the 5 buoy systems A to E.

The results indicate that the predominance of the swell events during a whole season focuses on the west direction between 330º to 210º on systems A to C, with a main focus in the west direction at 270º. Systems D and E have swell events covering a wider angle range. However, as the systems are located further south and detect a large number of swells at

higher values than 270°, the values could correspond to the relatively low geographical position of the systems, which in turn indicates a good correlation between the 5 systems detecting same events. The average number of swells detected in the direction WNW-WSW comprises almost 2/3 of all events for systems A, B, and C and 1/2 and 1/3 respectively for D and E. These west and northwest direction results show a large swell dominance from November to March, an example of which is the west dominance that has been mentioned by Adams et al. [50]. The C to D results detect a large incidence of swell events around the 180° direction, covering June to August. The detection of this surge of events occurs prominently in the month of July. A relatively high detection of events starts from earlier months, as of April, which indicates an active season in the east of the Mexican coast with lower numbers than the summer months.

The causes of both main swell directions can be linked to different phenomena. Radiating swells from the west and northwest will point to weather systems in the mid and northern Pacific Basin, while events at higher latitudes of the Pacific Basin could be linked to the storm season in the Siberian-Aleuthian area. The winter season where swell events are focused in this direction has been reported before as part of the winter seasonal weather [35]. The events occurring in the west are linked to an ENSO (El Nino Southern Oscillation) winter phenomena in the central Pacific area. The south direction events are shown for all systems, but the southern events that show a more concise fingerprint in the records are the ones from the summer season. It is well known that these correspond to southern swell events, which occur in the Antarctic Ocean. The Antarctic Ocean swells are related to the yearly winter oscillation, producing strong and long wave trains arriving from southern positions [49]. The earlier strong signals from the buoys E and D are probably linked to the cyclonic activity in the western Pacific Basin near Mexico's coast. The higher number in the summer months points to a superposition of both climatic events, as the cyclonic season and the winter oscillation will overlap from June to the end of October. Figures 7.4 and 7.5 on the next two pages show part of the

processed directional spectrum data of the systems A to D. The processed data will then deliver the main peak components and, using the formulations and properties mentioned at Chapter 3 in section 3.4.2, Figure 7.4 in next page shows the swell events related to the west-northwest detections in the month of January, probably related to the ENSO oscillation and the winter season around the mid and higher latitudes of the Pacific. It is also remarkable how a larger portion of the swell components come from 270^{o}.; meanwhile, Figure 7.5 in next page shows the increase of the swell events related to the southern direction focused in the month of October. The complete set of plots for the twelve months, at every buoy, is annexed in the Appendix section G.3.

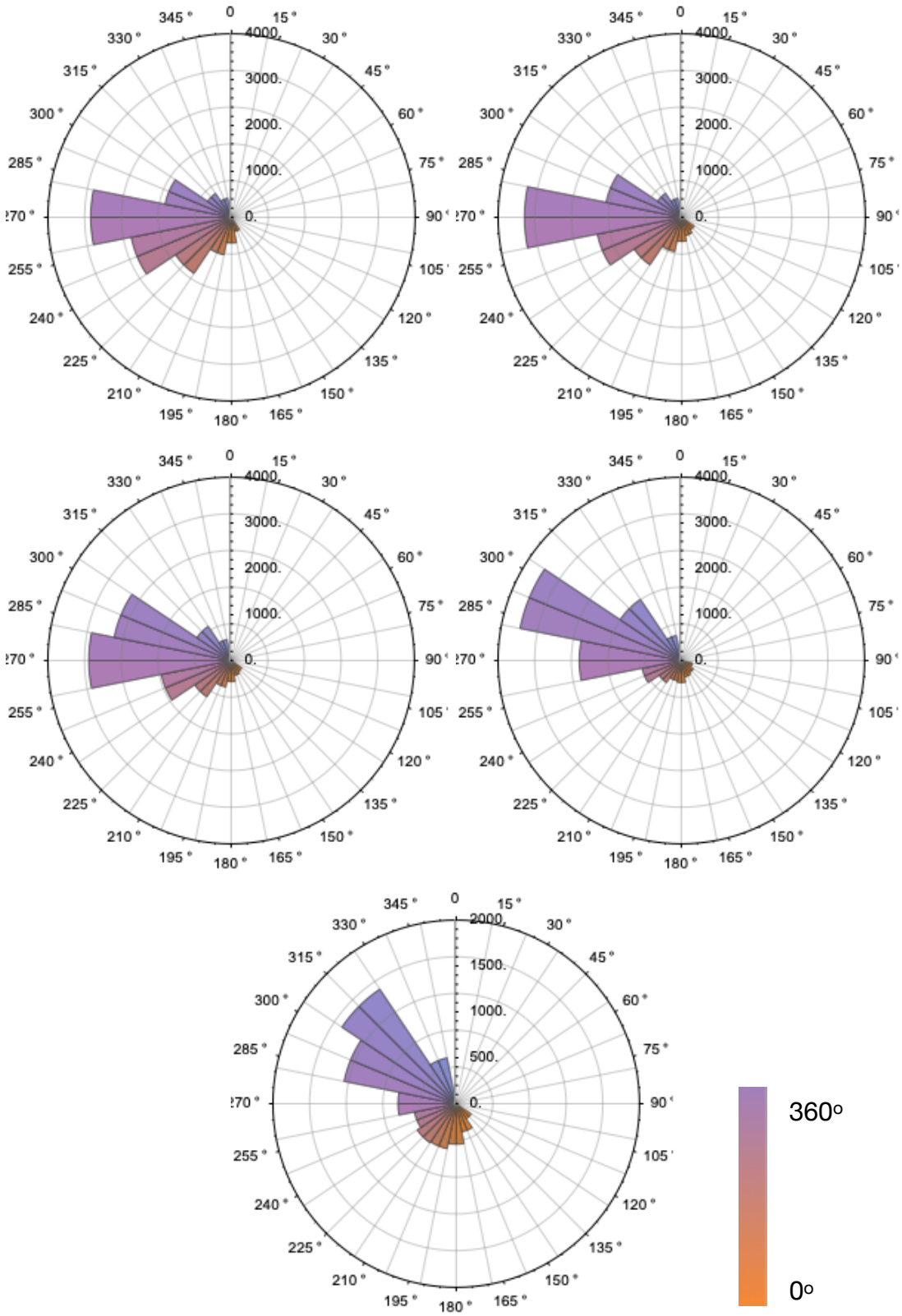

Figure 7.4: Swell event numbers for buoys A to E on the month of January, with the radius showing the number of swell occurrences and the spectral angle of incidence.

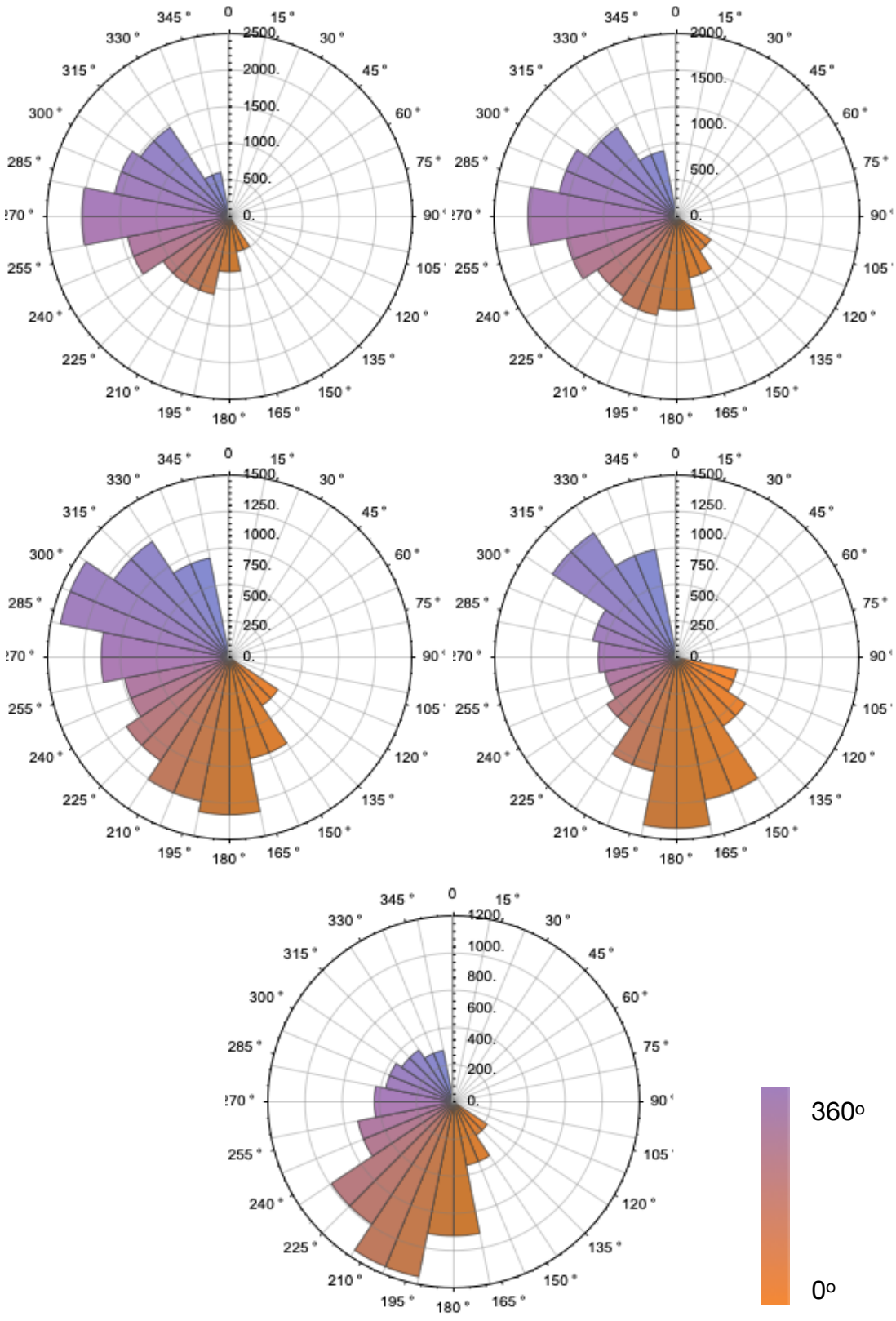

Figure 7.5: Swell event numbers for buoys A to E on the month of October, with the radius showing the number of swell occurrences and the spectral angle of incidence.

Wave modal frequencies for the local winds at systems are calculated, using the Pierson-Moskowitz and Jonswap spectrums in Tables 7.5 and 7.6.

Mean±σ	A(m/s,Hz)	B(m/s,Hz)	C(m/s,Hz)	D(m/s,Hz)	E(m/s,Hz)
Jan	$8.5^{\pm 3.5}$, (0.18)	$10.4^{\pm 4.4}$, (0.15)	$9.4^{\pm 4.4}$, (0.16)	$8.9^{\pm 4.1}$, (0.17)	$12.7^{\pm 7.0}$, (0.12)
Feb	$7,1^{\pm 3.3}$, (0.21)	$9.3^{\pm 4.3}$, (0.16)	$8.9^{\pm 4.2}$, (0.17)	$9.0^{\pm 4.1}$, (0.17)	$12.6^{\pm 6.8}$, (0.12)
Mar	$7.9^{\pm 4.5}$, (0.19)	$9.0^{\pm 4.0}$, (0.17)	$8.3^{\pm 3.9}$, (0.18)	$8.1^{\pm 3.9}$, (0.19)	$14.5^{\pm 7.2}$, (0.10)
Apr	$7.6^{\pm 3.6}$, (0.20)	$8.1^{\pm 4.0}$, (0.19)	$7.9^{\pm 3.7}$, (0.19)	$7.7^{\pm 3.5}$, (0.20)	$16.2^{\pm 6.9}$, (0.09)
May	$6.7^{\pm 3.6}$, (0.23)	$7.4^{\pm 3.4}$, (0.21)	$7.1^{\pm 3.3}$, (0.21)	$7.3^{\pm 3.2}$, (0.21)	$15.0^{\pm 6.7}$, (0.10)
Jun	$6.6^{\pm 3.2}$, (0.23)	$7.0^{\pm 3.2}$, (0.22)	$7.2^{\pm 3.0}$, (0.21)	$7.9^{\pm 3.3}$, (0.19)	$14.9^{\pm 6.9}$, (0.10)
Jul	$7.4^{\pm 3.1}$, (0.20)	$6.6^{\pm 2.9}$, (0.23)	$7.1^{\pm 2.9}$, (0.21)	$7.5^{\pm 3.2}$, (0.20)	$13.4^{\pm 6.0}$, (0.11)
Aug	$7.3^{\pm 3.1}$, (0.21)	$6.9^{\pm 3.0}$, (0.22)	$7.0^{\pm 3.0}$, (0.22)	$7.2^{\pm 3.0}$, (0.21)	$14.1^{\pm 5.5}$, (0.11)
Sep	$7.9^{\pm 3.3}$, (0.19)	$7.5^{\pm 3.6}$, (0.20)	$7.6^{\pm 3.3}$, (0.20)	$7.9^{\pm 3.5}$, (0.19)	$13.4^{\pm 5.7}$, (0.11)
Oct	$8.2^{\pm 4.1}$, (0.19)	$8.3^{\pm 4.4}$, (0.18)	$7.9^{\pm 3.8}$, (0.19)	$8.3^{\pm 3.7}$, (0.18)	$12.7^{\pm 6.0}$, (0.12)
Nov	$7.7^{\pm 4.1}$, (0.20)	$10.2^{\pm 4.6}$, (0.15)	$9.2^{\pm 4.2}$, (0.16)	$8.2^{\pm 3.9}$, (0.18)	$12.9^{\pm 6.9}$, (0.12)
Dec	$8.7^{\pm 4.4}$, (0.17)	$10.3^{\pm 4.6}$, (0.15)	$9.6^{\pm 4.5}$, (0.16)	$9.1^{\pm 4.3}$, (0.17)	$12.2^{\pm 7.0}$, (0.12)

Table 7.5: Mean wind value at buoy systems A to E and wave frequency associated with these speeds using the Pierson-Moskowitz spectrum.

Mean	A(Hz)	B(Hz)	C(Hz)	D(Hz)	E(Hz)
Jan	0.15	0.05	0.09	0.09	0.12
Feb	0.16	0.05	0.10	0.09	0.12
Mar	0.16	0.05	0.10	0.09	0.11
Apr	0.16	0.06	0.10	0.09	0.11
May	0.16	0.06	0.10	0.10	0.11
Jun	0.17	0.06	0.10	0.09	0.11
Jul	0.16	0.06	0.10	0.10	0.12
Aug	0.16	0.06	0.10	0.10	0.12
Sep	0.16	0.06	0.10	0.09	0.12
Oct	0.15	0.06	0.10	0.09	0.12
Nov	0.16	0.05	0.10	0.09	0.12
Dec	0.15	0.05	0.09	0.09	0.12

Table 7.6: Peak frequency for the local winds blowing over a fetch for systems A to E.

Wind data processed during the representative time indicates that the regional wind weather has an average of 8.0m/s, with a larger deviation on the south of the west Pacific Basin. The results for the modal frequency of the Pierson-Moskowitz spectrum show that waves with an average value of T=5s might dominate the spectrum of the local open sea area; however, large deviations of gusts producing wave periods over 8s are shown in the local area. Results for the local long waves produced by winds blowing continuously over the fetch x defined in Table 7.3 show that wind waves can reach values of f=0.1Hz, with a max deviation in buoy B of f=0.6Hz.

7.3 Characterisation of the local swell conditions

To track and record swells, the next boundaries were defined: a boundary for the frequencies to detect and discriminate short swells, and a threshold value to account for a large quantity of the swell spectrum occurring on the coast. The main angle of incidence and the chosen frequency value of f=0.1Hz were used to search for swell dominant conditions in a suitable geographical location on the coast. The aperture for this search was chosen to cover more than 50% of the swell events during eight years. Two of the systems listed below were used to track swells and determine the most common frequencies larger than f=0.1Hz in the west direction. The description of the methods, the systems where the data is taken, and the results are explained in the next sections.

7.3.1 Local swell measurement and local wave height

The local area designated as the Farallones area on the San Francisco coast was chosen to use a simple track and detection swell algorithm due to its wide data availability and also the detailed physiographical surveys that provide bathymetry data in the area. The buoys systems used to characterise the local swell events and their properties are shown next page in Figure 7.6. The buoys' number code and geographical

location can be found in Table 7.7. Swell conditions were measured using the algorithm defined in section 3.4.4.

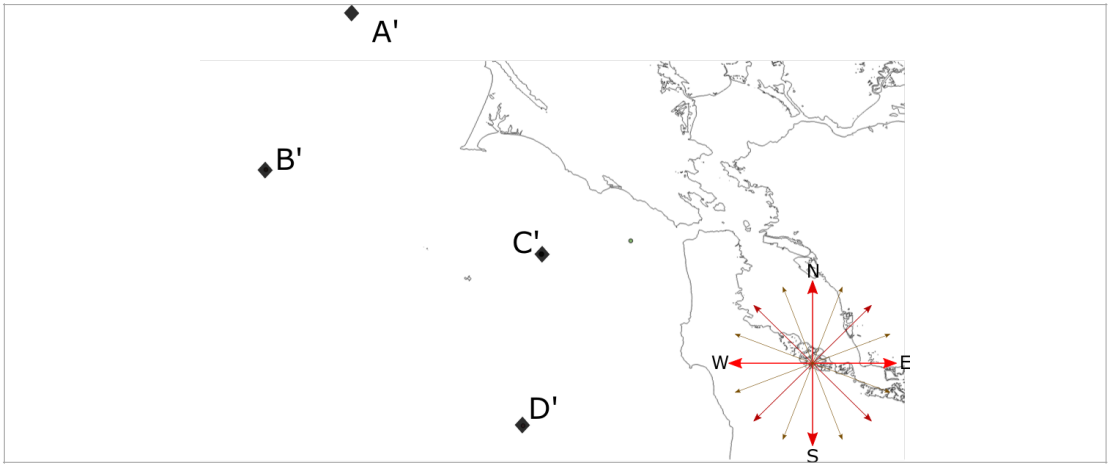

Figure 7.6: Buoy configuration A'-D' used to detect incoming swell from the direction adjusted at buoys A-E.

Buoy system	Coordinates	Depth (m)
(A') 46013	38°15'12" **N** 123°18'12" **W**	550
(B') 46214	37°56'12" **N** 123°27'47" **W**	550
(C') 46026	37°45'14" **N** 122°50'20" **W**	54.9
(D') 46237	37°47'11" **N** 122°38'6" **W**	550

Table 7.7: Buoy systems used for the swell local detection on the California coast.

The algorithm searches the swell propagating from the west direction, this direction being defined by the angle of aperture [281.25º-258.75º], which covers almost 50% of the swell events. The event search covered the spectral bands over f=0.1Hz. The analysis of the local conditions was conducted by characterising the local swell' propagation and the statistical significant wave height for the zone. The method used the systems B' and C' for the local swell propagation characterisation and the systems A', B', and D' to find the distribution for the significant wave heights at the dominant swell periods. To characterise the dominant swell propagation and its periods, data from systems B' and C' were used. The systems measure the sea weather conditions every 30min. If detection of dominant swell conditions occurred at system B' in deep waters, calculations for the wave

linearity using the statistically measured sea conditions are performed. To calculate the possible linearity of the sea weather during these events, the dominant peak frequency (*DPD*) and the significant wave height H_s were used. With the aforementioned values, the swell non-dimensional characteristics are calculated using equations 2.6 and 2.6 from Chapter 2, as seen below.

$$y = \frac{2H_s}{g_l DPD_{swell}^2} \tag{7.6}$$

$$x = \frac{h_0}{g_l DPD_{swell}^2} \tag{7.7}$$

Equations 7.6 and 7.7 use the local gravity g_l for the specific latitude and longitude. Swell events that dominate the spectrum and satisfy the linearity conditions are isolated. Isolated events used the dominant frequency band corresponding to the swell event being propagated to find its approximate velocity of propagation vp. The velocities of all events detected on system B' were used to calculate the swell arrival time at station C' in transitional water depths. The conditions matched for both systems were then stored and divided using their frequency bands, and the data stored shows the most common swell dominant conditions in the area. To characterise statistically significant wave height for the sea surface for the area, the data from the systems in Figure 7.6 was used to obtain the distribution of all wave events and their significant wave height. The method used the registered data from the year 2017. The data recovered from the systems registry was processed to create a distribution of the wave periods and wave height events during the decade covered. from this sample The data sample covers short waves of frequencies f=0.33Hz to long swells with frequencies f=0.04Hz. Wave height measured conditions range from H_s=0.5m to H_s=8.5m.

7.3.2 Local swell measurement and local wave height results

The results of the swell events analysed show a total number of 976 swell dominant events, where both events were found to be detected at

system B' and then propagated to system C'. The swell occurrences show that almost 94% of the events fall in the range of [0.085-0.059]Hz, which belongs to the period range T=[11.75-17]s. The percentage distribution of swell events distributed from f=0.094Hz to f=0.045Hz is shown in Figure 7.7.

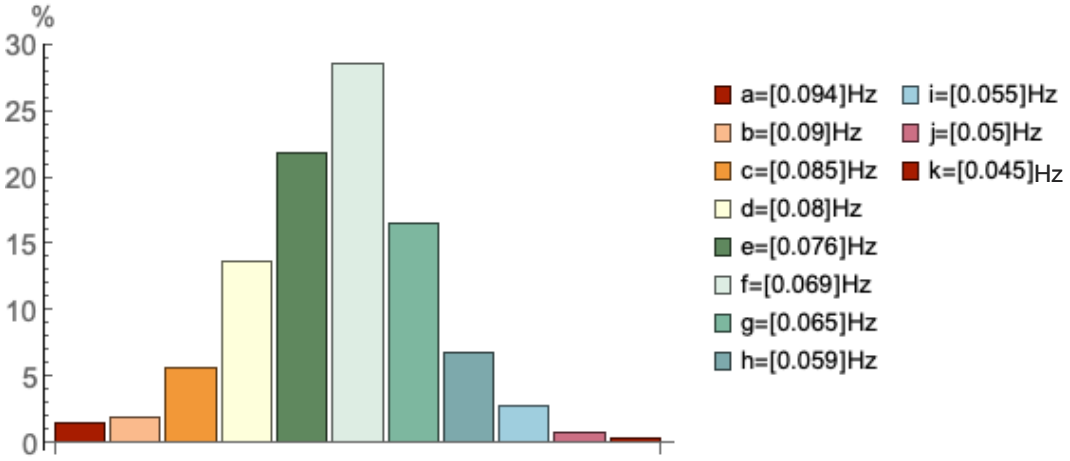

Figure 7.7: Percentage of occurrences of swell events, where spectra is divided into 10 frequency ranges from 0.094 Hz to 0.045 Hz.

The data analysed to find the statistical distribution of the dominant wave heights in the area is shown in Figure 7.8. Wave events occurring have a defined period range of T=7s to T=17s. Wave amplitudes were found to be less or equal to one metre with values of H_s<2m 60% of the time.

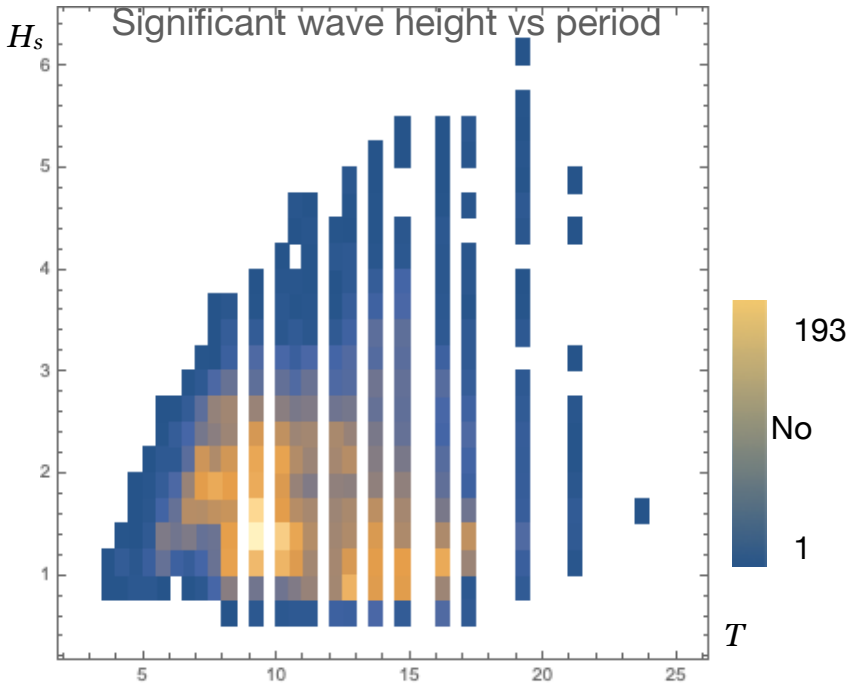

Figure 7.8: Percentage of occurrence relative to significant wave height in the local zone.

The moderate steepness values suggest that swell and long-wave systems are the dominant wave weather phenomena in the area. Lower amplitude values for frequencies above f=0.09Hz indicate that the swells detected might radiate to our positions from far away. Wave data for long waves in the range of T>7s to T<10s with larger amplitudes suggests wave systems are created in the near zone. The most frequent dominant swells with frequencies f=[0.085-0.059]Hz and wave heights H_s≤2m were used to characterise a representative set of swell conditions in the simulated zone.

The case study also includes values for wind waves. The simulation is run in this case with a swell-dominated seas and then a wind-dominated sea including swell components. The spectrum for waves with lower periods and higher amplitudes was extracted from sensors which belong to the Scripps Institution of Oceanography, which was the device with NBCD ID “46237”. A file with the wave conditions for smaller waves from which the conditions simulated were extracted is located in the Appendix section C, covering at least five years of measurements from where the representative data was extracted. The current values used for the simulations, are the predicted in the area outside the bay near the San Francisco Bay bar. Currents can range from 2 knots to 3-4 knots or [1-2]m/s. Velocities near, inside, and over the bar can be larger, topping [5-6] knots, however these conditions were not simulated as the author believes the changing physiography of the sand bar, and the denser area of navigation, might make the place inaccessible for any turbine case scenario. The velocities were taken from the model Operational Forecast System (OFS) which belongs to the NOAA and has been thoroughly validated by several case studies [133], [134], [135].

7.4 Geographical location for the simulated turbine

The modelled zone is known to have an abrupt bathymetry change in less than 100km due to the geological composition of the area. The area is composed of the subduction zone of the Pacific Plate and its border with the North American Plate, giving the shelf narrow and very steep

physiographical characteristics. The narrow length is composed of a transition zone from -3000m on the abyssal depths that rise to an average of 50m at system B'.

The area also features several faults that cover the coast and the shallow waters. The bathymetry result of this interaction is a very linear and plain platform, with very small variations of one metre along more than 1km of length. The shelf is known to be very accessible for any purpose and also to have large biodiversity. The currents in deep waters are known to have higher velocities relative to their depth. Values at 250m can reach 0.4m/s depending on the season, as pointed out by Noble et al. [136] and Steger et al. [137]. Studies have shown that feasible currents for energy production exist, and ADCP transects have shown high velocities around the Golden Gate area with peaks of [1.8-2.0]m/s [138]. These currents are produced by tides, however they are strong enough to reach over 1m/s in the area between the Farallones Gulf and the Golden Gate area, covering more than 20 kilometres inside the ocean. The area of interest is shown in Figure 7.9.

7.4.1 Turbine geographical position

The area chosen to simulate our wave and obstacle condition was a section on the parallel coordinates (-122.57,37.704) and (-123.738,37.708), in the shelf zone of the Farallones Gulf area. Publicly available data, part of the United States Geology Survey (USGS), was used to create a contour map which retained the main characteristics of the sea bathymetry surface. The area offers a gradual slope, going from 60m to 47m over a 20km extension along the designed swell main direction of incidence 270º.
The final transect of the approach to the simulated site covers a bathymetry jump from 48m to 36m depth. In this case, we modelled the turbine to sit at 30m after a jump from 38m. This makes our case scenario close to our simulation and experimentation case. The general transect is in Figure 7.9. The current value, used as a representative value of the peak currents of the area, was set at 2.0m/s, which is a top current found in the area during ebb

and flow according to the Operational Forecast System [139]. The turbine measures were kept in the same dimensions as the blade profile, hub height, and rotor radius, as in Chapter 6.

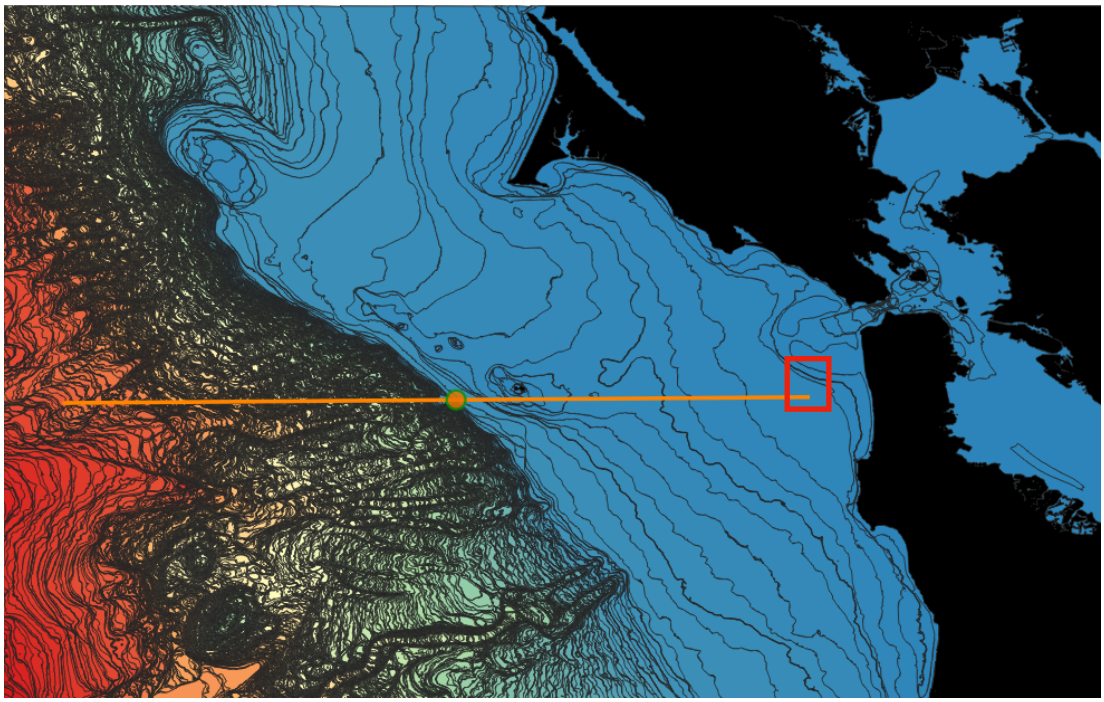

Figure 7.9: Map showing the area of the bathymetry cut chosen in orange, marking the end of the continental rise, where the length y covers approximately 50km. In the figure the square represents the area of turbine placement.

7.4.2 Case Scenario

To characterise the sea weather, three case scenarios were chosen under the 59.3% of wave weather conditions at the chosen site. The first scenario is composed of large swells with small wave heights of no more than $1.8m$ and periods larger than $14s$. The second case scenario is composed of shorter swells with periods between $12s$ to $7s$ and amplitudes reaching $2.5m$, and the third case is composed of soft swells and local wind waves. The conditions are the ones related to the swell weather analysed in this section and the periods, heights, and wave order can be found in Table 7.8.

The conditions studied are chosen to analyse three main points

- Characterise the mechanical response to swell weather composed of the large period with soft amplitudes vs shorter period with amplitudes.

- Characterise the changes in the mechanical thrust and torque if the BEMT model is modified to account for possible wave changes caused by a bathymetry rise.
- Characterise how the mechanical response changes if the model is modified to account for the wave propagating over an obstacle just before our simulated tidal turbine deployment.

$T\,(s)$	$H(m)$
Long swell	
15.38	1.27
16.67	0.8
18.18	1
13.3	1.27
19	1.4
14.24	1.8
Short swell	
12.5	1.33
11.76	1.5
10.5	2.1
9.09	2.5
7.57	2.2
8.33	2
Mixed (Wind waves)	
16.67	0.8
18.18	1
9.09	2.5
5.6	2
6.5	3
14.24	1.5

Table 7.8: Weather cases simulated in the chosen area.

7.4.3 Wave weather and mechanical turbine response

The responses to the three types of wave weather characterised show how different the responses for the torque and thrust can be depending on the type of waves propagating on the deployment site. The responses for the torque and thrust show how long swells with a limited amplitude cause a larger mechanical response than the soft swells and mixed wave weather with larger wind-wave amplitudes reaching $2m$ to $3m$ in height, which could represent steeper wind waves that are locally produced. The response to large swells in length and period shows an increase larger than 60% for the thrust and 40% for the torque in Figures 7.10 and 7.11.

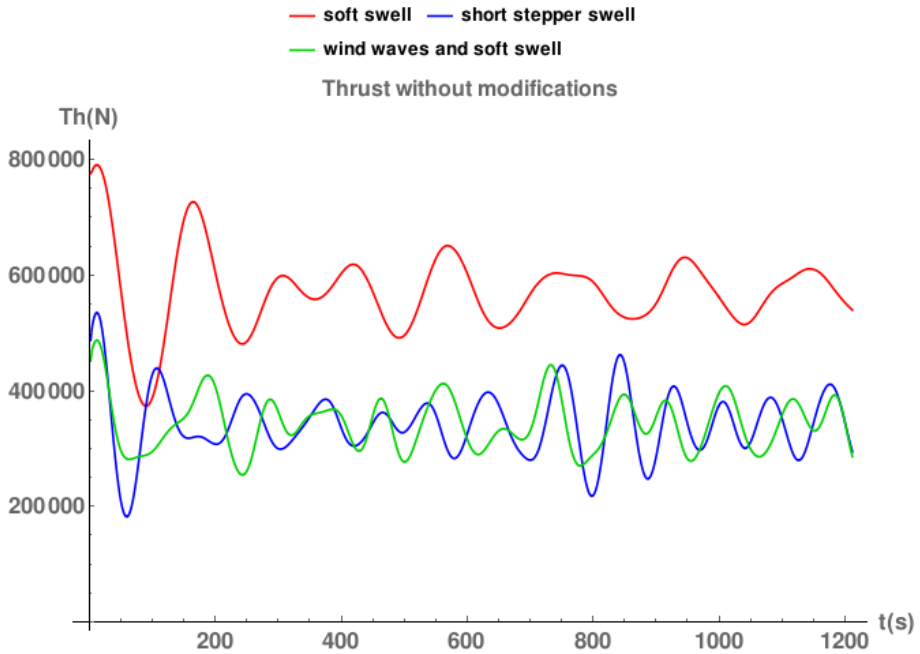

Figure 7.10: Mechanical response of the thrust to three types of wave weather in the studied zones using the BEMT model without modifications.

The difference between the response using wind waves in green and short steeper waves is very similar, almost 95%, which was caused by the amplitudes chosen. However, this shows a very small variation if higher wind waves are included compared to larger swells with moderate amplitude, which appear to dominate the signal produced by the turbine.

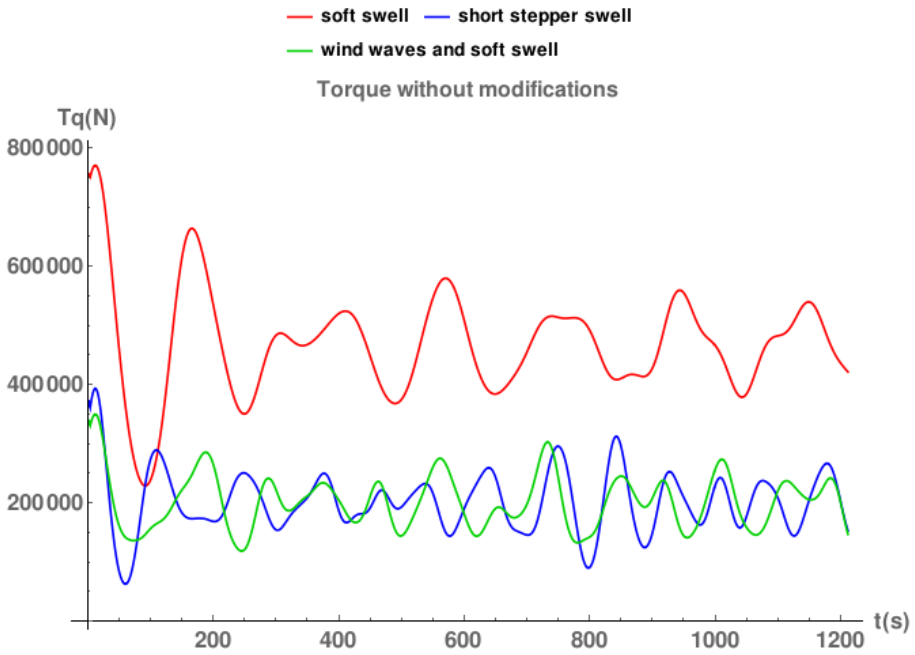

Figure 7.11: Mechanical response of the torque to three types of wave weather in the studied zones using the BEMT model without modifications.

7.4.4 Wave weather and mechanical turbine response using the modified model

The mechanical response of the turbine when the BEMT model is modified to take into account an obstacle before the turbine shows how the torque in the rotor of the device changes in the three cases. In this case, as the changes depend on the wave height, its relative size before and after has a large impact on how the model reacts to these changes.

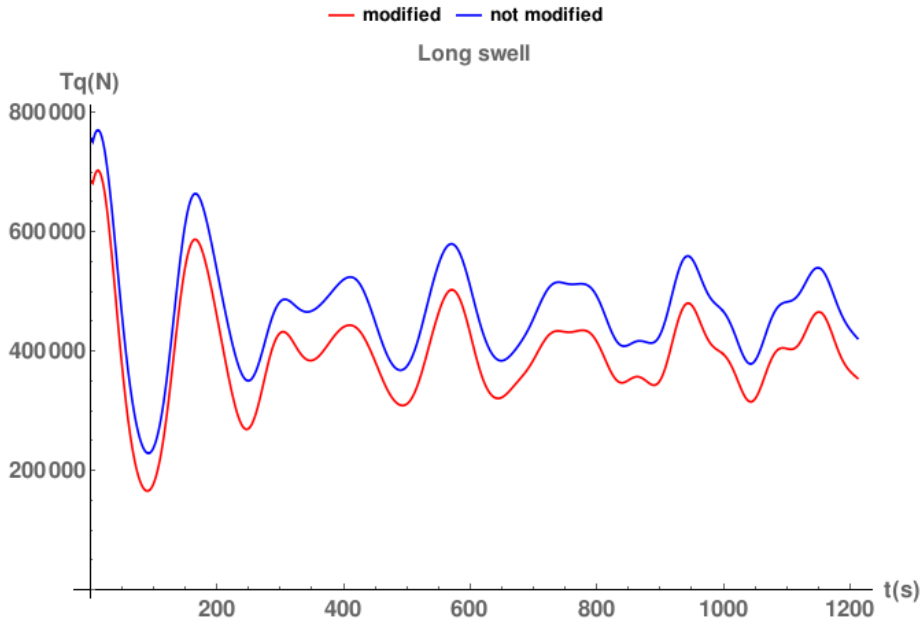

Figure 7.12: Mechanical response of the torque to a wave weather made of long and soft swells in the studied zone using the BEMT model, with and without modifications.

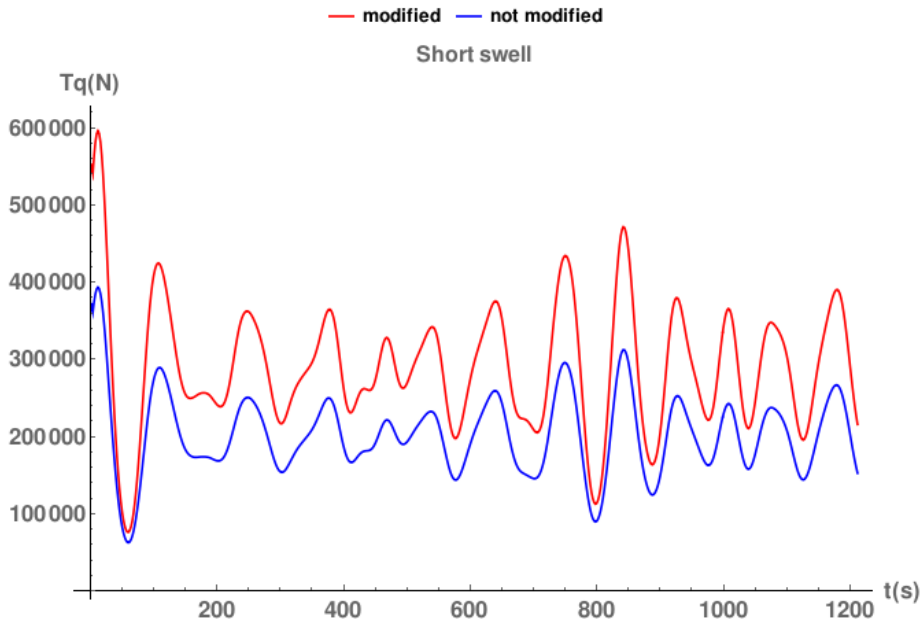

Figure 7.13: Mechanical response of the torque to a wave weather made of short steeper swells in the studied zone using the BEMT model with and without modifications.

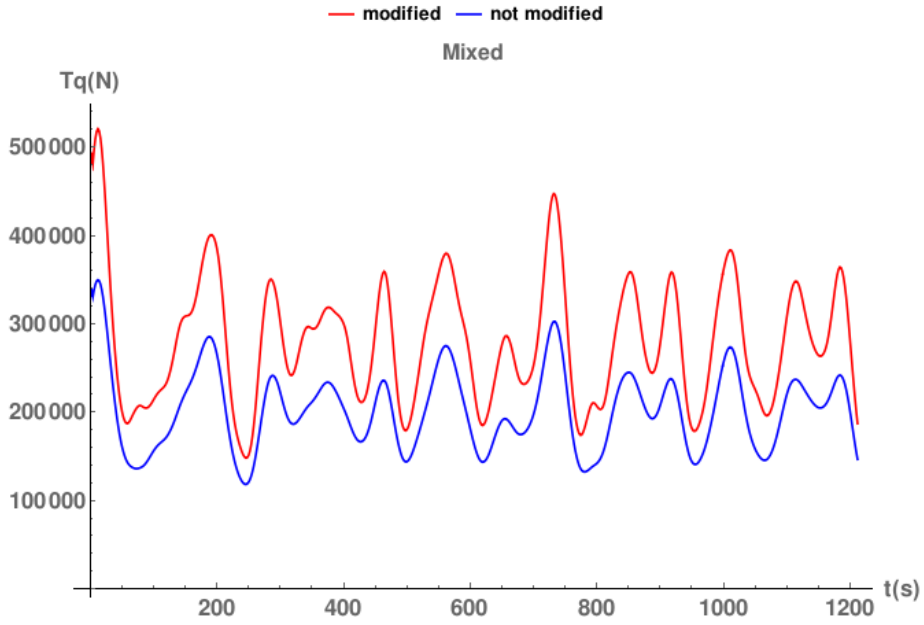

Figure 7.14: Mechanical response of the torque to a mixed wave weather in the studied zone using the BEMT model with and without modifications.

Larger swells with low height see a change of 11% in the torque value if the model is modified. Larger heights in shorter swells and wind waves see a larger change of 17% for the shorter swells and 16% for wind waves with higher amplitudes mixed with swells. The results for the torque can be seen in Figures 7.12, 7.13, and 7.14.

The thrust shows the same patterns, with larger differences of 30% and 27% for the short steer waves and the mixed wave weather respectively. The wave propagation only causes an 18% difference in the turbine thrust for long swells with moderate amplitude. If the values are then compared to the original cases, Figures 7.15 and 7.16 are obtained.

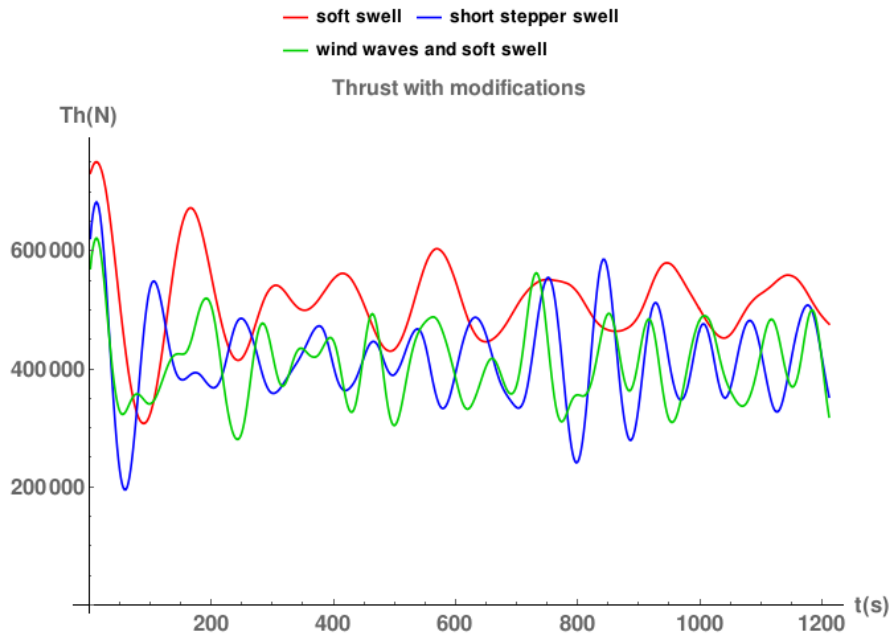

Figure 7.15: Mechanical response of the thrust to three types of wave weather in the studied zone using the BEMT model with modifications.

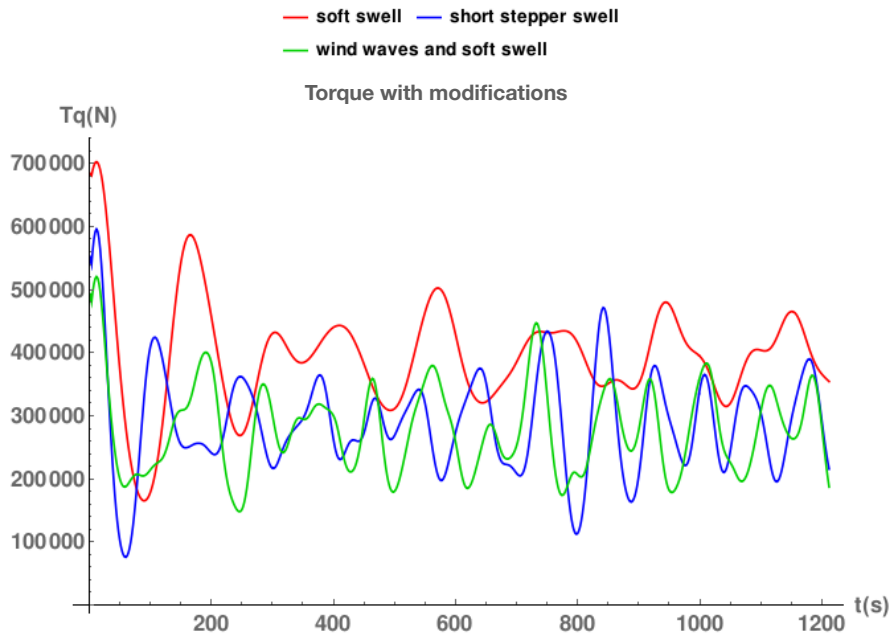

Figure 7.16: Mechanical response of the torque to three types of wave weather in the studied zone using the BEMT model with modifications.

The effects caused by the changes in the wave height after it propagates over the obstacle cause large differences in the signature of the torque and thrust for the BEMT model in Figures 7.15 and 7.16 compared to the original model in Figures 7.10 and 7.11, showing a high sensitivity to the wave height, as was found in the sensitivity analysis in Chapter 6. The differences between the torque and thrust for the long waves, compared to the short swells and mixed wave weather with steeper wind components, is 19% and 21% respectively for the thrust and 27% and 30% for the torque in the rotor. A table showing the differences in the percentage of mixed weather with wind waves and short swells compared to long swells is shown below in Table 7.9:

	Not modified		Modified	
	Short swell	Mixed	Short swell	Mixed
Torque	60%	60%	27%	30%
Thrust	40%	40%	19%	21%

Table 7.9 Torque and thrust difference in percentage for a mixed wave weather and short steeper swells vs wave a weather composed of soft large swells, as found in Table 7.8.

The values in Table 7.9 are compared against the soft large swell weather as found in Table 7.8. Values for the columns where the short swell and the mixed weather are not modified are compared against the case where the large swell is not modified. Values for the columns where the model is modified are compared against the case where the large swell wave weather is also modified. In general, the model reacts by producing more significant differences in the mechanical response for this wave weather than height changes, this being the case for a limited change in depth before and after the obstacle of $8m$.

It is necessary to say that this occurs at depths below 50m where the wave velocities caused by the wave heights would have a large impact. Waves simulated here have larger amplitudes and periods than the ones extracted to simulate the model reaction in the previous chapters, but all remain linear or second order.

7.5 Conclusions

The wave data analysed in this chapter proves to be consistent with a seasonal phenomenon, having a preferred directionality as shown in Figures 7.4 and 7.5. A zonal analysis shows how the wave weather is characterised statistically by the mean wave height and period, showing a clear height and period range in the local area, and having heights lower than 3m and periods between 7s to17s more than 66% of the time. This is particularly useful as it makes the sea weather easier to characterise for the purposes of tidal turbine deployment.

The case study using BEMT shows how three possible types of wave weather found in the area affect the tidal turbine response. In this aspect, it is clear how large swells are the first contributor to the non-steady response of the turbine for the torque and thrust, followed by steeper swells and wind waves. In this case, where the turbine is in a large plain area over the shelf, the torque and thrust signals are 60% and 40% greater than those caused by short swells and mixed water, as shown in 7.4.3.

The inclusion of changes in the wave height after the wave propagates over the obstacle results in a different response in the turbine's torque and thrust for all three types of wave weather. In these cases, the non-steady values for the mixed weather and the short swells produce a response which is closer to the torque and thrust produced by short swells with moderate amplitude.

The long swells remain the main contributor to non-steady forces felt by the turbine. However, in this case, the difference between wave weather dominated by gentle soft swells with heights no larger than 1.8m and the other two cases is reduced by half for both the torque and the thrust.

8 Discussion

A brief discussion of Chapters 5, 6, 7, and the mathematical models are made in the next pages. The discussion does not follow a chapter-by-chapter progression, but instead addresses the subjects of wave propagation, the turbine mechanical response, and the different wave weather effects on the simulated model. The discussion takes the mentioned chapters as a base and extracts useful information from them.

The key points of discussion will be:

- The model challenges and limitations;
- The scaling and harmonic generation;
- The experimental conditions;
- The predicted and measured effects;
- The sensitivity analysis and power output as predicted by the model;
- The wave weather analysis and case scenario results.

8.1 Experimental model

The two kinds of experiments run by past researchers are focused on two cases: solitary waves, as for Goring [83], and wave trains under relatively shallow water conditions, as for Ting et al. [79]. These experiments are designed for different purposes. The first aforementioned studies measure the propagation of a wave resembling a tidal wave, while the second one focus on the analysis of the harmonics and scattering of the incident waves produced by an obstacle.

In these cases, two main differences compared to our experiment are found: first, the depth of propagation for both cases before the obstacle;

and second, the depth of the obstacle obstructing the wave path in the experiments analysing the harmonics and scattering.

The depth of propagation was inadequate for our experiments if we take the physical conditions set for Goring [83] and other researchers like Newmann [70], where depths range from h=2$\pi\lambda$ to conditions where the wave behaves more like a tidal wave arriving over a shelf h<<λ. In the harmonic analysis cases, like Ting et al. [114] and Massel [76], obstructions in the tank are equal to the most extreme of our cases, and wave heights are at least 10 times higher in the case modelled by Massel's work with H=10m. Their conditions were in fact chosen to study harmonics, increasing the energy transmission to higher harmonics.

To minimise the possibility of our experiments enhancing the energy transfer to the upper harmonics, the depth over which the wave transmitted was larger than the experiments by Ting et al. and the amplitudes were lower than experiments by Massel, with waves having a very low height of 1.1m for the sensitivity analysis and no more than 3.5m for the case study. This does not eliminate the possibility of harmonic generation but made the possibility of energy transfer minimal so no large amplitudes produced by harmonics could obscure our wave signature in the instruments. However, it is possible that experiments using the larger obstruction ratio with the largest periods had a moderate energy transmission, as in the numbers shown in Table 4.11 for the ratio defined by Mei and Ünlata [81]. These cases where the obstruction is larger and where larger amplitudes occur would need a frequency analysis to analyse the effects caused by harmonics. Experiments to test a wider range of amplitudes and depths to characterise the energy transmission as the depth decreases and the amplitude increases could be necessary, but no such study exists to the author's knowledge.

In the case of the challenges related to the physical model occurring in a deeper wave regime, the experiment had to be designed with the aim of measuring the smallest changes in the amplitude over and after the

obstacle. It was not known if the models would be able to behave the same at different depths, even if scholars such as Newmann suggested a working region from shallow waters to transitional water, in the case of Lamb's theory. Validation of the theories, in this case, could not be the primary objective for the author, so it was theorised that measuring the wave-obstruction interaction was a better solution. Despite validation not being a primary objective, the results obtained where the accuracy of Naghdi and Marshall's theory was reasonable were useful to include this later on as a factor in our BEMT model.

8.2 Scaling and harmonic generation

For physical modelling of wave phenomena, it is normal to scale using the Froude number. In our case the Froude number is consistent, but another approach was taken. The scaling process first scales the wave trains depending on their wave order and depth of propagation in the wave tank, and later scales these conditions for a real case scenario for large swells which could normally be found in the sea. A comparison of the Froude number was done later, and here an error was found of $2m$ for the depth.

The method proved to be precise enough, but as the conditions need to be closer to the real ones, a cross-checking using the Froude number for both conditions is advised, as errors in the length of waves and depth of propagation could lead to different results and unknown margins of errors, as mentioned by Noble et al. [107]. The method proposed by Noble et al. proves to be very useful. In our case, the relative depths in the tank and area of interest using our method to scale the waves were initially calculated to be $40m$ depth per $0.6m$ inside the tank, later was found our model had an error of around 1.8m using the Froude number and it was corrected to ($42m$/ $0.6m$). The accuracy of Noble et al.'s diagram is close to giving us an error of $1.5m$, proving to be a useful way to crosscheck our initial calculations and later correct them using the Froude number.

Returning to the discussion about the harmonic generation, it is important to notice the central tendency values in Table 5.11, showing a very large data scatter for the larger waves. The large data scatter and the values for the factor defined by Mei and Ünlata [81] in the largest waves in Table 4.11 show the possibility of harmonics interfering. Neither author indicates how to identify when harmonic generation could start to be important as this depends on the experiment characteristics.

A good procedure could be to not only look at the number defined by the authors to account for the amplitude of the harmonics, but also the data scatter and irregularity of waves, while also using the aforementioned numbers. In cases where the obstructions are large and higher wave orders are tested, a frequency analysis would be required to know how the wave energy is transferred and how these harmonics could affect the induced wave velocities along the water column.

8.3 Experimental conditions

Experimentally, there were a number of limitations which make it harder to measure wave propagation in the tank, solutions for which had to be found so measurements could deliver useful information. In this case, the normal evolution of the waves, deforming themselves as they move in the tank, was particularly difficult.

Larger period waves registered an increase in their heights and a decrease in their detected lengths as they moved inside the tank. Meanwhile, shorter waves will increase their detected length as the wave shape deforms across the tank. In this case, this normal progression of the waves as they unfold, as in Figure 5.12, was used as a useful marker. If the wave's tendency was to shorten in length and increase in amplitude, any behaviour to the contrary after propagating over an obstacle was an indicator of the obstacle interaction. The effect is visible in Figures 5.31 and

5.37 where the lengths detected start to move away from the case where no obstacle is placed in the tank.

While measuring the detected wavelengths, the comparison between values was more important than the validation of theories, mostly because the length detected was not considered accurate enough, so tendencies will be the main marker to follow the obstacle and wave interaction for this parameter. Heights on the other side were easier to detect and follow.

8.4 Predicted and measured effects

The formulations validated to account for wave propagation show how Lamb's theory is less accurate than Naghdi and Marshall's for larger depths. There is however little variation in the theories validated because of the very limited wave height which makes their predicted values very close to each other.

In this case, again, an analysis of the effects rather than a simple validation seems more useful as it can divert attention to fit a model, rather than measuring the actual effects of the wave propagation. In these cases, the methods based on linear regression might be more useful if a very large set of waves are tested using methods such Ting et al.'s.

8.5 The sensitivity analysis and the predicted mechanical performance

When analysing the results of the sensitivity for an individual blade and the overall rotor, both were less sensitive to the obstacle size and the wave period than to the wave height and current velocity. The larger factor in the sensitivity analysis is the wave height.

If we take the results as they are, this could lead to misleading conclusions. If the obstacle size were to increase substantially, then this would have a direct effect on the wave height, leading to a link between the

smaller factor and the larger factor in the model. This also takes us to another connection between the variables where the sensitivity analysis is made, which is the wave period.

The theory proposed here and the one by Naghdi and Marshall point to dependence between the incident wave period, the obstacle ratio of obstruction, and the transmitted wave amplitude. Experiments by Goring, and Newmann and the one conducted in this research also point to this relationship. In this case, three variables where the sensitivity analysis is made are related to each other and, depending on their values, they could have a strong influence on the wave height after the obstacle. In this case, the Morris method gives us insightful information, but it does so under the limited range we gave to our variables. It is possible for steeper swells and larger swells under larger obstructions to have a different signature than the one seen in Figures 6.8 and 6.9. This leads us to the difference in the sensitivity and the thrust studied by Nevalainen and the author of this work. While for Nevalainen current is the first factor and wave height the second, in our case, this is the other way around.

The sensitivity analysis should also be used with care as it only indicates the way variables behave in the limited range of space where they are measured. The exact ratio of their monotonic behaviour, or the exact relationship of their non-linearity, is not known. Changes in the model will also alter the responses of the output as seen in this work for the wave height and current when compared to Nevalainen's work. The author believes it must be used as a tool to approximate the first possible interaction between the turbine mechanical response and their variables, but never as a tool to know (with certainty) their behaviour. However, it remains a useful first approach.

Despite its shortcomings, the usefulness of the Morris method is observed in Figures 6.12 to 6.15. Figures 6.12 to 6.15 show the torque and thrust variation, which is small because the values chosen for this induce only smaller changes. In the mentioned figures, thrust and torque are plotted

for two different types of waves with two different current values. The turbines sit over a sudden bathymetry rise which modifies the wave height. However, the limited amplitude, limited rise, and single wave component do not show a very large change in the mechanical signal. This is proven to be a misleading observation in the case where many wave systems interact and create larger crests and troughs.

8.6 Case study results and mechanical response

Observations were made for the mechanical response of the torque and thrust under different wave weather conditions, showing the importance of testing several data ranges for wave weather. For waves moving on a flat bottom, a calm sea without wind waves is a large contributor to the unsteady mechanical response of the turbine.

The model predicting a higher response than when using steeper waves and wind waves shows how local surface weather could be a bad indicator for the turbine response if only parameters such as the local height produced by wind-driven waves are taken.

It also observed how the results change if no wave propagation is included. Figures 7.10 and 7.11 show a very different response when the model includes the wave propagation in Figures 7.15 and 7.16. The large difference between results shows the limitations of the actual BEMT physical model and of its implementation. Despite the large differences, BEMT remains a useful preliminary tool to calculate the turbine behaviour. However, a need to upgrade the physical model could be necessary if more complex case scenarios were going to be solved in the future.

One of these possible complex scenarios is wave directionality which our case omits. Despite this omission, it is clear that if technologies can harvest low speeds and open ocean environments, swell directionality could be an important factor to take into account because swells have a large range of incidence, as shown in the Appendices section G3.

9 Conclusions

In the area of marine and tidal energy, a lot of emphasis has been put on the calculation of unsteady loads produced by wave events [36], [43], [44], [65], [120]. The work presented in the previous pages looks to contribute to the analysis of the mechanical response of a tidal turbine device using wave weather conditions that are common in the sea. It also includes a sudden obstacle interacting with the waves, modifying the local wave weather by changing the wave parameters, such as amplitude and wavelength. In this context, it is of greater importance to take into account not only the extreme events leading to higher loads and extreme mechanical responses, but also cases that can impact the lifecycle of the turbine in the long term.

9.1 Findings and contributions

The contributions of this thesis can be summarised in three main points:

- An analysis of the most important cases of wave propagation over an obstacle and the experimental validation of formulations for wave propagation under a wider range of depths and periods. The physical conditions tested try to resemble real-depth scenarios which are useful for engineering purposes in the coastal zone. Scenarios include a tidal turbine energy device under suitable deployment depths.
- The extension of the BEMT model to account not only for parameters with higher impact on the turbine such as current and wave height, but also for what could be considered local effects that are not linked directly to the flow over the rotor, such as a sudden rise in the sea bottom affecting the wave incident over the turbine.
- The proposal of an analytical and simple formulation to a model long waves propagating over an obstacle when they transmit from deep waters to transitional waters.

The findings, which can be linked directly to our main research questions, are as follows:

A) **Is there a given relationship between the changes produced in a wave after it propagates over an obstacle and its incident period?.** There are indications of a relationship between the transmitted amplitude of a wave, its wavelength, the obstacle size, and the incident wave period. The wavelength detected in these cases decreases consistently as the obstacle grows in size or length. However, the wave amplitude, which is also shown to be affected by the obstacle size, demonstrates a larger deviation in the values for the transmitted amplitude. We can divide these results as follows:

- Waves are disrupted by the obstacle, and the behaviour of the waves depends on the type of experiment. For exeriments where there is a decrease in the original tank's depth, waves with larger wavelengths increase their height by 40% in the most extreme cases and 3% for the lower values. The increase happens for the waves over the obstacle and after the waves propagated over the obstacle. For shorter-period waves, the effects are different. Short period waves see an increase in 20% of their original height of 20% in the most extreme cases over the obstacle. When waves proagate after their height can change 40% of their original value. The measurements to detect the change in the wave shape show other interesting effects of the wave propagation over the obstacle. Waves with larger wavelengths in the most extree cases have changes equal to 25% of its original value. Shorter waves see their original length changed by 10% of their original value.
- For experiments where the obstacle depth decreases, the waves transmitted are larger in height than the incident waves, as long as the obstacle is deeper. As the obstacle become shallower, waves

are more irregular in nature, and then even small amplitudes are detected.

- For experiments where the waves propagate over an obstacle of increased length, transmitted amplitudes are larger, reaching in the most extreme cases an increase of more than 10% of its original value for an obstruction of half the tank's original depth. However, all experiments where the obstacle obstructs 2/6 of the original tank depth show a large reduction in the wave heights.

- For the observations made about the calculated wavelengths detected by analysing the wave shape and movement, a direct effect is detected, especially for large waves which decrease their wavelength over the obstacle, as observed in Figure 5.36. However, this effect can be seen more clearly in Figures 5.37 and 5.31 for waves propagating over an obstacle of increasing length or decreasing depth.

- The results of the experiments are used to validate the theories of Naghdi and Marshall and Lamb, as well as the one proposed here. The results can be summarised as follows. Lamb's formulation predicts close values for the wave height, but Naghdi and Marshall's theory is accurate in predicting the transmitted height. The same is true for the formulation proposed here and the one by Naghdi and Marshall. The results behind the accuracy of Nahdi and Marshall can be linked to its formulation using finite depth water to solve the coefficient of transmission, this depth resembles most of our experiments. In this case, if a model of wave propagation should be used for long waves at moderate depths, Naghdi and Marshall's work is best suited for this. It is important to notice how then the formulation proposed here would suffice better for waves moving from deep waters to transitional waters, however, more experimentation is needed.

B) **Which variables are important for wave propagation over an obstacle and how do they influence it?.** Is observed how the length of the obstacle increases the wave height in a stronger manner than its height. The large variation in some cases for an increase of height suggests the creation of irregular waves over shallow and short obstacles. However, the variation is too large to obtain a clear relationship, telling us how much these values change the amplitude. It is very probable that the observed values are caused by non-linear interactions between the waves and the obstacle. In these cases, more experiments and a different type of study might be needed, for instance using statistical tools.

C) **Given a tidal turbine placed above a bathymetry change, could the wave trains propagated over the obstacle modify substantially the mechanical performance of the device after the wave trains change some of their parameters such as the wave height?.** The simulation of the turbine deployed after a bathymetry rise, using the formulation of Naghdi and Marshall to calculate the wave heights, shows how the mechanical response of the turbine changes if the wave propagation is taken into account.

- For larger swells and moderate amplitudes, the model shows that the torque and thrust are reduced if the turbine is placed after the obstacle. Short swells with steeper amplitudes and a mixed wave case scenario show an increase in the torque and thrust. The changes are 10% higher when compared to the model where no wave propagation occurs according to the BEMT model predictions in all cases.

- The sensitivity analysis of the system also shows a larger response to the wave height and a lesser response to the current velocity. This is contrary to what has been found by past researchers [36]. It is important here to observe how the obstacle size appears to be a small factor for both the overall rotor and the blade. However, it also

shows the importance of the interpretation of the sensitivity analysis results in some situations. In this case, the sensitivity analysis placing the obstacle size as a small factor is the result of the physical range we use for the depths and the obstacle size. Larger incident waves will create large wave heights if the obstruction is large enough, as observed in Chapter 7. The small effect of the obstacle size could be misleading if we only observe the Morris method results.

- The inclusion of the wave propagation also shows a large change if we compare three different types of wave weather. The model predicts a large difference between the response caused by long swells and shorter waves. If the wave propagation is included, for all cases the model shows a decrease as large as 50% in this difference.

D) **What are the effects of swell systems on the mechanical output of the tidal turbine rotor and its blades, compared to other types of wave weather?.** The model shows a large response to swells with moderate amplitude. It is observed how the response for larger waves with larger periods can be 19% larger than when using other wave weather conditions. In this sense, it shows how the wave period is a more important factor to take into account than the wave height when steady forces and loads are calculated at larger and even moderate depths. It is clear that wave height will have an important role, but because the wave velocities decrease as the depth grows and the depth of influence for the wave depends on the wavelength and depth, the period will be an important factor too. Swells with even moderate amplitudes will show a larger influence at larger depths. It is also important to observe how the measurements made only of the wave height on the surface will be insufficient to determine the response of a given tidal turbine simulated at a given depth in a specific location, but it would be equally important to utilise frequency analysis to determine the period T of the components.

9.2 Commentaries

The work carried out in this thesis shows how different sets of wave conditions and other changes such as a bathymetry constraints could have a substantial impact on a tidal turbine's mechanical performance. The work also shows how large unsteady forces caused by the waves are not unique to waves with larger crests, but also apply to waves with more moderate amplitude but larger wavelengths and periods, as observed using the case scenario. These observations move the attention from extreme events caused by larger waves to wave conditions which constitute a larger percentage of the wave weather in an area of deployment, such as steeper swells.

It is also necessary to comment on how this can have an impact on the understanding of wave loadings. It is true that wave systems will add their amplitudes, causing larger waves, but as the strength of the wave velocities depends on how far the wave penetrates into the water column, local wind waves that add height to the local wave conditions would theoretically have a small effect for unsteady loads at larger depths. In these cases, the height of the swell systems would have a more important role to play than local constructive or destructive interference of waves causing larger heights. This does not exclude wave height as an important value in order to calculate the loads caused by waves on a turbine, but puts into perspective how variables such as the depth of propagation and the period can have the same importance.

Regarding the BEMT model and the sensitivity analysis, the study shows how the difference in conditions can impact the analysis. The studies by Nevalainen et al. [36] point to the current being more important than in our study. This is because the ranges for the variables appear to have a large importance in the results obtained with the models. In this case, a sensitivity analysis of a device would not be applicable to another case scenario if the ranges for the variables are different.

The wave propagation model, unsurprisingly, shows how the inclusion of new conditions that can modify the wave parameters locally and a change in the depth has a large effect on the simulated results. As we mentioned in Chapter 7, these differences are large enough to give a more detailed look at how devices need to be modelled, as changes can be significant enough to modify the mechanical response considerably depending on the physical conditions, as shown in Table 7.9.

Experiments show how wave parameters change depending on the obstacle depth and length. It is especially important to see how the wave height increases as the obstacle length increases for the largest waves tested, as shown in Table 5.7. If swells are to behave in a similar manner after crossing an obstacle, this would mean different amplitudes as they propagate over a longer obstacle. The changes would be large for longer periods relative to the depth they move in, having also large amplitudes of several meters. These changes would mean two positions along the same trajectory could face differences in the underwater wave weather and the velocity components it produces. It is not known how important these local changes along different positions in the shelf might be, but it should depend on how much the wave heights and lengths have changed. Data in the experiments and simulations lead us to believe, that the important values to determine the changes, will be the relative depth to wavelength ratio after the obstacle and the steepness of the wave. In this case, if two turbines are placed in the same zone, affected by larger long swells and one of these turbines is placed after a bathymetry obstruction; the second one would face a different mechanical response to waves as the underwater velocity components would be different.

9.3 Future research and recommendations

The last point to discuss in this work is recommendations for future research and analysis of tidal turbine devices. Evidently, analysis of the relationship between the wave obstacle and the wave propagated cannot be conducted

by using simple analytical tools. Future research will require statistical analysis. The first recommendation and possible extension is the need to include more complex models that simulate a tidal turbine device. If BEMT is a fast model that can give reasonable results, as authors have found [117], [118], it also remains a tool that depends on the right set of conditions being given as the input. If these conditions vary, local changes in the waves or current velocities could have very different mechanical responses after simulations are made. The results can also lead to incorrect estimations of the loads and forces on the turbine rotor and blades.

The second recommendation is the study of long-term weather patterns. As Chapter 7 shows, wave weather has a certain seasonality and could be predicted with a certain margin of error. The seasonality and predictability open the possibility of studies on fatigue and failure to simulate long-term deployments if a large set of data is gathered on the sea conditions.

The third point is related to the inclusion of more complex physical conditions. As was observed, the inclusions of a moderate change in depth and an obstacle result in a large change in the mechanical response. In the same wave, other parameters (such as turbulence and changes in the currents) could lead to larger changes in the rotor and blade response (to the changes in the flow and other unsteady components such as turbulence and waves). In this case, turbulence, waves, and current will be the main drivers behind changes in the turbine's mechanical performance and also in elements as fatigue and failure.

The last point is a recommendation to researchers and practitioners regarding tools such as BEMT, the Morris method, and other mathematical formulations used here. Despite offering a useful way to observe preliminary results, in no way can these replace simulations or models using local conditions and more complex methods of analysis for the model variables. As observed in the case of the Morris method, which cannot tell us exactly the nature of the variable's relationship or the formulations which are

accurate to a certain range of values, other tools and models need to be explored. Further tools and models would enable us to see the response of marine energy devices once the points of interest have been identified after running preliminary tools of analysis, such as BEMT and the Morris method.

9.4 Closing remarks

This work tries to extend the models used to simulate the mechanical response of a tidal turbine to waves. It also looks to extend the understanding of how wave weather can affect tidal turbine devices, beyond the case study of extreme events. The models, experiments, and tools used here have their own limitations but, despite their limitations, they show how including different conditions into our physical representation of a tidal turbine could have important impacts that cause variations in turbine behaviour.

These changes could be missed if they are not studied in enough detail, and they could also have a larger impact on the turbine lifecycle. The study also raises the question of how to enhance our tools and physical models to make more realistic predictions of how tidal devices work by adding more complex scenarios.

Section A

Appendix A is composed of two sections; section A.1 has a resume of the formulas used to calculate the long wave properties at first order theory as has been discussed in Chapter 2 and 2. Second order terms used in Chapter 5 are included in the Appendix section D. The second part A.2, includes plots to calculate the Ursell number define possible linear swells; the plots cover depths from 30m to 100m.

A.1 Expressions for Airy or first order wave theory

A1, Table with the formulas for long waves with low amplitudes, better known as airy theory.

First order	Potential
Deep waters	$\lambda_i < \frac{h_d}{2}$
Potential	$\varphi(x,z,t) = \omega\alpha e^{kz} Cos[(\omega * t) + (k * x)]$
Velocities (x)	$V(x,z,t) = -\omega\alpha e^{kz} Sin[(\omega * t) + (k * x)]$
Velocities (z)	$V(x,z,t) = \omega\alpha e^{kz} Cos[(\omega * t) + (k * x)]$
Transitional waters	$\frac{h_d}{2} < \lambda_i < \frac{h_d}{20}$
Potential	$\varphi(x,z,t) = \omega\alpha \left(\frac{Cosh[k * (h_d + z)]}{Sinh[k * h_d]} \right) Cos[(\omega * t) + (k * x)]$
Velocities (x)	$V(x,z,t) = -k\omega\alpha * Cosh[k * (h_d + z)] * Csch[h_d * k] * Sin[(\omega * t) + (k * x)]$
Velocities (z)	$V(x,z,t) = k\omega\alpha * Sinh[k * (h_d + z)] * Csch[h_d * k] * Cos[(\omega * t) + (k * x)]$

A2, Equation terms.

Name	Term	Name	Term
Angular frequency	ω	Time	t
Wave number	k	Distance of propagation, arbitrary x=0	x
Amplitude	α	Incident wavelength	λ_i
Depth of propagation, surface z=0	h_d	Wave field depth	z

A.2 Long waves Ursell number for large period waves

Ursell number at depths (h_d) on the range [30-100]m, using wave periods (T) covering [7-22]s, for moderate wave heights (H) on the range [0.5-6]m. Red arrows show the cuts for the plots at different depths in Figures A.II to A.IX, meanwhile blue arrows show the depths of propagation in the wave tank (A) and the site chosen (B).

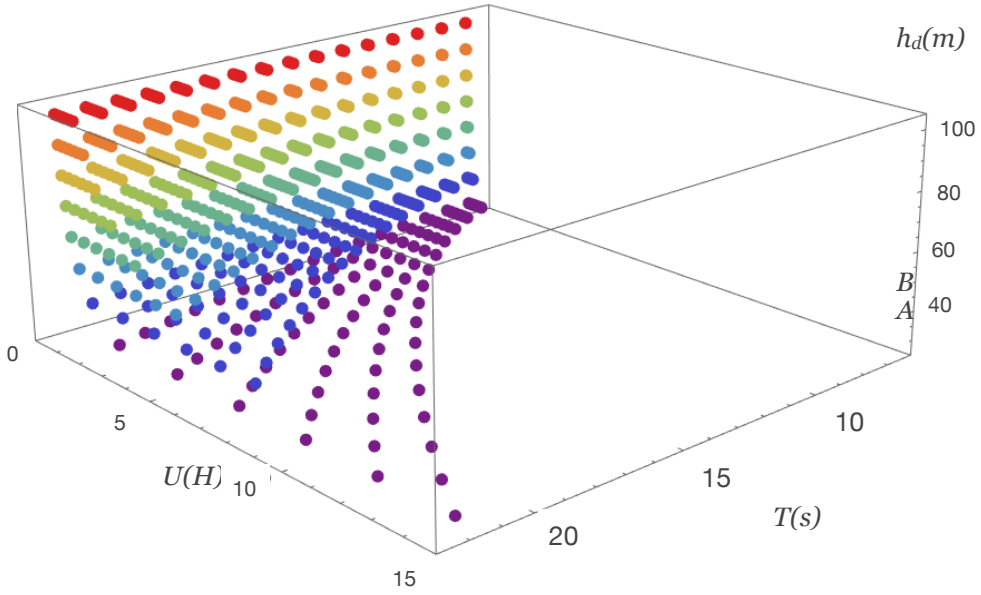

Figure A.I Ursell number at depths h_d=[30-40]m, under moderate wave heights H=[0.5-6]m, and its period T=[7-22]s at open sea h_d>1000m.

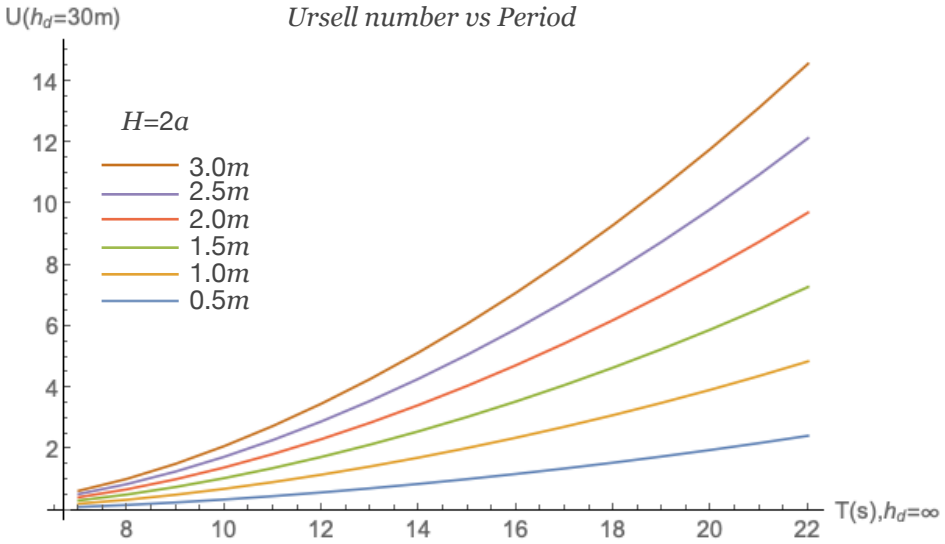

Figure A.II Ursell number at h_d=30m, for wave periods T=[7-22]s.

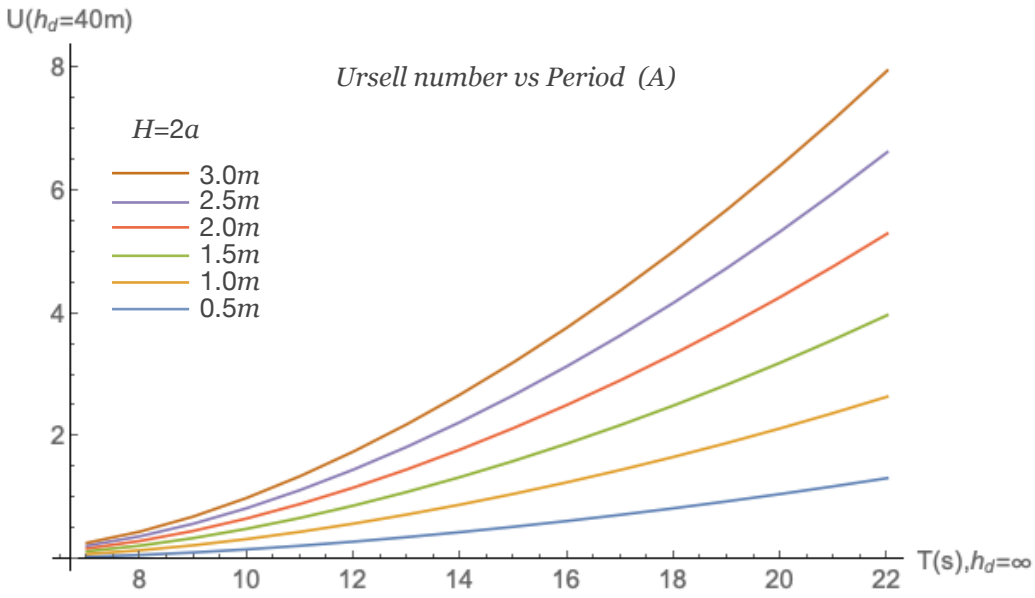

Figure A.III Ursell number at h_d=40m, for wave periods T=[7-22]s.

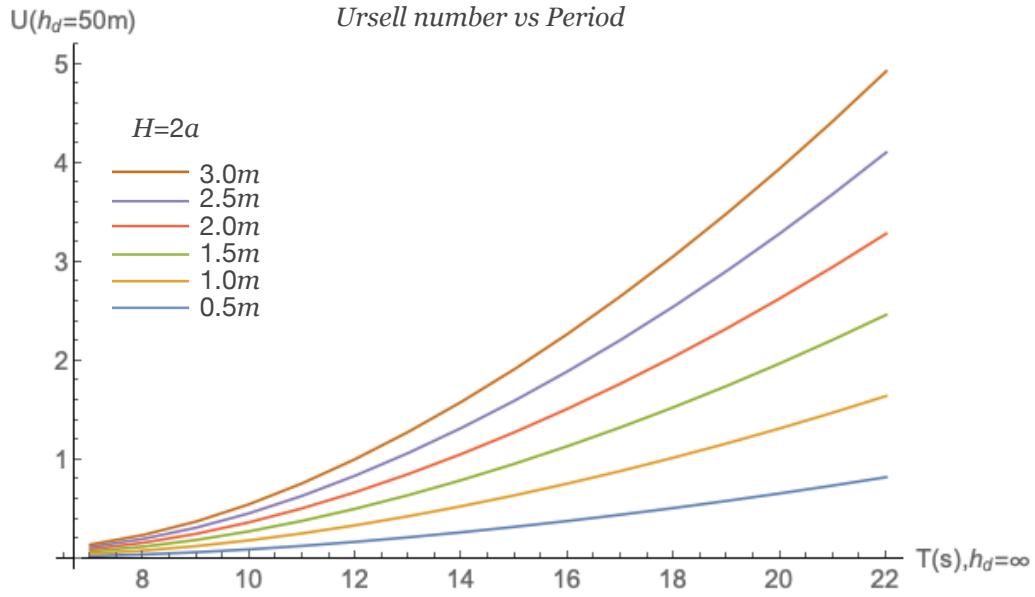

Figure A.IV Ursell number at h_d=50m, for wave periods T=[7-22]s.

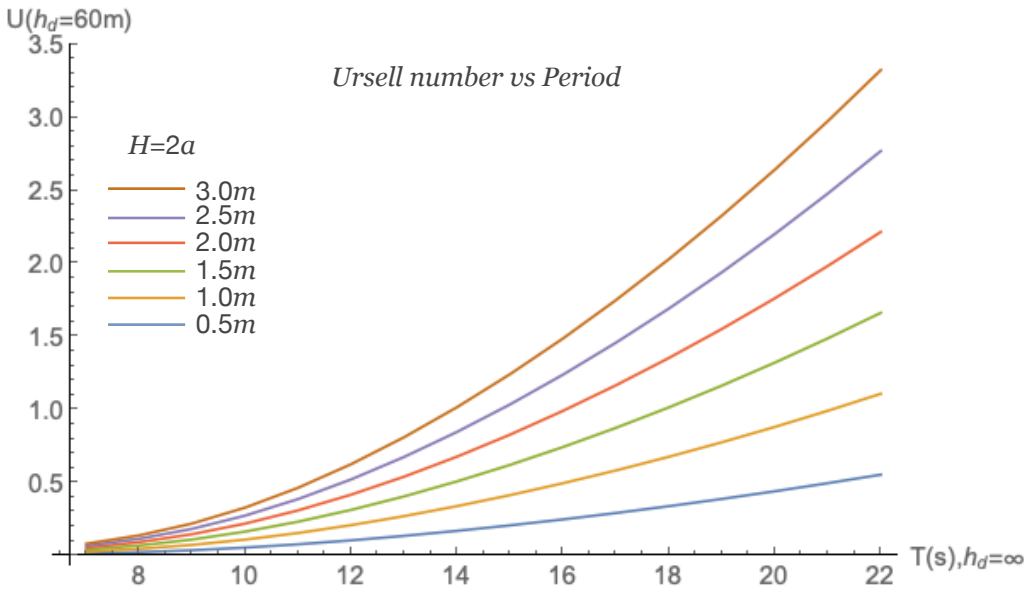

Figure A.V Ursell number at h_d=60m, for wave periods T=[7-22]s.

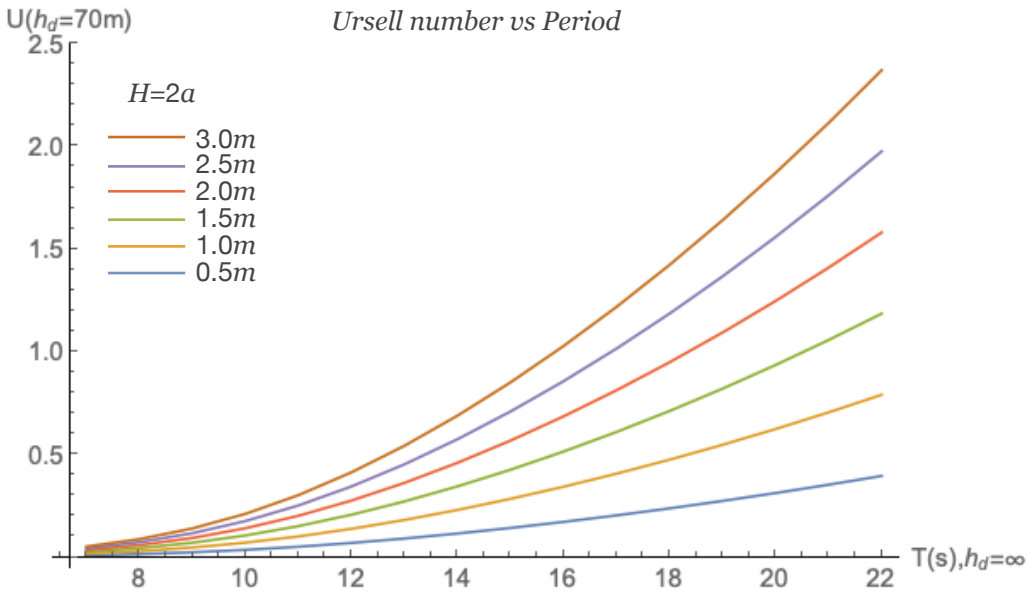

Figure A.VI Ursell number at h_d=70m, for wave periods T=[7-22]s.

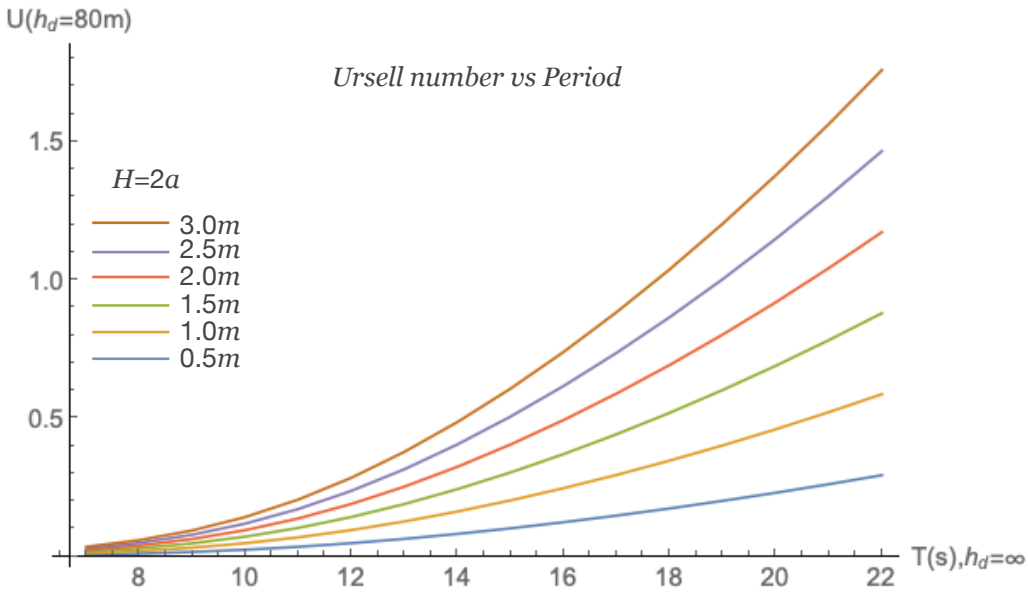

Figure A.VII Ursell number at h_d=80m, for wave periods T=[7-22]s.

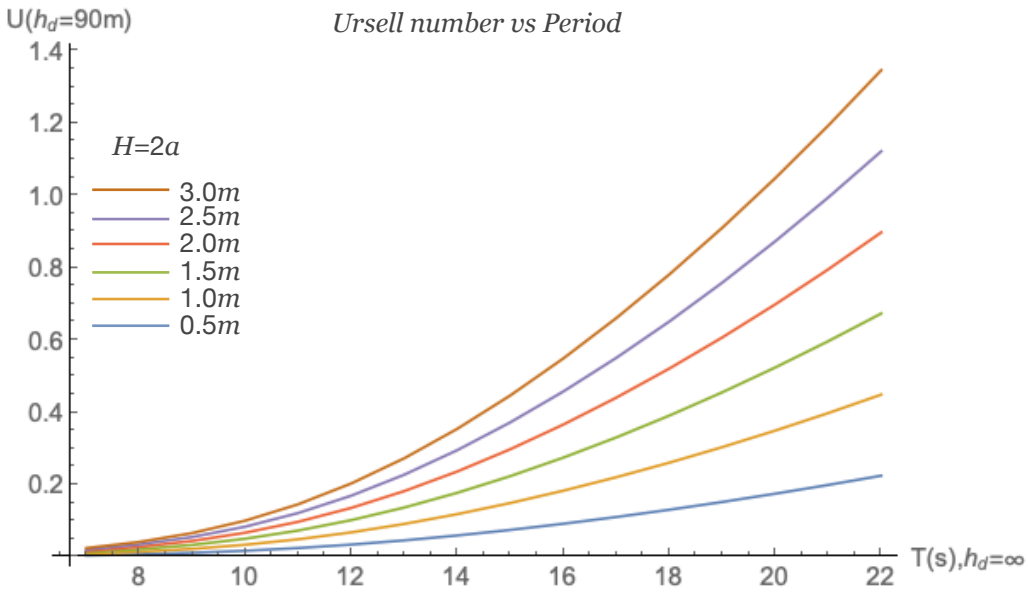

Figure A.VIII Ursell number at h_d=90m, for wave periods T=[7-22]s.

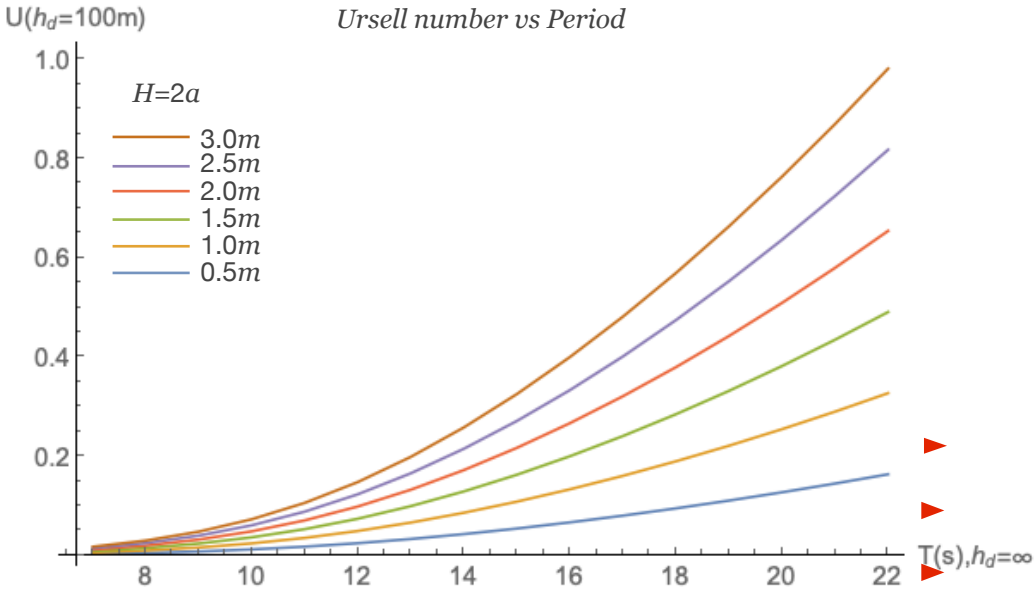

Figure A.IX Ursell number at h_d=100m, for wave periods T=[7-22]s.

Section B

Section B is divided into two parts, the first B.1 correspond to the values of the range of waves modelled in Chapter IV and used in Chapter V. The values included the maximum wave height, the non-dimensional depth/height range and the wavelength range; the values of the waves in a real 1:1 scale at open sea conditions are also shown. The second part B.2, includes the transfer functions of the wave probes during its first characterisation, as the voltage vs centimetres measured.

B.1 Wave period range and wave properties used at experimental testing and simulation.

B1, Table with values of the range of waves modelled in Chapter IV and analysed in Chapter 5.

T(s)	Hmax(mm)	λ(m)	Non-Dimensional Depth
T~[0.8 -1.7]	**Tank 0.6m depth**		
	15	**1-3.5**	**0.095-0.021**
T(s)	Hmax(m)	λ(m)	Non-dimensional depth
T~[6.9 -14.1]	**Sea 40m depth**		
	[0.35-1.7]	**[75-257]**	**0.095-0.021**

B.2 Transfer functions for all wave probes

B2, Transfer functions, wave probes A to D.

Wave Probe	Function
A	$-11.1933 + 167.834x$
B	$-9.89713 + 79.9405x$
C	$-8.87111 + 67.5139x$
D	$-9.89286 + 382.06x$

B3, Voltage vs depth h(cm) for all transfer functions.

$h(cm)$	0	10	20	30	40	50	60	70	80	90
V(A)	0.062	0.124	0.185	0.253	0.314	0.348	0.424	0.495	0.552	0.586
V(B)	0.125	0.253	0.370	0.497	0.622	0.747	0.872	0.999	1.124	1.252
V(C)	0.138	0.285	0.418	0.570	0.720	0.871	1.018	1.172	1.315	1.467
V(D)	0.026	0.053	0.077	0.103	0.129	0.156	0.181	0.209	0.235	0.262

Section C

Section C is divided into two parts, the first C.1 correspond to the links where the code for wave analysis is stored in a GitHub account, the files contain a little introduction and explanation on its inner workings. The code has a MIT license and uses Wolfram Language. Wolfram language has a free use and can be used with a limited license in platforms as in a Raspberry Pi computer. The code can be easily translated to Python. Section C.2 corresponds to the code itself and the annexed explanation on the measurements done and how they were done.

C.1 Addresses to data and code

Code, wave tank analysis:

Github: https://github.com/manelcamacho/wavetankanalisyscode

Zenodo: https://zenodo.org/record/4617236#.YLiBbC2ZMWo

Code, wave probe calibration and data sorting:

Github: https://github.com/manelcamacho/waveprobes

Zenodo: https://zenodo.org/record/4617267#.YLiDby2ZMWo

C.2 Code

———————————————————————————————————-

Mathematica code for wave feature extraction, with commentaries.

“Code Font”.

“Commentary font.”

———————————————————————————————————-

During the **1st block**, the main variables are set and data is imported from cvs files in order to be analysed. Also the boundaries of X (time) where our wave lives are set.

```
SetDirectory[“/Users/sialuk/Desktop/laboratory1sttest/
mathematica2/"]
```

“Sets the directory path where mathematica will search for the files”

```
Cdatam = Import["Test1sortedC.csv", {"Data", Range[10, 1000]}];
Bdatam = Import["Test1sortedB.csv", {"Data", Range[10, 1000]}];
Adatam = Import["Test1sortedA.csv", {"Data", Range[10, 1000]}];
```

%*datam [Cdatam, Bdatam, Adatam]:”* are arrays to store data from the first seconds of testing when the water is still, this data will be used to calculate a mean value. The wave

mean value of the 1st seconds will be used to plot the data moving it up from its deviation on the y axis caused by the function y=mx+b.

```
Cmean = Cdatam[[All, 2]];

Bmean = Bdatam[[All, 2]];

Amean = Adatam[[All, 2]];
```

%mean : [Cmean, Bmean, Amean]: The arrays will sure only the Y data to be averaged and then used to plot correctly the signal.

Due to the high degree of harmonics the signal had to be most of the time analysed one wave train each time, a value on time in milliseconds was chosen for the inferior and superior boundaries on each wave train.

```
cs1 = 2500; bs1 = 2600; as1 = 2700;

ci1 = 2400; bi1 = 2500; ai1 = 2600;
```

%s1-%i1: [cs1, bs1, as1, ci1,bi1, ai1]: These variables are the superior (s) and inferior (i) time for each analysis on the experiment number

```
datactest1 = Import[“Test1sortedC.csv", {"Data", Range[ci1, cs1]}];

datcx = datactest1[[All, 1]];
datcy = datactest1[[All, 2]];
cymean = Mean[Cmean];

datcy = datcy - Abs[cymean];
datactest1 = Transpose[{datcx, datcy}]; Length[datactest1]*100;

databtest1 = Import[“Test1sortedB.csv", {"Data", Range[bi1, bs1]}];

datbx = databtest1[[All, 1]];
datby = databtest1[[All, 2]];
bymean = Mean[Bmean];

datby = datby + Abs[bymean];
databtest1 = Transpose[{datbx, datby}]; Length[databtest1]*100;

dataatest1 = Import[“Test1sortedA.csv", {"Data", Range[ai1, as1]}];

datax = dataatest1[[All, 1]];
datay = dataatest1[[All, 2]];
aymean = Mean[Amean];

datay = datay + Abs[aymean];
dataatest1 = Transpose[{datax, datay}]; Length[dataatest1]*100;
```

data%test1: [dataatest1,databtest1,datactest1]: Are the variables that store the arrays containing the data from wave probes A,B,C. Each array goes from the inferior range to superior one. The data is imported from a .csv file.
dat%x-dat%y: [datay, datby, datcy, datax, datbx, datcx]: The array is divided in their sections x and y to work on each one individually.

%mean: [amean, bmean, cmean]: each sample from the first seconds on each wave prove is averaged with function Mean [].

dat%y: the data for the variables on y for each wave probe is then corrected after displacing it with the mean value of each wave probe first seconds.

data%test1: The data is again joined transposing the two arrays and then is measured to see if has the correct number of members with the command Lenght[].

```
{minci} = {MinimalBy[#, Last]} &@datactest1; {minbi} = {MinimalBy[#,
Last]} &@databtest1; {minai} = {MinimalBy[#, Last]} &@dataatest1;

Cplot = ListLinePlot[datactest1, PlotRange -> {{22, 30}, {-110,
60}}, PlotLegends -> "Load Coefficient",
Epilog -> {PointSize -> Medium, Red, Point@minci}]

Bplot = ListLinePlot[databtest1, PlotRange -> {{22, 30}, {-110,
60}}, PlotLegends -> "Load Coefficient",
Epilog -> {PointSize -> Medium, Red, Point@minbi}]

Aplot = ListLinePlot[dataatest1, PlotRange -> {{22, 30}, {-110,
60}}, PlotLegends -> "Load Coefficient",
Epilog -> {PointSize -> Medium, Red, Point@minai}]

Mindatactest1yi = minci[[All, 2]]; Mindatabtest1yi = minbi[[All,
2]]; Mindataatest1yi = minai[[All, 2]]; avgMindatactest1yi =
N[Mean[Mindatactest1yi]]; avgMindatabtest1yi =
N[Mean[Mindatabtest1yi]]; avgMindataatest1yi =
N[Mean[Mindataatest1yi]];

Mindatactest1xi = minci[[All, 1]]; Mindatabtest1xi = minbi[[All,
1]]; Mindataatest1xi = minai[[All, 1]]; avgMindatactest1xi =
N[Mean[Mindatactest1xi]]; avgMindatabtest1xi =
N[Mean[Mindatabtest1xi]]; avgMindataatest1xi =
N[Mean[Mindataatest1xi]];
```

min%: [minc,minb,mina]: are the values for the 1st maximum on the specific wave train time, this for each data set data%test1.

%plot: [Cplot, Bplot, Aplot]: A plot is made from all data sets and a marker is put to verify each maximum on the wave, see fig 3. From here the array name needs to be used data%test1 and the plot range on {x, y} has to be specified. The command ListLinePlot needs to take two arguments, the 1st one is the name of the array to be plotted, in this case the variable containing the datasets, and second the range to plot on {{x inferior, x superior} , {y inferior, y superior}}.

On the **2nd block** the analysis moves to the second part of our wave, this by dividing the wave in two sections with the crest as the middle part.

```
cs2 = 2600; bs2 = 2700; as2 = 2800;

ci2 = cs1; bi2 = bs1; ai2 = as1;
```

Here the superior boundary is changed and the inferior boundary is now the inferior boundary of our wave zone.

```
{maxc} = {MaximalBy[#, Last]} &@datactest1; {maxb} = {MaximalBy[#,
Last]} &@databtest1; {maxa} = {MaximalBy[#, Last]} &@dataatest1;
```

max%: [maxc,maxb,maxa]: are the values for the 1st maximum on the specific wave train time, this for each data set data%test1.

```
plot = ListLinePlot[datactest1, PlotRange -> {{22, PlotLegends ->
"Load Coefficient",
Epilog -> {PointSize -> Medium, Red, Point@maxc}]

Bplot = ListLinePlot[databtest1, PlotRange -> {{22, PlotLegends ->
"Load Coefficient",
Epilog -> {PointSize -> Medium, Red, Point@maxb}]

Aplot = ListLinePlot[dataatest1, PlotRange -> {{22, PlotLegends ->
"Load Coefficient",
Epilog -> {PointSize -> Medium, Red, Point@maxa}]

30}, {-110, 60}}, 30}, {-110, 60}}, 30}, {-110, 60}},
```

%plot: [Cplot, Bplot, Aplot]: A plot is made from all data sets and a marker is put to verify each maximum on the wave, see figure 5. From here the array name needs to be used data%test1 and

the plot range on {x, y} has to be specified.

```
Maxdatactest1y = maxc[[All, 2]]; Maxdatabtest1y = maxb[[All, 2]];
Maxdataatest1y = maxa[[All, 2]];
```

Maxdata%text1y: [Maxdatactest1y, Maxdatactest1y, Maxdatactest1y]: Cause is usual that we have several maximums on our data sets due to sampling at 100 hhz all of them are stored.

```
avgMaxdatactest1y = N[Mean[Maxdatactest1y]]; avgMaxdatabtest1y =
N[Mean[Maxdatabtest1y]]; avgMaxdataatest1y =
N[Mean[Maxdataatest1y]];
```

avg*Maxdata%text1y: [avgMaxdatactest1y, avgMaxdatactest1y, avgMaxdatactest1y]:* Each maximum appears at some time t around the main crest of our wave, this is due to the signal noise, several maximums appear at $t+\Delta\tau$. This delta is small enough that we can make an average of all points and then get the average time of our crest with a deviation of not more than ms.

```
Maxdatactest1x = maxc[[All, 1]]; Maxdatabtest1x = maxb[[All, 1]];
Maxdataatest1x = maxa[[All, 1]]; avgMaxdatactest1x =
N[Mean[Maxdatactest1x]]; avgMaxdatabtest1x =
N[Mean[Maxdatabtest1x]]; avgMaxdataatest1x =
N[Mean[Maxdataatest1x]];

velchbc = 2/(avgMaxdatabtest1x - avgMaxdatactest1x); velchab = 2/
(avgMaxdataatest1x - avgMaxdatabtest1x);
```

Maxdata%text1x: [Maxdatactest1x, Maxdatactest1x, Maxdatactest1x]: The time (coordinate x) of our array is tired for each maximum found around the crest main point, then they are averaged again.

velch%%: [velchab, velchbc]: Cuase our wave probes are at a distance of two meters each the averaged time for each wave peak is used to calculate the velocity.

In the **3rd block**, the exactly same procedure is applied to search now for a superior minimum; this block will be the superior bound of our wave. in this section the wavelengths

are calculated along with the creation of the arrays for each variable that will be plotted afterwards.

```
{mincs} = {MinimalBy[#, Last]} &@@datactest1; {minbs} = {MinimalBy[#,
Last]} &@@databtest1; {minas} = {MinimalBy[#, Last]} &@@dataatest1;

Cplot = ListLinePlot[datactest1, PlotRange -> {{22, 30}, {-110,
60}}, PlotLegends -> "Load Coefficient",
Epilog -> {PointSize -> Medium, Red, Point@mincs}]

Bplot = ListLinePlot[databtest1, PlotRange -> {{22, 30}, {-110,
60}}, PlotLegends -> "Load Coefficient",
Epilog -> {PointSize -> Medium, Red, Point@minbs}]

Aplot = ListLinePlot[dataatest1, PlotRange -> {{22, 30}, {-110,
60}}, PlotLegends -> "Load Coefficient",
Epilog -> {PointSize -> Medium, Red, Point@minas}]

Mindatactest1ys = mincs[[All, 2]]; Mindatabtest1ys = minbs[[All,
2]]; Mindataatest1ys = minas[[All, 2]]; avgMindatactest1ys =
N[Mean[Mindatactest1ys]]; avgMindatabtest1ys =
N[Mean[Mindatabtest1ys]];

deltatimeb = avgMindatabtest1xs - avgMindatabtest1xi; deltatimea =
avgMindataatest1xs - avgMindataatest1xi;

λc = velchbc*deltatimec;
λb = (velchbc + velchab)/2*deltatimeb; λa = velchab*deltatimea;

Hratioc = avgMindatactest1yi - avgMaxdatactest1y Hratiob =
avgMindatabtest1yi - avgMaxdatabtest1y Hratioa = avgMindataatest1yi
- avgMaxdataatest1y

listλc1 = {λc}
listλb1 = {λb}
listλa1 = {λa}
listvelbcnew1 = {velchbc} listvelabnew1 = {velchab} listMaxc1 =
{avgMaxdatactest1y} listMaxb1 = {avgMaxdatabtest1y} listMaxa1 =
{avgMaxdataatest1y} listHratioc12 = {Hratioc} listHratiob12 =
{Hratiob} listHratioa12 = {Hratioa}
```

deltatime%: [deltatimec, deltatimeb, deltatimea]: The
trough pass on each sensor is calculated simply subtracting time form each one.

λ%: [λa, λb, λc]: The wavelength is calculated multiplying the velocity of the wave and the difference of time between each trough passing at our sensor.

Hratio%= [Hratioc, Hratiob, Hratioa]: Apart from the maximums of each wavelength being calculated for that specific wave, the ratio between the maximum and the thought is specified. The reason for this, is because of shoaling the peak of the wave will decay but also the trough will attenuate giving a better value if we take the wave trough-peak ratio than just the maximum.

list%%%%: lists are created to store the data gathered, like the wavelength, velocity and maximums.

Particularities of the block

Cause each wave train is analyse separately then at the 1st script the function to create a lost is used:

```
listHratioa12 = {Hratioa}
```

That is:

```
“listname” = {variable to put on the list}
```

Then at the next script the next variable needs to be added at the end of the list using a new function called insert:

```
listHratioa12 = Insert[listHratioa12, Hratioa, -1]
```

That is:

```
“listname”=Insert[“listname”, v”ariable to insert on list”,
“position where it will be inserted”]
```

The procedure needs to be repeated each time a new script is called to obtain new variables to the list before export the file as .csv using:

```
Export["listc12ratioa.mx", listHratioa12]
```

———————————————————————————————————-

Mathematica code for wave probe calibration, with commentaries.

“Code Font”.

“Commentary font.”

———————————————————————————————————-

Voltage and depth of immersion are set into arrays, and then whet are transposed to create an (x,y) list. The data is then formatted into a Table and also plotted.

```
voltaged = {v0, v10, v20, v30, v40, v50, v60, v70, v80, v90};

heightd = {0, 10, 20, 30, 40, 50, 60, 70, 80, 90}; dataxyd =
Transpose[{voltaged, heightd}];
datad = TableForm[Tablexyd = Table[dataxyd]]
ad = ListPlot[dataxyd]
```

The data is fitted into a linear function as, our physical range of depths must satisfy a linear relationship for the sensor to be easy to read. The function fitted is then plotted and is compared to the data obtained in the tank.

```
std = Fit[dataxyd, {1, x}, x] add = Plot[{std}, {x, 0, 100}]

Show[{add, std}]
```

The same process if done for the wave probe as it is retrieved from the tank.

```
voltaged2 = {v02, v102, v202, v302, v402, v502, v602, v702, v802,

v902};
heightd2 = {0, 10, 20, 30, 40, 50, 60, 70, 80, 90}; dataxyd2 =
Transpose[{voltaged2, heightd2}];
```

```
datad2 = TableForm[Tablexyd2 = Table[dataxyd2]]
ad2 = ListPlot[dataxyd2]

std2 = Fit[dataxyd2, {1, x}, x] add2 = Plot[{std2}, {x, 0, 100}]

Show[{add2, std2}]
```

The difference between the voltage measured is calculated and it is transposed to the respective measured depths, this to create a list of the voltage lecture difference between the calibration by immersion and the calibration by subtraction. The standard deviation is calculated to search for any large deviation on the measured voltages.

```
Dif = Abs[voltaged2 - voltaged]
heightd = {0, 1, 2, 3, 4, 5, 6, 7, 8, 9}; Transpose[{heightc, Dif}]
StandardDeviation[Dif]
```

——-

Matlab code for wave probe cleaning and ordering, with commentaries.

“Code Font”.

“Commentary font.”

——-

During the **1st block,** we only call to the data stored in the file from a certain location of the computer using a readTable() command. Then we measure the table size cause this will work as our boundaries for our loop cycles.

```
datatotal=readtable(‘Directory where the file is stored');
HD=height(datatotal);
WD=width(datatotal);
i=1;
```

datatotal=readtable() The command readtable reads the text data stored in a file, every black space is treated as a division for a different cell of data and every jump in line as a different row on the table of data.

HD=height()/WD=width(): We set the variables of the table size, so our script will only read till the final of our file (HD-final time) and the end of the column (WD-final wave probe).

Then we simply set a counter to read every repetition till HD (final time is reached).

In the **2nd block** the information from each columns is stored on and individual list, one list will be used per counting time and the other ones to store the value of the wave height.

```
while i<=HD for j=1:5

if j==2 cd=datatotal{i,1}; CD{i,1}=cd; cd=datatotal{i,j}; CD{i,j}
=cd;

end

if j==3 cd2=datatotal{i,1}; CD2{i,1}=cd2; cd2=datatotal{i,j};
CD2{i,j}=cd2;

end
```

```
if j==4 cd3=datatotal{i,1}; CD3{i,1}=cd3; cd3=datatotal{i,j};
CD3{i,j}=cd3;

end

if j==5 cd4=datatotal{i,1}; CD4{i,1}=cd4; cd4=datatotal{i,j};
CD4{i,j}=cd4;

end

end i=i+1;

end
```

In our first cycle `while i<=HD` we will repeat the process till `i` reaches HD (final time value). Then we pass through every column that contains data being sorted as: Column 1 = time, Column 2 = wave probe 1, Column 3 = wave probe 2… Column n = wave probe n. If more sensors need to be added just a copy of the block if j == “wave prove number=n” needs to be added to this script.

```
if j==“n” cd”n”=datatotal{i,1}; CD”n”{i,1}=cd”n”;
cd”n”=datatotal{i,j}; CD”n”{i,j}=cd”n”;

end
```

`CD` is an array that will contain only two columns `CD{n,2}`, taken from `datatotal{mxn}`, the first one that we will call on each column datatotal`{i,1}` it stores the time and the second one `datatotal{i,2}` will store the wave height collected for each sensor.

The process will be repeated for every wave probe variable:

```
if j==3 cd2=datatotal{i,1};

CD2{i,1}=cd2; cd2=datatotal{i,j}; CD2{i,j}=cd2;

end

if j==4 cd3=datatotal{i,1}; CD3{i,1}=cd3; cd3=datatotal{i,j};
CD3{i,j}=cd3;

end

if j==5 cd4=datatotal{i,1}; CD4{i,1}=cd4; cd4=datatotal{i,j};
CD4{i,j}=cd4;

end
```

In the **3rd block** the tables are put into an individual file using the character / as a delimiter, this will add black spaces that can be then used to save it as a .csv file

```
Table=cell2table(CD);
writetable(Table,'Directory where the file will be stored, Sensor
1','Delimiter','\t');

Table2=cell2table(CD2);
```

```
writetable(Table2,'Directory where the file will be stored, Sensor
1','Delimiter','\t');

Table3=cell2table(CD3);
writetable(Table3,'Directory where the file will be stored, Sensor
1','Delimiter','\t');

Table4=cell2table(CD4);
writetable(Table4,'Directory where the file will be stored, Sensor
1','Delimiter','\t');
```

`Table=cell2table()` is used to write a cell type array like excel type to convert it into a text table. Then `writetable("tablename", "path and name of file to be saved")` is used to store it. The code at this point can use delimiters to separate the files.

In the **4th block** files are checked for blank spaces or other non-numeric data, this one will be erased from the files. Most of the time this data is just inserted wrong by the sensor and is not lost, data file then will contain a black space instead of the data; however this correct data will be stored on the next line.

```
% Read the file as cell string line by line:
fid = fopen('Directory where the file is stored, Sensor 1', 'r'); if
fid < 0, error('Cannot open file: %s'); end
Data = textscan(fid, '%s', 'delimiter', '\n', 'whitespace', '');
fclose(fid);

% Remove empty lines:
C = deblank(Data{1}); % [EDITED]: deblank added C(cellfun('isempty',
C)) = [];
% Write the cell string:
fid = fopen('Directory where the file is stored, Sensor 1', 'w'); if
fid < 0, error('Cannot open file: %s', FileName); end fprintf(fid,
'%s\n', C{:});
fclose(fid);

fid = fopen('Directory where the file is stored, Sensor 2', 'r'); if
fid < 0, error('Cannot open file: %s'); end
Data = textscan(fid, '%s', 'delimiter', '\n', 'whitespace', '');
fclose(fid);

C = deblank(Data{1}); % [EDITED]: deblank added C(cellfun('isempty',
C)) = [];
% Write the cell string:
fid = fopen('Directory where the file is stored, Sensor 2', 'w'); if
fid < 0, error('Cannot open file: %s', FileName); end fprintf(fid,
'%s\n', C{:});

fclose(fid);
fid = fopen('Directory where the file is stored, Sensor 3', 'r'); if
fid < 0, error('Cannot open file: %s'); end
Data = textscan(fid, '%s', 'delimiter', '\n', 'whitespace', '');
fclose(fid);

C = deblank(Data{1}); % [EDITED]: deblank added C(cellfun('isempty',
C)) = [];
% Write the cell string:
fid = fopen('Directory where the file is stored, Sensor 3', 'w'); if
fid < 0, error('Cannot open file: %s', FileName); end fprintf(fid,
'%s\n', C{:});
```

```
fclose(fid);
fid = fopen('Directory where the file is stored, Sensor 4', 'r'); if
fid < 0, error('Cannot open file: %s'); end
Data = textscan(fid, '%s', 'delimiter', '\n', 'whitespace', '');
fclose(fid);

C = deblank(Data{1}); % [EDITED]: deblank added C(cellfun('isempty',
C)) = [];
% Write the cell string:
fid = fopen('Directory where the file is stored, Sensor 4', 'w'); if
fid < 0, error('Cannot open file: %s', FileName); end fprintf(fid,
'%s\n', C{:});

fclose(fid);
```

Section D

Section D is divided into two parts. Section D.1 defines the online directions where the data is stored for public access; the section includes the public repositories, to store the scripts used to analyse the waves and calibrate the wave probes. Section D.2 includes the data obtained from the calibration test, which was also used to characterise the wave natural shoaling inside the tank.

D.1 Addresses data and code

Wave experimental data: https://pureportal.strath.ac.uk/en/datasets/wave-propagation-over-obstacles.

D.2 Wave tank calibration

D1, Wavelengths(m), red colour indicates abnormal larger wavelengths, in green two cases that are related to an irregular minimum wave train detection on sensor A:

T1	T2	T3	T4	T5	T6	T7
1.1888	1.3431	1.6800	1.8632	2.2453	4.4947	3.7800
1.0581	1.4394	1.6975	1.9823	2.2617	3.0495	3.4490
1.1944	1.2394	1.7142	2.0727	2.2018	2.7429	3.5306
1.2113	1.3188	1.6833	2.0180	2.2018	4.6776	3.2800
1.2361	1.4668	1.6949	1.9464	2.1261	3.3469	4.1042
1.2199	1.2727	1.7000	1.9649	2.1818	4.9681	3.5464
1.1944	1.2222	1.7094	2.0714	2.2000	3.2653	3.1456
1.2778	1.3188	1.6667	2.0000	2.1636	2.8269	5.8734
1.1831	1.2308	1.7119	1.9821	2.1802	3.2653	3.5208
1.2676	1.2222	1.6529	1.8120	2.2018	2.8350	4.8208
1.2222	1.3237	1.8018	2.0180	2.1818	5.0235	3.6907
					2.8077	
					4.6923	
					3.3265	

D2, Wavelengths(m), red colour indicates abnormal larger wavelengths, in green two cases that are related to an irregular minimum wave train detection on sensor B:

T1	T2	T3	T4	T5	T6	T7
1.2917	1.3971	1.7900	1.8418	2.2489	4.8251	3.9861
1.2054	1.6491	1.6993	2.0013	2.2562	2.9163	3.1814
1.4344	1.3795	1.7950	2.0212	2.2530	2.6040	3.3943
1.4855	1.3628	1.7571	2.0189	2.2433	4.0258	3.0992
1.4696	1.6340	1.7656	2.0188	2.2323	3.1364	3.8109
1.4961	1.3695	1.7477	2.0178	2.2507	4.7532	3.4405
1.4402	1.3905	1.7637	2.0097	2.2150	3.0962	2.9211
1.4402	1.4789	1.7504	2.0456	2.2426	2.6860	5.0802
1.4440	1.3695	1.7862	2.0278	2.2323	3.0666	3.4024
1.3051	1.3649	1.7472	1.8512	2.2530	2.6867	5.0145
1.4696	1.4946	1.6270	2.0198	2.2426	5.0991	3.5078
1.4450	1.4146				2.7241	
					4.8132	
					3.1364	

D3, Wavelengths(m), red colour indicates abnormal larger wavelengths, in green two cases that are related to an irregular minimum wave train detection on experiment 6:

T1	T2	T3	T4	T5	T6	T7
2.6345	1.4026	1.9030	1.8525	2.2301	4.9778	3.8913
1.4638	1.7886	1.7619	1.9832	2.2478	2.7843	2.9623
1.6154	1.5267	1.9191	1.9833	2.2478	2.4673	3.1400
1.6250	1.4074	1.7778	2.0513	2.2105	3.9184	2.9423
1.6124	1.7800	1.7480	2.0000	2.2832	2.9703	3.6596
1.5455	1.5758	1.7920	2.0000	2.2807	4.2174	3.2500
1.6124	1.6154	1.7778	2.0342	2.2281	2.9505	2.8704
1.6279	1.5231	1.7638	2.0000	2.2832	2.5660	4.4086
1.5692	1.5909	1.8226	2.0000	2.2655	2.8738	3.1633

Continuation of table D3						
T1	T2	T3	T4	T5	T6	T7
1.3431	1.5758	1.8065	1.8699	2.2478	2.5421	5.0115
1.5969	1.5504	2.0600	2.0000	2.3186	4.0206	3.2653
1.5814	1.5400				2.5849	
					4.2637	
					2.9109	
					2.8824	

D4, Wave velocities(m/s), sensors A to B

T1	T2	T3	T4	T5	T6	T7
1.3986	1.4599	1.6800	1.7094	1.8868	2.1053	2.0000
1.2903	1.5152	1.6807	1.7699	1.8692	1.9802	2.0408
1.3889	1.4085	1.6800	1.8182	1.8349	1.9048	2.0408
1.4085	1.4493	1.6667	1.8018	1.8349	2.1858	2.0000
1.3889	1.5150	1.6949	1.7857	1.8018	2.0408	2.0833
1.4184	1.3986	1.6667	1.7544	1.8182	2.1277	2.0619
1.3889	1.3889	1.7094	1.7857	1.8182	2.0408	1.9417
1.3889	1.4493	1.6667	1.8018	1.8182	1.9231	2.5316
1.4085	1.3986	1.6949	1.7857	1.8018	2.0408	2.0833
1.4085	1.3889	1.6529	1.7094	1.8349	1.9417	2.3121
1.3889	1.4388	1.8018	1.8018	1.8182	2.3529	2.0619
1.3986	1.4286				1.9231	
					2.1978	
					2.0408	

D5, Wave velocities(m/s), sensors B to C:

T1	T2	T3	T4	T5	T6	T7
1.3793	1.4815	1.6120	1.6393	1.7699	2.2222	2.1739
1.4493	1.6260	1.5873	1.6807	1.7699	1.9608	1.8868

Continuation of table D5						
T1	T2	T3	T4	T5	T6	T7
1.5385	1.5267	1.6120	1.6667	1.7699	1.8692	2.0000
1.5625	1.4815	1.5873	1.7094	1.7544	2.0408	1.9231
1.5504	1.6200	1.5748	1.6949	1.7699	1.9802	2.1277
1.5152	1.5152	1.6000	1.6949	1.7544	2.1739	2.0833
1.5504	1.5385	1.5873	1.7094	1.7544	1.9802	1.8519
1.5504	1.5385	1.5748	1.6949	1.7699	1.8868	2.1505
1.5385	1.5152	1.6129	1.6807	1.7699	1.9417	2.0408
1.4599	1.5152	1.6129	1.6260	1.7699	1.8692	2.2989
1.5504	1.5504	1.4280	1.6807	1.7699	2.0619	2.0408
1.5504	1.5000				1.8868	
					2.1978	
					1.9802	

Figure D.I Abnormal detections in green, these abnormal values appear to be related to large and irregular troughs in the records:

	Sensor C
Exp 1	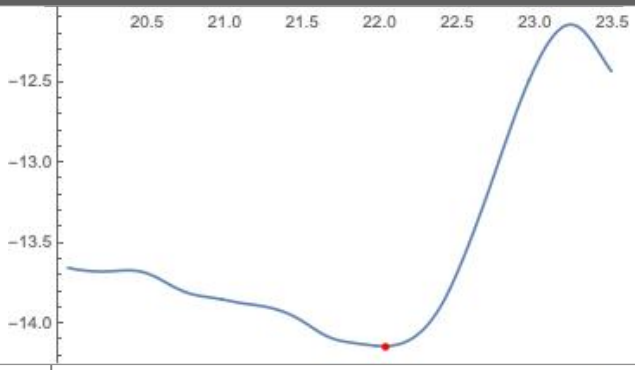
Exp 11	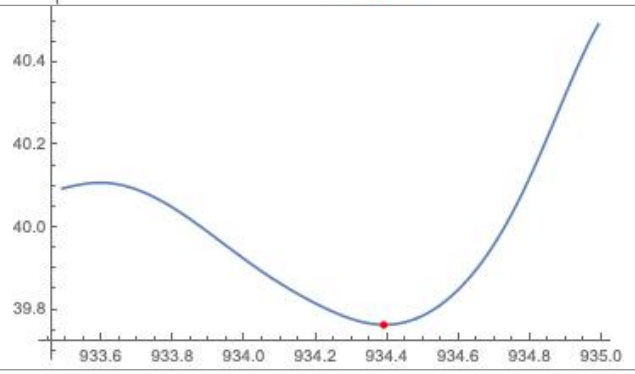

Continuation Figure C1	
Exp 13	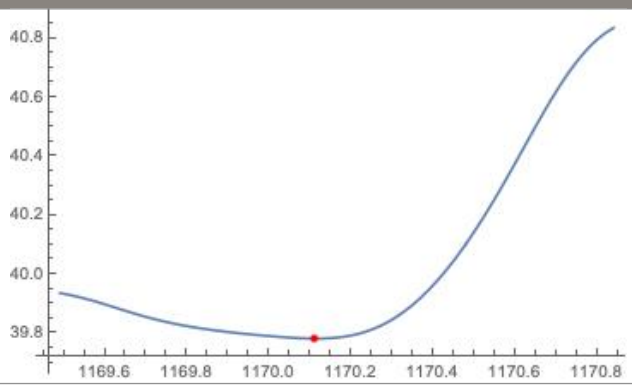

Section E

Section E is solely composed of the plot of the wavelength transmitted ratios fitted for all the periods T1 to T7 on the experiments composed of an obstacle of 1/6 of length and a depth from 0 to 1/2 of the tank's depth. This is described in section 5.2.1.

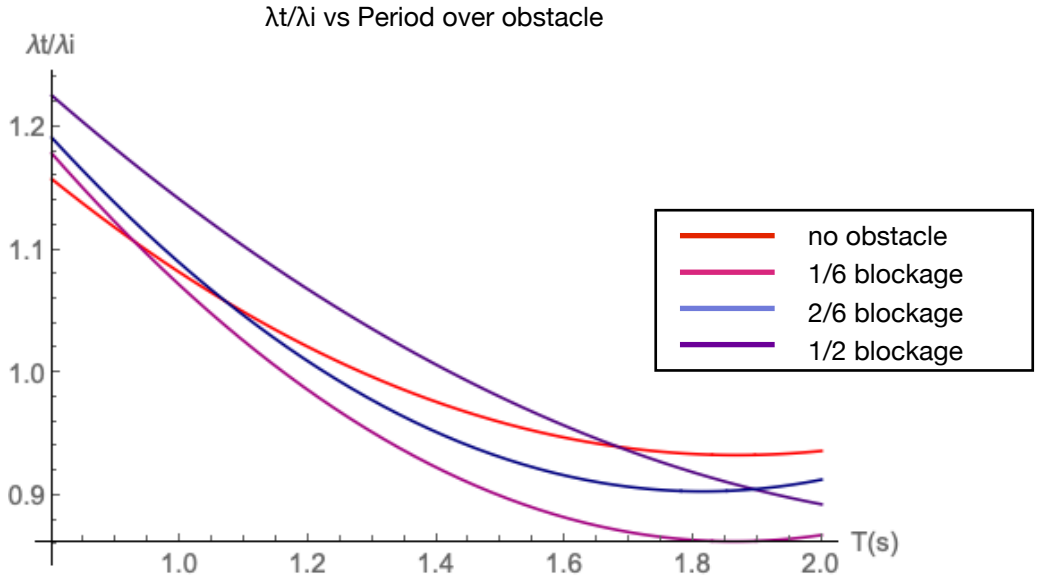

E.1 Fitted data for the wavelength ratio of propagation vs wave period, the data shown is for waves passing over the obstacle.

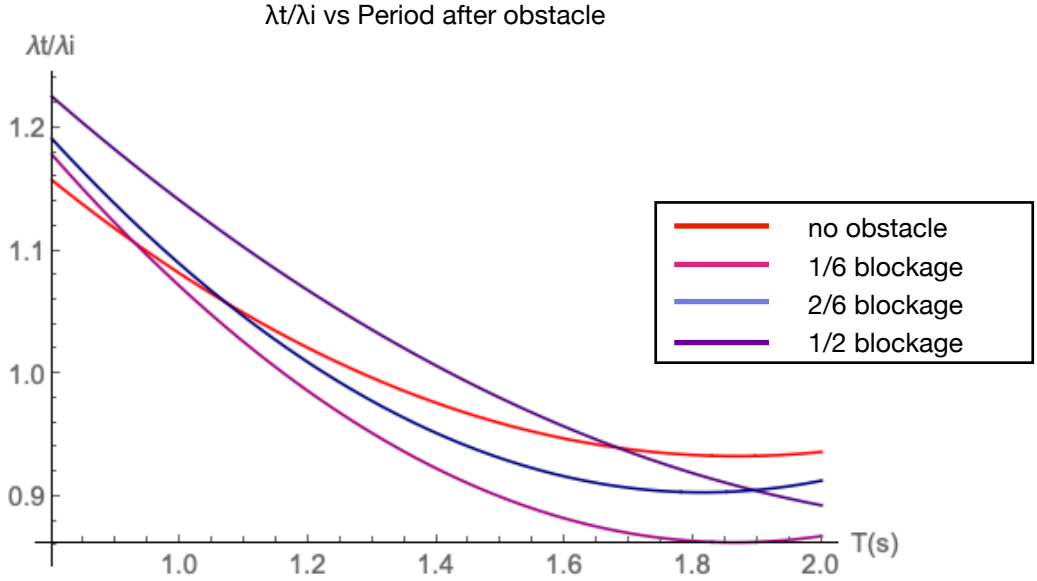

E.2 Fitted data for the wavelength ratio of propagation vs wave period, the data shown is for waves passing after the obstacle.

Section F

Section F is solely composed of the mathematical terms used to model and describe second-order wave velocities, the terms are part of the Stokes expansion in Chapter 6.

$$L = Coth[2 * k * h]$$

$$C_0 = [g * k * Tanh[k * h]]^{1/2}$$

$$K = Coth[k * h]$$

$$X = (x - ct)$$

$$Z = z$$

$$b_{22} = \frac{K * (3 * K^2 - 1) + \omega * (2 * a_{11} + \omega * K))}{(4 * a_{11}{}^2)}$$

$$a_0 = -(\omega * k * h) - \frac{\left((\omega^2 + 4 * K^2)^{1/2} - \omega\right)}{(2 * K)};$$

$$a_{01} = \frac{\omega}{2}$$

$$a_{11} = \frac{\omega^2 + 4 * K^2 - \omega}{2 * K}$$

$$a_{22} = \frac{\left(3 * K * k^2 - 1 + \omega * (3 * a_{11} + \omega * K)\right)}{(4 * a_{11})}$$

$$a_{20} = \frac{-(a_{11} * a_{22} + \frac{b_{22}}{2}) * K^2 - K + 0.5 * b_{22} * a_{11}^2 - \omega * (a_{22} * L + \frac{(b_{22} * K)}{(2 * a_{11})} - \frac{a_{11}}{4})}{\left(2 * a_{11} * K + \omega\right)}$$

$$B_1 = \frac{2 * Z * a_{01} * k^2 + (a_{11} * \epsilon * k * Cos[X * k] .* Cosh[Z * k])}{Sinh[h * k]/k;}$$

$$A_1 = \frac{(C_0 * (+a_0 * k + \epsilon^2 * (a_{20} * k + (2 * a_{22} * k * Cos[2 * X * k] .* Cosh[2 * Z * k])}{Sinh[2 * h * k]}$$

$$V_x(x, z, t) = A_1 + B_1$$

$$B_2 = \frac{(a_{11} * k * Sin[X * k] * Sinh[Z * k] * \epsilon)}{Sinh(h * k)/k}$$

$$A_2 = \frac{(C_0 * (2 * a_{22} * k * Sin[2 * X * k] .* Sinh[2 * Z * k] * \epsilon^2)}{Sinh[2 * h * k]}$$

$$V_z(x, z, t) = A_2 + B_2$$

Section G

Section F is composed of three subsections, the subsection G.1 includes the web addresses of the products used to feed data into the swell search algorithms. This section also contains the public web addresses for the code used in Chapter 7. The second subsection G.2, includes the full data used for the wind-wave generation in Chapter 7. The data was obtained through the NDBC program, which address can be found also in this section. Wind data is composed of the mean value of the local winds at the buoy areas; fpP refers to the Pierson Moskowitz modal frequency, and fpJ refers to the Jonswapp modal frequency. The third subsection G.3, includes the complete seasonal wave directional data for buoy systems A to E. This data covers the full-wave weather season of 2017 from January to December.

G.1 Wave data and code for swell detection

Bathymetry data products: https://www.usgs.gov/products/data-and-tools/data-and-tools-topics

Buoy data products: https://www.ndbc.noaa.gov/maps/Northwest.shtml

Code to process swell data: https://github.com/manelcamacho/wavecodebuoys

G.2 Modal frequency wave data

Wind data used in Chapter 7, to calculate the modal frequency of the wave weather at the buoy systems is shown below, this using the maximum and minimum monthly averaged wind data velocity WVM.

G1, Maximums and minimums data of winds at buoy systems A to E.

Month\Buoy	A[m/s]	B[m/s]	C[m/s]	D[m/s]	E[m/s]
Jan	4.69, 11.32	5.50, 13.58	4.58, 12.66	4.32, 11.97	5.14, 18.05
Feb	3.58, 9.80	4.58, 12.56	4.32, 12.03	4.42, 11.97	5.28, 17.74
Mar	3.17, 11.66	4.57, 12.00	4.05, 11.21	3.82, 11.06	6.68, 19.8
Apr	3.72, 10.493	3.83, 11.17	3.87, 10.76	3.82, 10.21	8.43, 21.12
May	2.89, 9.73	3.63, 9.97	3.52, 9.57	3.72, 9.65	7.55, 19.89
Jun	3.10, 9.25	3.44, 9.41	3.89, 9.49	4.17, 10.26	7.35, 19.92
Jul	4.07, 9.87	3.43, 8.76	3.90, 9.22	3.97, 9.81	6.70, 17.78

290

Continuation table G1					
Month\Buoy	A[m/s]	B[m/s]	C[m/s]	D[m/s]	E[m/s]
Aug	3.93, 9.87	3.61, 9.12	3.72, 9.23	3.87, 9.35	7.76, 17.93
Sep	4.28, 10.63	3.60, 10.21	3.92, 10.07	4.02, 10.46	6.99, 17.50
Oct	3.79, 11.52	3.59, 11.67	3.74, 10.81	4.22, 11.06	6.10, 17.19
Nov	3.45, 11.11	5.14, 13.59	4.58, 12.38	3.92, 11.16	5.45, 18.14
Dec	4.07, 12.35	5.23, 13.76	4.68, 12.94	4.32, 12.27	4.68, 17.60

G2, Corrected mean wind data at 10m height in buoy systems A to E.

Month\Buoy	A[m/s]	B[m/s]	C[m/s]	D[m/s]	E[m/s]
Jan	8.57	10.40	9.40	8.95	12.74
Feb	7.17	9.34	8.91	9.01	12.65
Mar	7.94	9.03	8.32	8.18	14.56
Apr	7.61	8.18	7.98	7.71	16.23
May	6.76	7.42	7.14	7.35	15.07
Jun	6.61	7.01	7.30	7.93	14.98
Jul	7.46	6.65	7.16	7.57	13.45
Aug	7.39	6.94	7.07	7.27	14.11
Sep	7.98	7.53	7.62	7.96	13.45
Oct	8.20	8.32	7.93	8.40	12.80
Nov	7.80	10.21	9.24	8.29	12.96
Dec	8.79	10.35	9.60	9.12	12.24

G3, Modal frequencies using the Pierson-Moskowitz (fpP) spectrum and Jonswapp (fpJ) spectrum at buoys A to E.

Buoy	A[Hz]		B[Hz]		C[Hz]		DHz]		E[Hz]	
Month	fpP	fpJ	fpP	fpJ	fpP	fpJ	fpP	fpJ	fpP	fpJ
Jan	0.18	0.16	0.06	0.05	0.10	0.10	0.09	0.09	0.16	0.13
Feb	0.22	0.17	0.06	0.06	0.09	0.10	0.09	0.09	0.16	0.13
Mar	0.20	0.16	0.05	0.06	0.09	0.10	0.08	0.10	0.18	0.12

Continuation table G3										
Month	*fpP*	*fpJ*	*fpP*	*fpJ*	*fpP*	*fpJ*	*fpP*	*fpJ*	*fpP*	*fpJ*
Apr	0.21	0.16	0.05	0.06	0.09	0.11	0.08	0.10	0.19	0.12
May	0.23	0.17	0.05	0.06	0.08	0.11	0.08	0.10	0.18	0.12
Jun	0.24	0.17	0.05	0.06	0.08	0.11	0.08	0.10	0.18	0.12
Jul	0.21	0.16	0.04	0.06	0.08	0.11	0.08	0.10	0.17	0.12
Aug	0.21	0.16	0.04	0.06	0.08	0.11	0.08	0.10	0.17	0.12
Sep	0.20	0.16	0.05	0.06	0.08	0.11	0.08	0.10	0.17	0.12
Oct	0.19	0.16	0.06	0.07	0.09	0.11	0.08	0.10	0.16	0.13
Nov	0.20	0.16	0.06	0.06	0.09	0.10	0.08	0.10	0.16	0.12
Dec	0.18	0.16	0.06	0.06	0.10	0.10	0.09	0.09	0.16	0.13

G.3 Wind directional data

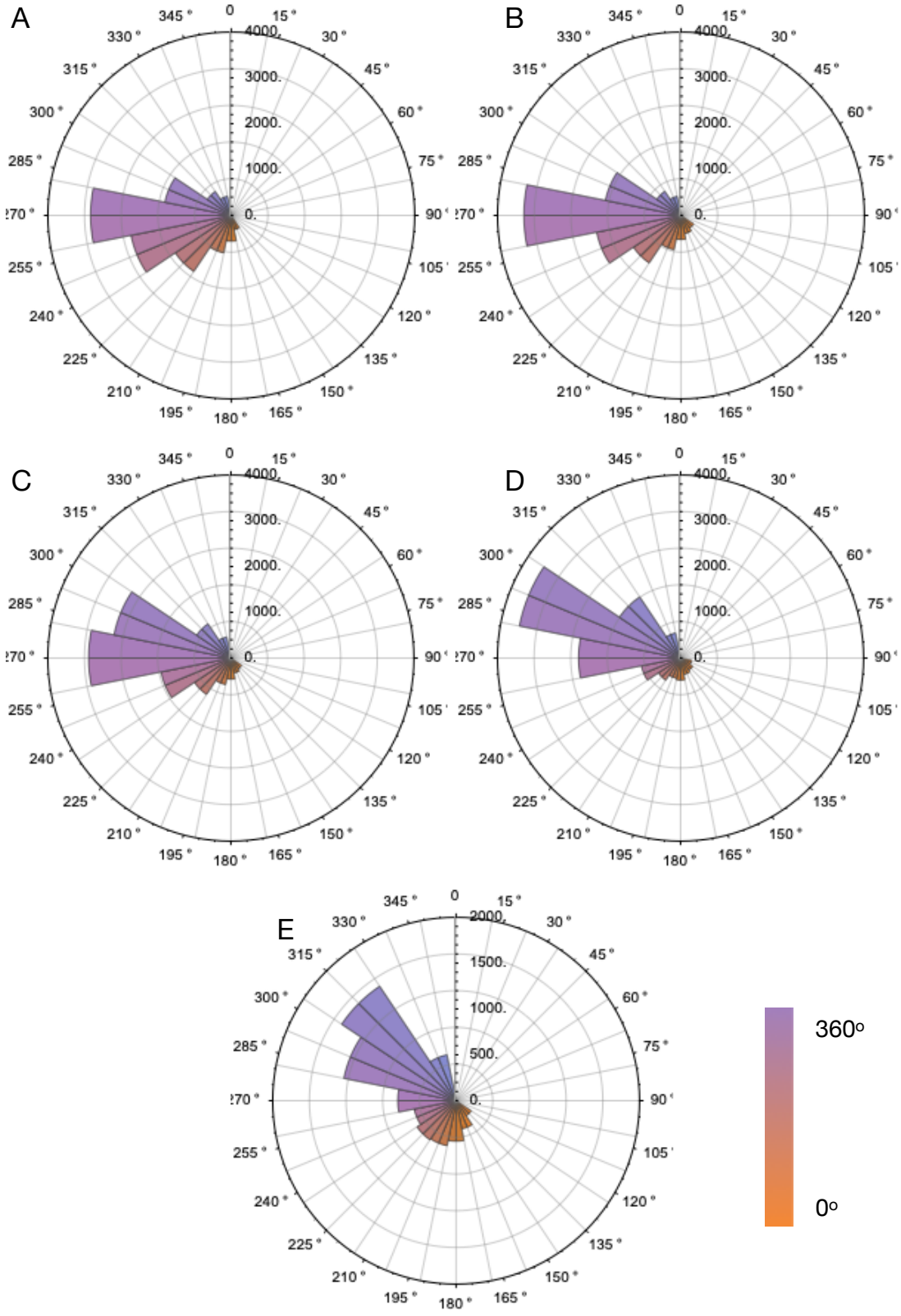

Figure G.I Swell events number for buoys A to E on the month of January, radius shows the number of swell occurrences and its spectral angle of incidence.

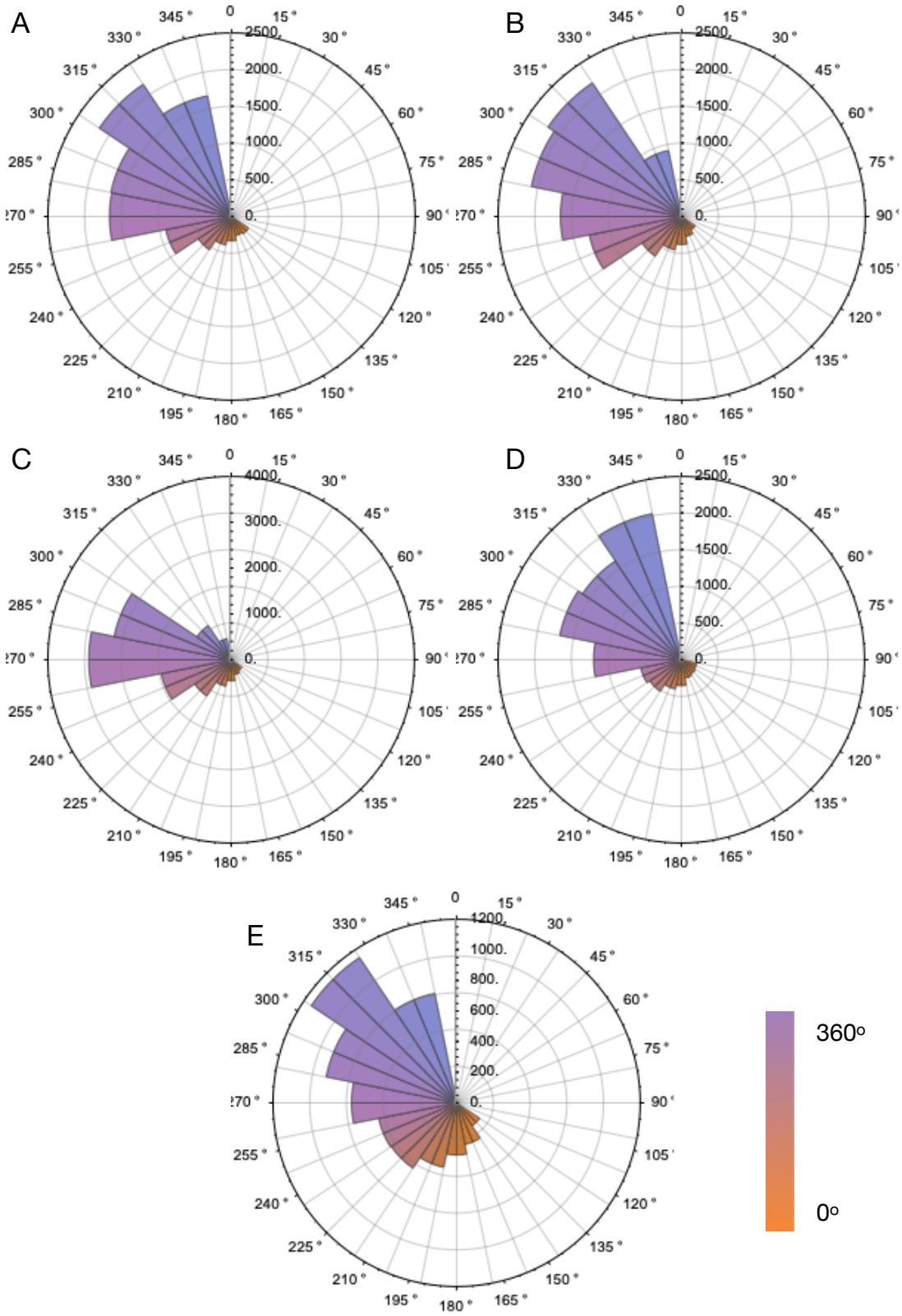

Figure G.II Swell events number for buoys A to E on the month of February, radius shows the number of swell occurrences and its spectral angle of incidence.

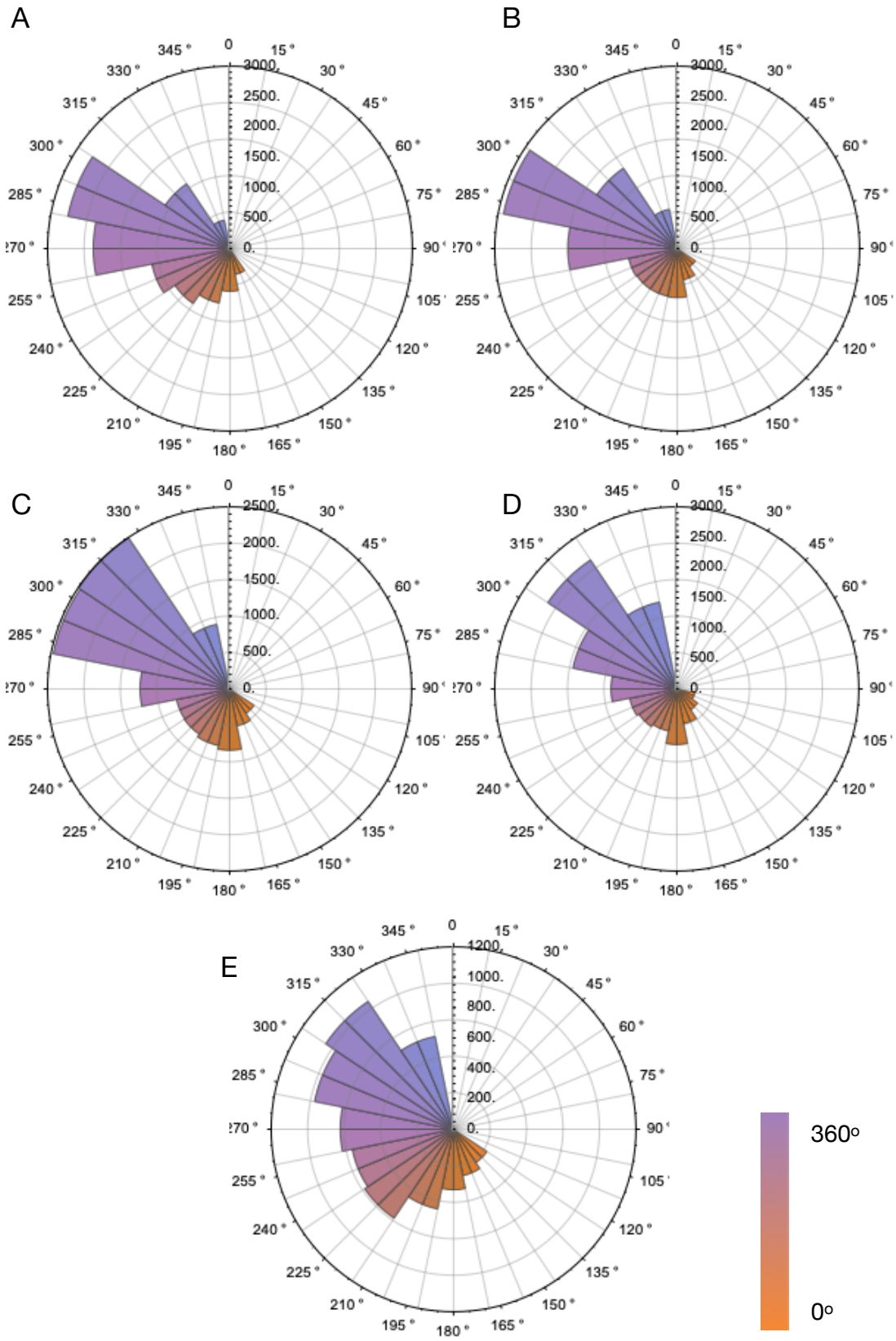

Figure G.III Swell events number for buoys A to E on the month of March, radius shows the number of swell occurrences and its spectral angle of incidence.

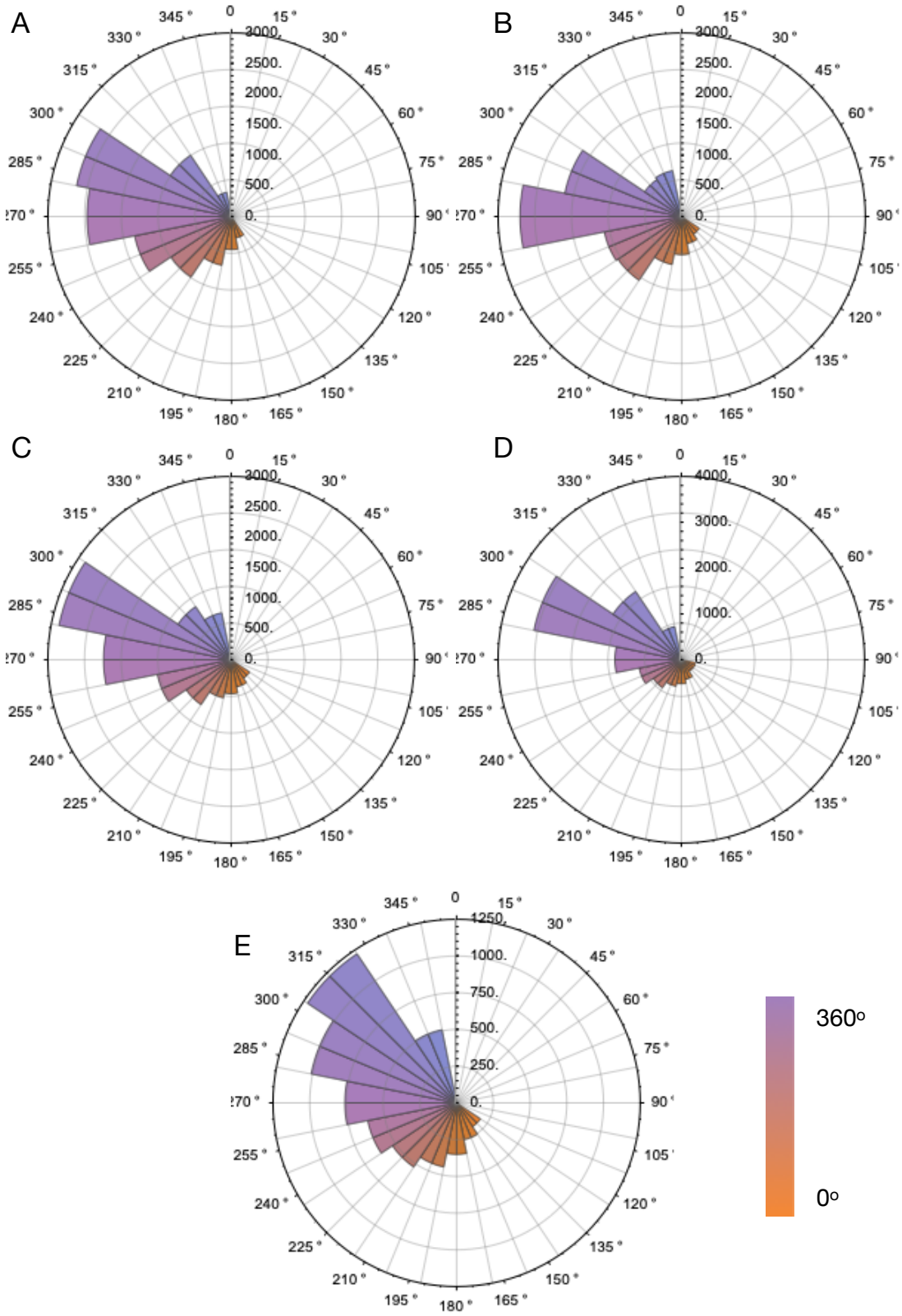

Figure G.IV Swell events number for buoys A to E on the month of April, radius shows the number of swell occurrences and its spectral angle of incidence.

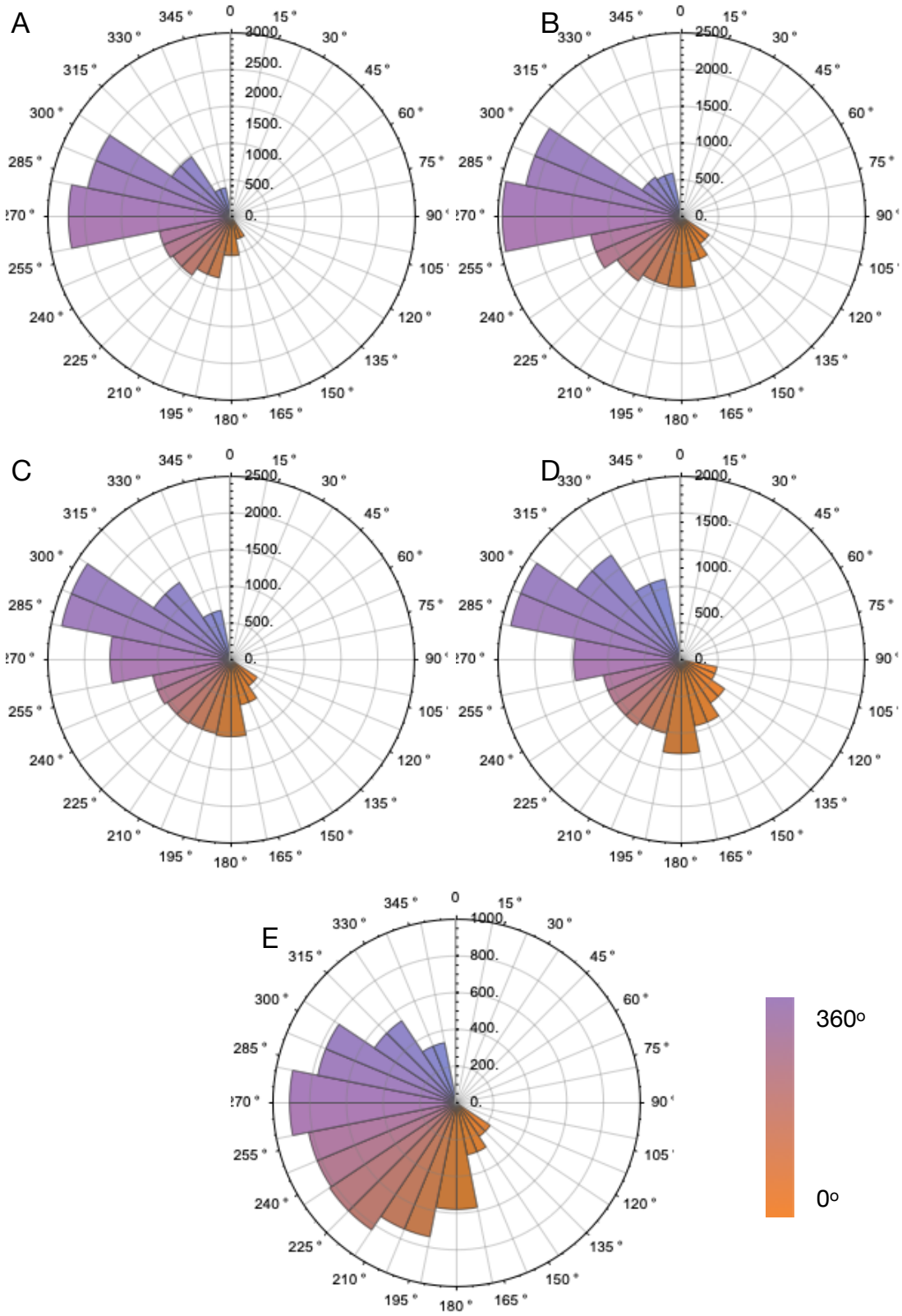

Figure G.V Swell events number for buoys A to E on the month of May, radius shows the number of swell occurrences and its spectral angle of incidence.

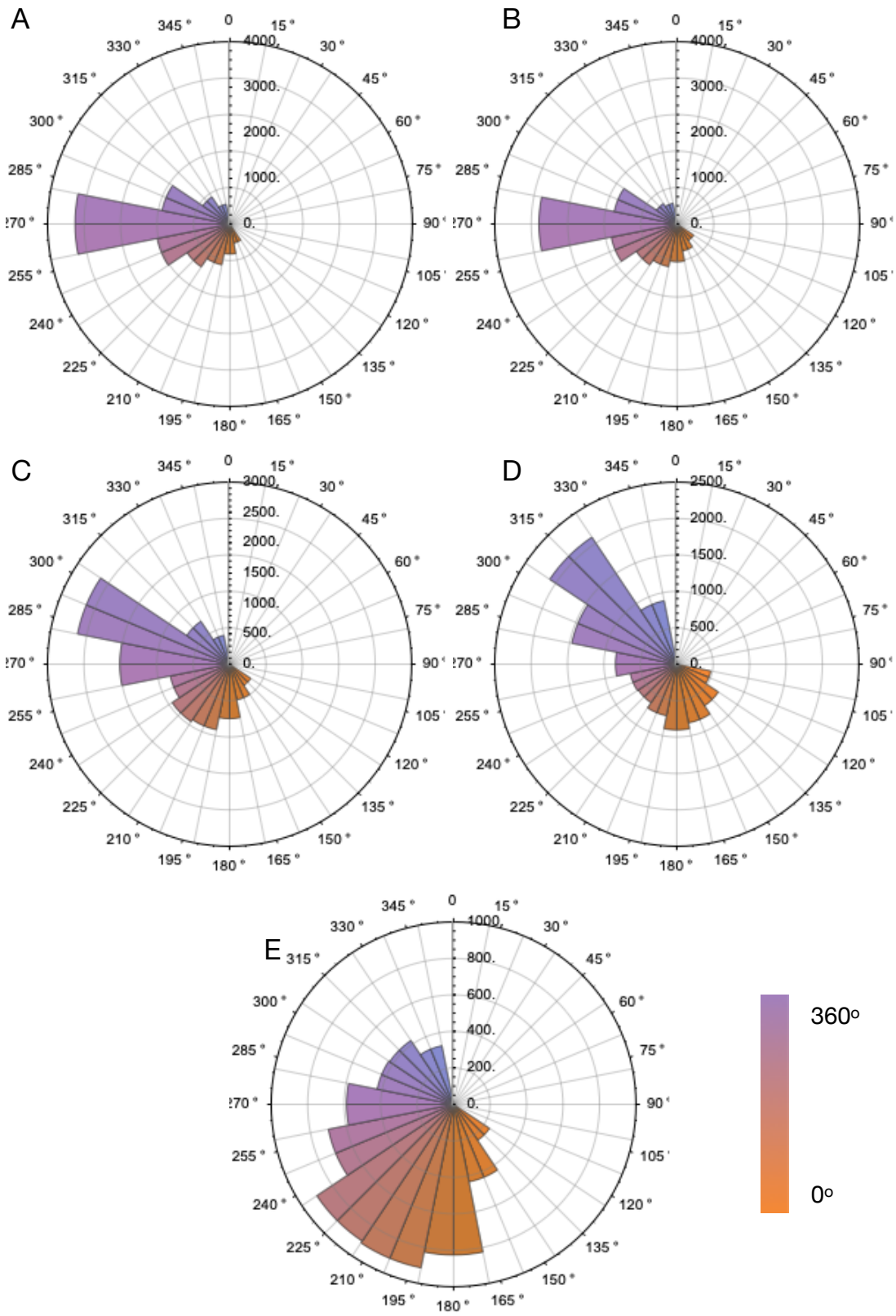

Figure G.VI Swell events number for buoys A to E on the month of June, radius shows the number of swell occurrences and its spectral angle of incidence.

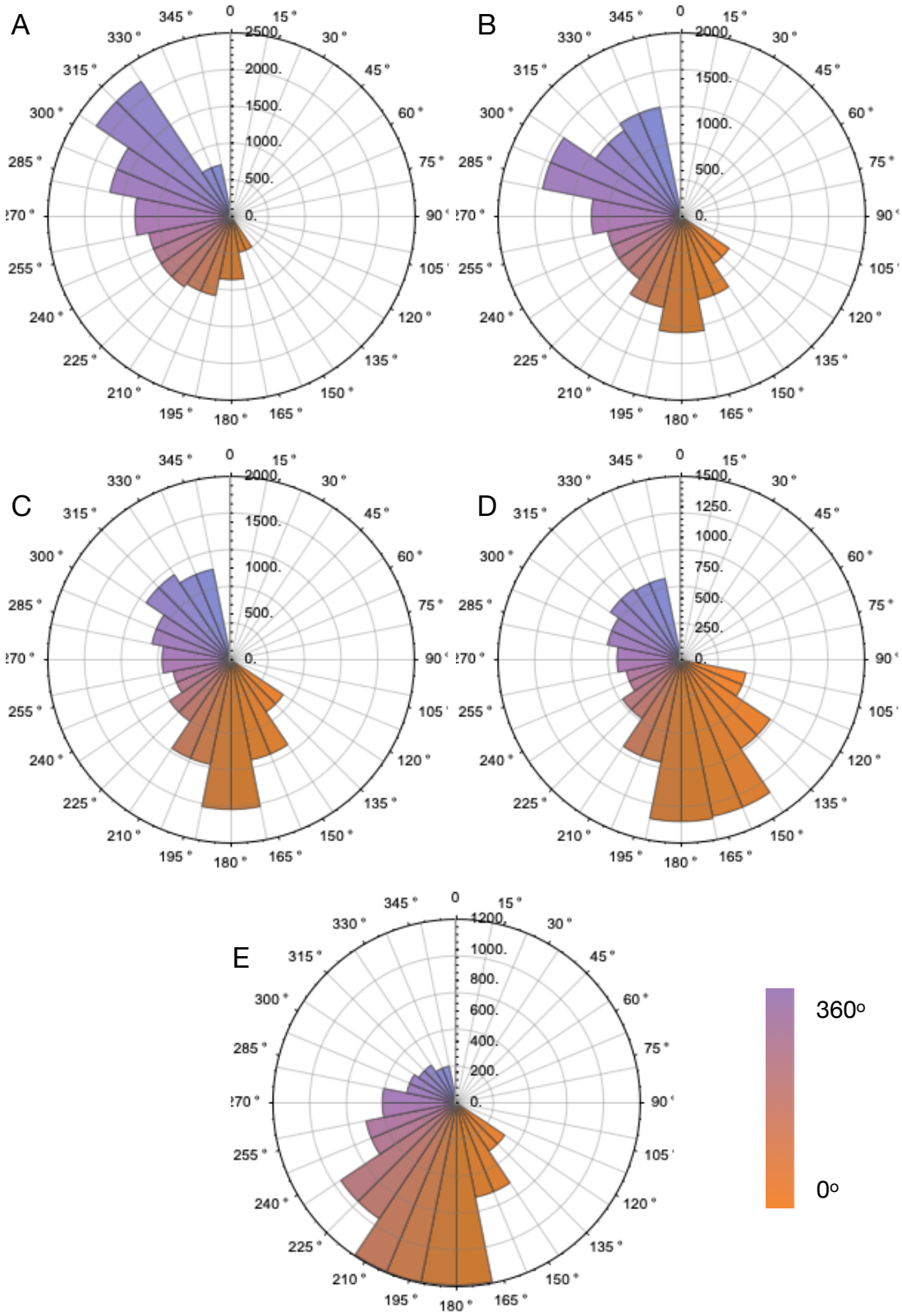

Figure G.VII Swell events number for buoys A to E on the month of July, radius shows the number of swell occurrences and its spectral angle of incidence.

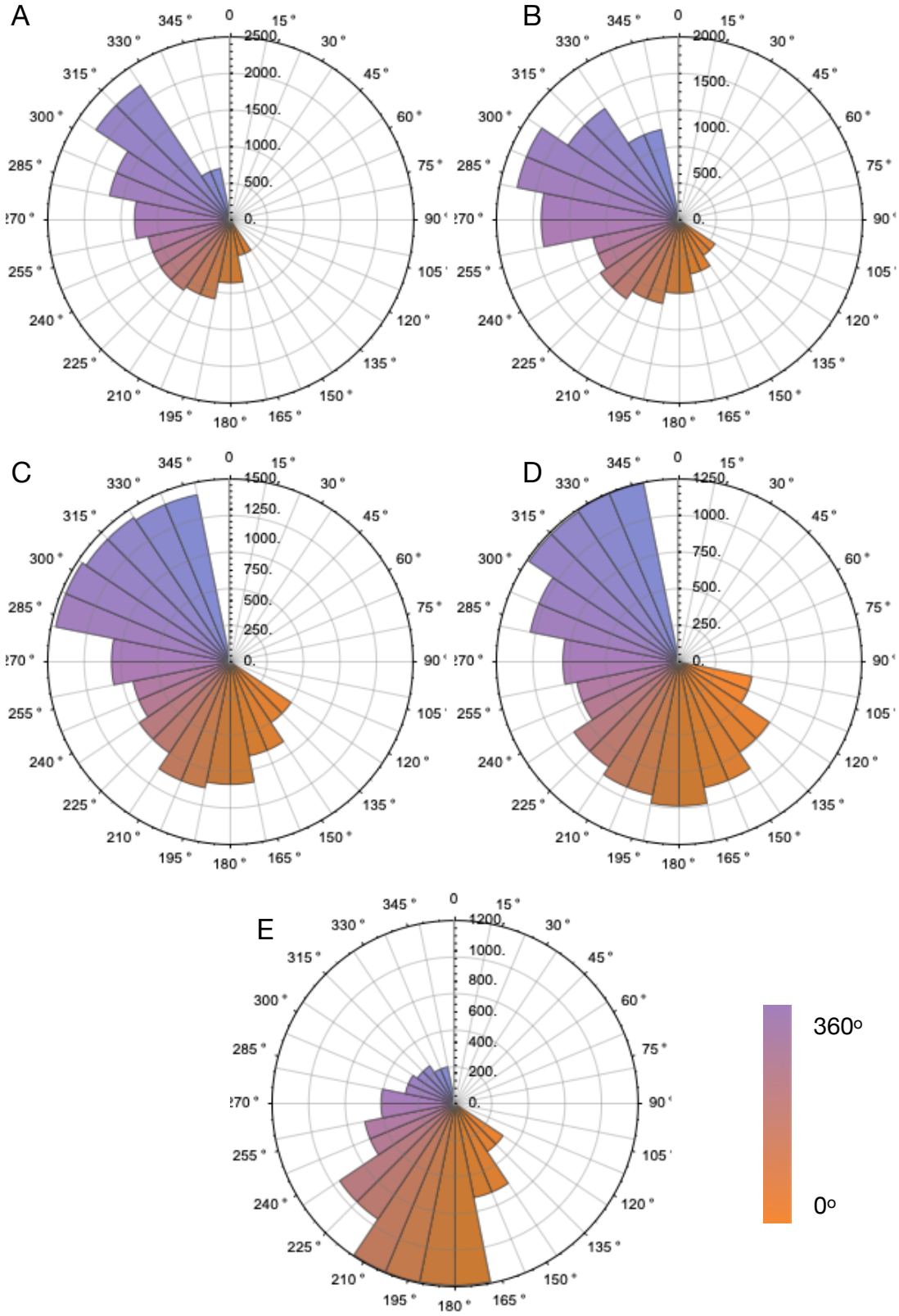

Figure G.VIII Swell events number for buoys A to E on the month of Aug, radius shows the number of swell occurrences and its spectral angle of incidence.

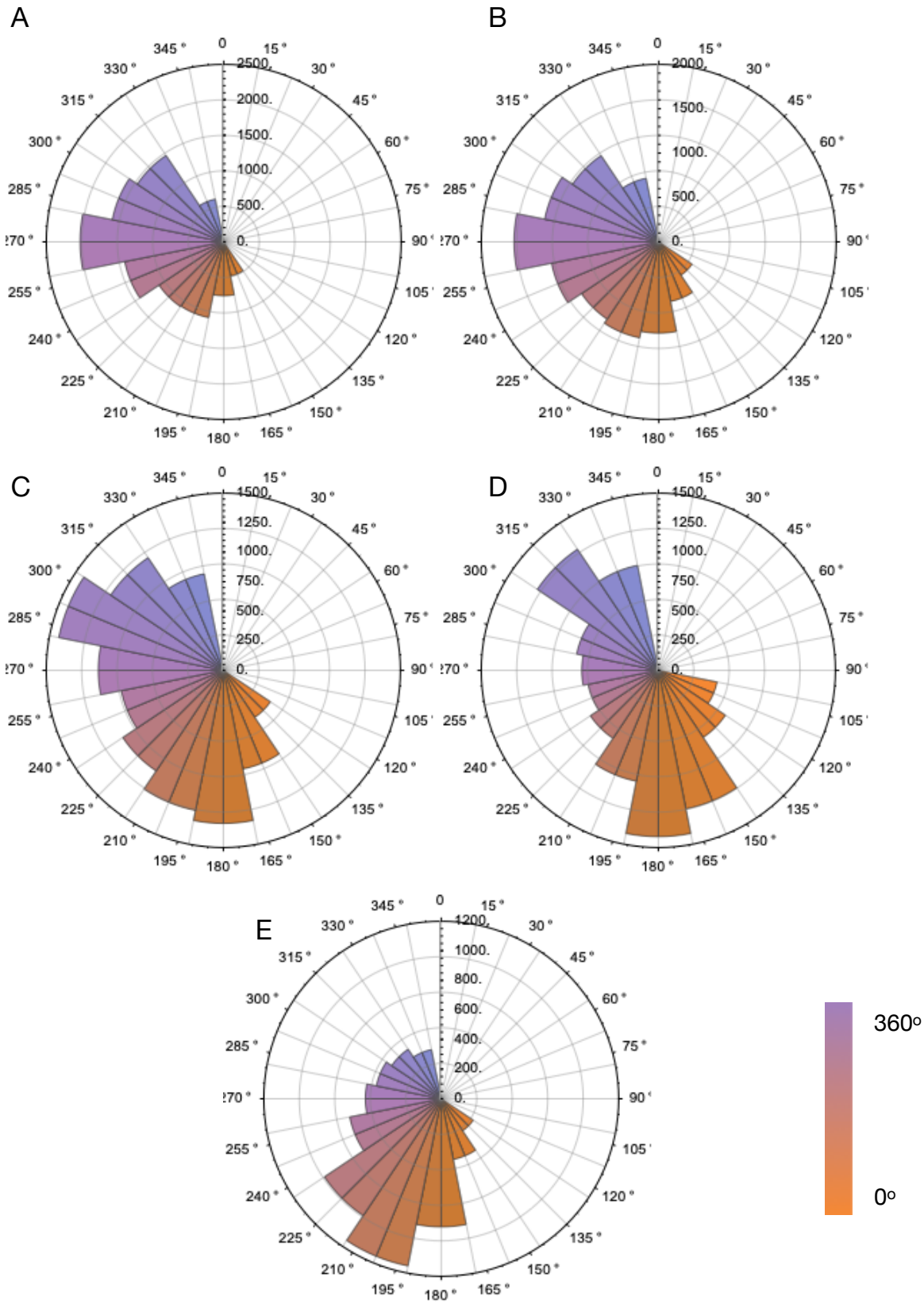

Figure G.IX Swell events number for buoys A to E on the month of Sep, radius shows the number of swell occurrences and its spectral angle of incidence.

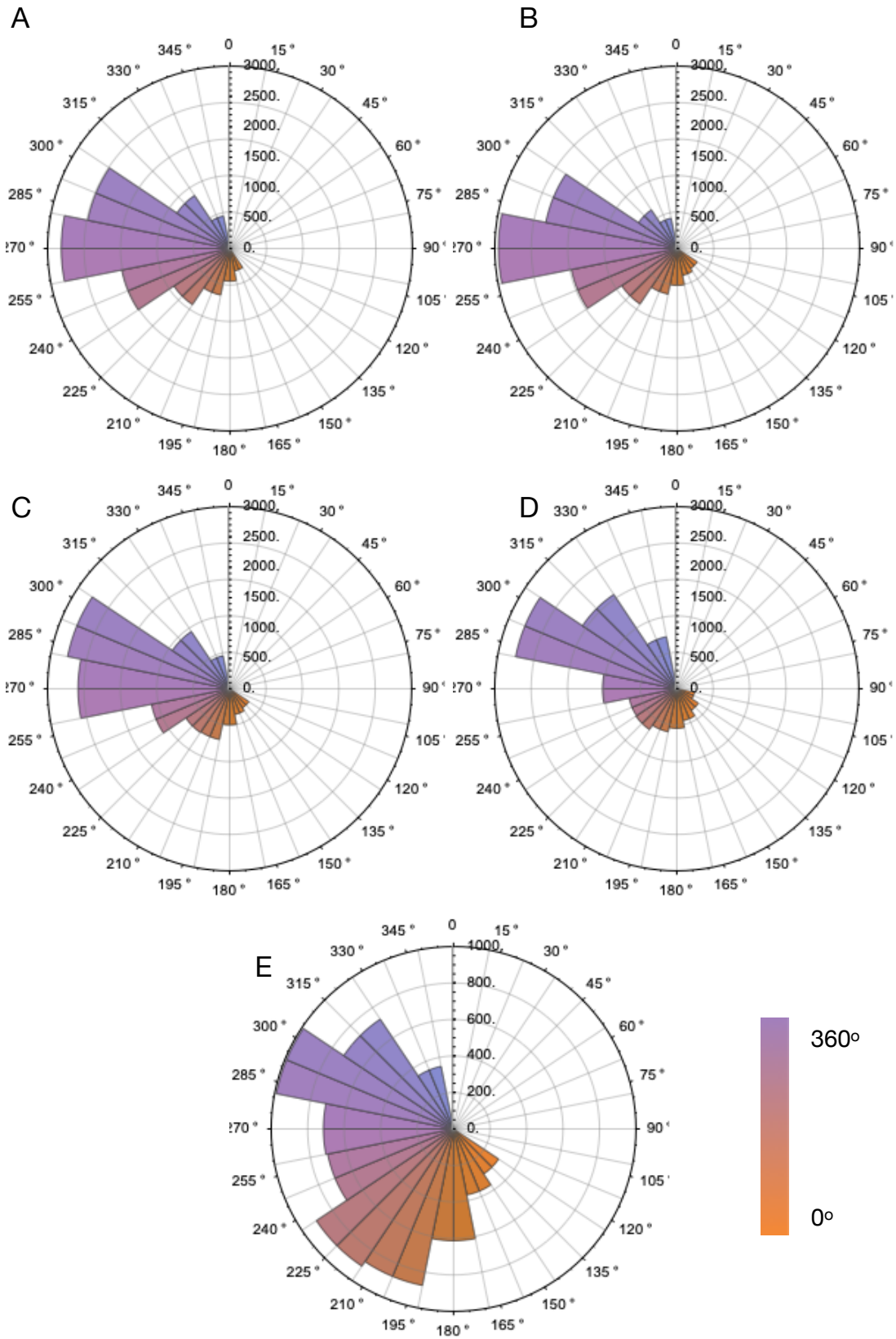

Figure G.X Swell events number for buoys A to E on the month of Oct, radius shows the number of swell occurrences and its spectral angle of incidence.

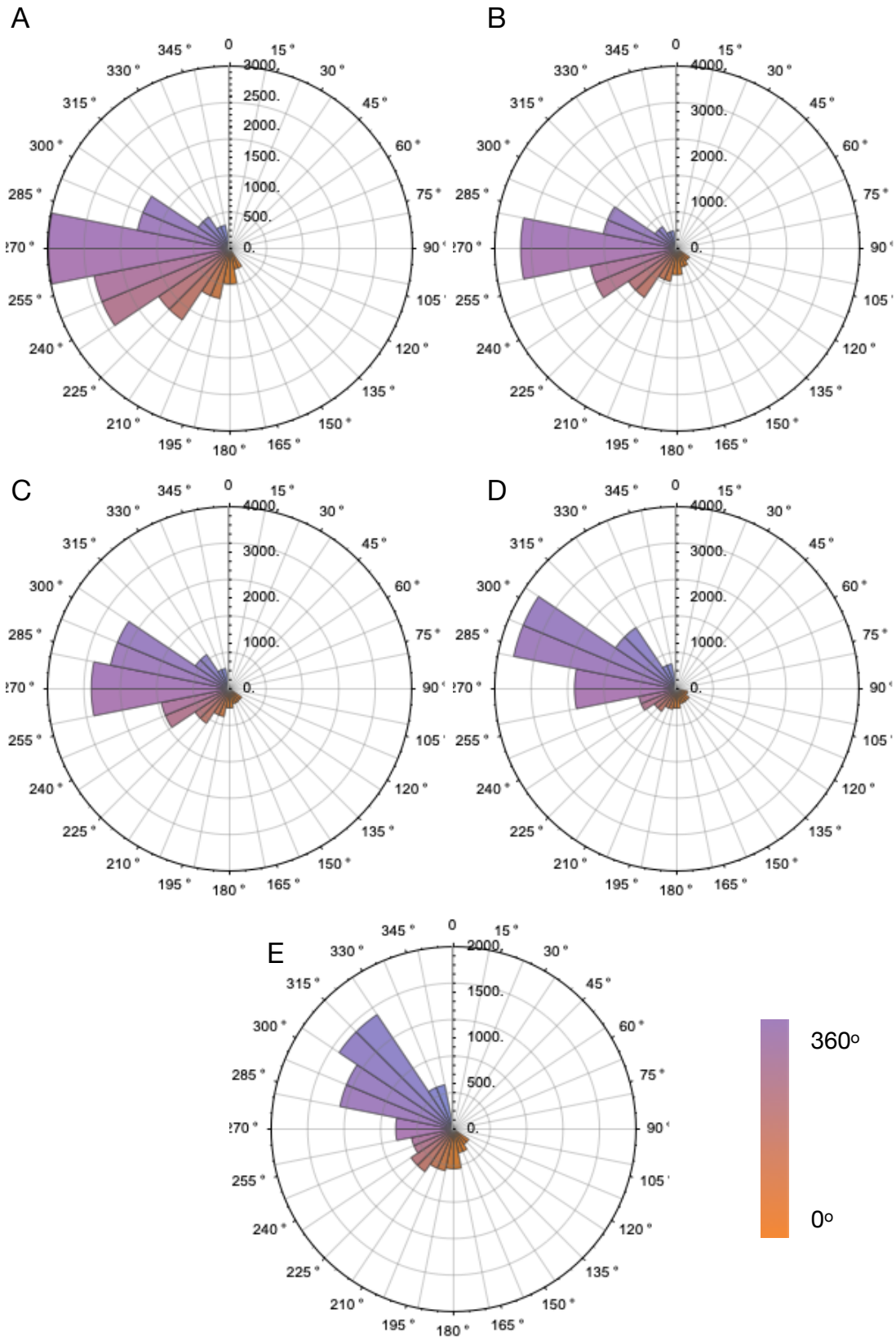

Figure G.XI Swell events number for buoys A to E on the month of Nov, radius shows the number of swell occurrences and its spectral angle of incidence.

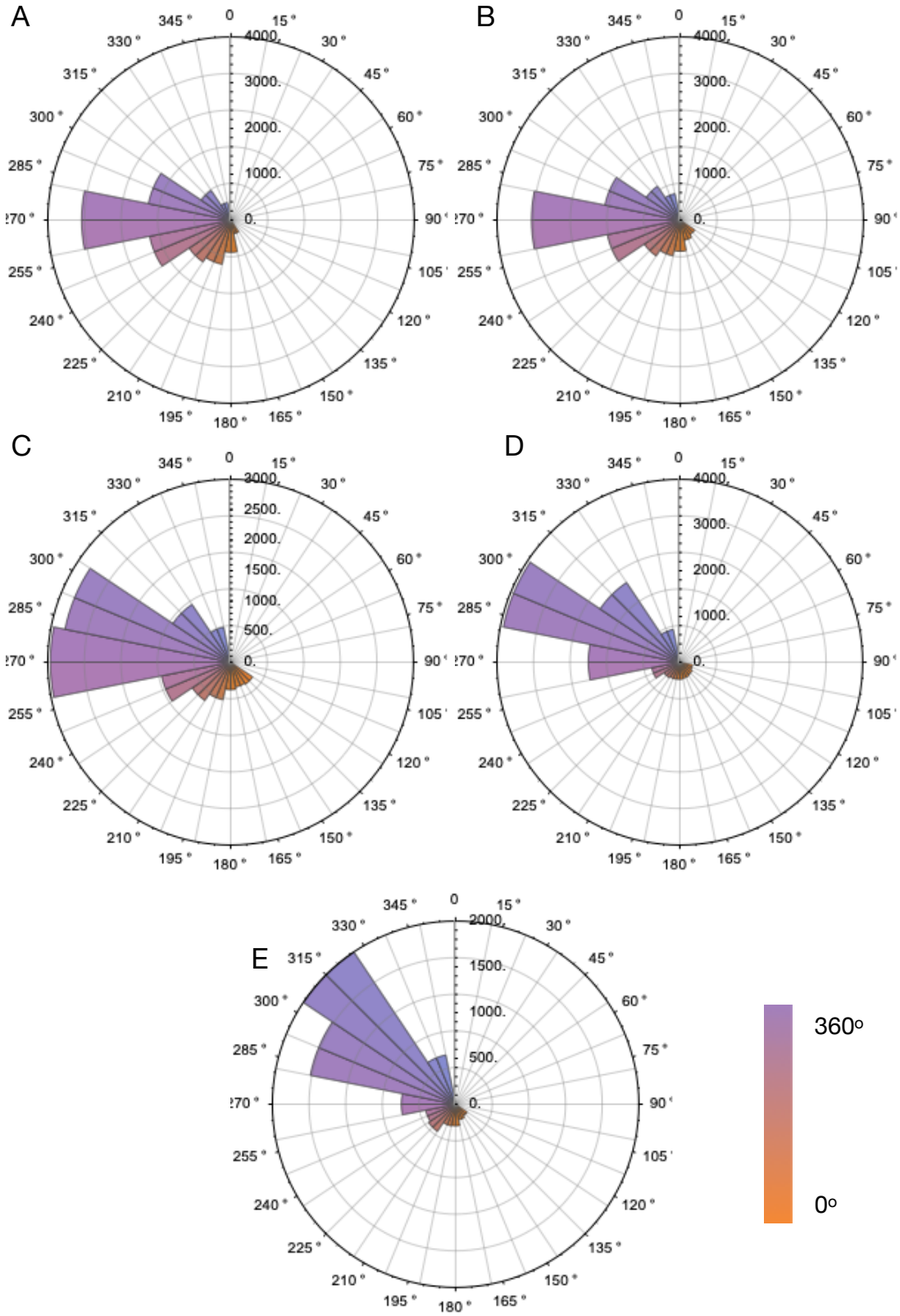

Figure G.XII Swell events number for buoys A to E on the month of Dec, radius shows the number of swell occurrences and its spectral angle of incidence.

Section H

Section H is composed of the maps used to compose the bathymetry profile of the Farallones area in the SF Bay region, the seeds used for the sensitivity analysis and the link to the ESRU software website containing the BEMT tool.

Data files:

Github: https://github.com/manelcamacho/SFBaythesis

Contains:

Point data file: dsf X, Y, Z file corresponding to the latitude, longitude and elevation of the terrain from 88X.XX meter elevation to -35XX meter depth.

Raster data file: dsfcontour Raster file that contains the interpolated points to create a 2D contour map.

Vector data files: dsf_depth and depth500to0 that contain the vector shape files to create a simplified bathymetry cut perpendicular to the coastline.

CVS data files: Files containing the latitude and longitude of the buoy systems along with their names.

Seed data files: https://github.com/manelcamacho/morrisseeds

ESRU website: https://www.esru.strath.ac.uk//applications/

Section I

Section I contains the tables for the mean values of all wavelengths detected for all experiments. The first table refers to the experiments where the obstacle has a constant length and decreases its depth. As also the maps of the case scenario. The maps correspond to the area of study in Chapter 7. Map I.1 is adapted from NOAA [140] and the direction to the GitHub service that contains the GIS files are in section H.

I1, Mean wavelengths values for and experiment where the obstacle blocks 1/6 of the tank's original depth at a constant length, all values are expressed in meters.

		T1	T2	T3	T4	T5	T6	T7
A	x	1.13743	1.31799	1.58793	1.82907	2.17459	3.48797	2.39818
	σ	0.195566	0.176692	0.0497626	0.0535513	0.017529	0.702308	0.540108
B	x	1.27436	1.40505	1.68485	1.89515	2.26669	3.20321	2.90734
	σ	0.162102	0.115268	0.12213	0.0759954	0.0558865	0.648636	0.50571
C	x	1.46741	1.4845	1.76072	1.96067	2.36088	2.8382	3.44271
	σ	0.151537	0.10803	0.182151	0.0857275	0.0266264	0.491769	0.38522

I2, Mean wavelengths values for and experiment where the obstacle blocks 2/6 of the tank's original depth at a constant length, all values are expressed in meters.

		T1	T2	T3	T4	T5	T6	T7
A	x	1.14795	1.38285	1.45817	1.70054	1.99996	4.02103	4.37234
	σ	0.0826228	0.60711	0.0432306	0.0869258	0.0137808	0.933449	0.825524
B	x	1.43429	1.46846	1.66305	1.85563	2.22585	3.6283	3.92938
	σ	0.0642133	0.3103	0.0739506	0.0781999	0.00490688	0.575983	0.50571
C	x	1.64574	1.61176	1.91243	2.01777	2.42634	3.42917	3.59118
	σ	0.0647102	0.0298121	0.0755227	0.101986	0.0338743	0.552256	0.38522

I3, Mean wavelengths values for and experiment where the obstacle blocks 1/2 of the tank's original depth at a constant length, all values are expressed in meters.

		T1	T2	T3	T4	T5	T6	T7
A	x	1.13743	1.31799	1.58793	1.82907	2.17459	3.48797	2.39818
	σ	0.195566	0.176692	0.0497626	0.0535513	0.017529	0.702308	0.540108
B	x	1.27436	1.40505	1.68485	1.89515	2.26669	3.20321	2.90734
	σ	0.162102	0.115268	0.12213	0.0759954	0.0558865	0.648636	0.50571
C	x	1.46741	1.4845	1.76072	1.96067	2.36088	2.8382	3.44271
	σ	0.151537	0.10803	0.182151	0.0857275	0.0266264	0.491769	0.38522

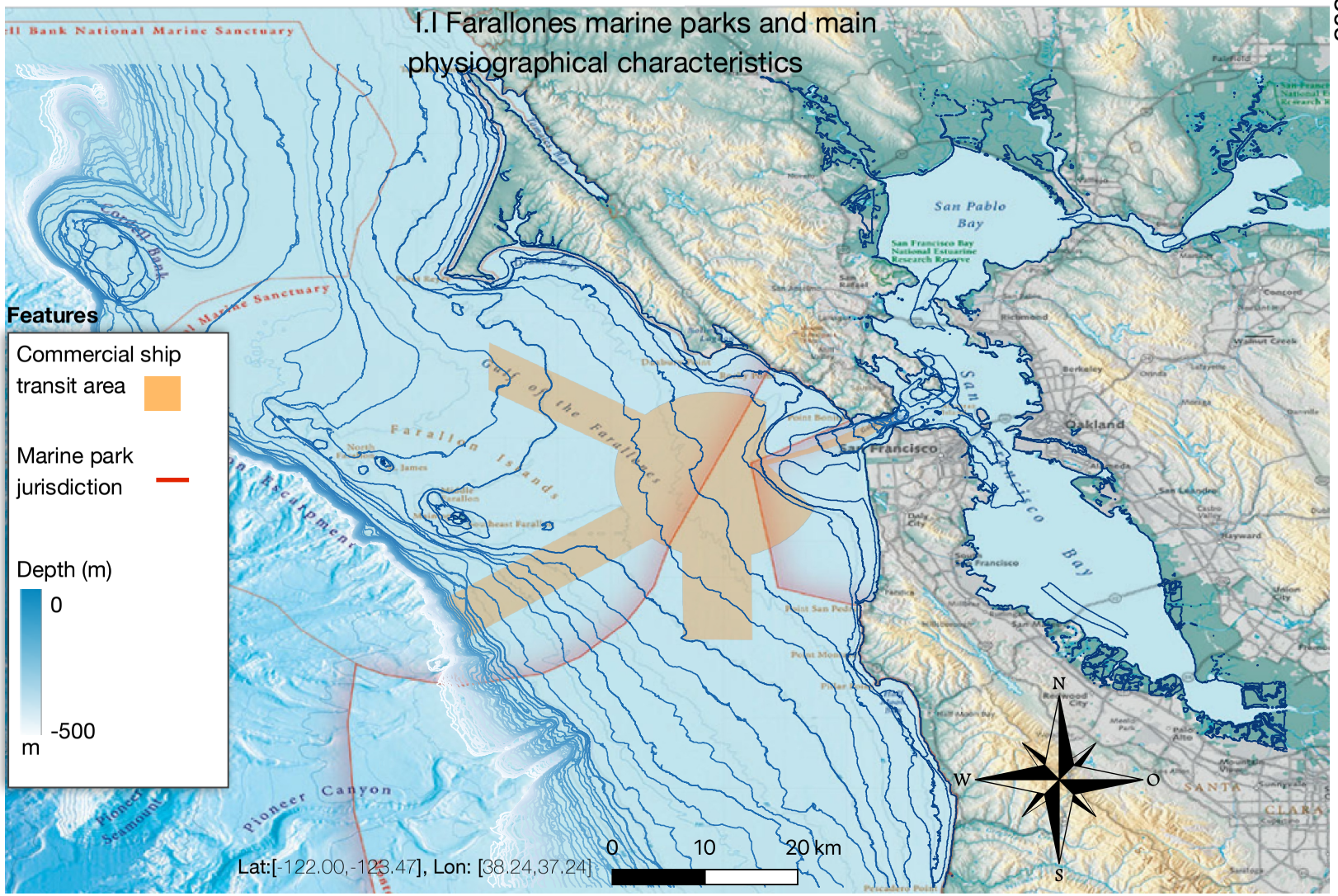
I.I Farallones marine parks and main physiographical characteristics
Features
Commercial ship transit area
Marine park jurisdiction
Depth (m)
0
-500
m
Cordell Bank
Gulf of the Farallones
Farallon Islands
Pioneer Canyon
San Pablo Bay
San Francisco Bay National Estuarine Research Reserve
San Francisco
Oakland
Berkeley
Richmond
Concord
Walnut Creek
Hayward
N
W
O
S
0
10
20 km
Lat:[-122.00,-123.47], Lon: [38.24,37.24]

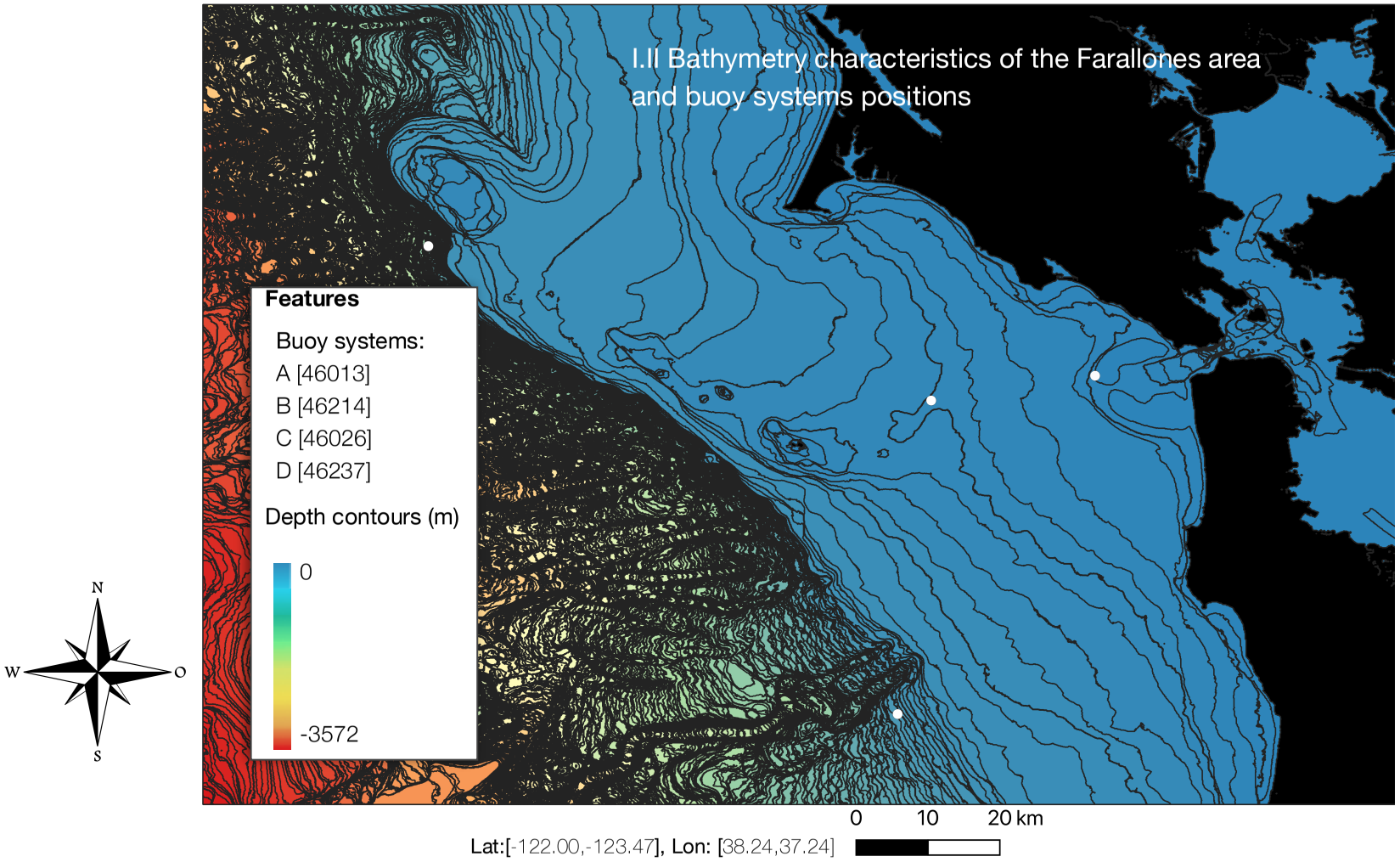
I.II Bathymetry characteristics of the Farallones area
and buoy systems positions
Features
Buoy systems:
A [46013]
B [46214]
C [46026]
D [46237]
Depth contours (m)
0
-3572
N
W
O
S
0
10
20 km
Lat:[-122.00,-123.47], Lon: [38.24,37.24]

Bibliography

1 IRENA, Global Renewables Outlook: Energy transformation 2050. 2020.

2 Mørk, G., Barstow, S., Mollison, D. & Cruz, J. 2008. The wave energy resources. In: Cruz, J. (ed.) Ocean Wave Energy – Current Status and Future Perspectives. Berlin, Heidelberg: Springer-Verlag.

3 IRENA, Innovation outlook: Ocean energy technologies. 2020.

4 W. E. Council, “World Energy Resources Marine Energy | 2016,” World Energy Resour., 2016, [Online]. Available: http://large.stanford.edu/courses/2018/ph240/rogers2/docs/wec-2016.pdf.

5 Draper S, Adcock TAA, Borthwick AGL, Houlsby GT. The extractable power from the Pentland Firth. Renew. Energy.

6 C. Garrett and P. Cummins, “The efficiency of a turbine in a tidal channel,” J. Fluid Mech., vol. 588, pp. 243–251, 2007, doi: 10.1017/S0022112007007781.

7 S. Draper, G. T. Houlsby, M. L. G. Oldfield, and A. G. L. Borthwick, “Modelling tidal energy extraction in a depth-averaged coastal domain,” IET Renew. Power Gener., vol. 4, no. 6, pp. 545–554, 2010, doi: 10.1049/iet-rpg.2009.0196.

8 T. A. A. Adcock, S. Draper, G. T. Houlsby, A. G. L. Borthwick, and S. Serhadlioğlu, “The available power from tidal stream turbines in the pentland firth,” Proc. R. Soc. A Math. Phys. Eng. Sci., vol. 469, no. 2157, 2013, doi: 10.1098/rspa.2013.0072.

9 D. Pugh and P. Woodworth, “Tidal analysis and prediction,” Sea-Level Sci., pp. 60–96, 2014, doi: 10.1017/cbo9781139235778.007.

10 B. L. Polagye, J. Epler, and J. Thomson, “Limits to the predictability of tidal current energy,” MTS/IEEE Seattle, Ocean. 2010, no. October, 2010, doi: 10.1109/OCEANS.2010.5664588.

11 I. Masters et al., “A comparison of numerical modelling techniques for tidal stream turbine analysis,” Energies, vol. 8, no. 8, pp. 7833–7853, 2015, doi: 10.3390/en8087833.

12 R. Fouquet, “Historical energy transitions: Speed, prices and system transformation,” Energy Res. Soc. Sci., vol. 22, pp. 7–12, 2016, doi: 10.1016/j.erss.2016.08.014.

13 Smil, V. (2000). ENERGY IN THE TWENTIETH CENTURY: Resources, Conversions, Costs, Uses, and Consequences. Annual Review of Energy and the Environment, 70, 261–285. https://doi.org/10.1146/annurev.energy.25.1.21

14 IEA, International Renewable Energy Agency, United Nations Statistics Division, The World Bank, & World Health Organization. (2019). Tracking SDG 7: The Energy Progress Report 2019. The World Bank, 176. https://trackingsdg7.esmap.org/

15 Young, O. R. (2011). Effectiveness of international environmental regimes: Existing knowledge, cutting-edge themes, and research strategies. Proceedings of the National Academy of Sciences of the United States of America, 108(50), 19853–19860. https://doi.org/10.1073/pnas.1111690108

16 Benzohra, O., Echcharqaouy, S. S., Fraija, F., & Saifaoui, D. (2019). Integrating wind energy into the power grid: Impact and solutions. Materials Today: Proceedings, 30(xxxx), 987–992. https://doi.org/10.1016/j.matpr.2020.04.363

17 Lehtola, T., & Zahedi, A. (2019). Solar energy and wind power supply supported by storage technology: A review. Sustainable Energy Technologies and Assessments, 35(February), 25–31. https://doi.org/10.1016/j.seta.2019.05.013

18 Amusat, O. O., Shearing, P. R., & Fraga, E. S. (2018). Optimal design of hybrid energy systems incorporating stochastic renewable resources fluctuations. Journal of Energy Storage, 15, 379–399. https://doi.org/10.1016/j.est.2017.12.003

19 Charlier, R. H., & Menanteau, L. (1997). The saga of tide mills. Renewable and Sustainable Energy Reviews, 1(3), 171–207. https://doi.org/10.1016/S1364-0321(97)00005-1

20 Charher, R. H., Menanteau, L., & Chaineux, M. P. (2004). The rise and fall of the tide mill. Ocean Sciences Bridging the Millennia: A Spectrum of Historical Accounts, 315–338.

21 Minchinton. (2017). Early Tide Mills : Some Problems Published by : The Johns Hopkins University Press and the Society for the History of Technology Stable URL : http://www.jstor.org/stable/3103639. 20(4), 777–786.

22 Stergiopoulou, A., & Stergiopoulos, V. (2013). Archimedes in cephalonia and in euripus strait: Modern horizontal archimedean screw turbines for recovering marine power. Journal of Engineering Science and Technology Review, 6(1), 44–51. https://doi.org/10.25103/jestr.061.09

23 Holmes, T. (1955). A History of the Passamaquoddy Tidal Power Project (3219). [MAster Thesis, University of Maine]. History Commons

24 Mecherikunnel, A. T., & Richmond, J. C. (1980). NASA Technical Memorandum 82021- Spectral Distribution of Solar Radiation. September 1980, 93.

25 G. D. Mehta, S. C. Jain, M. D. Fraser, S. J. Senatore, and H. L. Rothstein, “Salinity Gradient Energy Conversion.,” Ocean. Conf. Rec., no. June, pp. 566–571, 1979, doi: 10.1109/oceans.1979.1151215.

26 IEA. White Paper Ocean Thermal Energy Conversion. https://www.ocean-energy-systems.org/documents/15692-oes-white-paper-on-otec.pdf/

27 S. Goto, Y. Motoshima, T. Sugi, T. Yasunaga, Y. Ikegami, and M. Nakamura, “Construction of simulation model for OTEC plant using Uehara cycle,” Electr. Eng. Japan (English Transl. Denki Gakkai Ronbunshi), vol. 176, no. 2, pp. 1–13, 2011, doi: 10.1002/eej.21138.

28 International Renewable Energy Agency (IRENA), “Ocean Thermal Energy Conversion: Technology Brief,” IIRENA Ocean Energy Technol. Br. 1, no. June, p. 32, 2014, [Online]. Available: www.irena.org.

29 Mofor, L., Goldsmith, J., & Jones, F. (2014). Ocean Energy:Techmology Readiness, Patents, Deployment Status and Outlook. International Renewable Energy Agency IRENA, August, 76. http://www.irena.org/DocumentDownloads/Publications/IRENA_Ocean_Energy_report_2014.pdf

30 IRENA. (2014). Wave Energy Technology Brief. IRENA Ocean Energy Technology Brief 4, June, 28.

31 Mørk, G., Barstow, S., Kabuth, A., & Pontes, M. T. (2010). Assessing the global wave energy potential. Proceedings of the International Conference on Offshore Mechanics and Arctic Engineering - OMAE, 3(January), 447–454. https://doi.org/10.1115/OMAE2010-20473

32 Landau, L. D.,& Lifshits, E. M. (1959). Fluid mechanics. London: Pergamon Press.

33 Garrison, T. D. (2011). Essentials of Oceanography. Brooks Cole.

34 Owen, A. (2013). Tidal Current Energy. Origins and Challenges. Future Energy: Improved, Sustainable and Clean Options for Our Planet, 335–356. https://doi.org/10.1016/B978-0-08-099424-6.00016-8

35 Ouro, P., Harrold, M., Stoesser, T., & Bromley, P. (2017). Hydrodynamic loadings on a horizontal axis tidal turbine prototype. Journal of Fluids and Structures. https://doi.org/10.1016/j.jfluidstructs.2017.03.009

36 Nevalainen, T. M., Johnstone, C. M., & Grant, A. D. (2016). A sensitivity analysis on tidal stream turbine loads caused by operational, geometric design and inflow parameters. International Journal of Marine Energy, 16, 51–64. https://doi.org/10.1016/j.ijome.2016.05.005

37 Lavidas, G., Venugopal, V., & Friedrich, D. (2017). Wave energy extraction in Scotland through an improved nearshore wave atlas. International Journal of Marine Energy, 17, 64–83. https://doi.org/10.1016/j.ijome.2017.01.008

38 Neill, S. P., Lewis, M. J., Hashemi, M. R., Slater, E., Lawrence, J., & Spall, S. A. (2014). Inter-annual and inter-seasonal variability of the Orkney wave power resource. Applied Energy, 132, 339–348. https://doi.org/10.1016/j.apenergy.2014.07.023

39 Munk, W. H. (2010). Origin and Generation of Waves. Coastal Engineering Proceedings, 1, 1-4. https://doi.org/10.9753/icce.v1.1

40 Stewart, Robert. (2008). Introduction To Physical Oceanography. Orange Groove Books.

41 Lewis, M. J., Neill, S. P., Hashemi, M. R., & Reza, M. (2014). Realistic wave conditions and their influence on quantifying the tidal stream energy resource. Applied Energy, 136, 495–508. https://doi.org/10.1016/j.apenergy.2014.09.061

42 Saruwatari, A., Ingram, D., & Cradden, L. (2013). Wave-Current Interaction Effects on Marine Energy Converters. Ocean Engineering, 73, 106–118. https://doi.org/10.1016/j.oceaneng.2013.09.002

43 Faudot, C., & Dahlhaug, O. G. (2012). Prediction of wave loads on tidal turbine blades. Energy Procedia, 20, 116–133. https://doi.org/10.1016/j.egypro.2012.03.014

44 Mccann, G. N. (2007). Tidal current turbine fatigue loading sensitivity to waves and turbulence – a parametric study. EWTEC proceedings. 7.

45 Tatum, S. C., Frost, C. H., Allmark, M., Doherty, D. M. O., Prickett, P. W., Grosvenor, R. I., Byrne, C. B., & Doherty, T. O. (2016). International Journal of Marine Energy Wave – current interaction effects on tidal stream turbine performance and loading characteristics. 14, 161–179.

46 Nevalainen, T. (2017). The effect of unsteady sea conditions on tidal stream turbine loads and durability [Doctoral thesis, University of Strathclyde]. The University of Strathclyde: digital collections. http://digitool.lib.strath.ac.uk/R/?func=dbin-jump-full&object_id=27963

47 Fu, S., & Johnstone, C. (2017). Evaluating the Dynamics of Tension Mooring Supported Tidal Turbines. Proceedings of the 12th European Wave and Tidal Energy Conference, Cork, Ireland, 1, 1–8.

48 Semedo, A., SušElj, K., Rutgersson, A., & Sterl, A. (2011). A global view on the wind sea and swell climate and variability from ERA-40. Journal of Climate, 24(5), 1461–1479. https://doi.org/10.1175/2010JCLI3718.1

49 Jiang, H., & Chen, G. (2013). A global view on the swell and wind sea climate by the Jason-1 mission: A revisit. Journal of Atmospheric and Oceanic Technology, 30(8), 1833–1841. https://doi.org/10.1175/JTECH-D-12-00180.1

50 Adams, P. N., Inman, D. L., & Graham, N. E. (2008). Southern California Deep-Water Wave Climate: Characterization and Application to Coastal Processes. Journal of Coastal Research, 244(4), 1022–1035. https://doi.org/10.2112/07-0831.1

51 Snodgrass, F. E., Groves G. W., Hasselman K. F., Miller G. R., Munk W. H., Powers W. H. (1966). Propagation of ocean swell across the Pacific. Mathematical and Physical Sciences , 259, 431-497–1035.

52 Snodgrass, F. E., Munk W. H., Powers W. H. (1957).Measurements of southern swell at Guadalupe island. Mathematical and Physical Sciences, Deep Sea Research, 4, 272–286. https:// doi:10.1016/0146- 6313(56)90061-2

53 Snodgrass, Barber N. F. and Ursell F. 1948The generation and propagation of ocean waves and swell. I. Wave periods and velocitiesPhilosophical Transactions of the Royal Society of London. Series A, Mathematical and Physical Sciences, **240,** 527–560, http:// doi.org/10.1098/rsta.1948.0005

54 Sevedo, A., Sušelj, K., Rutgersson, A. (2009). Variability of Wind Sea and Swell Waves in the North Atlantic Based on ERA-40 Re-analysis. EWTEC proceedings. 8.

55 Storlazzi, C. D., Griggs, G. B. (2000) Influence of El Niño–Southern Oscillation (ENSO) events on the evolution of central California's shoreline. GSA Bulletin ; 112 (2): 236–249. https://doi.org/ 10.1130/0016-7606(2000)112<236:IOENOE>2.0.CO;2

56 Ikhennicheu, M. (2019). Étude expérimentale de la turbulence dans les zones à forts courants et de son impact sur les hydroliennes. [Doctoral thesis, Université de Lille]. Institut français de recherche pour l'exploitation de la mer. https://archimer.ifremer.fr/doc/ 00590/70177/68193.pdf

57 Holthuijsen, L.H. (2007). Waves in oceanic and coastal waters. Cambridge University Press.

58 Ursell, F. (1953). The long-wave paradox in the theory of gravity waves. Mathematical Proceedings of the Cambridge Philosophical Society, 49(04), 685. https://doi:10.1017/s0305004100028887

59 Hedges, T. S. (1995).Regions of validity for analytical water theories. Proceedings of the ICE - water maritime and energy, 112(2), 111-114. https://doi.org/10.1680/iwtme.1995.27656

60 Ardhuin, F., Collard, F., Chapron , B. (2009). Observations of swell dissipation across the ocean. Geophysical research letters, 36(3).https://doi.org/10.1029/2008GL037030

61 Babanin, A.V. (2012) Swell Attenuation due to Wave-Induced Turbulence. Proceedings of the ASME 2012 31st International Conference on Ocean, Offshore and Arctic Engineering. 2. 439-443. https://doi.org/10.1115/OMAE2012-83706

62 Young, I. R., A. V. Babanin, and S. Zieger (2013). The Decay Rate of Ocean Swell Observed by Altimeter. Journal of physical. Oceanography, 43, 2322–2333, https://doi.org/10.1175/JPO-D-13-083.1.

63 Ordonez-Sanchez, S., Porter, K., Frost, V., Allmark, M., Johnstone, C., O'Doherty, T. (2016). Effects of extreme wave-current interactions on the performance of tidal stream turbines. EWTEC proceedings. 3.

64 Draycott, S., Nambiar, A., Sellar, B., Davey, T., & Venugopal, V. (2019). Assessing extreme loads on a tidal turbine using focused wave groups in energetic currents. Renewable Energy, 135, 1013–1024. https://doi.org/10.1016/j.renene.2018.12.075

65 Martinez, R., Payne, G. S., & Bruce, T. (2018). The effects of oblique waves and currents on the loadings and performance of tidal turbines. Ocean Engineering, 164(May), 55–64. https://doi.org/10.1016/j.oceaneng.2018.05.057

66 Garrison, T., Ellis, R. (2016). Oceanography: An Invitation to Marine Science. Cengage Learning , https://doi.org/10.1201/9781315152929.

67 Prost, B., Prost, G. (2017).The Geology Companion Essentials for Understanding the Earth. Taylor and Francis, https://doi.org/10.1201/9781315152929.

68 Horace, L. (1945). Hydrodynamics, New York https://doi.org/10.1201/9781315152929.

69 Kreisel, H. (1949). Surface waves. Quart. Applied Mathematics., 7, 21-44.

70 Newman, J. N. (1965). Propagation of water waves over an infinite step. *Journal of Fluid Mechanics*, *23*(2), 399–415. https://doi.org/10.1017/S0022112065001453

71 Miles, J. W. (1967). Surface-wave scattering matrix for a shelf. Journal of Fluid Mechanics, 28(4), 755–767. https://doi.org/10.1017/S0022112067002423

72 Takano, K. (1960). Effets d'un obstacle parallelepipedique sur la propagation de la houle. LaHouille Blanche 15, 247-267.

73 Mei, C. C., & Black, J. L. (1969). Scattering of surface waves by rectangular obstacles in waters of finite depth. Journal of Fluid Mechanics, 38(3), 499–511. https://doi.org/10.1017/S0022112069000309

74 Macagno, E. O. (1954), Houle dans un canal présentant un passage en charge. La houille blanche. 9 , 10-37.

75 Seabra-Santos, F. J., Renouard, D. P., & Temperville, A. M. (1987). Numerical and experimental study of the transformation of a solitary wave over a shelf or isolated obstacle. Journal of Fluid Mechanics, 176, 117–134. https://doi.org/10.1017/S0022112087000594

76 Massel, S. R. (1983). Harmonic generation by waves propagating over a submerged step. Coastal Engineering, 7(4), 357–380. https://doi.org/10.1016/0378-3839(83)90004-2

77 Jolas, P. (1960). Passage de la houle sur un seuil. Houille Blanche, 2, 148–152. https://doi.org/10.1051/lhb/1960031

78 Szmidt, K. (2010). Finite Difference Analysis of Surface Wave Scattering by Underwater Rectangular Obstacles. Archives of Hydro-Engineering and Environmental Mechanics, 57(3), 179–198.

79 C. L. Ting, W. T. Chao, and C. C. Young, “Experimental investigation of nonlinear regular wave transformation over a submerged step: Harmonic generation and wave height modulation”, Coast. Eng., vol. 117, pp. 19–31, 2016, doi: 10.1016/j.coastaleng.2016.07.005.

80 Mason, M.A., Keulegan, G.H., 1944. A wave method for determining depths over bottom discontinuities. Tech. Memo. No. 5, U.S. Beach Erosion Board, Corps of Engineers, 29.

81 C. C. Mei and Ü. Ünluata, “Harmonic Generation in Shallow Water Waves,” Waves Beaches Resulting Sediment Transp., pp. 181–202, 1972, doi: 10.1016/b978-0-12-493250-0.50010-2.

82 Mason, M.A., Keulegan, G.H., 1944. A wave method for determining depths over bottom discontinuities. Tech. Memo. No. 5, U.S. Beach Erosion Board, Corps of Engineers, 29.

83 Jung, T.-H., & Cho, Y.-S. (2009). Analytical Approach for Long Wave Solution to an Arbitrarily Varying Topography. Journal of Coastal Research, 251(1), 216–223. https://doi.org/10.2112/07-0930.1

84 Xie, J. J., Liu, H. W., & Lin, P. (2012). Analytical solution for long-wave reflection by a rectangular obstacle with two scour trenches. Journal of Engineering Mechanics, 137(12), 919–930. https://doi.org/10.1061/(ASCE)EM.1943-7889.0000293

85 Belibassakis, K. A., Athanassoulis, G. A. (2006). A coupled-mode technique for weakly nonlinear wave interaction with large floating structures lying over variable bathymetry regions. *Applied Ocean Research*. https://doi.org/10.1016/j.apor.2005.12.003

86 Belibassakis, K., Athanassoulis, G. A. (2002). Extension of second-order Stokes theory to variable bathymetry. *Journal of Fluid Mechanics, 464*, 35-80. doi:10.1017/S0022112002008753

87 Goring, G. D. (1978).Tsunamis the propagation of long waves onto a shelf. [Doctoral thesis, California Institute of technology], https://thesis.library.caltech.edu/10524/

88 Marshall, J. S., Naghdi, P. M. (1990). Theoretical and Computational Fluid Dynamics Wave Reflection and Transmission by Steps and Rectangular Obstacles in Channels of Finite Depth 1. Theoretical and Computational Fluid Dynamics, 287–301.

89 Masters, I., Chapman, J. C., Willis, M. R., & Orme, J. A. C. (2011). A robust blade element momentum theory model for tidal stream turbines including tip and hub loss corrections. *Journal of Marine Engineering and Technology*, *10*(1), 25–35. https://doi.org/10.1080/20464177.2011.11020241

90 Togneri, M., & Masters, I. (2014). Synthetic Turbulence Generation for Turbine Modelling with BEMT. Proceedings of Oxford energy workshop, 3.

91 Masters, I., Williams, A., Croft, T. N., Togneri, M., Edmunds, M., Zangiabadi, E., Fairley, I., & Karunarathna, H. (2015). A comparison of numerical modelling techniques for tidal stream turbine analysis. *Energies*, *8*(8), 7833–7853. https://doi.org/10.3390/en8087833

92 Manwell, J. F.,McGowan, J. G., Rogers, A. L. (2010).Wind Energy Explained: Theory, Design and Application. John Wiley & Sons, https://10.1002/9781119994367

93 Fenton, J. D., McKee, W. D. (1990). On calculating the lengths of water waves. Coastal Engineering, 14(6), 499–513. https://doi.org/10.1016/0378-3839(90)90032-R

94 le Mehaute, B. (1976). *An introduction to hydrodynamics and water waves.* 85567. https://doi.org/10.1007/978-3-642-85567-2 ++

95 Bender, C. J., Dean, R. G. (2003). Wave transformation by two-dimensional bathymetric anomalies with sloped transitions. *Coastal Engineering*, *50*(1–2), 61–84. https://doi.org/10.1016/j.coastaleng.2003.08.002

96 Dean, R. G. (1964).Long Wave Modification by Linear Transitions. Journal of the Waterways and Harbors Division, 90(1), 1–30.

97 Naghdi, P. M., Green A. E. (1976). Directed Fluid Sheets. Royal society, 347(1651), 447-473. https://doi.org/10.1098/rspa.1976.0011

98 Buckley, W. H., Green A. E. (1988). Extreme and climatic wave spectra for use in structural design of ships. Naval Engineers Journal, 100(5), 36–58. https://doi:10.1111/j.1559-3584.1988.tb01523.x

99 Earle, M. D. (1996). Nondirectional and Directional Wave Dat Analysis Procedures. NDBC Technical Document 96-01. 002(January).

100 Gerling, T. W. (1992).Partitioning Sequences and Arrays of Directional Ocean Wave Spectra into Component Wave Systems. Journal of Atmospheric Oceanic Technology. 9(4): 444–458.

101 Gilhousen, D. B., (1987): A field evaluation of NDBC moored buoy winds. J. Atmos. Oceanic Technol., 4, 94–104.

102 Pierson, W. J. and L. Moskowitz, (1964). A proposed spectral form for fully developed wind-seas based on the similarity theory of S. A. Kitaigorodskii. *J. Geophys. Res.*, 69(24), 5181–5190.

103 Hasselmann K., Barnett T. P., Bouws E., Carlson H., Cartwright D. E., K. Enke, Ewing J. A., Gienapp H., Hasselmann D. E., Kruseman P., Meerburg A., Muller P., Olbers D. J., Richter K., Sell W., Walden H. , (1973). Measurements of Wind-Wave Growth and Swell Decay during the Joint North Sea Wave Project (JONSWAP). Deutsche hydrographische Zeitschrift. 8(12), 1-94.

104 Morris, M. D. (1991). Factorial Sampling Plans for Preliminary Computational Experiments (Vol. 33, Issue 2). ++

105 Bendykowska,G., (1980). Wave transmission due to its propagation over a submerged step. Archive. Hydrotechnology., 2,171– 187.

106 Charland, J. (2014). Modélisation de la propagation de la houle en présence d'un courant inhomogène et au-dessus d'une topographie variable, [Doctoral thesis, Université de Toulon], https://tel.archives-ouvertes.fr/tel-01135889/document.

107 Noble, D. R., Draycott, S., Davey, T. A. D., & Bruce, T. (2017). Design diagrams for wavelength discrepancy in tank testing with inconsistently scaled intermediate water depth. *International Journal of Marine Energy*, *18*, 109–113. https://doi.org/10.1016/j.ijome.2017.04.001 ++

108 Jiang, X., Day, S., & Clelland, D. (2018). Hydrodynamic responses and power efficiency analyses of an oscillating wave surge converter under different simulated PTO strategies. *Ocean Engineering*, *170*, 286–297. https://doi.org/10.1016/j.oceaneng.2018.10.050 ++

109 The National Oceanography Centre. The UK Marine Science and Technology Compendium. https://naqbase.noc.ac.uk/institution/university-strathclyde-naval-architecture-ocean-and-marine-engineering/equipment/henry ++

110 Galvin, C. J. (1964). WAVE-HEIGHT PREDICTION IN SHALLOW WATER.

111 Lawrence, J., Holmes, B., Bryden, I., Magagna, D., Torre-Enciso, Y., Rousset, J.-M., Smith, H., Paul, M., Margheritini, L., & Cândido, J. (2012). Wave Instrumentation Database. MARINET Report, 60.

112 ITTC (2014). Recommended Procedures and Guidelines ITTC. https://ittc.info/media/1323/75-02-07-032.pdf

113 Ohana, J., & Bourdier, S. (2014). Tank test related instrumentation and best practice. MARINET Report. https://archimer.ifremer.fr/doc/00214/32572/

114 Ting, F. C. K., & Kim, Y.-K. (1994). COASTAL ENGINEERING Vortex generation in water waves propagating over a submerged obstacle.

115 Dixon, S. L., & Hall, C. A. (2014). Wind Turbines. In *Fluid Mechanics and Thermodynamics of Turbomachinery* (pp. 419–485). Elsevier. https://doi.org/10.1016/B978-0-12-415954-9.00010-3

116 Stokes G. G. (1847). On the theory of oscillatory waves. Trans. Camb. Phil. Soc. 8, 441455. http://pordlabs.ucsd.edu/wryoung/theorySeminar/pdf15/Stokes1847.pdf

117 Porter, K., Ordonez-Sanchez, S., Nevalainen, T., Fu, S., & Johnstone, C. (2016). Comparative Study of Numerical Modelling Techniques to Estimate Tidal Turbine Blade Loads. Proc. of 3rd Asian Wave & Tidal Energy Conference.

118 Ordonez-Sanchez, S., Porter, K., Ellis, R., Frost, C., Allmark, M., Doherty, T. O., & Johnstone, C. (2017). Numerical modelling techniques to predict rotor imbalance problems in tidal stream turbines. Proc. of 12th European Wave & Tidal Energy Conference.

119 Tangier, J. L., Somers, D. M. . (1984). *NREL Airfoil F es for HAWTs.* https://www.nrel.gov/docs/legosti/old/7109.pdf.

120 Barltrop, N., Varyani, K. S., Grant, A., Clelland, D., & Pham, X. P. (2007). Investigation into wave-current interactions in marine current turbines. *Proceedings of the Institution of Mechanical Engineers, Part A: Journal of Power and Energy*, *221*(2), 233–242. https://doi.org/10.1243/09576509JPE315

121 Max D. Morris (1991) Factorial Sampling Plans for Preliminary Computational Experiments, Technometrics, 33:2, 161-174, DOI: 10.1080/00401706.1991.10484804

122 Campolongo, F., Cariboni, J., & Saltelli, A. (2007). An effective screening design for sensitivity analysis of large models. *Environmental Modelling and Software*, *22*(10), 1509–1518. https://doi.org/10.1016/j.envsoft.2006.10.004

123 Wentworth, M. T., Smith, R. C., & Banks, H. T. (2016). Parameter selection and verification techniques based on global sensitivity analysis illustrated for an HIV model. *SIAM-ASA Journal on Uncertainty Quantification*, *4*(1), 266–297. https://doi.org/10.1137/15M1008245

124 Chen, G., Chapron, B., Ezraty, R., Vandemark, D., (2002) A Global View of Swell and Wind Sea Climate in the Ocean by Satellite Altimeter and Scatterometer. J. Atmos. Oceanic Technol., 19, 1849–1859, https://doi.org/10.1175/1520-0426(2002)019<1849:AGVOSA>2.0.CO;2.

125 McMillan, J., Lickley, M. (2008). The Potential of Tidal Power from the Bay of Fundy. SIAM Undergraduate Research Online, 20–37. https://doi.org/10.1137/08S010062.

126 Neil, J., Hassard, J., & Jones, A. T. (2003). Tidal power for San Francisco. Oceans 2003: Celebrating the Past... Teaming Toward the Future, 1, 7–9. https://doi.org/10.1109/OCEANS.2003.284394

127 Chen, G., Jiang, H., Stopa, J. E., Wang, H., Houston, R., Mouche, A., Chapron, B. (2016). Tracking the attenuation and nonbreaking dissipation of swells using altimeters. Journal of Geophysical Research., 121(2), 1446–1458, https://doi.org/10.1002/2015JC011536

128 Young, I. R., Donelan, M. A. (2018). On the determination of global ocean wind and wave climate from satellite observations. Remote Sensing of Environment, 215(March), 228–241. https://doi.org/10.1016/j.rse.2018.06.006

129 Young, I. R., Sanina, E., & Babanin, A. V. (2017). Calibration and cross validation of a global wind and wave database of altimeter, radiometer, and scatterometer measurements. Journal of Atmospheric and Oceanic Technology, 34(6), 1285–1306. https://doi.org/10.1175/JTECH-D-16-0145.1

130 Herbers, T. H. C., Hendrickson, E. J., & O'Reilly, W. C. (2000). Propagation of swell across a wide continental shelf. Journal of Geophysical Research: Oceans, 105(C8), 19729–19737. https://doi.org/10.1029/2000jc900085

131 Gon, C. J., MacMahan, J. H., Thornton, E. B., & Denny, M. (2020). Wave dissipation by bottom friction on the inner shelf of a rocky shore. Journal of Geophysical Research: Oceans. https://doi.org/10.1029/2019jc015963

132 Troen, I. and E.L. Petersen (1989). European Wind Atlas. Risø National Laboratory, Roskilde. 656 pp. ISBN 87-550-1482-8.

133 Spring, S. (2011). NOAA Technical Memorandum NOS CS 24 SKILL ASSESSMENT OF THE DELAWARE RIVER AND BAY OPERATIONAL FORECAST SYSTEM (DBOFS).

134 Spring, S. (2011). THE SECOND GENERATION CHESAPEAKE BAY OPERATIONAL FORECAST SYSTEM (CBOFS2): MODEL DEVELOPMENT AND SKILL ASSESSMENT.

135 Spring, S. (2011). THE TAMPA BAY OPERATIONAL FORECAST SYSTEM (TBOFS): MODEL DEVELOPMENT AND SKILL ASSESSMENT.

136 Noble, M., Ramp, S. R., Kinoshita, K., & Geological Survey (U.S.). (1992). Current patterns over the shelf and slope adjacent to the Gulf of the Farallones executive summary. Open-File Report 92-382.

137 Steger, J. M., Schwing, F. B., Collins, C. A., Rosenfeld, L. K., Garfield, N., & Gezgin, E. (2000). The circulation and water masses in the Gulf of the Farallones. Deep-Sea Research Part II: Topical Studies in Oceanography, 47(5–6), 907–946. https://doi.org/10.1016/S0967-0645(99)00131-9

138 Muhammad, K., (2012). Characterization of the vertical structure of tidal currents in the Golden Gate (San Francisco) inlet. [Master's thesis, California naval postgraduate school], https://apps.dtic.mil/sti/citations/ADA573936

139 NOAA. OFS. Retrieved April 10, 2021, from https://tidesandcurrents.noaa.gov/models.html

140 NOAA. Monterey Bay. Retrieved June 12, 2018, from https://sanctuaries.noaa.gov/about/maps.html